FREEZE-THAW ENVIRONMENT OF PRECAST CONCRETE CROSSTIES AND EFFECT OF VIBRATION ON FRESH MATERIALS

BY

DANIEL I. CASTANEDA

DISSERTATION

Submitted in partial fulfillment of the requirements
for the degree of Doctor of Philosophy in Civil Engineering
in the Graduate College of the
University of Illinois at Urbana-Champaign, 2016

Urbana, Illinois

Doctoral Committee:

Professor David A. Lange, Chair
Associate Professor Kyle A. Riding, Kansas State University
Assistant Professor Randy H. Ewoldt
Professor John S. Popovics
Associate Professor Paramita Mondal

ABSTRACT

High performance concrete is typically designed to achieve high strength and low permeability. These suppositions lead practitioners to install high performance concrete in outdoor environments assured that members will remain durable over scores of years. One such outdoor environment is in railroad lines where timber ties (alternatively known as crossties or sleepers) are being replaced with high performance concrete crossties. Additionally, concrete crossties are being installed in burgeoning high speed rail networks across the United States of America. It has been observed, however, that these high performance concrete crossties are subject to multiple deterioration mechanisms including freeze-thaw damage. This early degradation in critical transportation infrastructure necessitates a better understanding of the durability of high performance concrete in wet, wintry climates.

In particular, the concrete crossties have been found to degrade at the rail seat area where the crosstie is physically joined to the rail. Among several failure mechanisms, including abrasion and hydraulic pressure cracking, it is hypothesized that the dense configuration of the rail line, pad, clips, and crosstie leads to pooling of water at the underside of the pad. This stagnant water sits atop the concrete crosstie at the rail seat area and can permeate into the material leading to scaling and freezing-thawing damage in colder climates.

In this study, the resiliency of high performance concrete crossties against freezing-thawing damage is assessed in a collaborative effort with researchers at Kansas State University and the University of Illinois at Urbana-Champaign. In this dissertation, specifically, the extent of internal moisture and temperature fluctuations of instrumented crossties installed in ballast is examined. Half-space approximations are applied to predict the fluctuation of internal conditions as affected by external environmental conditions. Additionally, this dissertation also examines the stability of chemically entrained air bubbles in fresh concrete when the fresh material is subjected to varying time and degree of vibration. The propagation and attenuation of the vibratory peak acceleration as a function of distance from the vibrating source and the volume content of aggregate is studied and compared against the extent of air loss and aggregate segregation as evidenced in polished, 2-dimensional sections.

Summarily, the mutual instances of critical moisture saturation and freezing temperatures in concrete crossties are experimentally measured and predicted. The predictive models are modified to create a concrete crosstie freeze-thaw susceptibility index based on historical weather data. This susceptibility index better informs owners of concrete crosstie infrastructure of environmental design criteria for freezing-thawing damage potential. The vibratory experimental results lend insight into rheological phenomenon that can to enhanced guidelines for the consolidation of non-conventional concrete that optimizes compaction while mitigating the loss of entrained air and aggregate segregation. Taken together, these two research thrusts enhance the civil engineering community's understanding of the durability and resiliency of high performance concrete exposed to cold climates.

ACKNOWLEDGEMENTS

I greatly thank the principal investigators, David A. Lange and Kyle A. Riding, and doctoral committee members, John S. Popovics, Randy H. Ewoldt, and Paramita Mondal, for supervising and offering constructive feedback of my dissertation research. I also thank Cameron Stuart, Program Manager of High Speed Rail Research and Development at the United States Department of Transportation Federal Railroad Administration, for financially supporting this study. I also thank the project's industrial partners: Jim Parsley of LB Foster CXT Concrete Ties, and Nigel Peters of CN Railway.

This dissertation was greatly enhanced by the extensive amount of collaboration and assistance of other persons. At the University of Illinois at Urbana-Champaign, I thank graduate students Jeremy Koch, Yu Song, and Ruofei Zou; and I also thank undergraduate students Ivan Chung, Clare Curtin, Mark Keller, Sarah Klarich, Josh Kohlenbrener, Kevin Kuntz, Marvin Lim, Nanaissa Maiga, and Kevin Marks. At Kansas State University, I thank graduate students Mohammed Albahttiti and Ahmad Ghadban. At the University of British Columbia, Okanagan, I thank Professors Gord Lovegrove and Ahmad Rteil, and I also thank graduate students Trevor Billows and Kyle Stratton.

My life was also vastly simplified by the supportive staff within the Civil and Environmental Engineering Department. In particular, I thank Tim Prunkard, Jamar Brown, Marc Killion, and Jim Meister from the machine shop; Sue Lowry, Jim Reeder, and Catherine Somers from the business office; and materials area secretaries Robin Ray, Flannery Ellis, and Donna Schubert.

I could not have kept my sanity without Mary Russell and staff at the Counseling Center for their much needed help during the final, stressful months of my dissertation.

I am also greatly thankful to my friends at the U of I who have come and gone over the years: Armen Amirkhanian, James Bittner, Amanda Bordelon, Ian Bradley, Alex Brand, Piyush Chaunsali, Jaime Clark, Emily van Dam, Eshan Dave, Federico Figueroa, Carolina Fineman, Martin Geiger, Elaine Giron, Justin Grasse, Tim Gregor, Kerry Hall, Ali Hamed, Nicole Helregel, Jacob Henschen, Will Hunnicutt, Hyungu Jeong, Andres Jurado, Jaymie Kaiser, Eric Kim,

Seungmin Lim, Ana Martinez, Jason Mote, Ranjani MV, Scott Parker, Tarun Prabhu, Sravanthi Puligilla, Emily Purcell, Ofelia Romero, Rich Santos, Agustin Spalvier, Jeevaka Somaratna, Pete Stynoski, Raul Tenorio, Travis Welt, Bill Wilson, and Bin Zhang. You all encouraged my alcoholism at some point or another for which I am eternally grateful.

And of course, my family and closest friends will support me no matter what I do. My mother, Guadalupe, and father, Julio; my three sisters: Valeria (and brother-in-law Luis), Jacqueline, and Priscilla; my aunts: Lourdes and Mercedes; my cousins: Fidel, Susy, Karina, Ivan, and Francisco; and good friends: Erika, Carlota, and Steffany. Go Bears!

The last person I want to acknowledge and thank is Pronoy Rai. I am happy to have found you at this point in my life!

TABLE OF CONTENTS

CHAPTER 1 – INTRODUCTION

1.1 Introduction

The United States is increasingly moving toward the construction of a national high speed rail network. The implementation of high speed rail within the United States is currently being accomplished through track upgrades or the construction of new rail lines with longer stretches of straight track and re-alignment of old track to have larger radii of curvature. Along with upgrades of old track and construction of new track, high performance concrete crossties (also known as sleepers) are replacing timber ties because of their improved rigidity, higher strength, reduced cost of maintenance, and longer service life [Zeman, 2010]. However, structural and material degradation has been observed in concrete crossties several short years after installation in ballast. This early degradation is particularly problematic at the rail seat area where the Federal Railroad Administration (FRA) has guidelines stating that 3/8" lateral movement of the rail line at the rail seat necessitates replacement of the concrete crosstie in its entirety [49 C.F.R. §213.335].

The observed rail seat deterioration (RSD) is attributed to several structural and material factors including "the presence of water, high tonnage (static wheel loads larger than 25,000 lbs), steep track grades," and track with curves greater than two degrees [Hanna, 1979]. One material-degradation hypothesis is that there is an excess amount of liquid moisture that becomes entrapped at the rail seat due to the confining geometry of the polyurethane pad between the rail and concrete crosstie. Once this pooling of water occurs, the stagnant water has more time to permeate into the high performance concrete and subsequently freeze at low temperatures. The volume of water expands 9% of its original volume during freezing which leads to cracking of the brittle concrete microstructure. Repetitive cycling of freezing and thawing temperatures induces cracking which ultimately deteriorates the quality of the aggregates and/or the hydrated cement paste. High performance concrete with low water-to-cement ratios are generally thought to be impermeable to moisture ingress and have reduced pore water in their microstructure leading to very little liquid water being available for ice formation [Page and Page, 2007]. Despite the material mix proportion for concrete crossties designed to be high performing with low permeability and high strength, localized freeze-thaw damage at the surface of the concrete crosstie rail seat area has still been

observed in the field and can significantly compromise the integrity of the steel rail fastened system to the concrete crosstie warranting the costly replacement of the entire concrete crosstie

1.2 Literature Review of Freeze-Thaw Durability of Concrete and Concrete Crossties

Freeze-thaw damage can initiate in either the hydrated cement paste or the aggregates contained within concrete. In order for freeze-thaw damage to occur in either instance, it is necessary for there to be liquid water within the porous microstructure and an intermediary level of connectivity of the pore network. It is possible to purposefully entrain disconnected air voids into the hardened concrete in order to alleviate increasing hydraulic pressures during freezing events. A standard, accelerated testing method exists to evaluate the freeze-thaw durability of concrete, but this test method is arguably insufficient of representing the resilience of concrete materials that are excised from pre-stressed elements because the prismatic samples crack from saw-cutting operations and bursting strains.

1.2.1 Porosity of hydrated cement paste and aggregates

Portland cement reacts with water to produce several hydration products including calcium silicate hydrates (CSH), calcium hydroxide (CH), and calcium sulfo-aluminate hydrate (CĀSH). The interlayer space between CSH layers is reported to range from 0.5 nm [Feldman and Sereda, 1970] to 3.8 nm [Jennings, 2000]; and the interlayer spacing is variable due to irregular layering, local relative humidity, and possible colloidal nature of CSH. The porosity between hydration products are called capillary pores and range from 10 nm to 5 μm [Mehta and Monteiro, 2006]. These capillary pores are strongly affected by the cement grain gradation, subsequent particle packing, (internal) curing conditions, and ultimate degree of hydration. Large capillary pores are often the result of high water-to-cementitious ratios and poor cement particle packing, and they can lead to increased permeability and loss of mechanical strength. Entrapped air voids are voids larger than 5 μm and can be as large as several millimeters. These large pores are entrapped during the mixing of fresh concrete and can be minimized with appropriate consolidation techniques including vibration. Most researchers adhere to the simple classification established by the International Union of Pure and Applied Chemistry (IUPAC) where the diametrical size of pores are separated into three categories where micro-pores are those pores smaller than 2 nm; meso-

pores are those pores between 2nm and 50 nm; and macro-pores are those larger than 50 nm in average diameter size [Kaneko, 1994; Aligizaki, 2006].

Aggregates also range in porosity size distribution and interconnectivity. In large part, the porosity is governed by the origin of the rock (igneous, sedimentary, and metamorphic) and the crushing process. Intrusive igneous rocks, for example, can have porosity values upwards of 2% by volume while sedimentary rocks can range from 5% (dense) to 10-40% (porous) by volume [Mehta and Monteiro, 2006]. The interconnectivity of these pores are often indirectly assessed by measuring the bulk specific gravity of the aggregate and its absorption capacity. Batch water is drawn into the empty pores of the aggregate and travels through the interconnected pore network. Additionally during the manufacturing process, natural fissures and cracks within the rock that contribute toward the porosity and interconnectivity of pores can be diminished if the aggregate is crushed to a critical maximum size that is smaller than the inherent spacing of the natural fissures and cracks.

1.2.2 Saturation of the pores and rate of absorption

Water can travel through the interconnected pore network of hydrated cement paste or aggregates in a number of different manners. Liquid water can be drawn into the microstructure through capillary suction [Wilson *et al.*, 1999] while gaseous water can diffuse through the microstructure driven by differential concentration gradients [Sakata, 1983]. When a pressure differential acts on the fluid (gravity or head, e.g.), then the permeability of the fluid through the microstructure is generally governed by Darcy's Law [Basheer *et al.*, 2001]. Cracking at any scale in the microstructure can increase the moisture transport and allow for an overall increase in the amount of total water that can enter the bulk material [Yang *et al.*, 2006]; however, fine cracking (drying shrinkage cracking, e.g.) is found to have more impact on transport properties than structurally-induced cracking [Hearn, 1999]. The increase of moisture transport also increases the transport of solutes (chlorides, sulfates, e.g.) into the bulk material.

The presence of ions within pore water alters the characteristics of the fluid including the surface tension [Petersen and Saykally, 2006], viscosity [Bentz *et al.*, 2008], equilibrium relative humidity [Castro *et al.*, 2010], and freezing and melting points [Kaufmann, 2004]. Taken together, these factors affect the ability to saturate the porous microstructure when ion concentrations

change. Moreover, when the concentration of ions is large, then it is possible for a solution to become super-saturated leading to the precipitation and crystallization of solids [Scherer, 1999]. The precipitation of solid crystalline phases within the porous microstructure inherently modifies the pore size distribution and additionally affects transport properties as pores become obstructed. Pores of different sizes and level of connectedness may differentially saturate leading to the development of osmotic pressures. The connectedness of the pore structure also strongly affects the rate of moisture absorption as a minimally connected network needs approximately three to six years for its pores to become fully saturated whereas a highly connected pore network only requires four to six days [Li *et al.*, 2012].

1.2.3 Freezing mechanisms in pores of hydrated cement paste and aggregate

Concrete consists of three solid phases: hydrated cement paste, fine aggregates, and coarse aggregates. Incomplete packing of particles, mixing, and intrinsic porosity in the aggregates additionally define a fourth phase of air. The combination of porosity within hydrated cement paste, porosity within aggregates, and entrapped air produce a large three-dimensional network of pores within the composite material. This percolated pore structure thusly varies in size from tens of nanometers within the CSH layers to several millimeters in entrapped air voids. This percolated structure can be partially or fully saturated with liquid water (a fifth phase), so upon a freezing event the expanding ice induces cracking in the concrete composite.

In hydrated cement paste, the presence of water in the variously-sized pores freeze at different temperatures depending on the pore size radius [Bager and Sellevold, 1986; Beddoe and Setzer, 1988] and the alkalinity of the pore solution [Kaufmann, 2004]. Pore water in the largest sized pores (entrapped air, e.g.) freezes near 0^{o}C while macro- (> 50 nm); semi-macro-sized (2 to 50 nm) freeze between-8^{o}C to -16^{o}C; and micro-sized pores with pore sizes of < 2 nm freeze at temperatures as low as -38^{o}C [Beddoe and Setzer, 1988]. When liquid water freezes, solid ice precipitates at a pore surface and expands in volume by approximately 9% exerting hydraulic pressure on the remaining unfrozen liquid. This hydraulic pressure drives water movement through the microstructure and, if not alleviated by permeation, induces cracking in the tensile hydrated cement paste [Powers, 1958]. Liquid water in unfrozen, smaller pores moves toward pores with ice crystals in order to restore thermodynamic equilibrium which leads to the development of

osmotic pressures [Powers and Helmuth, 1953]. Those smaller pores are said to be super-cooled and are in a higher energy state than solid ice. To maintain equilibrium, super-cooled water migrates into neighboring pores with crystalize ice where the super-cooled water can expand and freeze into solid ice. This can drive crystalline growth, which can exert pressure onto the microstructure. When the large pore fills with solid ice, then the osmotic pressure may still drive the movement of liquid water which increases the hydraulic pressure that, if unalleviated, can drive cracking of the microstructure. Osmotic pressures can also be created due to rapid freezing of the pore solution with large concentrations of ions like alkalis, chlorides, and calcium hydroxide [Grübl, 1980]. This rapid freezing has a large consequence in observed damage of samples subjected to freeze-thaw cycles.

Osmotic pressures can, thusly, desiccate small sized pores leading to experimentally observed shrinkage during freezing events and the accumulation of expansive solid ice in large sized pores [Litvan, 1976]. The accumulation of this solid ice in the large sized pores leads to cracking in the freeze event that, when temperatures thaw, can fill with liquid water. After numerous thawing and subsequent freezing events, the concrete material accumulates extensive cracking that diminishes the load carrying capacity of the structural member. Moreover, the presence of cracks allows external water and other deleterious agents to access the interior of the concrete material leading to accelerated deterioration caused by other mechanisms (e.g. carbonation, chloride ingress, sulfate attack, etc.).

1.2.4 Critical aggregate size and spacing factor

The selection of aggregate type and size has a large effect on the freeze-thaw durability of the concrete composite. Typically, impermeable aggregates are desirable as porous aggregates like "certain cherts, sandstones, limestones, and shales" can store water, expand upon freezing, and exert hydraulic pressure [Mehta and Monteiro, 2006]. Verbeck and Landgren categorized the susceptibility of aggregates to suffer from freeze-thaw damage based on their permeability and strength. Those aggregates with high permeability are susceptible to freeze-thaw damage if their sieve size exceeds a critical aggregate size [Verbeck and Landren, 1960]. Chiefly, the critical aggregate size is related to the maximum travel distance of approximately 0.20 mm that freezing water must travel in order to reach either an empty aggregate pore or the aggregate surface. The

travel distance of 0.20 mm to 0.25 mm [Neville, 2011] is characteristically related to the medium and large capillary pore size (10 nm to 10 μm) where liquid water freezes near 0°C to -8°C in either hydrated cement paste or aggregates and are temperatures that are commonly encountered in environments. Smaller travel distances (spacing factors) are necessary for smaller-sized pores but are only required at substantially reduced temperatures that are less commonly encountered during cyclic freeze-thaw conditions.

Extremely porous aggregates like lightweight aggregates have been observed to improve freeze-thaw resistance when carefully selected [Kucharczyková *et al.*, 2012]. Recycled aggregates can also be incorporated into concrete when properly washed and soaked before batching to offer comparable freeze-thaw damage resistance as virgin aggregates [Richardson *et al.*, 2011]. These porous aggregates typically feature increased porosity, which allows hydraulic pressures to be alleviated during rapid freezing events.

1.2.5 Chemically entrained air bubbles

Air entraining chemical admixtures are typically surfactants which are incorporated into fresh concrete during mixing in order to create well dispersed, empty air voids within the hardened hydrated cement paste and act as pressure-relief valves for freezing water. The hydrocarbon structure of the chemical admixture commonly features hydrophobic (non-polar) and hydrophilic (anionic) ends, which form into characteristic spheres in the presence of high moisture such as that in fresh concrete. Large-sized spheres initially form but are broken into smaller-sized spheres by the mechanical mixing and aggregate shearing to create entrained air voids with diameter sizes ranging from 50 μm to 1 mm [Mehta and Monteiro, 2006]. At these sizes, the surface tension energy, dG, of the entrained air bubbles is proportionally related by the surface area energy, γ, and to the surface area, dA, by the classical expression

$$dG = \gamma dA. \qquad \text{Equation 1-1}$$

Moreover, the anionic end of the hydrocarbon surfactant can interact with the positively charged surface of cement particles [Marchand *et al.*, 1995]. The entrained air bubbles are in equilibrium when the energy gained by decreasing the size of the pores is equal to the work done by the surroundings to compress that same pore [Hunter, 2001]. Also, small entrained air voids

have larger internal pressures compared to their surroundings which make them stable particularly during vibration [Mielenz *et al.*, 1958].

Entrained air has been utilized in concrete in order to alleviate internal pressures during freezing and mitigate expansion damage. Powers postulates that entrained air voids alleviate buildup of hydraulic pressures as slow cooling freezing fronts travel through concrete [Scherer and Valenza, 2005]. Litvan instead postulates that entrained air voids mitigate crystallization pressures by allowing freezing ice to expand into the empty entrained air voids [Pigeon and Pleau, 1995]. Chatterji alternatively postulates that the entrained air voids act as preferential nucleation sites for the formation of ice [Chatterji, 2003]. Irrespective of any of these cases, the addition of entrained air leads to the increased air content of concrete and has long been accepted by the civil engineering community to improve concrete's resistance to freeze-thaw damage.

There are three important factors of air entrainment in hardened concrete. The first is total air content, typically specified from two to six percent and largely driven by environmental conditions and total volume of pore water in the microstructure [Mohamed *et al*., 2000]. The second is spacing factor which is the travel distance liquid water travels from a fully saturated pore to the boundary of an empty air void. Of critical concern is freezing water in capillary pores (10 nm to 10 μm) whose hydraulic pressure during rapid freezing is alleviated with spacing factor values of 0.008 to 0.0098 in (0.20 to 0.25 mm) [ASTM C666, 2008; CSA 23.1, 2014]. Measurably large values of total air content do not increase the freeze-thaw durability of hydrated cement paste without being well dispersed and achieving small spacing factors meaning that the average diameter size of an entrained air bubble is near 50 μm [Neville, 2011]. This target of achieving a well distributed suspension of small-sized entrained air bubbles can be called the specific surface and it is the ratio of the surface area to volume.

1.2.6 Freeze-thaw damage of concrete crossties and ASTM C666

In concrete crossties, freeze-thaw damage has primarily been observed as a problem in the ballast due to poor drainage [Hartmark, 1978]. Poor drainage in the ballast can lead to frost heaving which creates an unevenness in the railway track and can create a hazardous situation for high speed rail. The stagnation of this un-drained water can also make the concrete crossties susceptible

to freeze-thaw damage. In a study conducted by the CN Rail Research Centre, air-entrained concrete crossties were tested in various cold climates and subjected to three typical types of loading: none, light, and heavy [Duggan *et al.*, 1979]. The inclusion of entrained air improved the performance of the concrete crossties while the varying loading conditions did not alter the freeze-thaw durability of the lab-specimens. However, the authors concluded that the accelerated laboratory testing was observed to be an upper bound limit to the track environment, meaning that the field environment is more aggressive than (un-accelerated) laboratory-controlled conditions.

The material design of concrete crossties has improved since the 1970s where concrete crossties are presently designed with high strength, high flowable concrete. High strength is achieved through low water-to-cement ratio mixtures that are mixed with superplasticizing chemical admixtures to maintain workability. Low water-to-cement ratios result in incomplete hydration of Portland cement particles, meaning that the intake of any external water can chemically react with unhydrated Portland cement to form new product at later ages. The low water content in a low water-to-cement mixture also produces a minimal volume of capillary pores that can be densely filled with hydration products instead of being filled excess batched water. The low volume of capillary pores strongly limits the total volume of liquid water that can exist in a saturated microstructure, which diminishes the effect of freeze-thaw expansion and damage [Detwiler *el al.*, 1989]. This percolated pore network tends to be highly disconnected leading to appreciably low permeability, meaning that the ingress of external water is strongly hindered. The structural design of concrete crossties has also improved since the 1970s where pre-stressing is utilized in order to increase the flexural strength for North American track loading and to allow for quicker manufacturing [Lutch *et al.*, 2009]. Freeze-thaw damage of concrete crossties has been observed to occur in non-air-entrained concrete, so fouled ballast is typically cleaned or replaced when drainage becomes poor [Nurmikolu and Kolisoja, 2008].

Despite these advancements and raised awareness on maintenance requirements of the aggregate ballast, freeze-thaw damage can still occur in regions with temperate climates and moderate precipitation such as the northern United States and Canada [Bakharev and Struble, 1997]. In these types of environments, a combination of abrasion, freeze-thaw damage, and hydraulic pressure damage have all been observed at the rail seat area. In these types of regions, there is also a large number of freeze-thaw cycles [Hershfield, 1973; and Fraser, 1959] that can

decrease the service life of a concrete crosstie. Freeze-thaw damage has also been observed to occur at greater depths away from the rail seat area in environments with a low number of annual freeze-thaw cycles but undergo extended periods of freezing [Stark, 1989]. Generally, increasing the durability of the concrete material by appropriate aggregate selection, designing with a low water-to-cementitious ratio, and incorporation of pozzolanic mineral admixtures can increase the resistance of a concrete crosstie against freeze-thaw damage [Huo *et al.*, 2011].

Typically, the durability of concrete against freeze-thaw damage is assessed by ASTM C666 *Standard Test Method for Resistance of Concrete to Rapid Freezing and Thawing*. In this method, concrete is frozen in either water (Procedure A) or air (Procedure B); both procedures subsequently thaw the concrete samples in water. The concrete specimen is subjected to repeated freeze-thaw cycling and the deterioration is assessed by the length change, mass change, and loss of dynamic modulus with respect to the number of freeze-thaw cycles. The concrete specimens can either be cast in a standalone mold or excised from an in-situ concrete. During quality control and assurance testing of concrete crossties, companion beams can be cast alongside concrete crossties. Alternatively, beams can also be excised from the end of the concrete crosstie. This excision of material can lead to artificial damage (see Figure 1-1) when the concrete is saw-cut. Additionally, removal of the material from a pre-stressed element can result in strain bursting and other cracking associated with the sudden change in stress. A combination of both sources of damage can consequently result in exacerbated conditions during rapid freeze-thaw testing [Blaszkiewicz, 2013]. This erroneous result can lead to the rejection of an otherwise freeze-thaw durable concrete crosstie. Moreover, as found by Duggan *et al.*, laboratory conditions such as ASTM C666 cannot wholly characterize the resiliency of the in-situ concrete because of the differing environments where the field environment can be far more aggressive [Duggan *et al.*, 1979].

Figure 1-1 Example of artificial damage of excised beam from concrete crosstie for ASTM C666 testing. Circles point to extensive cracking due to saw-cutting (from Riding *et al.*, 2016).

1.3 Scope of Dissertation Research

In light of the increased utilization of high performance concrete crossties in track and high speed rail lines, the FRA has launched partnerships with several research institutions under a Broad Agency Announcement (BAA) to better understand the structural and material degradation mechanisms that are responsible for premature failures. Among these partnerships is a collaborative program between Kansas State University and the University of Illinois at Urbana-Champaign where the freeze-thaw material durability of concrete crossties is investigated. In this extensive research program, practical questions regarding the moisture conditions of in-track concrete crossties, the appropriateness of chemically entrained air in high performance concrete, the effect of form and immersion vibration on the air voids in a fresh concrete mix, and the suitability of ASTM C666 to assess the freeze-thaw susceptibility of concrete crossties are evaluated.

1.4 Organization of Dissertation

The aforementioned practical questions are of concern to every researcher involved in this project including this dissertation. However, this dissertation more closely examines six specific questions:

1) What is the extent of fluctuating temperature and moisture gradients inside concrete crossties installed in track as affected by external weather conditions?

2) What correlation can be made between internal relative humidity measurements against degree of saturation?
3) Can an overarching predictive model be formulated to assess the freeze-thaw damage potential risk of concrete crossties installed across North America?
4) How does the rheology of cementitious and model fluids change with the incorporation of aggregates and vibration?
5) How does the propagation and attenuation of peak vibrational acceleration travel in fresh concrete and model materials?
6) To what extent does the presence of aggregates and rheology have on the loss of air as evidenced in 2-dimensional polished cross sections?

The six posed questions are addressed by two major thrusts in this dissertation. The first thrust focuses on better understanding the effect of external environmental conditions on the internal conditions of concrete crossties. The second thrust focuses on the rheological stability of entrained air bubbles suspended within a Bingham plastic (concrete) when the material is subjected to extensive time periods of vibration. As such, the six questions are the basis for six chapters where Chapters 2 through 4 focus on the first thrust while Chapters 5 through 7 focus on the second thrust.

Chapter 2 focuses on a study of instrumented concrete crossties and rectangular prisms installed in ballast as they are affected by the changing environment over a time span of 1 year. Chapter 3 focuses on correlating internal humidity measurements with internal electrical resistance gypsum block measurements. Chapter 4 combines the work presented in Chapters 2 and 3 into a predictive model that utilizes publicly available weather station data and assesses the freeze-thaw damage potential of concrete crossties installed in track across North America.

Chapters 5, 6, and 7 pivot away from a hygrothermal study of concrete crossties and instead focus on the rheological behavior of fresh high performance concrete when subjected to vibration. Chapter 5 expands on previously observed behaviors of concrete rheology as affected by increasing aggregate contents and increasing degrees of vibration. Chapter 6 investigates the extending radius of vibratory action as a function of aggregate volume content. Chapter 7 focuses

on the yielding of interstitial cement paste fluid between vibrating aggregates which leads to the onset of movement of entrained air bubbles.

Finally, Chapter 8 offers concluding remarks based on the studies in their entirety.

1.5 Impact of Results

The outcome of this dissertation provides insight in a number of ways. Firstly, the extent of moisture fluctuations in high performance concrete crossties at the rail seat area in field conditions is better understood. This outcome raises valid questions about the appropriateness of air entrainment in materials with critically low degrees of saturation, which can be better assessed in future research. Secondly, compaction techniques have long been codified for mechanical strength optimization; in this dissertation, the extent of vibration through fresh concrete material is studied and the ramification toward aggregate segregation and air loss is analyzed. The outcome of this dissertation develops physical models that is of use to practitioners to optimize fresh concrete compaction for mechanical strength and retention of entrained air.

The work in this dissertation, along with the work of other researchers within the collaborative effort, has been prepared as a technical report to the FRA [Riding *et al.*, 2016]. The immediate consequence of this work provides evidence and guidance to precast concrete crosstie manufacturers while the longer-term consequence of this work will provide better guidance to all practitioners on compaction techniques.

1.6 References

Aligizaki, K. K. *Pore Structure of Cement-Based Materials: Testing, Interpretation and Requirements*. Eds. Benture and Mindess, 2006 New York: Taylor and Francis Group.

ASTM Standard C666, 2003 (2008), Standard Test Method for Resistance of Concrete to Rapid Freezing and Thawing," ASTM International, West Conshohocken, PA.

Bager, D. H., and Sellevold, E. J. "Ice formation in hardened cement paste, Part I – room temperature cured pastes with variable moisture contents." *Cement and Concrete Research* 16 (1986): 709 – 720.

Bakharev, T. and Struble, L. J. "Microstructural features of railseat deterioration in concrete ties." *Journal of Materials in Civil Engineering* 9 (1997): 146 – 153.

Basheer, L, Kropp, J., and Cleland, D. J. "Assessment of the durability of concrete from its permeation properties: a review." *Construction and Building Materials* 15 (2001): 93 – 103.

Beddoe, R. E., and Setzer, M. J. “A low-temperature DSC investigation of hardened cement paste subjected to chloride action.” *Cement and Concrete Research* 18 (1988): 249 – 256.

Bentz, D. P., Snyder, K. A., Cass, L. C., and Peltz, M. A. “Doubling the service life of concrete structures. I: Reducing ion mobility using nanoscale viscosity modifers.” *Cement & Concrete Composites* 30 (2008): 674 – 678.

Castro, J., Lura, P., Rajabipour, F., Henkensiefken, R., and Weiss, J. “Internal curing: discussion of the role of pore solution on relative humidity measurements and desorption of lightweight aggregate." *ACI Special Publication* 270 (2010): 89 – 100.

Chatterji, S. “Freezing of air-entrained cement-based materials and specific actions of air-entraining agents.” *Cement and Concrete Composities* 25 (2003): 759 – 765.

Code of Federal Regulations (C.F.R.). Title 49. Subtitle B. Chapter II. Part 213 Track Safety Standards. Subpart G Train Operations at Track Classes 6 and Higher. Section 213.225 Crossties.

CSA Standard A23.1-14/A23.2-14. “Concrete Materials and Methods of Concrete Construction/Methods of Test and Standard Practices for Concrete.” Canadian Standards Association, Toronto, ON.

Detwiler, R. J., Dalgleish, B. J., and Williamson, R. B. “Assessing the durability of concrete in freezing and thawing.” *ACI Materials Journal* 86 (1989): 29 – 35.

Duggan, C. R., Dalton, C. J., and Scott, J. F. “Freeze-thaw tests of concrete ties.” *CN Rail Research Centre* Report No. 15 (1979).

Feldman, R. F. and Sereda, P. J. A. “A new model for hydrated Portland cement and its practical implications.” *Engineering Journal Canada* 53 (1970): 53 – 59.

Fraser, J. K. “Freeze-thaw frequencies and mechanical weathering in Canada.” *ARCTIC North America* 12 (1959).

Grübl, P. “Rapid ice formation in hardened cement paste, mortar and concrete due to supercooling.” *Cement and Concrete Research* 10 (1980): 333 – 345.

Hanna, A. N. “Prestressed concrete ties for North American Railroads.” *PCI Journal* 24 (1979): 29.

Hartmark, H. “Frost protection of railway lines.” *Engineering Geology* 13 (1979): 505 – 517.

Hearn, N. “Effect of shrinkage and load-induced cracking on water permeability of concrete.” *ACI Materials Journal* 96 (1999): 234 – 242.

Hershfield, D. M. “The frequency of freeze-thaw cycles.” *Journal of Applied Meteorology* 13 (1973): 348 – 354.

Huo, J., Ji, X., and Yang, H. “Experimental study on freeze-thaw resistance durability of high performance concrete.” *Advanced Materials Research* 168 – 170 (2011): 393 – 397.

Jennings, H. M. “A model for the microstructure of calcium silicate hydrate in cement paste.” *Cement and Concrete Research* 30 (2000): 101 – 116.

Kaneko, K. “Determination of pore size and pore size distribution 1. Adsorbents and catalysts.” *Journal of Membrane Science* 96 (1994): 59 – 89.

Kaufmann, J. P. “Experimental identification of ice formation in small concrete pores.” *Cement and Concrete Research* 34 (2004): 1421 – 1427.

Kuchrczyková, B., Keršner, Z., Pospíchal, O., Misák, P., Daneˇk, P., and Schmid, P. “The porous aggregate pre-soaking in relation to the freeze-thaw resistance of lightweight aggregate concrete.” *Construction and Building Materials* 30 (2012): 761 – 766.

Li, W., Pour-Ghaz, M., Castro, J., and Weiss, J. "Water absorption and critical degree of saturation relating to freeze-thaw damage in concrete pavement joints." *Journal of Materials in Civil Engineering* 24 (2012): 299 – 307.

Litvan, G. G. "Frost action in cement in the presence of de-icers." *Cement and Concrete Research* 6 (1976): 351 – 356.

Lutch, R. H., Harris D. K., and Ahlborn, T. M. "Causes and preventative methods for rail seat abrasion in North America's railroads." *14th Conference on Cold Regions Engineering* (2009): Duluth, MN.

Marchand, J., Pleau, R., and Gagne, R. "Deterioration of concrete due to freezing and thawing." *Materials Science of Concrete IV*. Eds. Skalny and Mindess. 1995. American Ceramics Society, Westerville, OH.

Mehta, P. K. and Monteiro, P. J. M. *Concrete: Microstructure, Properties, and Materials 3rd Edition*. 2006, New York: McGraw-Hill Companies, Inc.

Mielenz, R. C., *et al*. "Origin, evolution, and effects of the air void system in concrete Part 1 – Entrained air in unhardened concrete." *American Concrete Institute* 55 (1958): 95 – 121.

Mohammed, O. A., Rens, K. L., and Stalnaker, J. J. "Factors affecting resistance of concrete to freezing and thawing damage." *Journal of Materials in Civil Engineering* 12 (2000): 26 – 32.

Neville, A. M. *Properties of Concrete 5th Ed*. 2011, New York: Pearson.

Nurmikolu, A. and Kolisoja, P. "The effect of fines content and quality on frost heave susceptibility of crushed rock aggregates used in railway track structure." *9th International Conference on Permafrost* (2008): Fairbanks, AK.

Page, C. L., and Page., M. M. *Durability of Concrete and Cement*. 2007, Cambridge, England: Woodhead Publishing Limited.

Petersen, P. B., and Saykally, R. J. "On the nature of ions at the liquid water surface." *Annual Review of Physical Chemistry* 57 (2006): 333 – 364.

Powers, T. C. "The physical structure and engineering properties of concrete." *Bulletin 90 Portland Cement Association* (1958).

Powers, T. C., and Helmuth, R. A. "Theory of volume changes in hardened Portland cement paste during freezing." *Highway Research Board Bulleting* 32 (1953): 285 – 297.

Richardson, A., Coventry, K., and Bacon, J. "Freeze/thaw durability of concrete with recycled demolition aggregate compared to virgin aggregate concrete." *Journal of Cleaner Production* 19 (2011): 272 – 277.

Riding, K. A., Lange, D. A., Castaneda, D. I., Koch, J. A., Albahttiti, M. T., Ghadban, A. A., Song, Y., and Zou, R. "Concrete Material and Manufacturing Requirements for Freeze-Thaw Durable Concrete Railroad Ties: Volume I and Volume II." *Technical Report to U.S. Department of Transportation Federal Railroad Administration Office of Research and Development*, Washington, D.C., January 2016.

Sakata, K. "A study on moisture diffusion in drying and drying shrinkage of concrete." *Cement and Concrete Research* 13 (1983): 216 – 224.

Scherer, G. W. "Crystallization in pores." *Cement and Concrete Research* 29 (1999): 1347 – 1358.

Scherer, G. W. and Valenza, J. J. "Mechanisms of frost damage." *Materials Science of Concrete VII*. Eds. Young and Skalny. 2005. American Ceramics Society: Westerville, OH.

Stark, D. "Effect of length of freezing period on durability of concrete." *Portland Cement Association* Report (1989): Skokie, IL.

Verbeck, G. J. and Landgren, R. “Influence of physical characteristics of aggregates on frost resistance of concrete.” *Proceedings of ASTM* 60 (1960): 1063 – 1079.

Wilson, M. A., Carter, M. A., and Hoff, W. D. “British Standard and RILEM water absorption tests: A critical evaluation.” *Materials and Structures* 32 (1999): 571 – 578.

Yang, Z., Weiss, J. W., and Olek, J. “Water transport in concrete damaged by tensile loading and freeze-thaw cycling.” *Journal of Materials in Civil Engineering* 18 (2006): 424 – 434.

Zeman, J. C. “Hydraulic mechanisms of concrete-tie rail seat deterioration.” *University of Illinois at Urbana-Champaign* (2010): MS Thesis.

CHAPTER 2 – MEASURING AND PREDICTING RELATIVE HUMIDITY AND TEMPERATURE PROFILE DISTRIBUTIONS INSIDE RAILROAD CONCRETE CROSSTIES

2.1 Acknowledgement

The development of this chapter is accomplished with field testing carried out in two locations: Rantoul, IL, and Lytton, BC, Canada. Researchers at the University of British Columbia, Okanagan, supported the project by collecting field data on behalf of the author in Lytton, BC, Canada. For that, I am very grateful to Professors Gord Lovegrove and Ahmad Rteil, and to students Trevor Billows and Kyle Stratton. Additionally, I am grateful to industrial partner Jim Parsley and staff at LB Foster CXT Concrete Ties where numerous crossties were instrumented during the manufacturing process for this study.

2.2 Abstract

Concrete crossties (alternatively known as ties or sleepers) are subjected to a wide range of climatic conditions across North America. Among these environments are those that include cyclic freezing and thawing air temperatures. In conventional concrete, freeze-thaw cyclic damage is mitigated by chemically entraining microscopically-sized air bubbles in the fresh concrete. These empty air voids in hardened concrete allow for hydraulic pressures to be alleviated during freezing events. In high performance concrete, however, the low water-to-cementitious ratio and pozzolanic mineral admixtures can result in a highly impermeable microstructure that may not allow for an increase of liquid moisture to a critical level (86-88%) in which freeze-thaw damage would occur. As a consequence, high performance concrete crossties may be freeze-thaw resistant without the incorporation of chemically entrained air. In order to better understand the appropriateness of air-entrainment in high performance concrete crossties, several concrete crossties were instrumented with hygrothermal sensors during manufacturing. These concrete crossties were installed in track in Lytton, British Columbia, Canada, and in model ballast in Rantoul, Illinois, United States. The internal relative humidity and temperature of the concrete crossties and complementary concrete beams, as well as ambient readings in air and ballast, were observed for a time span of one year. Predictive models based on half-space approximations are

applied in order to predict the concrete crosstie internal profiles of relative humidity and temperature. It is found that modifications to boundary conditions at the top surface (at the rail seat area) improves the predictive fit to the experimental data, which suggests that internal relative humidity and temperature profiles can be predicted utilizing these modifications to the boundary conditions and environmental weather data alone.

2.3 Introduction and Background

2.3.1 Deterioration of railroad concrete crossties

Concrete crossties have been replacing timber ties over the last several decades because of the ability of concrete crossties to sustain higher freight loads, higher train speeds, and have reduced maintenance costs [Zeman, 2010]. However, early-age deterioration can render the last point moot if premature material damage necessitates repair or replacement of the concrete crosstie. Concrete crossties are typically manufactured in precast plants and are additionally pre-stressed for enhanced mechanical performance. As a result, concrete crossties manufactured in the United States in the 1970s with steam curing often suffered deterioration mechanisms like delayed ettringite formation [Tepponen and Eriksson, 1987; Ferdous and Manalo, 2014]. However, present-day concrete crossties are manufactured without steam curing and incorporate new chemical admixtures not previously available to manufacturers. These chemical (and mineral) admixtures have led to the development of high performance concrete that is highly flowable. However, new early-age deterioration mechanisms have become apparent, which is of great concern to the Federal Railroad Administration (FRA) as the United States continues to move toward the construction of a national high speed rail network that implement these high performance concrete crossties.

Early-age deterioration mechanisms of concrete crossties are generally structural (abrasion, crushing, e.g.) and material (cavitation erosion, hydraulic pressure, e.g.) in nature [Ferdous and Manalo, 2014]. These damages can additionally be affected by frost heaving (the action in which water in fouled ballast freezes leading to large-scale upheaval of concrete crossties) [Hakon, 1978]. It is also possible for freeze-thaw damage to occur within the concrete crosstie since the material is exposed to outdoor environments. In particular, freeze-thaw damage can be problematic at the

rail seat area where the confined geometry of the concrete crosstie, pad, clips, shoulder, and rail line converge. The highly confined rail seat area possibly leads to pooling of water from precipitation (rain or melting snow) which can lead to absorption of water, scaling, and freeze-thaw damage at low temperatures [Bakharev and Struble, 1997]. However, recent research has demonstrated that freeze-thaw damage is exacerbated above critical levels of saturation higher than 86-88% [Li *et al.*, 2012]. As such, it is necessary to gain a better understanding of moisture levels and freezing temperatures inside concrete crossties to better assess their freeze-thaw damage potential.

2.3.2 One-dimensional modeling of internal relative humidity distribution

Simulating the extent of moisture and temperature gradients within concrete is highly sought in pavement engineering because of moisture and thermal curling of slabs, which leads to durability issues. As such, infinite halfspace solutions exist for pavements. In this study, two halfspace solutions to predict relative humidity and temperature distributions are applied to concrete crossties. Limitations to this 1-dimensional modeling approach is discussed in greater detail in later sections. Figure 2-1 shows the simplified approach of a 3-dimensional concrete crossties in aggregate ballast overlayed by a polyurethane pad and steel rail as a series of stacked, infinite halfspaces.

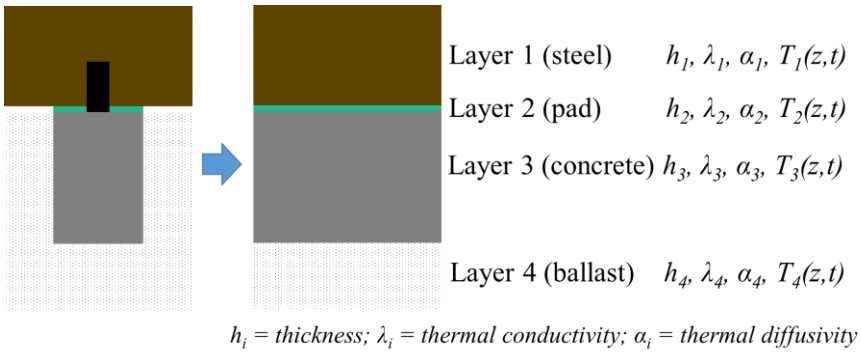

Figure 2-1 Depiction of a concrete crosstie at the rail seat area (left) where the steel rail line, polyurethane pad, concrete crosstie, and aggregate ballast are depicted as layered, infinite halfspaces (right).

Relative humidity can be modeled by the 1-dimensional moisture transport equation [Kim and Lee, 1999]

$$\frac{\partial RH(t,z)}{\partial t} = div(D \cdot grad(RH(t,z))) - \frac{\partial RH_S(t,z)}{\partial t} \quad \text{Equation 2-1}$$

where *RH* is a function of time (sec), *t*, and depth (m), *z*; $\frac{\partial RH_S(t,z)}{\partial t}$ is the change in relative humidity due to hydration for early-age concrete (assumed as $\frac{\partial RH_S(t,z)}{\partial t} = 0$ for hardened concrete; and *D* is the moisture diffusivity, which is a function of both internal relative humidity and concrete porosity. The moisture diffusivity factor is non-linear (where at low RH, vapor- and gas-pressure gradients govern transport properties while at high RH, capillary suction governs transport properties). The moisture diffusivity can be expressed by an effective diffusivity [Bažant and Najjar, 1972]

$$D = D_o \left(\alpha_o \frac{1-\alpha_o}{1+\left(1-RH/_{1-RH_c}\right)^n} \right) \quad \text{Equation 2-2}$$

where D_o (m^2/s) is the moisture diffusivity at complete saturation; *n* is a regression coefficient ranging from 6 to 16 for concrete [Leech *et al.*, 2003]; $\alpha_o = D_1/D_o$, where D_1 is the diffusivity at 0% RH; and RH_c is the bifurcate point above which capillary suction governs (typically 75 to 80%) [Qin and Hiller, 2014]. The moisture diffusivity at complete saturation can be related to the water-to-cementitious ratio as shown in Table 2-1.

Table 2-1 Moisture diffusivity at saturation estimated from w/c ratio (from [1]Kang *et al.*, 2012, and [2]Qin and Hiller, 2014).

w/c	D_o (10^{-6} m^2/hour)[1]	D_o (10^{-6} m^2/hour)[2]
0.28	2.02	0.68
0.40	2.10	1.59
0.50	2.26	-
0.68	2.87	2.57

The boundary conditions are defined at the top and underside of the crosstie by two hygrochron sensors installed within the ballast. The boundary condition at the top of the crosstie is modified in order to better represent wetting events due to precipitation (rain or melting snow). Table 2-2 shows weather conditions which increase the measured relative humidity value to 100% RH over a given time frame.

Table 2-2 Modified boundary condition at the top of concrete crossties and beams as subject to reported weather conditions (adapted from Qin and Hiller, 2014).

Reported Weather Condition	Modified Wetting Duration
Drizzle	RH_{upper} = 100 % for 1 hour
Fog	
Mist	
Light Rain	RH_{upper} = 100 % for 4 hours
Light Thunderstorms and Rain	
Thunderstorms and Rain	RH_{upper} = 100 % for 8 hours
Rain	
Heavy Thunderstorms and Rain	RH_{upper} = 100 % for 10 hours
Heavy Rain	
Light Snow	
Snow	RH_{upper} = 100 % for 15 hours
Heavy Snow	RH_{upper} = 100 % for 20 hours

Equation 2-1 is iteratively solved in MatLab until the *RH (t)* converges to within 1% RH.

2.3.3 One-dimensional modeling of internal temperature distribution

Several models exist to predict the temperature distribution inside concrete pavements [Barber, 1957; Dempsey and Thompson, 1970; Solaimanian and Kennedy, 1993]. Dempsey and Thompson's model is well regarded for long-term pavement temperature predictions. However, modeling a concrete crosstie presents two challenges: it is 3-dimensional and multi-layered. Adopting a closed-form solution, thusly, yields an incorrect representation of the crosstie at its exterior edges. However, a first-principles understanding can be pursued where the suitability of a 1-dimensional model can be evaluated for use in predicted concrete crosstie internal temperature distributions.

Wang and Roesler [2014] proposed a separation of variables method to predict the internal temperature profile, $T_i\ (z,t)$, inside a multi-layered rigid pavement system. A 1-dimensional heat transfer problem is modeled using

$$\frac{\partial T_i}{\partial t}(z,t) = \alpha_i \frac{\partial^2 T_i}{\partial z^2}(z,t) \qquad \text{Equation 2-3}$$

where α_i is the thermal diffusivity coefficient (m^2/h); $H_{i-1} < z < H_i$ is the cumulative depth through the multi-layered system (m); $H_i = \sum_{k=1}^{i} h_k$ is the individual thickness of each layer (m); i = 1, 2,

…, $n-1$ are individual layers where $H_0 = 0$ and $H_n = \infty$; and $n \geq 4$ is the number of layers required in this analysis.

Two boundary conditions constrain the final solution to be continuous along the intermediary interfaces between any consecutive layers:

$$T_i(H_i, t) = T_{i+1}(H_i, t) \qquad \text{Equation 2-4}$$

$$\lambda_i \frac{\partial T_i}{\partial t}(H_i, t) = \lambda_{i+1} \frac{\partial T_{i+1}}{\partial z}(H_i, t) \qquad \text{Equation 2-5}$$

where λ_i is the thermal conductivity coefficient (kcal/m h ^oC). The third boundary condition is an energy balance between the surface of the concrete and environmental conditions

$$-\lambda_i \frac{\partial T_i}{\partial t}(0, t) = a_s Q(t) - F(t) + B[T_a(t) - T_1(0, t)] \qquad \text{Equation 2-6}$$

where a_s is the surface material absorptivity relative to the solar radiation (unitless); $Q(t)$ is the solar radiation flux (kcal / m^2 h) at time t (hour); $F(t)$ is the irradiation flux emitted by the pavement surface (kcal / m^2 h ^oC); B is the surface material convection coefficient (kcal / m^2 h ^oC); and $T_a(t)$ is the ambient air temperature (^oC) at time t (hour). Continuous functions of $Q(t)$ and $T_a(t)$ are desired in order to produce a closed-form final solution, so an interpolatory trigonometric set of polynomials using the least squares approximation can be used [Burden and Faires, 2001; Wang and Roesler, 2014]. By incorporating these trigonometric polynomials and simplifying the irradiation energy by a factor of 1/3 [Barber, 1957], then Equation 2-6 can be written in the compact form

$$-\lambda_i \frac{\partial T_i}{\partial t}(0, t) = B[\sum_{i=1}^{2m} A_i \sin(\omega_i t + \phi_i) - T_1(0, t)] \qquad \text{Equation 2-7}$$

where $2m$ is the number of sub-intervals used to create the interpolatory trigonometric set of polynomials; and A_i, ω_i, and ϕ_i are mathematical representations of amplitude, frequency, and phase angle, respectively, and are defined elsewhere [Wang and Roesler, 2014].

Wang and Roesler observe that the sinusoidal term $\sin(w_i t + \phi_i)$ can be related to the complex number $e^{j(\omega t + \phi)}$ via the Euler formula where $j^2 = -1$. As such, the complex-valued

function can be solved where the imaginary final solution corresponds to the real solution for the 1D temperature profile $T_i(z,t)$. Because the principle of superposition is applied k times in order to solve the complex-valued function, the individual solutions of $T_{ik}(z,t)$ must be summed across the k-th index in order to yield the final solution for the n-th layered temperature profile distribution. The solution from one iteration of solving the imaginary part of the complex-valued function are

$$T_{ik}(z,t) = \Delta_{11} e^{-\upsilon_1 z} \sin(\omega t - \upsilon_i z + \delta_{11} + \phi) + \Delta_{12} e^{\upsilon_1 z} \sin(\omega t + \upsilon_i z + \delta_{12} + \phi) \quad \text{Equation 2-8}$$

for $0 \leq z \leq H_1$;

$$T_{ik}(z,t) = \Delta_{i1} e^{H_{i-1}\upsilon_{i-1} + \upsilon_i (H_{i-1} - z)} \sin(\omega t - \upsilon_i z + \delta_{i1} + \phi) + \Delta_{i2} e^{H_{i-1}\upsilon_{i-1} - \upsilon_i (H_{i-1} - z)} \sin(\omega t + \upsilon_i z + \delta_{12} + \phi) \quad \text{Equation 2-9}$$

for $H_{i-1} \leq z \leq H_i$, and $i = 2, 3, \ldots, n-1$; and

$$T_{nk}(z,t) = \Delta_n e^{H_{n-1}\upsilon_{n-1} + \upsilon_n (H_{n-1} - z)} \sin(\omega t - \upsilon_n z + \delta_{n1} + \phi) \quad \text{Equation 2-10}$$

for $z \geq H_{n-1}$. The variables Δ_{i1}, δ_{i1} for $i = 1, 2, \ldots, n$ and Δ_{i2}, δ_{12} for $i = 1, 2, \ldots, n-1$ in Equations 2-8 through 2-10 are defined elsewhere [Wang and Roesler, 2014].

2.3.4 Estimating solar radiation as an input for the one-dimensional temperature model

The predictive temperature model requires two input parameters in order to predict the internal temperature profile distribution inside concrete: ambient air temperature and solar radiation. Although ambient air temperature is available in many locations from meteorological data, solar radiation is not as readily available and is prone to incomplete data sets [Al Riza *et al.*, 2011]. Solar radiation estimation is employed within agricultural disciplines in order understand soil temperature and soil moisture conditions. As such, a number of different estimations exist throughout the literature [Monteith, 1965; Bristow and Campbell, 1984; Hargreaves and Samani, 1985; Liu, 1996; McVicar and Jupp, 1999] for solar radiation with varying degrees of simplicity.

Spokas and Forcella [2006] estimate incoming solar radiation as affected by changing weather conditions and changing geo-temporal attributes at a given location. Their model is advantageous because it is sensitive to changing hourly conditions as opposed to other models

which only account for mean daily fluctuations and site-calibration. In their model, they assume that total incoming solar radiation, Q_T, is divided into two components

$$Q_T = Q_B + Q_D \qquad \text{Equation 2-11}$$

where Q_B is direct beam radiation and Q_D is indirect, diffuse radiation. Direct beam radiation is transmitted parallel to the sun's rays (zenith angle) and is dependent upon the location on Earth, the time of day, the time of year, and the extent of transmittance through the atmosphere. Direct beam radiation is assumed to be [Liu and Jordan, 1960]

$$Q_B = Q_{Bo}\tau^m \qquad \text{Equation 2-12}$$

where Q_{Bo} is the solar constant (1,360 W/m^2), τ is the atmospheric transmittance, and m is the optical air mass number. The optical air mass number is a function of atmospheric pressure, zenith angle, and elevation of the site [Campbell and Norman, 1998]. Indirect, diffuse radiation is reflected or absorbed in the atmosphere, clouds, or dust and a fraction of this radiation is scattered toward the surface of Earth. It is assumed to be [Liu and Jordan, 1960]

$$Q_D = 0.30(1 - \tau^m)Q_{Bo}cos\Psi \qquad \text{Equation 2-13}$$

where Ψ is the zenith angle in radians. The zenith angle is dependent upon the latitude of the site, standard time, time at solar noon, and calendar day [Campbell and Jordan, 1998]. Figure 2-2 depicts the direct beam and diffuse solar radiation emanating from the sun, transmitting and reflecting through clouds and the atmosphere, and cumulatively hitting the top surface of the (simplified) multi-layered concrete crosstie system.

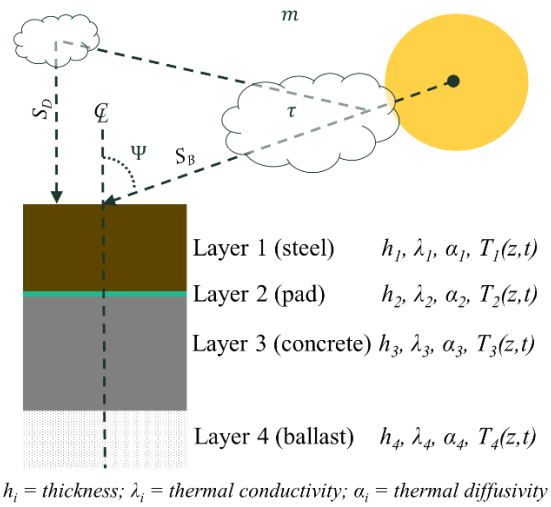

Figure 2-2 Depiction of a concrete crosstie at the rail seat area where the steel rail line, polyurethane pad, concrete crosstie, and aggregate ballast are depicted as layered, infinite halfspaces.

2.4 Significance of Research

Concrete crossties, like any outdoor concrete structure, are susceptible to freeze-thaw damage, yet the distribution of internal liquid moisture within concrete crossties is not well understood. In particular, the state of liquid moisture at the rail seat area is complicated due to the configuration of the rail line, pad, clips, and shoulders. This study aims to enhance the concrete crosstie industry's understanding of freeze-thaw susceptibility by measuring the internal relative humidity and temperature of instrumented crossties installed in track. Additionally, the results of this study can be compared against current standard tests in order to achieve improved environmental design criteria for concrete crosstie freeze-thaw damage.

2.5 Experimental Methods

2.5.1 Sensor type and preparation of installation method

Hygrochron sensors, able to measure both relative humidity and temperature, called iButtons (DS1923-F5) were selected because of each sensor's ability to record data and operate under battery-power. These benefits eliminated the need to devise an external data-acquisition support system. For relative humidity measurements, the sensors make use of two electrodes joined by a capacitive film. When water vapor accumulates onto the film, then the dielectric constant, κ,

measured between the two electrodes changes in a linear relationship. As such, a linear relationship can be established by experimentally measuring the dielectric constant with respect to changing relative humidity in controlled environments.

The sensors execute software correction algorithms for both relative humidity and temperature measurements based on the conversion of 8-bit or 16-bit data formats to decimal formats [Maxim Integrated, 2013]. Additionally, whenever a capacitive film is exposed to high relative humidity environments (greater than 70% RH, e.g.), for extended periods of time, then the reading may become affected in a phenomenon known as *saturation drift*. It is possible to account for this saturation drift by correcting the measured relative humidity value, RH_N, at the Nth hour the device has been continuously exposed to 70% RH and higher (or 20% RH and lower) with the following expression

$$RH_{saturation\ drift\ corrected} = RH_N - \sum_{k=1}^{N} \frac{(0.0156)(\overline{RH_k})(2.54^{-0.3502k})}{1+{}^{(\overline{T_k}-25)}/_{100}} \quad \text{Equation 2-14}$$

where RH_N is the relative humidity at the end of the Nth hour when the device is exposed to high or low relative humidity, $\overline{RH_k}$ is the average relative humidity through the kth hour that that device has been exposed to high or low relative humidity, and $\overline{T_k}$ is the average temperature (in Celsius) through the kth hour the device has been continuously exposed to high or low relative humidity. The numbers in the equation are empirical and are derived from curve-fitted data sets [Maxim Integrated, 2013].

The sensors were fitted into iButton retainers (DS9098P) which introduced soldering points for wiring. Multi-conductor shielded cabling was soldered onto the retainer in order to enable remote communication with each individual sensor. The sensor and retainer were fitted inside of a plastic dip coated eye bolt which was additionally affixed onto a steel angle bracket with unthreaded holes spaced one inch apart (see Figure 2-3). Eleven individual brackets with 2-inch nominal spacing (see Figure 2-4) were constructed. A single layer of GORE-TEX fabric (a fabric that allows water vapor to pass through but not liquid water) was wrapped around each sensor in order to protect the wiring connections.

Figure 2-3 Construction of iButton sensors (left), fitted with rubber bands (center), and covered in GORE-TEX fabric (right).

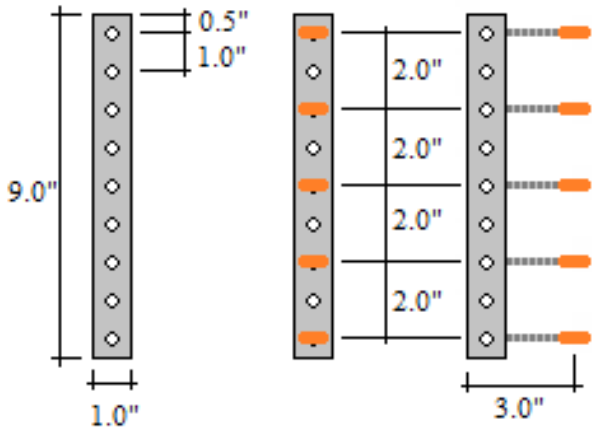

Figure 2-4 Depiction of nine inch tall brackets (left) with half-inch clearance at top and bottom. Sensors (orange) were affixed in regular two-inch increments (right).

2.5.2 Instrumentation of concrete crossties at manufacturing facility

Eleven brackets were installed into seven concrete crosstie molds at the LB Foster CXT Concrete Crossties production facility located in Tucson, AZ. The seven crosstie are uniquely identified as A-444, A-445, A-446, A-447, A-448, A-449, and A-450. Crossties A-444 through A-447 were cast with brackets at both rail seat areas while crossties A-448 through A-450 were cast with brackets at one end only. The location of the sensor at either end of the crosstie is denoted by IDS or USA depending on the location of the identifying stamp number at either end of the crosstie. A schematic of the location of the brackets within the crosstie is shown in Figure 2-5. Each bracket

was directly fastened onto the pre-stressed tendons utilizing zip ties. The bracket was positioned such that the center of the hygrothermal sensors corresponded to the geometric center of the rail seat area. The multi-conductor shielded cabling was routed to the nearest crosstie end where the cables were encased within a threaded PVC access plug. The access plug was firmly affixed onto the bottom surface of the mold such that the cable ends could be easily accessed after de-molding. After de-molding, a cap was added onto the PVC access plug to further protect the cabling ends during monitoring (see Figure 2-6).

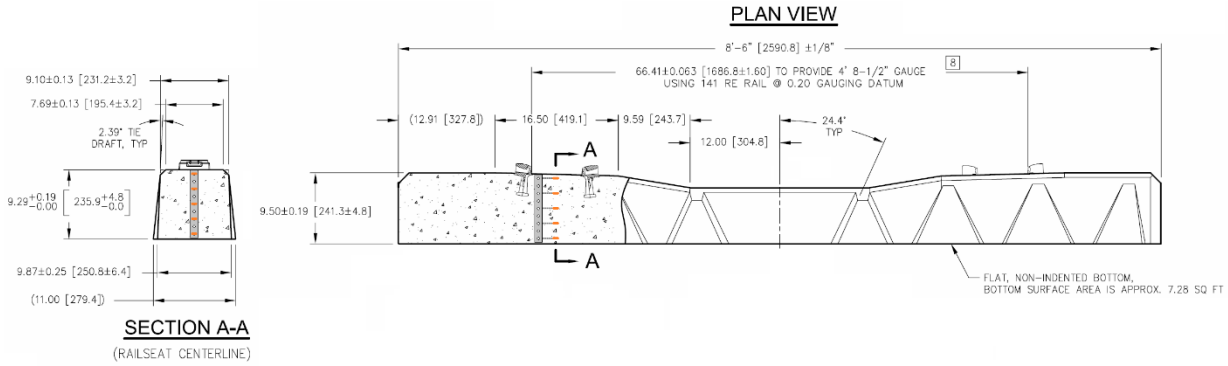

Figure 2-5 Crossties A-448 through A-450 were manufactured with brackets only at one end.

Figure 2-6 De-molded concrete crossties with square cap added to PVC access plug where multi-conductor shielded cables are encased.

The concrete crossties were manufactured no differently from the rest of the plant operations. The approximate concrete mixture design is shown in Table 2-3.

Table 2-3 Approximate concrete mix design of railroad crossties.

Material Type	**Pounds Per Cubic Yard**	**Kilograms Per Cubic Meter**
Type III Portland Cement	650	386
#57 Aggregate	1150	682
#8 Aggregate	750	445
Sand	829	492
Class F Fly Ash	195	116
Water	247	146
Air Entrainer	1.5 fl. oz per 100 lb. cementitious (97.8 mL per 100 kg cementitious)	
High Range Water Reducer	8 fl. oz per 100 lb. cementitious (522 mL per 100 kg cementitious)	

2.5.3 Installation of crossties in model ballast and track

Three of the seven crossties (A-444, A-448, and A-449) were transported to Rantoul, IL, where they were installed inside a model ballast. The model ballast is a 1-1.5 inch top-size yard ballast that conforms to Union Pacific Railroad (UPRR) Class-2 Ballast Specifications. The model ballast and concrete crossties were installed into a 3-compartment box measuring 12-ft by 16-ft and 16 inches in height (see Figure 2-7). Along the 16-ft length, the box was partitioned into approximately 5-ft sections for ease of construction and filling. A level surface of ballast was initially filled into each of the three compartments. The box sits atop an angled asphalt lot, which resulted in one end of each of the compartments being filled with 5 to 6 inches of ballast while the other end was filled with 3 to 4 inches (see Figure 2-8). This angled surface at the underside of the model ballast facilitates rainfall runoff and prevents stagnant water from accumulating within the ballast. Reflective heat from the asphalt lot is minimized with a clearance of 1.75 feet to each end of the crossties from the compartment box edge and an additional distance of 1.9 feet to the instrumented location of the crosstie. This cumulative distance of 3.67 feet is assumed to be sufficiently far from any radiant heat that the asphalt surface may impart onto the underside of the concrete crosstie through 3-6 inches of aggregate ballast. Each crosstie was lifted and positioned into the center of each compartment and seated atop the level ballast. Once the crosstie was positioned, additional ballast was then added in order to reach the top surface of the crosstie. Pads,

clips, and sections of rail line were installed onto the crossties in order to better simulate track conditions.

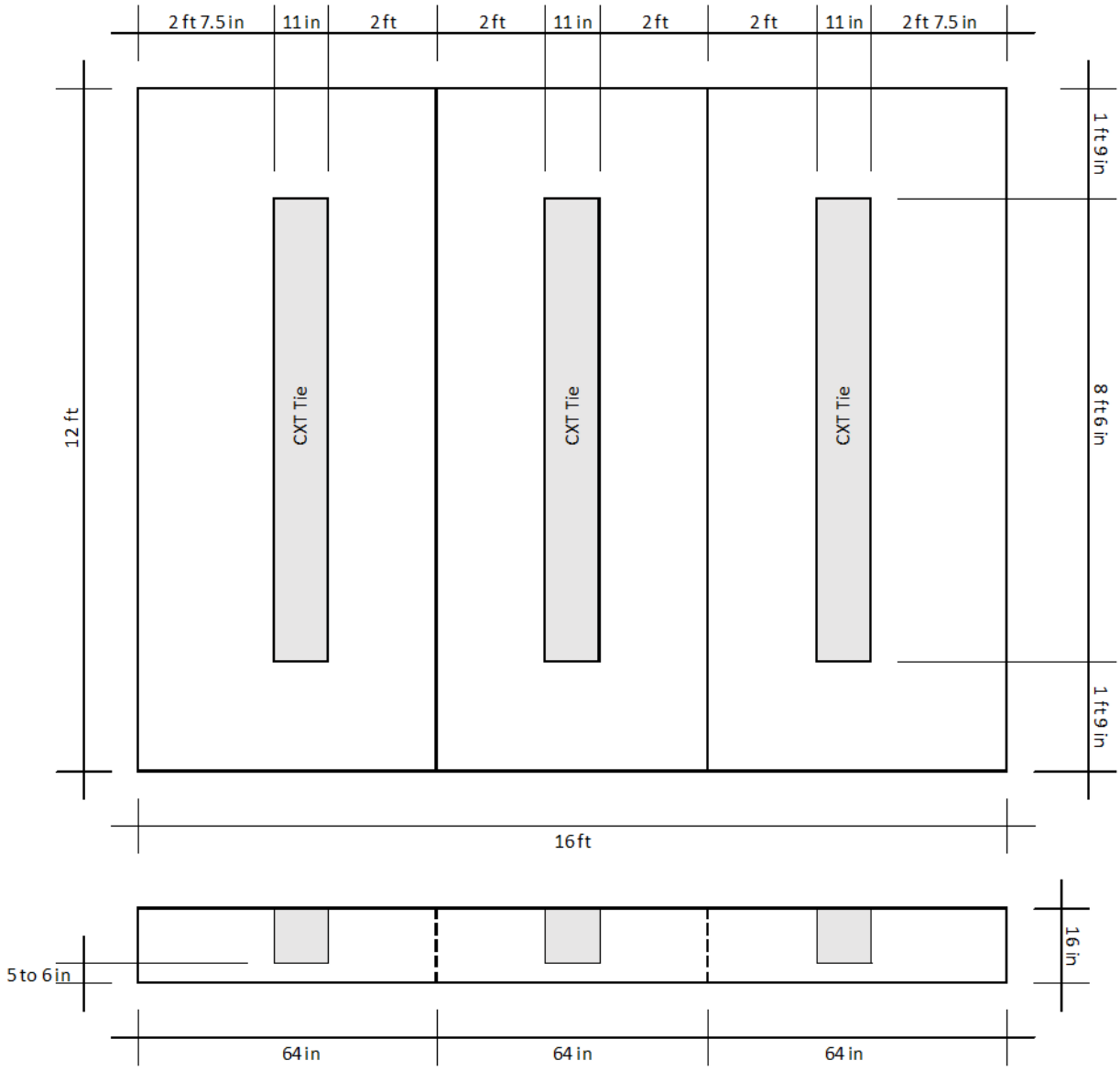

Figure 2-7 Three-compartment model ballast box housing three of the crossties atop yard ballast.



Figure 2-8 Construction of ballast box (left) and final configuration (right).

Publicly available weather information for Rantoul, IL, indicates that there is an average annual snowfall of 37.1 inches and average annual rainfall of 18.2 inches. The average daily high and nightly low temperatures regularly fluctuates between freezing and non-freezing resulting in a relatively high number of freeze-thaw cycles of approximately 80 to 100 [Hershfield, 1973].

The remaining four crossties (A-445, A-446, A-447, and A-450) were transported to a location approximately 10 kilometers south of Lytton, British Columbia, Canada, to be installed in track. The selected track is owned by Canadian National (CN) and runs between Hope, BC, and Lytton, BC, along the Trans-Canada Highway and Fraser River. The four crossties were installed near the Cisco Bridges along track mile markers 103.8 and 104.2 (see Figure 2-9). Additionally, hygrothermal sensors were installed in an electrical conduit box in order to record ambient air temperatures and relative humidity immediately adjacent to the installation site.

Figure 2-9 Google satellite image showing approximate location of four ties installed in track near Cisco Bridges, Lytton, BC.

Publicly available weather information for Lytton, BC, indicates that there is extensive snowfall along this area of the Fraser River valley. Lytton, BC, records an average annual snowfall of 46.22 inches and average annual rainfall of 13.33 inches. The warm season lasts from June 17 to September 9 while the cold season lasts from November 15 to February 19. More importantly, the average daily high and nightly low temperatures regularly fluctuates between freezing and non-freezing from March to May and from September to November. This fluctuating temperature results in a relatively high number of freeze-thaw cycles of approximately 60 to 80 [Fraser, 1959]. After installation in October 2013, research partners at the University of British Columbia, Okanagan, retrieved recorded data every 3 months through March 2015.

2.5.4 Complementary installation of modulus of rupture beams and model concrete crossties in model ballast

Additionally, three instrumented modulus of rupture (MOR) beams measuring 6-inch by 6-inch by 21-inch and two model crossties measuring 9-inch by 9-inch by 16-inches were installed into the model ballast such that their top surface was level with the crossties. The nominal concrete mixture design for these complementary members is shown in Table 2-4. The concrete mix design is intended to be comparable to the concrete crossties installed in track and in model ballast. Each MOR beam was instrumented with 4 hygrothermal sensors positioned 11.5 inches from either end of the beam and at depths of 0.5, 1.5, 4.5, and 5.5 inches, as shown in Figure 2-10. The benefit of these beams is that they are more easily removed from ballast than the crossties in order to re-condition them in an environmentally controlled room whenever necessary. Each model crosstie was instrumented with 4 hygrothermal sensors positioned 8 inches from either end of the length and at depths of 0.5, 2.5, 5.5, and 8.5 inches, as shown in Figure 2-11. Additionally, one model tie was constructed with anchors such that a polyurethane bad and section of rail could be fastened at a later point in time in order to better simulate track environments.

Table 2-4 Nominal concrete mix design of modulus of rupture beams and model crossties.

Material Type	**Pounds Per Cubic Yard**	**Kilograms Per Cubic Meter**
Type I Portland Cement	718	426
#7 Aggregate	2085	1236
Sand	1257	746
Water	216	128
High Range Water Reducer	12 fl. oz per 100 lb. cementitious (782 mL per 100 kg cementitious)	

Figure 2-10 Illustration of 6 x 6 x 21 inch modulus of rupture concrete beam instrumented with hygrochron sensors at depths of 0.5, 1.5, 4.5, and 5.5 inches from the top surface. The sensors are centrally situated in the beam 3 inches from the width of the beam at 10.5 inches from either end. The beams are installed in model ballast in Rantoul, IL.

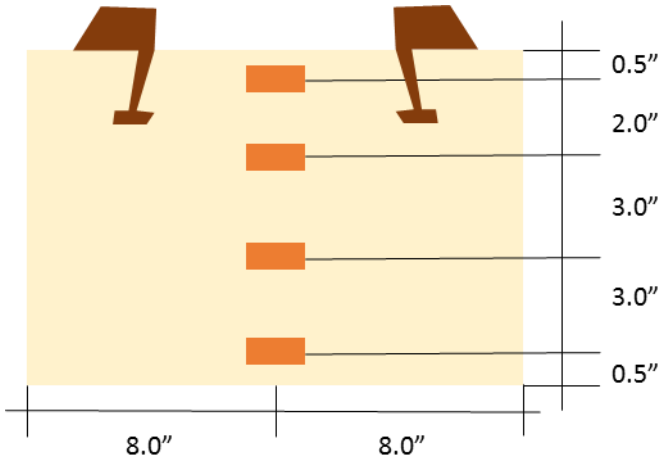

Figure 2-11 Illustration of model 9 x 9 x 16 inch model concrete crosstie instrumented with hygrochron sensors at depths of 0.5, 2.5, 5.5, and 8.5 inches from the top surface. The sensors are centrally situated in the model crosstie approximately 4 inches from the width of the prism at 8 inches from either end. The model crossties are installed in model ballast in Rantoul, IL.

2.6 Results

The instrumented concrete crossties, model crossties, and modulus of rupture beams typified similar behaviors. Namely, hygrothermal sensors functioned appropriately at early ages and failed at later ages. However, the large data set observed over the 1 year period allows for meaningful observations and conclusions to be drawn.

2.6.1 Relative humidity results over observation period

Although relative humidity of ambient conditions fluctuates daily, internal relative humidity of concrete members fluctuate in a more seasonal manner except for the near surface of the concrete surface. Figure 2-12 shows a model concrete crosstie moved from a dry, indoor environment to model ballast in Rantoul, IL, where sensors closer to the exterior surface (0.5 and 8.5 inches) rise in relative humidity value. Internal relative humidity at depths of 2.5 and 5.5 inches remain significantly high and do not respond to the change in environment in a drastic manner. A similar trend is observed in a modulus of rupture beam installed in ballast (see Figure 2-13).

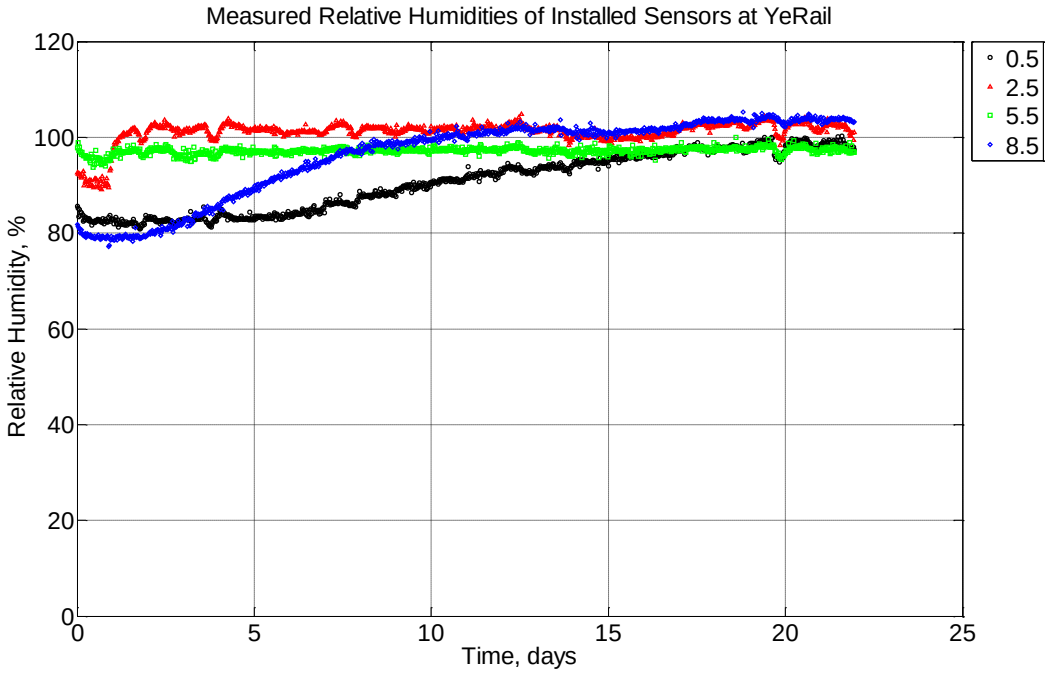

Figure 2-12 Measured relative humidity at depths of 0.5 inches (12.7 mm), 2.5 inches (63.5 mm), 5.5 inches (139.7 mm), and 8.5 inches (215.9 mm) from the surface of a model concrete crosstie (labeled YeRail) installed in ballast in Rantoul, IL, between November 29, 2014, through December 21, 2014. An 8 mm thick polyurethane pad and 12 in (30.48 cm) length 136 lb/yd (67.5 kg/m) section of steel rail are additionally installed atop the model concrete crosstie.

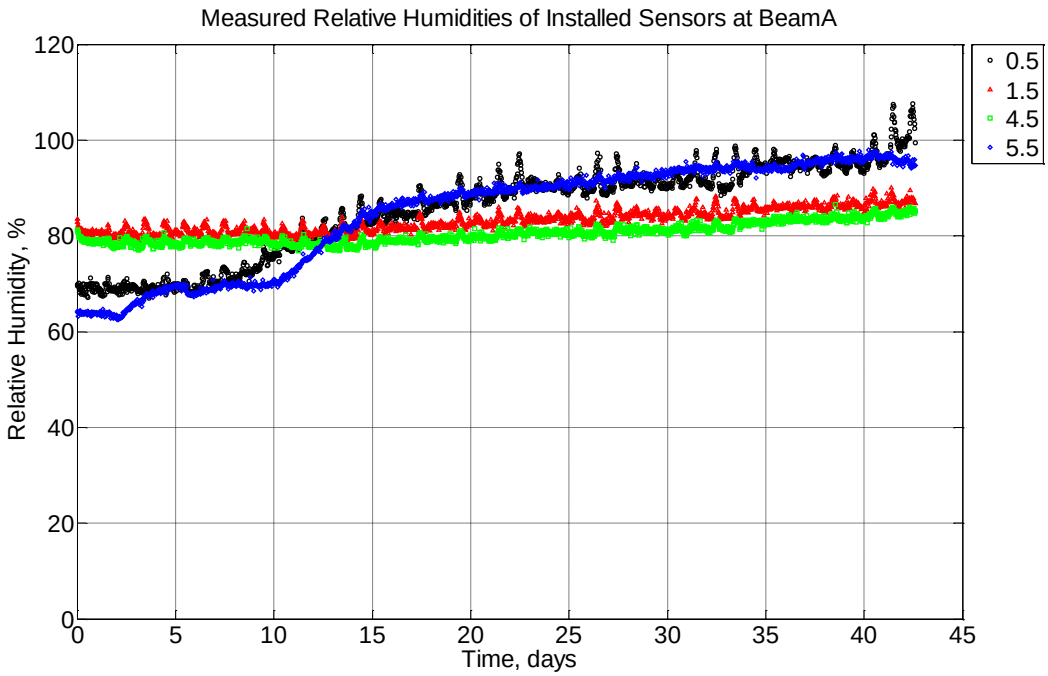

Figure 2-13 Measured relative humidity at depths of 0.5 inches (12.7 mm), 1.5 inches (38.1 mm), 4.5 inches (114.3 mm), and 5.5 inches (139.7 mm) from the surface of a modulus of rupture beam (labeled A) installed in ballast in Rantoul, IL, between October 19, 2014, through November 30, 2014.

Whenever these concrete members were installed in ballast, measureable relative humidity values inside the concrete steadily increased and did not appreciably decrease. In order to confirm that the proposed 1-dimensional relative humidity model is appropriate for the finite-width concrete member in a drying case, the modulus of rupture beams were removed from ballast, on occasion, and moved into an environmentally controlled room where the ambient relative humidity was maintained at 50% relative humidity. The response of the sensors is as expected where internal humidity near the exterior of the concrete surface (0.5 and 5.5 inches) fell more quickly than what was measured at the interior of the concrete member (1.5 and 4.5 inches) (see Figure 2-14).

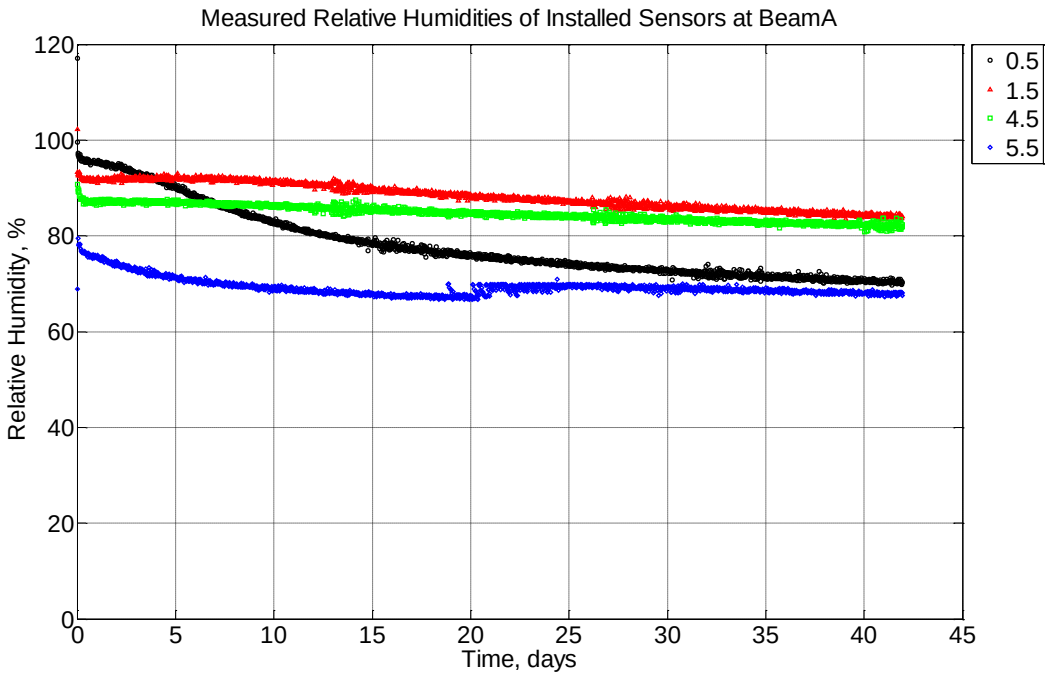

Figure 2-14 Measured relative humidity at depths of 0.5 inches (12.7 mm), 1.5 inches (38.1 mm), 4.5 inches (114.3 mm), and 5.5 inches (139.7 mm) from the surface of a modulus of rupture beam (labeled A) located inside an environmentally controlled room (50% RH, 23ºC) between July 29, 2014, through September 9, 2014.

2.6.2 Temperature results over observation period

Concrete exposed to ambient conditions undergo greater temperature fluctuations than relative humidity fluctuations. Figure 2-15 shows a concrete crosstie installed in track near Lytton, BC, for 85 days in the winter season and Figure 2-16 shows greater detail of fluctuations across 10 days in that same period. Each of its embedded hygrothermal sensors depict wide ranging temperature fluctuations mostly attributable to the daily temperature changes. Moreover, it is observed that fluctuations at the top and bottom of the crosstie will undergo freezing events in a cyclic manner. Figures 2-17 and 2-18 similarly depicts a concrete crosstie installed in model ballast in Rantoul, IL, in the summer months. Similar to Figure 2-16, the daily and daily and nightly fluctuations in Figure 2-18 are more prominently evident because of a shorter observation period. It is worth noting that near the surface of the concrete crosstie, the temperatures will increase to values much higher than the interior of the member. During nighttime temperatures, the concrete crosstie appears to reach comparable values.

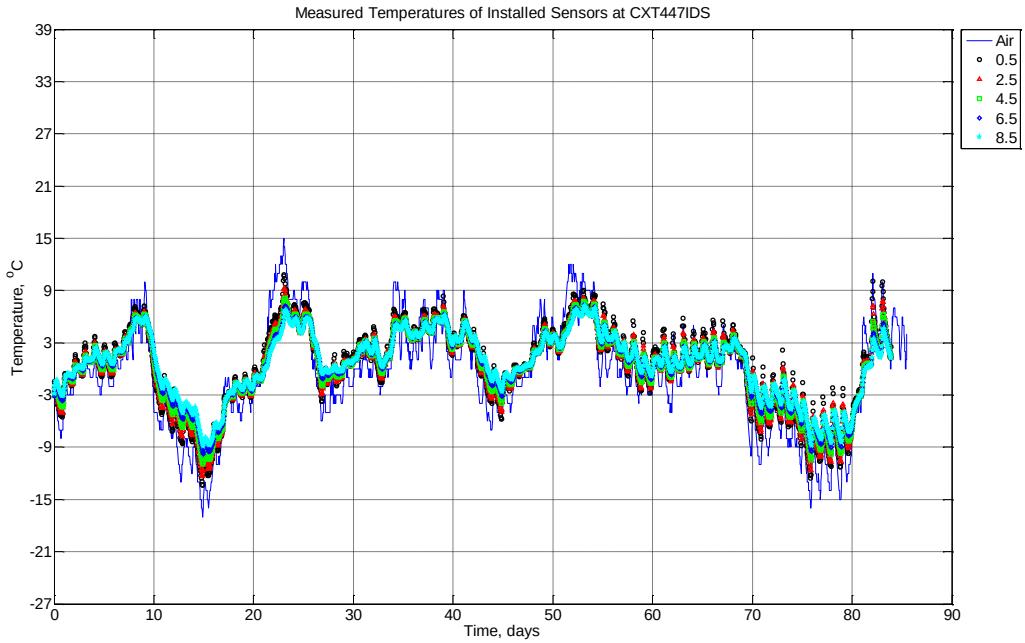

Figure 2-15 Measured air temperature and measured temperature values at depths of 0.5 inches (12.7 mm), 2.5 inches (63.5 mm), 4.5 inches (114.3 mm), 6.5 inches (139.7 mm), and 8.5 inches (215.9 mm) from the surface of a concrete crosstie (labeled CXT447IDS) installed in track near Lytton, BC, between November 22, 2013, through February 14, 2014. An 8 mm thick polyurethane pad and steel rail are additionally installed atop the concrete crosstie.

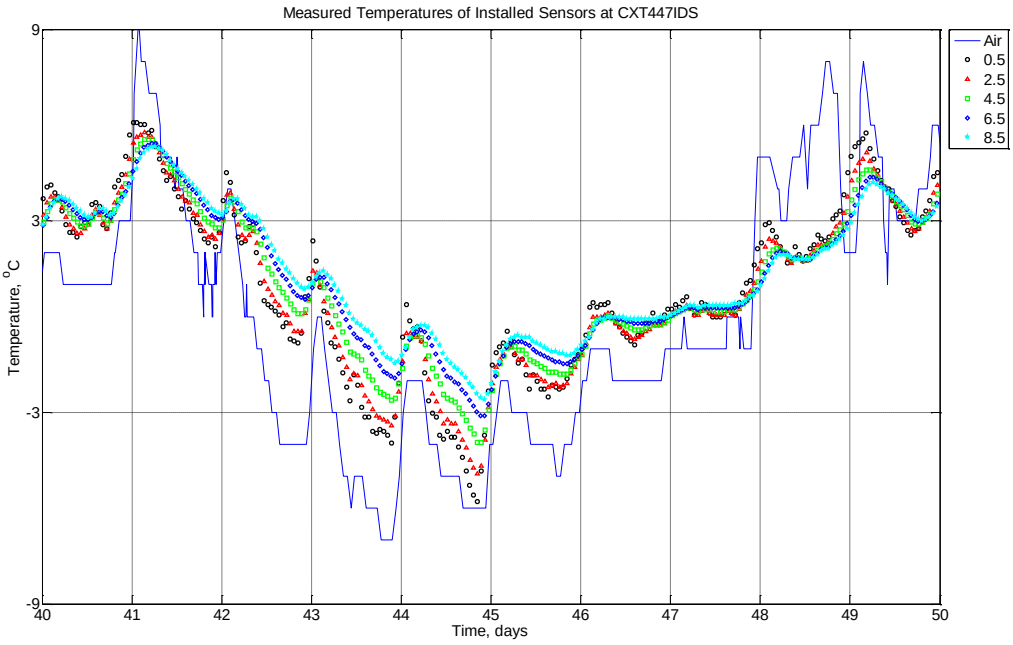

Figure 2-16 Measured air temperature and measured temperature values at depths of 0.5 inches (12.7 mm), 2.5 inches (63.5 mm), 4.5 inches (114.3 mm), 6.5 inches (139.7 mm), and 8.5 inches (215.9 mm) from the surface of a concrete crosstie (labeled CXT447IDS) installed in track near Lytton, BC, between January 1, 2014, through January 10, 2014. An 8 mm thick polyurethane pad and steel rail are additionally installed atop the concrete crosstie.

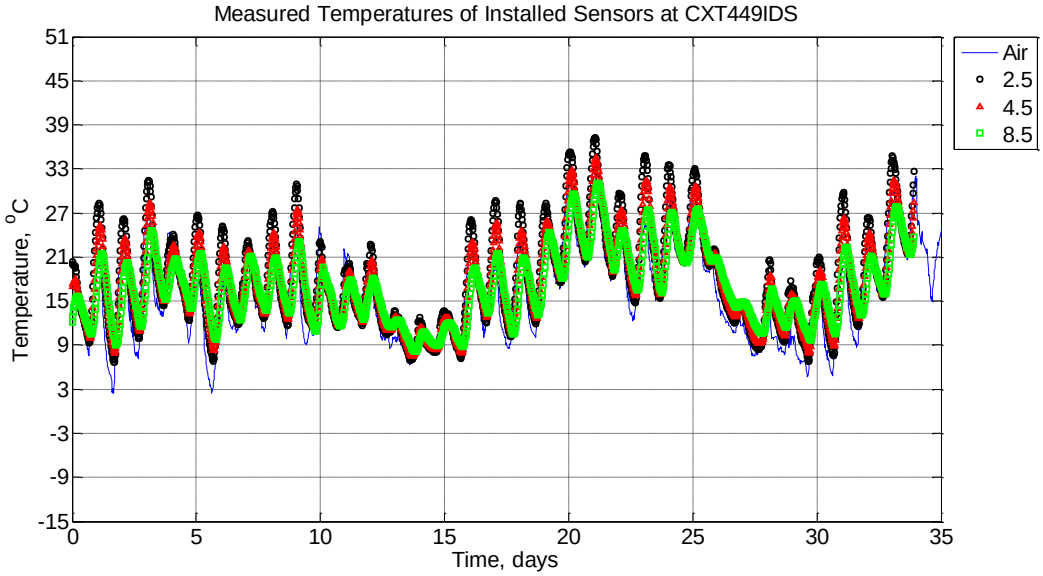

Figure 2-17 Measured air temperature and measured temperature values at depths of 2.5 inches (63.5 mm), 4.5 inches (114.3 mm), and 8.5 inches (215.9 mm) from the surface of a concrete crosstie (labeled CXT449IDS) without a polyurethane pad nor rail installed in ballast in Rantoul, IL, between April 17, 2014, through May 21, 2014.

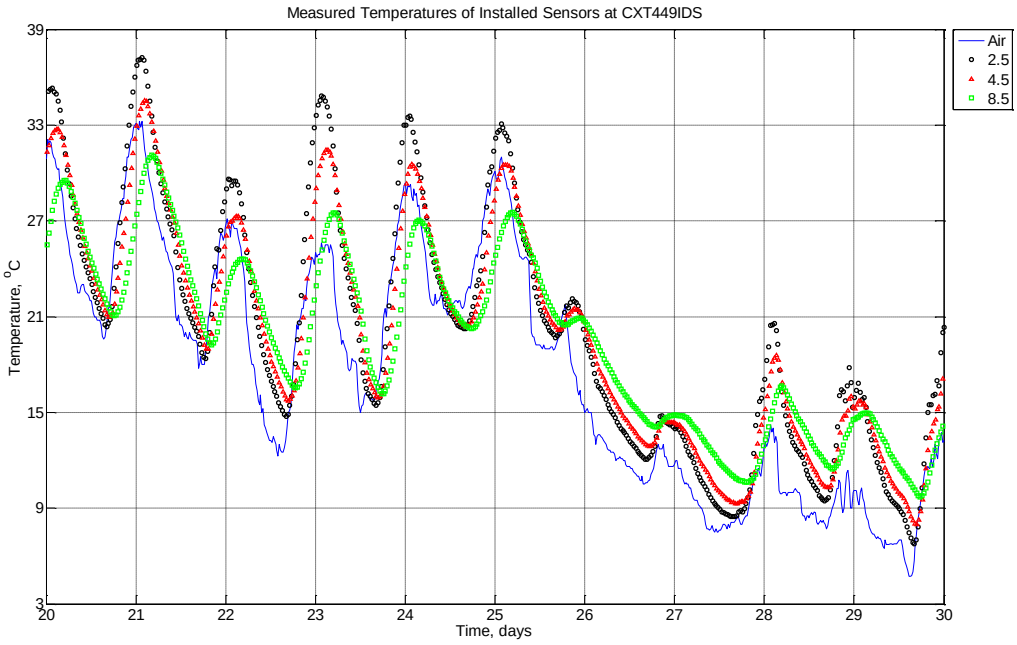

Figure 2-18 Measured air temperature and measured temperature values at depths of 2.5 inches (63.5 mm), 4.5 inches (114.3 mm), and 8.5 inches (215.9 mm) from the surface of a concrete crosstie (labeled CXT449IDS) without a polyurethane pad nor rail installed in ballast in Rantoul, IL, between May 7, 2014, through May 17, 2014.

2.7 Discussion of Results and Predictive Modeling

2.7.1 Internal relative humidity distribution

The predictive 1-dimensional moisture transport equation shown in Equation 2-1 is executed in a Matlab script to predict the relative humidity distribution across the depth of 6 inch (153 mm) or 9 inch (230 mm) depending on whether the concrete sample being analyzed is a modulus of rupture beam or a (model) crosstie. However, other parameters are held near constant throughout the entirety of the analysis, namely because of the similarity of the concrete mixture design. The moisture diffusivity at complete saturation is 0.86×10^{-6} m^2/hr, the regression coefficient is selected as 15, α is 0.05 [Kang *et al.*, 2012], and the bifurcation relative humidity point is 75% RH.

In Figure 2-19, the depth across a model concrete crosstie is depicted with an initial condition where the interior of the concrete sample is saturated while the exterior of the concrete sample is in equilibrium with the surrounding environment (approximately 80% RH). The

surrounding environment is defined as the boundary conditions where externally positioned hygrothermal sensors monitor the ballast conditions. The hygrothermal sensor located at the top surface of the ballast is additionally modified according to Table 2-2. Over the span of 20 days, the model concrete crosstie is subjected to high relative humidity values which leads to its relative humidity values to increase over time. This increase with respect to time is encapsulated by the model (continuous line) moving rightward, not exceeding 100% relative humidity.

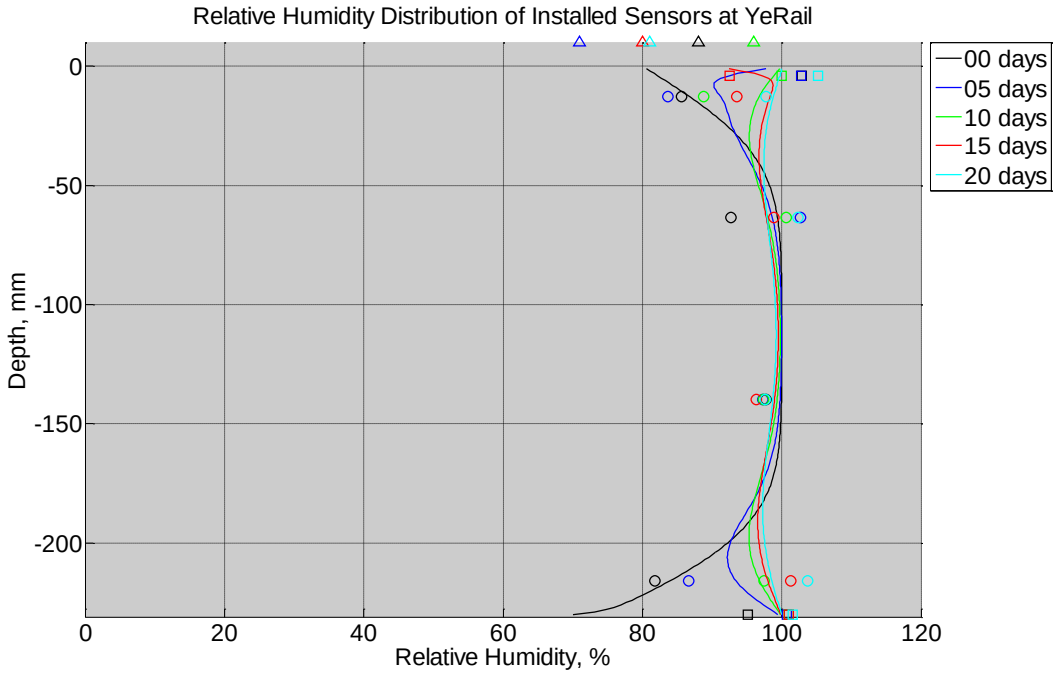

Figure 2-19 Measured (markers) and modeled (continuous line) relative humidity profile distribution as a function of depth inside a model concrete crosstie (labeled YeRail) installed in ballast in Rantoul, IL, between November 29, 2014, through December 21, 2014. An 8 mm thick polyurethane pad and 12 in (30.48 cm) length 136 lb/yd (67.5 kg/m) section of steel rail are additionally installed atop the model concrete crosstie. The model does not incorporate a polyurethane pad nor steel rail line. Triangular markers denote relative humidity value from KTIP weather station, square markers denote measured relative humidity values from ballast, and circular markers denote measured relative humidity values inside concrete.

The predicted values throughout the depth of the model concrete crosstie can be compared against the experimentally determined relative humidity values as measured by the hygrothermal sensors. This comparison produces Figure 2-20 where each point represents a singular moment in time and whose coordinates represent predicted and measured relative humidity values. A perfect prediction of relative humidity values would produce a scatter of data that suitably overlies the

line of equality. Figure 2-20 shows a relatively good agreement between predicted and measured relative humidity values at each of the four depths inside the model concrete crosstie.

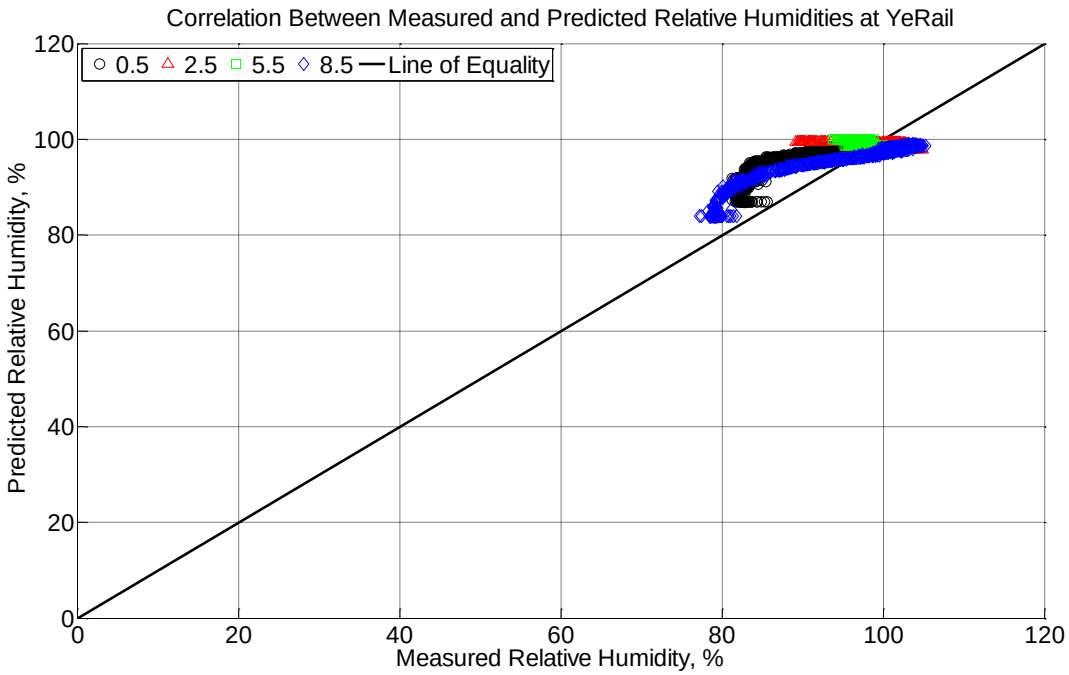

Figure 2-20 Correlation between measured and predicted relative humidity values 0.5 inches (12.7 mm), 2.5 inches (63.5 mm), 5.5 inches (139.7 mm), and 8.5 inches (215.9 mm) from the surface of a model concrete crosstie (labeled YeRail) installed in ballast in Rantoul, IL, between November 29, 2014, through December 21, 2014. An 8 mm thick polyurethane pad and 12 in (30.48 cm) length 136 lb/yd (67.5 kg/m) section of steel rail are additionally installed atop the model concrete crosstie. The model does not incorporate a polyurethane pad nor steel rail line.

The inclusion of modified boundary conditions to reflect moisture becoming entrapped by the polyurethane pad and rail line is not wholly isolated due to the finite-width nature of the model concrete crosstie. Figure 2-21 shows the same predictive model applied to a modulus of rupture beam similarly installed in the model ballast in Rantoul, IL. However, no confining polyurethane pad nor rail line are installed. In this scenario, the modulus of rupture beam is not wholly saturated at the interior at the start of the simulation. However, a similar trend is observed that the modeled line is moving rightward indicating an increase in predicted internal relative humidity. Figure 2-22 compares the predicted and measured relative humidity values to again find a comparably good agreement.

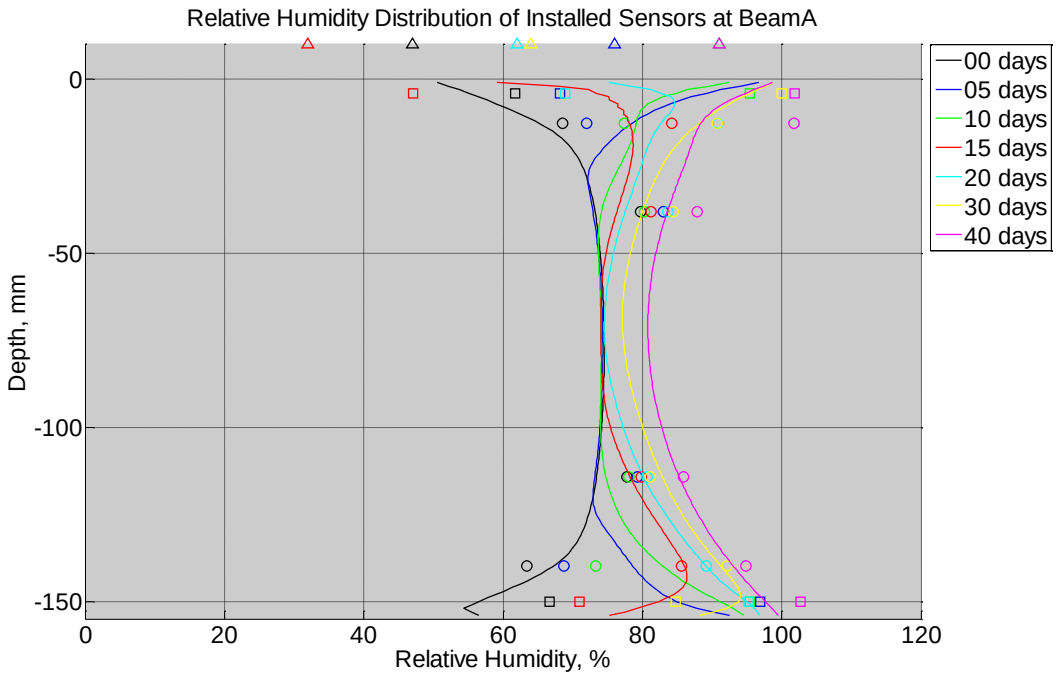

Figure 2-21 Measured (markers) and modeled (continuous line) relative humidity profile distribution as a function of depth inside modulus of rupture beam (labeled A) installed in ballast in Rantoul, IL, between October 19, 2014, through November 30, 2014. Triangular markers denote relative humidity value from KTIP weather station, square markers denote measured relative humidity values from ballast, and circular markers denote measured relative humidity values inside concrete.

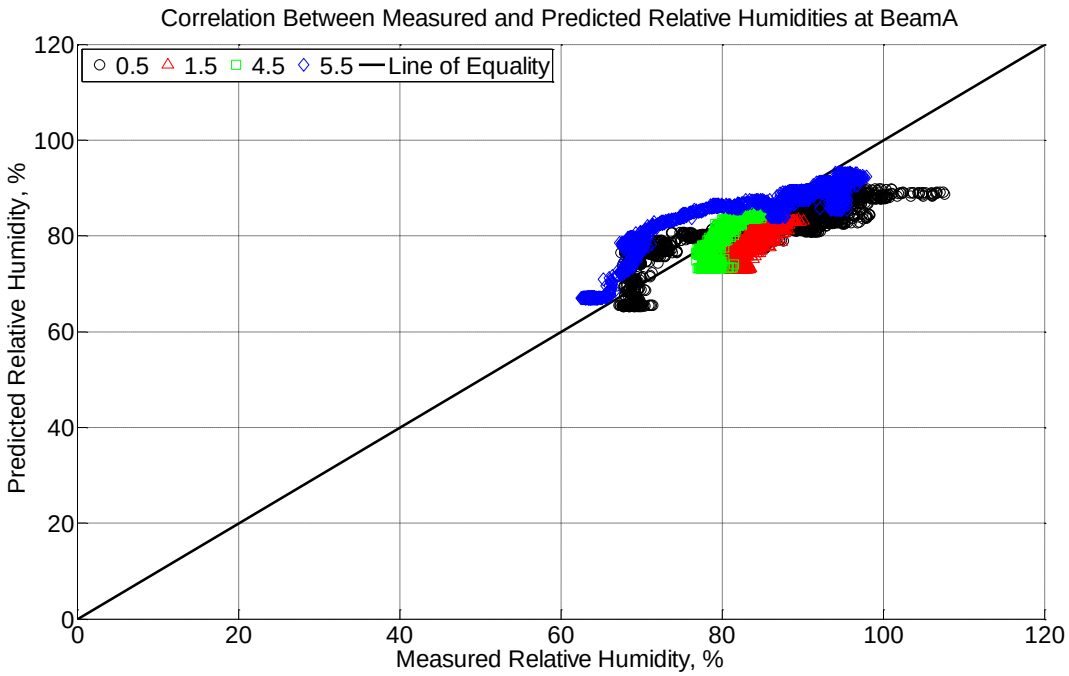

Figure 2-22 Correlation between measured and predicted relative humidity values 0.5 inches (12.7 mm), 1.5 inches (38.1 mm), 4.5 inches (114.3 mm), and 5.5 inches (139.7 mm) from the surface of a modulus of rupture beam (labeled A) installed in ballast in Rantoul, IL, between October 19, 2014, through November 30, 2014.

In these instances of wetting as depicted in Figures 2-12 and 2-13, the predictive moisture transport model is suitable in characterizing the increasing internal relative humidity. In the event of drying, the boundary conditions can be altered to remain constant at both the topside and underside of a modulus of rupture beam when it is moved to an environmentally controlled room. Figure 2-23 shows the predicted change in relative humidity when a nominally saturated concrete modulus of rupture beam is moved into a 50% relative humidity controlled environment. It is evident that the predicted values (continuous line) shifts leftward indicating drying. When these predicted values are again compared to measured values (see Figure 2-24), the good agreement between predicted and measured relative humidity values becomes apparent again.

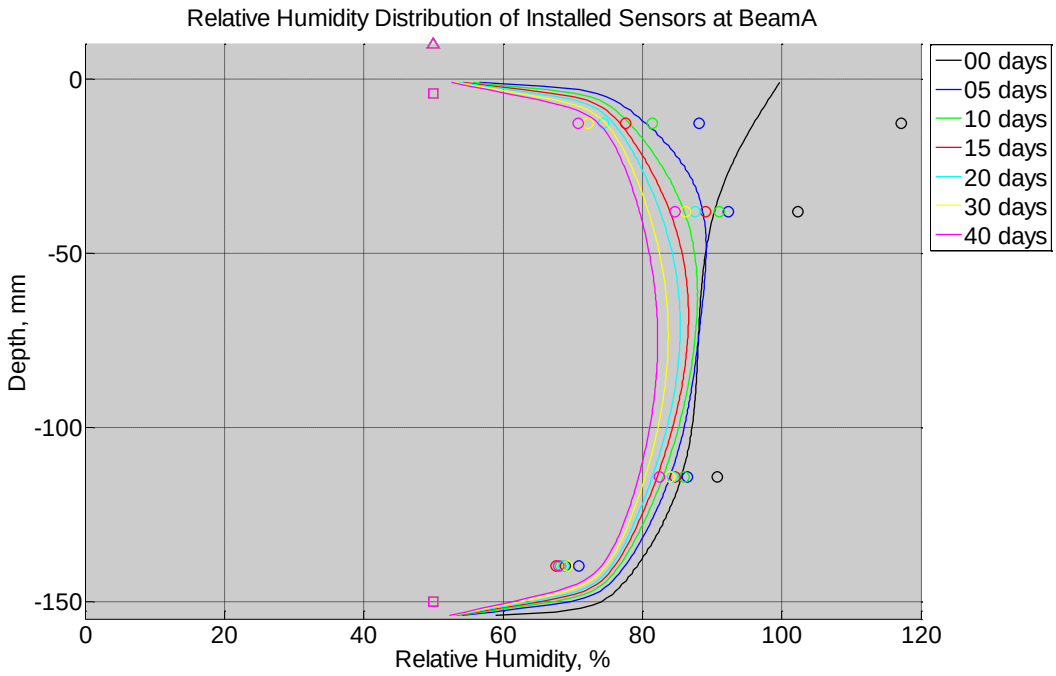

Figure 2-23 Measured (markers) and modeled (continuous line) relative humidity profile distribution as a function of depth inside modulus of rupture beam (labeled A) located inside an environmentally controlled room (50% RH, 23°C) between July 29, 2014, through September 9, 2014. Triangular markers denote relative humidity value from control panel, square markers denote measured relative humidity values from ambient sensors, and circular markers denote measured relative humidity values inside concrete.

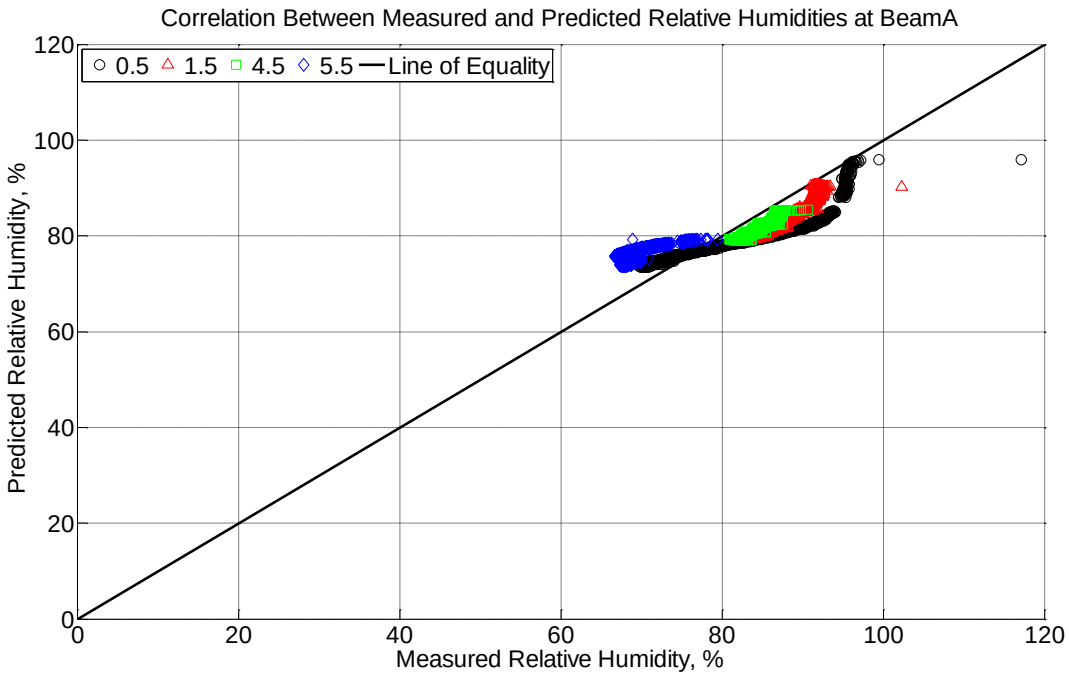

Figure 2-24 Correlation between measured and predicted relative humidity values 0.5 inches (12.7 mm), 1.5 inches (38.1 mm), 4.5 inches (114.3 mm), and 5.5 inches (139.7 mm) from the surface of a modulus of rupture beam (labeled A) located inside an environmentally controlled room (50% RH, 23ºC) between July 29, 2014, through September 9, 2014.

2.7.2 Solar radiation estimation

The solar radiation at a given geo-temporal location must be estimated in order for the predictive 1-dimensional, multi-layered temperature model to work suitably. As such, Equation 2-11 is solved in order to estimate the total incoming solar radiation in Rantoul, IL, and Lytton, BC, throughout the same time period that the predictive temperature modeling is conducted. Figure 2-25 shows the observed temperature and relative humidity in Rantoul, IL, during cool, winter months. In this figure, the estimated solar radiation is relatively low in value. This is sensible due to the shorter length of daytime and increased amount of cloud cover in the winter months. Figure 2-26 shows a similar estimation of the solar radiation in Lytton, BC, during the summer months. Again, the increased estimated solar radiation during this time period is sensible due to lengthier daylight hours and decreased instances of extensive cloud cover.

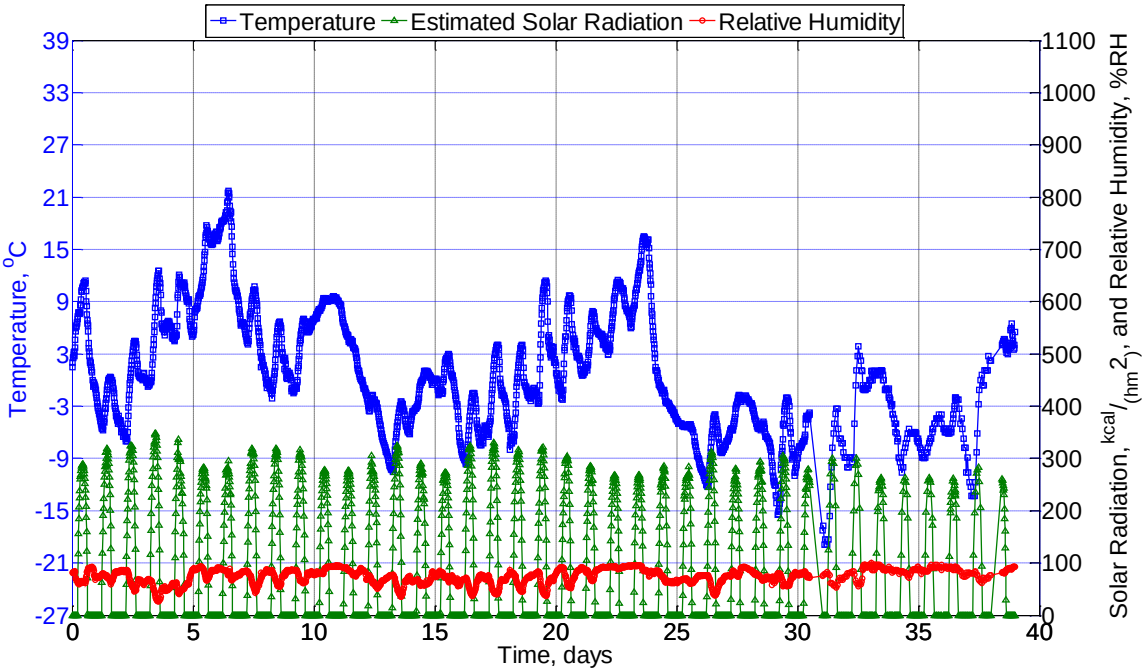

Figure 2-25 Temperature and relative humidity collected from weather station KTIP in Rantoul, IL, from November 12, 2013, through December 18, 2013. Solar radiation is estimated over this same timeframe.

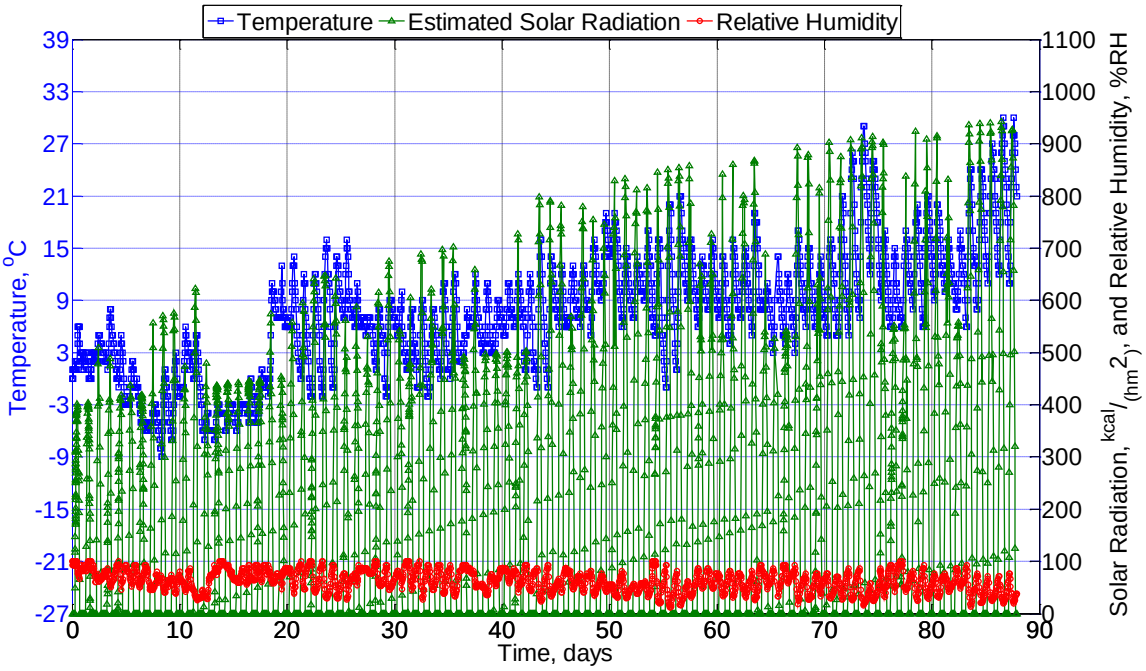

Figure 2-26 Temperature and relative humidity collected from weather station CWLY in Lytton, BC, from February 18, 2014, through May 14, 2014. Solar radiation is estimated over this same timeframe.

2.7.3 Internal temperature distribution

The predictive 1-dimensional temperature equation shown in Equation 2-9 is executed in a Matlab script in order to predict temperature distribution across the depth of a 6 inch (153 mm) or 9 inch (230 mm) depending on whether the concrete sample being analyzed is a modulus of rupture beam or a (model) crosstie. The parameters involved in order to predictively solve the temperature distribution are held constant throughout the analysis. The pavement surface convection coefficient is 16.29 kcal/m^{2}C^o, the effective absorptivity is 0.55 throughout the entire time period, and the thermal conductivities and thermal diffusivities of each material type are defined in Table 2-5.

Table 2-5 Thermal conductivity and thermal diffusivity of material types used in the temperature predictive modeling. Values are adapted from either reference values, [1]Qin and Hiller, 2014, or [2]Prociak *et al.*, 2000.

Material Type	**Thermal Conductivity, λ (kcal/hmC^o)**	**Thermal Diffusivity, α (m^2/h)**
1025 Carbon Steel	31.2480	0.0531
Polyurethane	0.0172	0.0022[2]
Portland Cement Concrete	1.85[1]	0.0025[1]
Aggregate	2.58[1]	0.0030[1]

In Figure 2-27, the predictive model is shown at seven discrete points in time across 90 days of analysis of a concrete crosstie installed in track near Lytton, BC. The only boundary condition inputted into this model are the ambient air temperature at the topside of the concrete crosstie as measured from a nearby weather station and the estimated solar radiation. The multi-layered predictive temperature model is modeled in two manners: with a polyurethane pad and steel rail, or without a polyurethane pad nor steel rail. The results from these two formats is extensively shown in Appendix A4, A6, A8, and A10. It is readily observed that the incorporation of a polyurethane pad and steel rail line does not greatly enhance the predictive fit of the model. This is strongly evidenced in Figure 2-28 where the predicted temperature values are compared against the measured temperature values. In this modeling effort, the correlation between the predicted and measured values is good. This is accomplished despite not incorporating a polyurethane pad nor steel rail line. In an effort to more properly depict the physical thicknesses of the overlying materials, an analysis is performed where the polyurethane pad is constructed with

a thickness of 8 mm while the steel rail line is constructed with a thickness of 10 mm. The result of this fit is shown in Figure A10-42 (in Appendix A) where the increased insulation from the polyurethane pad blunts the effect of the ambient air temperature and the incoming solar radiation.

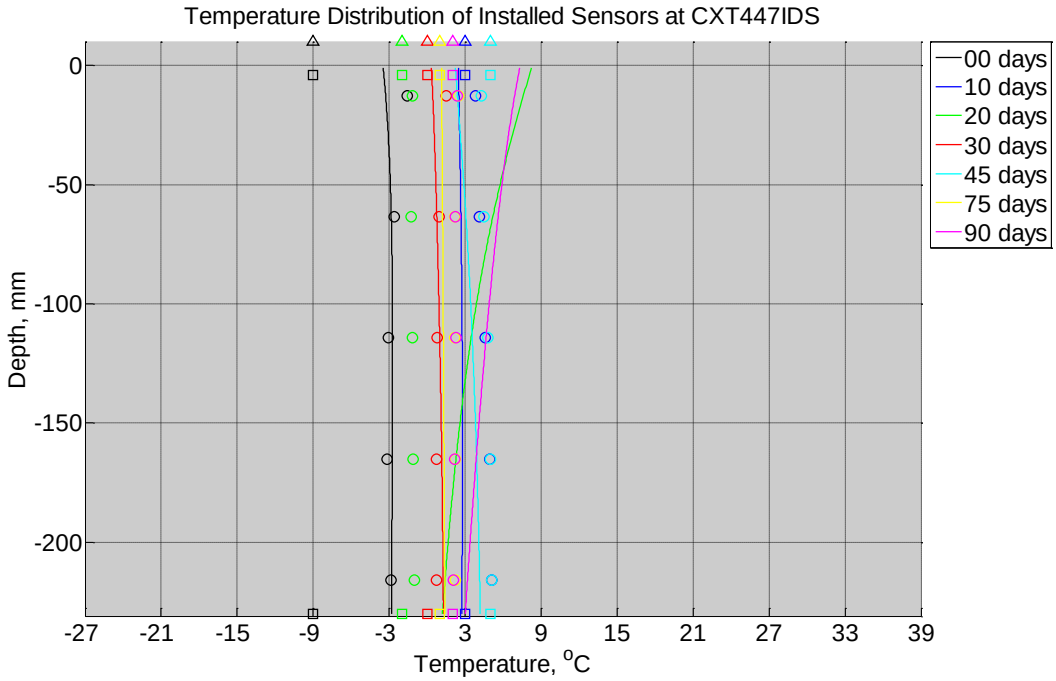

Figure 2-27 Measured (markers) and modeled (continuous line) temperature profile distribution as a function of depth inside a concrete crosstie (labeled CXT447IDS) installed in track near Lytton, BC, between November 22, 2013, through February 14, 2014. An 8 mm thick polyurethane pad and steel rail are additionally installed atop the concrete crosstie. The model does not incorporate a polyurethane pad nor steel rail line. Triangular markers denote temperature value from CWLY weather station, square markers denote assumed temperature values in ballast, and circular markers denote measured temperature values inside concrete.

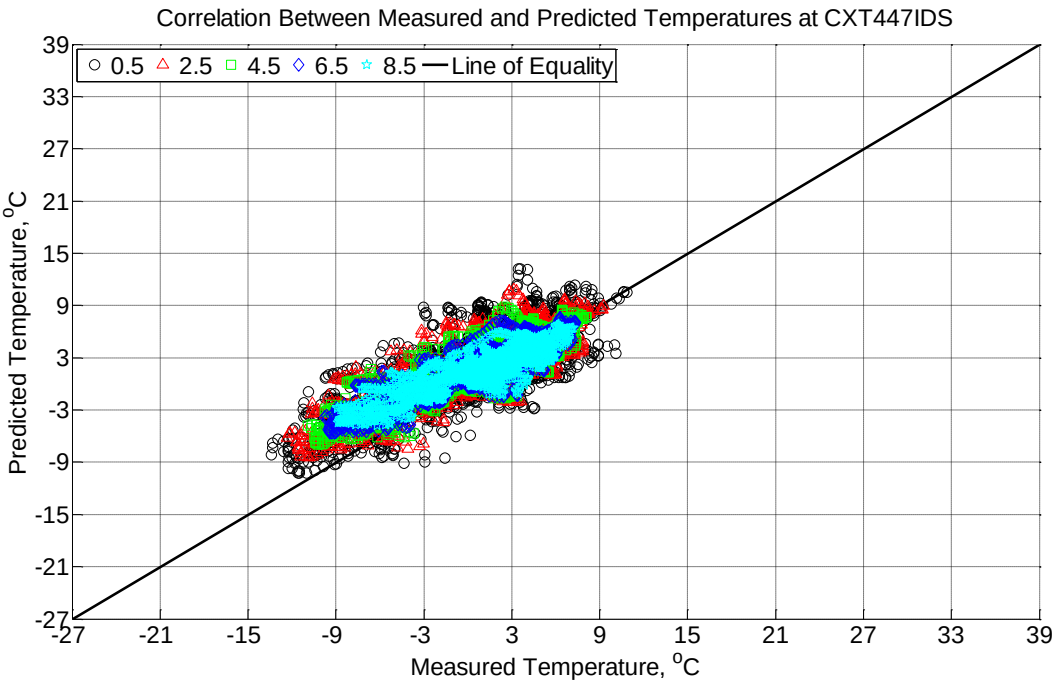

Figure 2-28 Correlation between measured and predicted temperature values 0.5 inches (12.7 mm), 2.5 inches (63.5 mm), 4.5 inches (114.3 mm), 6.5 inches (139.7 mm), and 8.5 inches (215.9 mm) from the surface of a concrete crosstie (labeled CXT447IDS) installed in track near Lytton, BC, between November 22, 2013, through February 14, 2014. An 8 mm thick polyurethane pad and steel rail are additionally installed atop the concrete crosstie. The model does not incorporate a polyurethane pad nor steel rail line.

Figures 2-29 and 2-30 are also predictions of internal temperature, although these depict summer months. Unlike the prediction during wintry months in Figures 2-27 and 2-28, it is evident that the model temperature is over predicted in summer months. This is possible due to a variety of effects. Firstly, the temperature model is reliant upon an estimation of incoming solar radiation. Although the estimation adapted from Spokas and Forcella [2006] is demonstrably good, it is anticipated that there are inherent irregularities with regards to recorded weather when applied to specific instances in time. Passing cloud cover, hazy conditions, and shade from nearby structures potentially obstruct the true incoming solar radiation. Secondly, and of greater importance, is the notion of applying a 1-dimensional pavement model to a 3-dimensional concrete crosstie in ballast. Heat radiation is not occurring linearly through the multiple layers. Instead, heat is transmitting through the layers and is also transmitting through the ballast which is in contact with the side of the crossties. As such, it is likely that an improved model incorporate this additional transference of heat through the aggregate ballast.

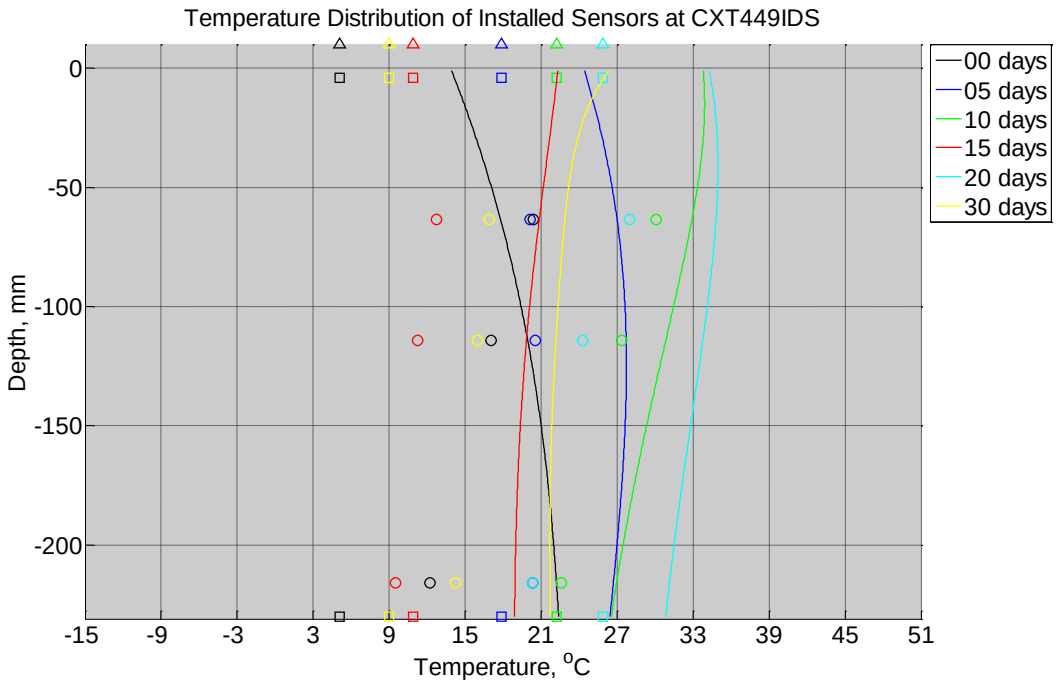

Figure 2-29 Measured (markers) and modeled (continuous line) temperature profile distribution as a function of depth inside a concrete crosstie (labeled CXT449IDS) without a polyurethane pad nor rail installed in ballast in Rantoul, IL, between April 17, 2014, through May 21, 2014. Triangular markers denote temperature value from KTIP weather station, square markers denote measured temperature values from ballast, and circular markers denote measured temperature values inside concrete.

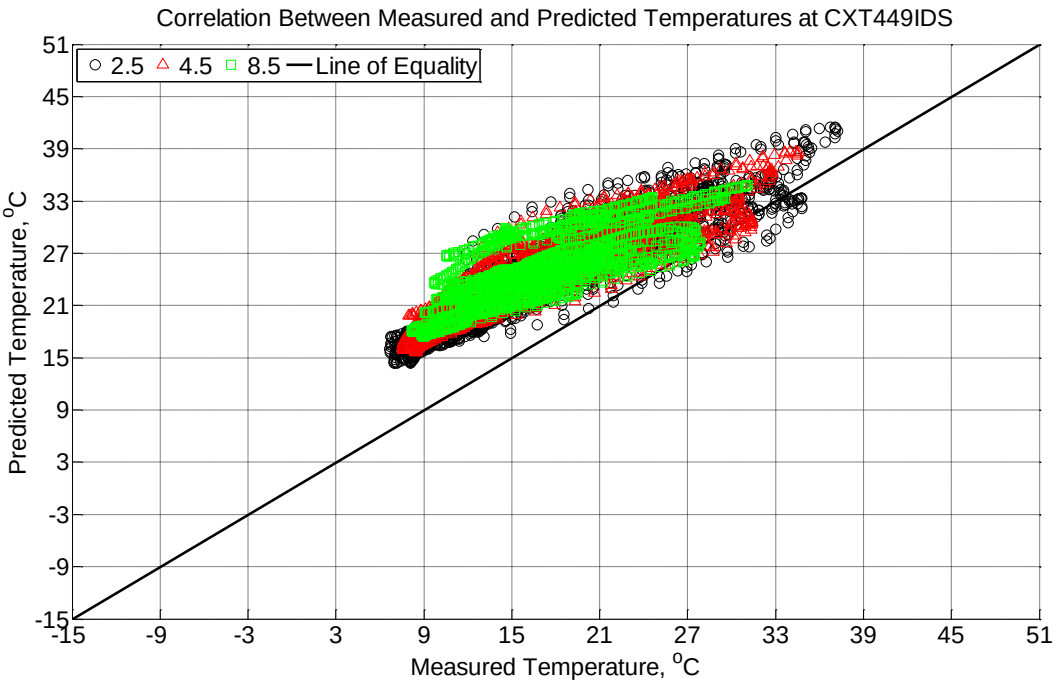

Figure 2-30 Correlation between measured and predicted temperature values 2.5 inches (63.5 mm), 4.5 inches (114.3 mm), and 8.5 inches (215.9 mm) from the surface of a concrete crosstie (labeled CXT449IDS) without a polyurethane pad nor rail installed in ballast in Rantoul, IL, between April 17, 2014, through May 21, 2014.

2.7.4 Effect of ballast conditions

The effect of the ballast acts in two manners upon the concrete crosstie: firstly, it serves as a fast-track avenue for liquid moisture to travel through and (in a well-drained ballast) flow away from the crosstie; secondly, it acts as an additional source of heat transmittance. Both of these factors have an effect on the internal relative humidity and temperature of a concrete crosstie installed in ballast.

Hygrothermal sensors installed in ballast at the topside and underside of a concrete crosstie measured both relative humidity and temperature, depicted in Figures 2-31 and 2-32, respectively. In Figure 2-31, it is evident that the sensor installed at the topside of a crosstie in the ballast undergoes large fluctuations that are comparable to the fluctuations seen in ambient relative humidity measurements. This indicates that aggregates in ballast react rapid to changing moisture conditions and can act as a desiccating force for the concrete crosstie. However, at the underside of the concrete crosstie, it is evident that relative humidity can remain consistently high and near 100% RH. This high relative humidity does not necessarily indicate a poorly drained ballast. It

instead suggests that moisture is trapped within the highly absorptive aggregate and creates a locally humid environment. As a result, this drained, humid ballast acts to slow any drying of the concrete crosstie itself. In large part, this supports the results seen in Figures 2-12 through 2-14 where the internal relative humidity of any concrete member is steadily rising whenever the member is installed within ballast.

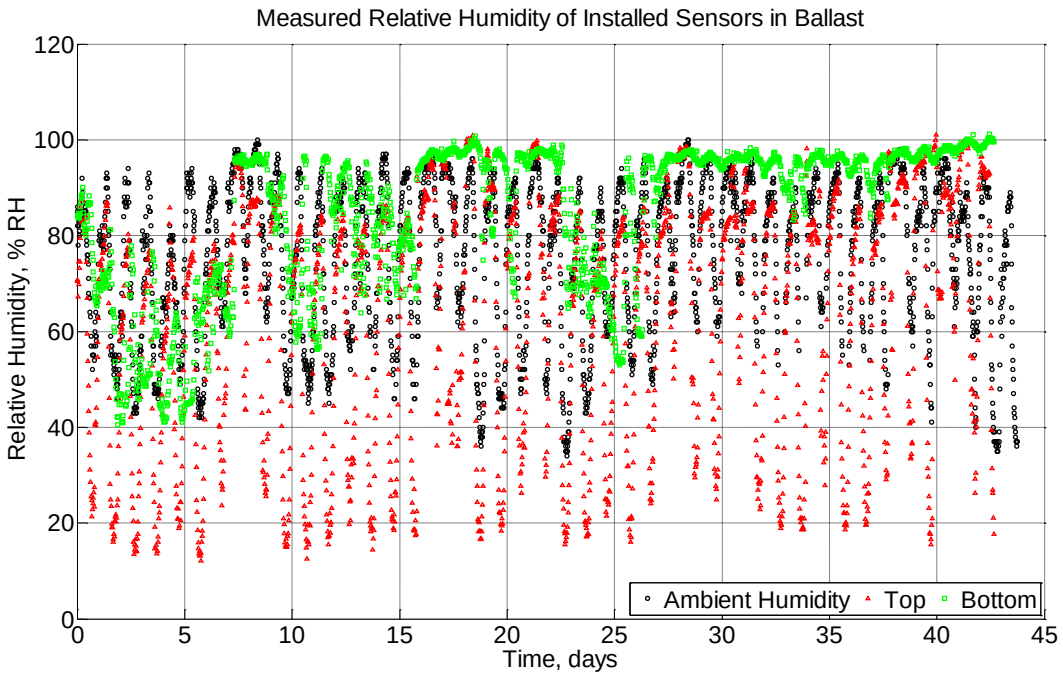

Figure 2-31 Measured relative humidity of model ballast at top and bottom of concrete crosstie in Rantoul, IL, between August 1, 2015, through September 13, 2015. Ambient relative humidity measured from a nearby weather station KTIP is also shown.

Similarly, temperature changes within the ballast are observable in Figure 2-30. At the topside of the ballast, measured temperatures fluctuate to values much higher than ambient air temperatures suggesting that incoming solar radiation is heating the ballast. In turn, this increased temperature immediately adjacent to the concrete crosstie can act to additionally overly increase the internal temperature in the summer months as evidenced in Figure 2-30. At the underside of the concrete crosstie, the hygrothermal sensor installed in ballast shows a muted response due to changing daily temperatures suggesting that the ballast at the underside of the crosstie is partially insulated. While this temperature observation in the ballast may not entirely affect concrete crosstie freeze-thaw resiliency performance, this observation may have an impact on the frost heaving potential of the ballast.

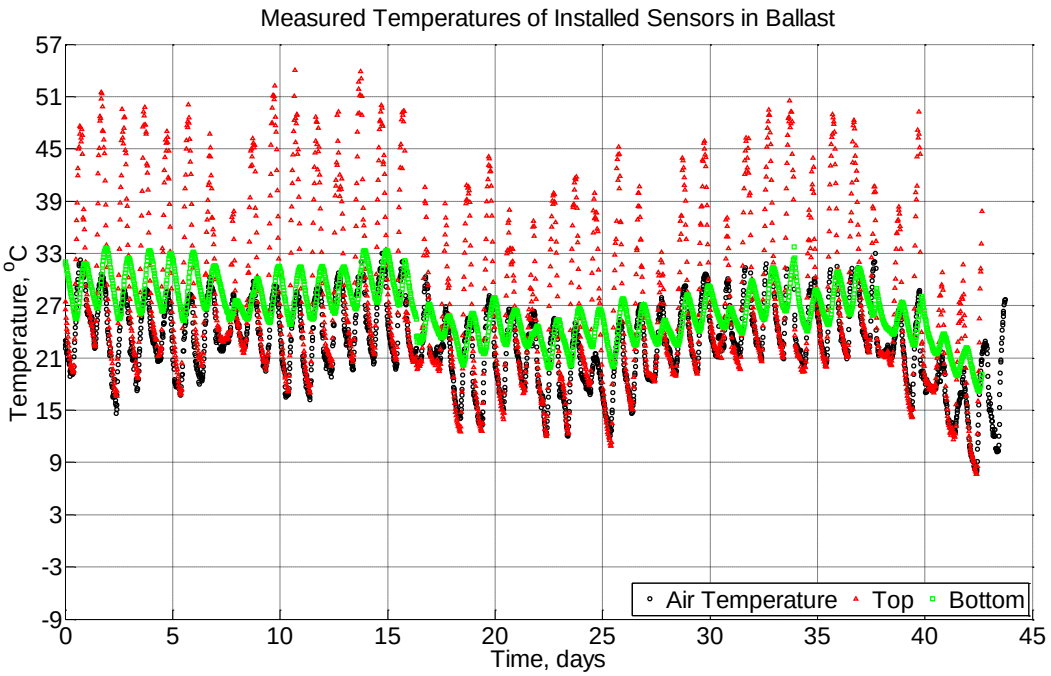

Figure 2-32 Measured temperature of model ballast at top and bottom of concrete crosstie in Rantoul, IL, between August 1, 2015, through September 13, 2015. Ambient air temperature measured from a nearby weather station KTIP is also shown.

2.8 Summary of Chapter

Concrete crossties are subjected to freeze-thaw climates across North America which can lead them to be susceptible to freeze-thaw cyclic damage. Concrete crossties, modulus of rupture beams, and model crossties were instrumented with hygrothermal sensors in order to monitor their internal relative humidity and temperature in two locations: Rantoul, IL, and Lytton, BC. Two 1-dimensional models are applied in order to predict the 3-dimensional response of the concrete crossties in track. It is found that:

- Hygrothermal sensors performed well at early-ages yet failed at later ages. At the time of failure, measured relative humidity values were in excess of 95% suggesting that a combination of persistently high relative humidity, alkalinity from the hydrated cement paste, and possibly high liquid moisture contributed to the material failure of the capacitance film of the hygrothermal sensor. This is indicative, but not definitive, of high moisture inside concrete crossties (modulus of rupture beams, or model crossties) when installed in aggregate ballast.

- A 1-dimensional moisture transport model is adequate to predict the change of internal relative humidity of a concrete member installed in aggregate ballast. The suitability of the model is limited to the geometric center of the rail seat area where the hygrothermal sensors were installed. It is highly likely that the relative humidity closer to the sides of the crossties directly exposed to the aggregate ballast are subject to higher relative humidity values. An improved 2-dimensional (or 3-dimensional) model may better predict the state of internal relative humidity inside a concrete crosstie installed in ballast.
- A 1-dimensional heat transfer model is adequate to predict the change of internal temperature of a concrete member installed in aggregate ballast particularly during wintry months. During this colder time of the year, it is likely that the effect of heat transferring from the immediately adjacent aggregate ballast is minimal. During the summer months, it is found that the model overly predicts the internal temperature. The effect of the polyurethane pad and steel rail is very limited on the predictive temperature model suggesting that a 2- or 3-dimensional model would better serve to predict summer months. In the case of identifying the instances of freezing events, a 1-dimensional pavement model is adequate to predict the 3-dimensional response of a concrete crosstie installed in aggregate ballast. Moreover, the temperature distribution between measured values and predicted values agree well with each where the upper portions of the concrete are more responsive to ambient temperature fluctuations than are interior portions of the concrete. This conclusion, however, is limited to the geometric center of the crosstie at the rail seat area where the study was conducted.

2.9 References

Al Riza, D. F., ul Haq, S. I., and Aris, M. S. "Hourly solar radiation estimation using ambient temperature and relative humidity data." *International Journal of Environmental Science and Development* 2 (2011): 188 – 193.

Barber, E. S., "Calculation of maximum pavement temperatures from weather reports." *Highway Research Board Bulletin* 168 (1957): 1 – 8.

Bakharev, T., and Struble, L. J. "Microstructural features of railseat deterioration in concrete ties." *Journal of Civil Engineering Materials* 9 (1997): 146 – 153.

Bažant, Z., and Najjar, L. "Nonlinear water diffusion in nonsaturated concrete." *Materials and Structures* 5 (1972): 3 – 20.

Bristow, K. L., and Campbell, C. S. "On the relationship between incoming solar radiation and daily maximum temperature and minimum temperature." *Agricultural and Forest Meteorology* 31 (1984): 159 – 166.
Burden, R. L., and Faires, J. D. *Numerical Analysis 7th Ed.* 2001, Pacific Grove, California: Brooks/Cole.
Campbell, G. S., and Norman, J. M. *Introduction to Environmental Biophysics 2nd Ed.* 1998, New York: Springer-Verlag.
Dempsey, B. J., and Thompson, M. R. "A heat transfer model for evaluating frost action and temperature related effects in multilayered pavement systems." *Highway Research Record* 342 (1970): 39 – 56.
Ferdous, W., and Manalo, A. "Failures of mainline railway sleepers and suggested remedies – Review of current practice." *Engineering Failure Analysis* 44 (2014): 17 – 35.
Fraser, J.K. "Freeze-thaw frequencies and mechanical weathering in Canada." *ARCTIC North American* 12 (1959).
Hakon, H. "Frost protection of railway lines." *Engineering Geology* 13 (1978): 505 – 517.
Hargreaves, G. H., and Samani, Z. A. "Reference crop evapotranspiration from temperature." *Applied Engineering in Agriculture* 1 (1985): 96 – 99.
Hershfield, D. M. "The frequency of freeze-thaw cycles." *Journal of Applied Meteorology* 13 (1973): 348 – 354.
Kang, S-T, Kim, J-S, Lee, Y., Park, Y-D, and Kim, J-K. "Moisture diffusivity of early age concrete considering temperature and porosity." *KSCE Journal of Civil Engineering* 16 (2012): 179 – 188.
Kim, J-K, and Lee, C-S. "Moisture diffusion of concrete considering self-desiccation at early ages." *Cement and Concrete Research* 29 (1999): 1921 – 1927.
Leech, C., Lockington, D., and Dux, P. "Unsaturated diffusivity functions for concrete derived for concrete derived from NMR images." *Materials and Structures* 36 (2003): 413 – 418.
Li, W., Pour-Ghaz, M., Castro, J., and Weiss, J. "Water absorption and critical degree of saturation relating to freeze-thaw damage in concrete pavement joints." *Journal of Materials in Civil Engineering* 24 (2012): 299 – 307.
Liu, B. Y., and Jordan, R. C. "The interrelationship and characteristic distribution of direct, diffuse, and total solar radiation." *Solar Energy* 4 (1960): 1 – 19.
Liu, D. L. "Incorporating diurnal light variation and canopy light attenuation into analytical equations for calculating daily gross photosynthesis." *Ecological Modelling* 93 (1996): 175 – 189.
Maxim Integrated. (March 2013). *DS1923 Revision 5*. Retrieved from http://datasheets.maximintegrated.com/en/ds/DS1923.pdf.
McVicar, T. R., and Jupp, D. L. B. "Estimating one-time-of-day meteorological data as inputs to thermal remote sensing based energy balance models." *Agricultural and Forest Meteorology* 96 (1999): 219 – 238.
Monteith, J. L. 1965. "Evaporation and the Environment. In the state and movement of water in living organisms." *Proceedings of the 19th Symposium, Society for Experimental Biology* (pp 205 – 234). Cambridge: Cambridge University Press.
Prociak, A., Pielichowski, J., and Sterzynski, T. "Thermal diffusivity of rigid polyurethane foams blown with different hydrocarbons." *Polymer Testing* 19 (2000): 705 – 712.

Solaimanian, M., and Kennedy, T. W. “Predicting maximum pavement surface temperature using maximum air temperature and hourly solar radiation.” *Transportation Research Record* 1417 (1993): 1 – 11.

Spokas, K., and Forcella, F. “Estimating hourly incoming solar radiation from limited meteorological data.” *Weed Science* 54 (2006): 182 – 189.

Tepponen, P., and Eriksson, B-E. “Damages in concrete railway sleepers in Finland.” *Nordic Concrete Research* 6 (1987): 199 – 209.

Qin, Y., and Hiller, J. E. “Simulating moisture distribution within concrete pavement slabs: model development and sensitivity study.” *Materials and Structures* 47 (2014): 351 – 365.

Wang, D., and Roesler, J. R. “One-dimensional temperature profile prediction in multi-layered rigid pavement systems using a separation of variables method.” *International Journal of Pavement Engineering* 15 (2014): 373 – 382.

Zeman, J. C. “Hydraulic mechanisms of concrete-tie rail seat deterioration.” *University of Illinois at Urbana-Champaign* (2010): MS Thesis.

CHAPTER 3 – CORRELATING RELATIVE HUMIDITY TO DEGREE OF SATURATION INSIDE CONCRETE CROSSTIES

3.1 Abstract

Moisture levels within concrete is often assessed using relative humidity probes and sensors. However, relative humidity is a direct measurement of water vapor content and not a measurement of liquid water content. This limitation is problematic when attempting to understand the extent of liquid moisture inside concrete during freeze-thaw events. Although correlations of relative humidity to liquid water within porous media can be made, it is necessary to know the pore size distribution of the media beforehand. This distribution of pore sizes, however, may not always be known nor remain constant with respect to time inside a cement-based material. In the case of railroad high performance concrete crossties (alternatively known as ties or sleepers), the variation of pore size distributions at locations within the bulk material among thousands of concrete crossties is large. Consequently, relative humidity measurements alone cannot fully characterize the degree of saturation in concrete crossties. In this study, relative humidity sensors and electrical resistance blocks (or gypsum sensor blocks) are embedded in model concrete crossties installed in aggregate ballast. The impedance observed in these gypsum sensor blocks is directly correlated to liquid water content and is compared against the relative humidity measurements. A simple concrete adsorption isotherm model is applied in order to predict the degree of saturation from the relative humidity measurements. However, it is found that the relationship between relative humidity and degree of saturation during wetting (adsorption) and drying (desorption) in the high performance concrete is better characterized by two 3-parameter S-shaped curves.

3.2 Introduction and Background

3.2.1 Critical degree of saturation for freeze-thaw damage

Freeze-thaw damage of concrete is primarily enabled by the presence of water inside the concrete microstructure. Upon freezing, water expands by 9% of its original volume which exerts pressure onto the microstructure and results in cracking damage. Air entrainment introduces microscopically-sized air bubbles that can alleviate stresses caused by freezing water in one of

several manners: hydraulic pressure theory proposed by Powers in 1945, the diffusion and growth of capillary ice by Powers and Helmuth in 1953, the dual mechanism theory by Litvan in 1972, the osmotic pressure theory, the energy solidification theory, the ice nucleation theory, the freezing point depression, and unidirectional solidification (interface stability and stability criterion) [Carlos, 2005]. Without the presence of water in any of these cases, however, freeze-thaw damage would not occur.

The degree of saturation, *S*, in concrete is defined as the volumetric amount of liquid (V_L) and solid (V_S) water filling the open pore volume (V_P)

$$S = \frac{V_L + V_S}{V_P}. \qquad \text{Equation 3-1}$$

Alternatively, the degree of saturation can be defined as the total volumetric amount of evaporable water (V_W) at 105°C with respect to the open pore volume [Fagerlund, 1977]. This extended definition, thus, more closely adheres to the study of psychrometry where the degree of saturation is additionally defined by the volume of water vapor filling the open pore volume.

Recent research indicates that there exists a critical degree of saturation (S_{CR}) necessary for significant freeze-thaw damage to occur. Li *et al* investigated the rate of fluid ingress of different concretes with increasing amounts of entrained air content [Li *et al.*, 2012]. They found that a degree of saturation above 86-88% leads to freeze-thaw damage regardless of the amount of entrained air. The same level of damage due to freeze-thaw damage was found to occur in both poorly and properly air-entrained slabs. Several other researchers have found that there may exist a critical degree of saturation whereby no freeze-thaw damage is found to occur if the state of moisture is below the critical degree of saturation [Bentz *el al*, 2001; Litvan, 1988; Litvan and Sereda, 1980; Shimada *et al.*, 1991; Beaudoin and Cameron, 1972]. Freeze-thaw damage is often alleviated by larger measured values of entrained air which results in smaller average distances between individual entrained air voids. Thus, a freezing event in concrete with a well-dispersed spacing of air bubbles is well alleviated of high stresses. Li *et al.*, however, concluded that those specimens with poorly air-entrained voids achieved degree of saturation greater than 88% much more quickly (on the order of several days) whereas those specimens with good air-entrained voids surpassed a degree of saturation greater than 88% at a much later time (on the order of 3 to 6 years).

3.2.2 Extent of liquid moisture in high performance concrete

High performance concrete is typified by several features, one of which is incomplete hydration of the Portland cement particles by design. This incomplete hydration is accomplished by designing a low water-to-cement mass ratio and increasing the dosage of water-reducing admixtures in order to produce a workable mix that can be appropriately placed and consolidated. These low water-to-cement ratios range from 0.36 to 0.42 depending on whether saturated pores are considered [Mindess *et al.*, 2003]. As a consequence, any additional water that ingresses into the incompletely hydrated concrete matrix is purported to contribute to additional hydration which results in solid-phased hydration products (and the depletion of free liquid moisture). This phenomenon is strongly desired as the additional hydration products fills the voids in the concrete microstructure leading to a more dense and impermeable concrete matrix. Other research, in fact, has utilized saturated, porous aggregates to accomplish this purposely delayed, internal curing of the concrete microstructure [Bentz, 2009; Henkensiefken *et al.*, 2009]. High performance concrete, thus, has been postulated by some in the concrete industry to be sufficiently impermeable and resistant to the accumulation of free liquid moisture to warrant relaxed requirements on minimum air entrainment values. However, as previously discussed, it is of greater importance to understand the degree of saturation within a concrete member than it is to know its impermeability or air entrainment in order to predict the long-term performance with regards to freeze-thaw damage [Li *et al.*, 2012] and, in the specific case of railroad concrete crossties, hydrostatic pressure damage due to wheel impact loading [Zeman *et al.*, 2010].

3.2.3 Relationship between degree of saturation, absolute humidity, and relative humidity

The degree of saturation of concrete is directly assessed by measuring the volume or mass of liquid that ingresses into a known concrete volume, often through absorption testing. Water inside the concrete microstructure can exist as solid ice, liquid water, and gaseous vapor. Absolute humidity is a measurement of water content present as a gaseous vapor irrespective of the amount of water content as solid ice or liquid water. A change in the temperature or pressure affects the maximum concentration of water content in the gaseous vapor. Table 3-1 shows the vapor pressure of water, or saturation pressure, with respect to increasing temperatures. At temperatures below 0^{o}C, the vapor pressure above solid ice is dominated by sublimation. In the presence of ions in

solution, the water vapor pressure is driven downward in accordance to Raoult's Law of partial pressures, where the vapor pressure is proportional to the molar fraction of water in solution.

Absolute humidity, thus, is affected by several factors and is not often useful in assessing the degree of saturation of concrete. Instead, the absolute humidity at a given temperature can be normalized with respect to the absolute saturated humidity at that same temperature. This normalized value is called the relative humidity and is typically reported as a percent ranging from 0% to 100% when the value is measured over a flat surface of water. As such, in order to understand the degree of saturation in concrete, it is necessary to understand its relationship with the oft measured relative humidity.

Table 3-1 Change in saturation vapor pressure with respect to temperature (from Rotronic Humidity Handbook).

Temperature (°C)	Water Vapor Pressure Above Liquid (kPa)	Water Vapor Pressure Above Ice (kPa)	Ratio Ice/Liquid
-30	0.049	0.037	0.75
-25	0.081	0.064	0.78
-20	0.126	0.103	0.82
-15	0.191	0.165	0.86
-10	0.287	0.260	0.91
-5	0.422	0.402	0.95
0	0.611	0.611	1.0
10	1.23	-	-
20	2.34	-	-
30	4.24	-	-
40	7.37	-	-
50	12.33	-	-
60	19.92	-	-
70	31.18	-	-
80	47.34	-	-
90	70.11	-	-
100	101.33	-	-

3.2.4 Kelvin-LaPlace equation, modeling of pores, and hysteresis of adsorption isotherms

The Kelvin-LaPlace equation predicts the vapor pressure of a gas over the curved surface of a liquid. Its relationship is defined as

$$\frac{RT}{V_L}\ln(\frac{p}{p_s}) = 2\gamma\kappa \qquad \text{Equation 3-2}$$

where R is the universal gas constant ($^{J}/_{molK}$), T is the temperature (Kelvin), V_L is the molar volume of the liquid, p is the absolute vapor pressure and p_s is the absolute saturated vapor pressure, γ is the surface tension of the pore fluid, and κ is the curvature of the liquid surface. For a sphere with radius r_{sphere} suspended in another medium, the curvature is equal to $^{2}/_{r_{sphere}}$. In concrete, liquid moisture does not suspend itself as a collection of spheres. Instead, it adheres onto surfaces in the complex concrete microstructure. Two simple models to describe this complicated pore structure are cylinders (see Figure 3-1a) and ink-bottles (see Figure 3-1b) [Espinosa and Franke, 2006].

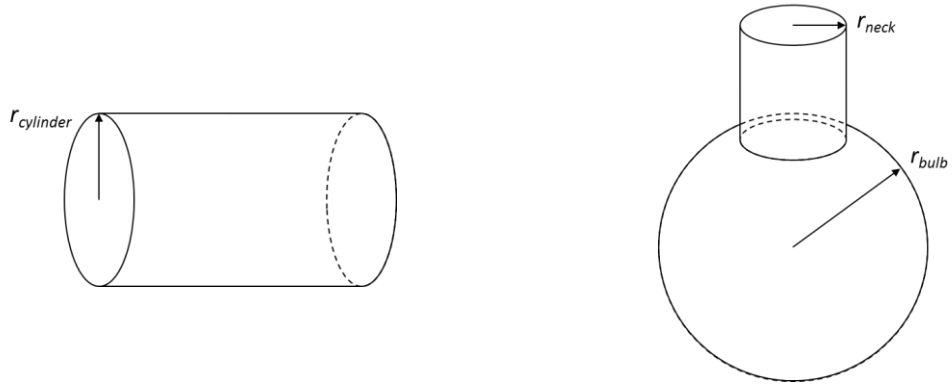

Figure 3-1 Simplification of concrete microstructure with a) cylinders (left) and b) ink-bottles (right).

For condensation of liquid onto the interior surface of a cylinder with radius $r_{cylinder}$, the curvature is equal to $-{}^{1}/_{r_{cylinder}}$. The thickness of the adsorbate, δ, can be accounted for by subtracting it from the radius as shown in Figure 3-2a. This correction leads to a revised curvature of $-{}^{1}/_{(r_{cylinder}-\delta)}$. After the cylindrical pore is fully saturated, the drying of the same cylindrical pore must be accomplished at the ends of the pore where a meniscus with radius $r_{meniscus}$ is the drying surface. The curvature of a meniscus adhered onto the interior of a cylindrical pore is $-{}^{2\cos\theta}/_{r_{meniscus}}$, where θ is the contact angle between the meniscus and the cylindrical wall. For small angles, this curvature can be approximated as $-{}^{2}/_{r_{meniscus}}$. Again, the thickness of the adsorbate can be accounted for leading to a curvature approximated as $-{}^{2}/_{(r_{meniscus}-\delta)}$ as shown in Figure 3-2b.

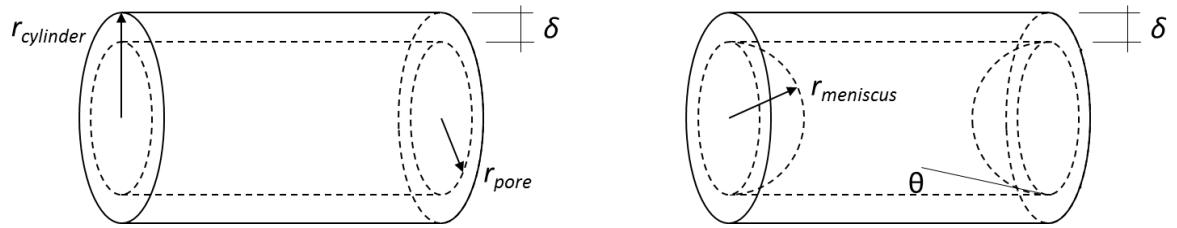

Figure 3-2 a) Wetting of the interior of a cylindrical pore with an adsorbate layer (left) and b) drying of the interior of a cylindrical pore with an adsorbate layer (right).

A similar effect is seen in an ink-bottle geometry where an adsorbate layer will grow on the inside surface of both the neck and bulb sphere of the ink-bottle until the neck becomes fully saturated. If the radius of the neck is smaller than the radius of the bulb sphere, then the neck is fully saturated while the sphere continues to grow an adsorbate layer. If the radius of the neck is larger than the radius of the bulb sphere, then the bulb sphere is fully saturated while the neck will transition to filling with a meniscus. Upon drying of the ink-bottle system, if the bulb sphere had been fully filled, then the neck will dry with a meniscus until it reaches the sphere at which a complicated drying of the sphere occurs (transitioning from a meniscus to desorption of the adsorbate layer on the bulb sphere surface). If the bulb had not been fully filled, then the sphere undergoes desorption until a meniscus forms in the neck. While a cylindrical model of pores is easier to compute, it is found that an ink-bottle model better captures the hysteretic nature of concrete adsorption curves [Espinosa and Franke, 2006].

A significant implication of the formation of menisci during the wetting and drying of pores is the resulting hysteric nature of an ideal adsorption isotherm. The wetting of a cylindrical pore has a curvature that is approximately half of the curvature of a drying meniscus. Equation 3-2 is applied to produce Figure 3-3 which is an idealized adsorption isotherm of an arbitrary distribution of pore sizes. It is evident that drying of pores results in a curve that is shifted higher than the wetting curve. This illustrates, additionally, that for a given relative humidity value, the saturation of pores can vary over a range of values as it is dependent upon the history of saturation.

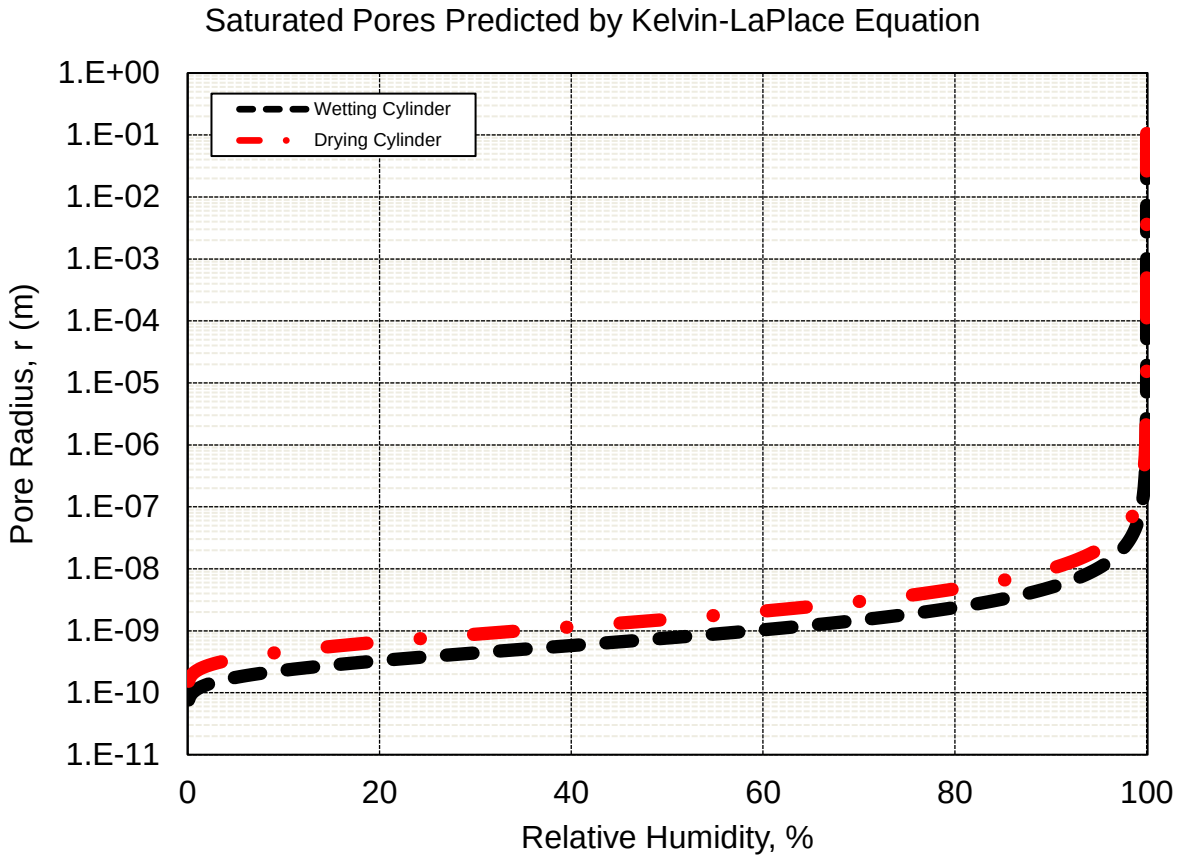

Figure 3-3 Idealized adsorption isotherm of cylindrical pores undergoing wetting and drying.

Lastly, Figure 3-3 also implies that small-radius pores become fully saturated at relative humidity values of less than 100% RH. As such, localized saturation may occur while the bulk material is not yet fully saturated. Additionally, in order for large pores (on the order of 1 μm and larger), it is necessary for there to be a constant relative humidity of 100% RH. At high relative humidity, equilibrium drives gaseous vapor to precipitate into liquid. As such, it is necessary to have both high relative humidity and a supply of adsorbate in order to continually fill very large-sized pores.

3.2.5 Typical adsorption isotherms for concrete and mortar

Isotherms can be modeled in number of different ways (Freundlich, Langmuir, BET, e.g.), yet concrete is often modeled with an empirical-fit because of the number of material challenges. Sorption isotherms for concrete are complicated by several material factors such as age, type of cement, temperature, air entrainment, water-to-cement ratio, incorporation of pozzolanic mineral

admixtures, and other material properties [Xi *et al.*, 1993; Yang, 1999; Poyet and Charles, 2009]. The effect of pores has a tremendous effect on observed relative humidity measurements. At the nano-scale within calcium-silicate-hydrate (CSH) pores, for example, the nano-pores can become fully saturated at relative humidity values of 20 %RH [Bonnaud *et al.*, 2012]. The adsorption of water within CSH swells the interlayer spacing which inherently affects the pore size distribution making this a non-linear problem. Moreover, at a larger scale of arbitrarily-sized nano-pores, the deposition of water molecules onto the pore surface can assume complicated hemispherical, conical, cylindrical, semi-elliptical, and paraboloidal menisci shapes [Dobruskin, 2008]. Additionally, concrete is a heterogeneous material wherein the pore size distribution and extent of cracking within fine aggregate, coarse aggregate, low-density hydrated cement paste (in the interfacial transition zone), and high-density hydrated cement paste are not equal.

These complications result in simplified concrete sorption curves (see Figure 3-4) where the change in mass of a concrete is shown with respect to changing relative humidity at equilibrium. The shape of the curve (additionally evident in Figure 3-3) is characterized by three phenomena: a non-linear rise near 0-10 % RH (dominated by condensation in nano- and micro-pores, linear rise between 10-80% RH (dominated by single- and multi-layer adsorption onto meso- and macro-pores), and non-linear rise at 80-100 % RH (dominated by capillary condensation in macro-pores).

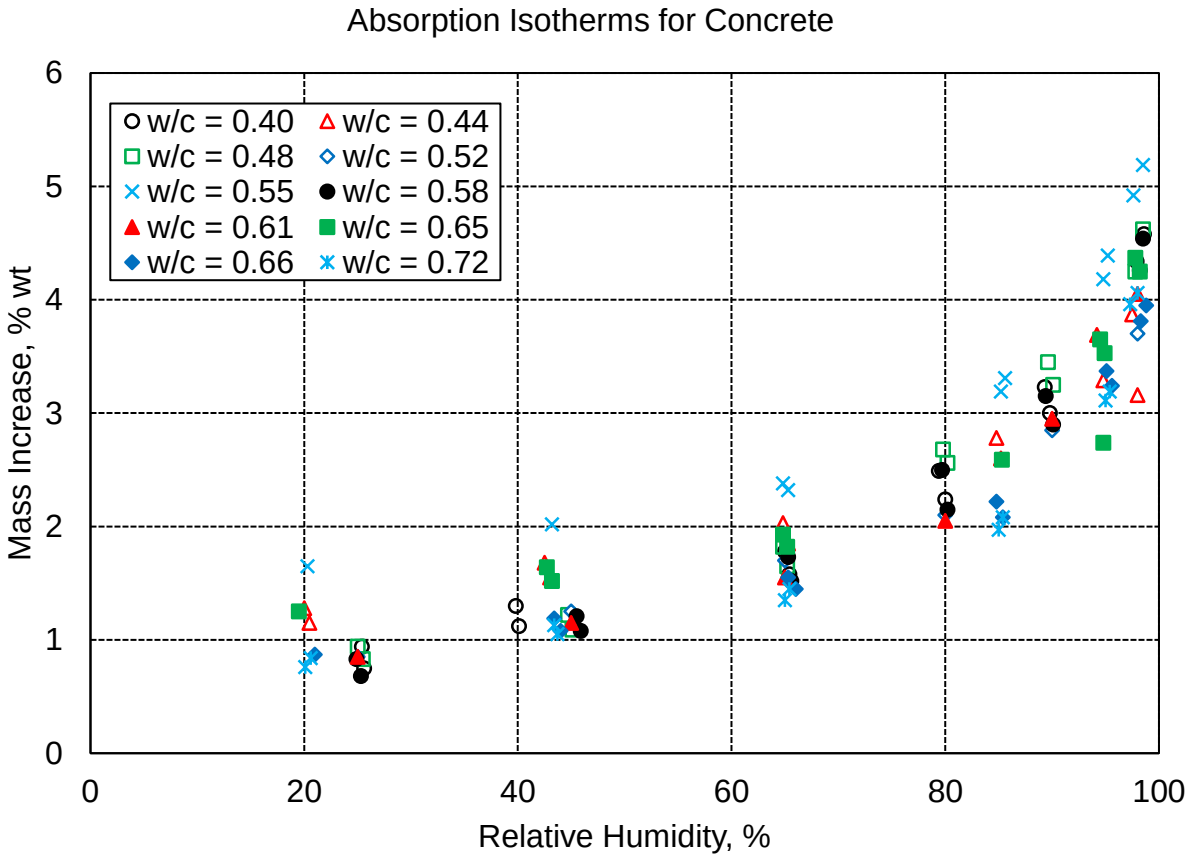

Figure 3-4 Absorption isotherms for concrete with different water-to-cement ratios (adapted from Hansen, 1986).

A simple absorption isotherm proposed by Pruckner disregards the changing material factors and assumes constant material properties as shown in the following expression

$$S = \frac{1 - ln\left|\frac{RT\ln(\frac{p}{p_s})}{\Delta\mu_{mono}}\right|}{1 - ln\left|\frac{RTln(0.999)}{\Delta\mu_{mono}}\right|} \qquad \text{Equation 3-3}$$

where $\Delta\mu_{mono}$ is the change of chemical potential at monolayer coverage [Pruckner, 2013]. Monolayer coverage of a cement-based material is primarily appropriate at low relative humidity because multi-layer coverage governs in capillary condensation. Because of this simplification, Pruckner empirically found $\Delta\mu_{mono}$ = -17.0 kJ/mol while other researchers have estimated chemical potential values of 30.7 to 42.4 kJ/mol in hardened cement paste [Adolphs and Setzer, 1996].

3.3 Significance of Research

Liquid moisture inside conventional concrete is often measured indirectly utilizing relative humidity sensors. However, relative humidity sensors alone cannot fully characterize the extent of liquid moisture within the microstructure since the relative humidity is a direct measure of vapor. Instead, it is necessary to infer a correlation between relative humidity and degree of saturation or directly measure the extent of liquid moisture. Electrical resistance blocks (or gypsum blocks) can be utilized to directly measure the degree of saturation inside concrete and be compared against complimentarily installed relative humidity sensors. Moreover, this correlation can be investigated in high performance concrete where there is incomplete hydration of the Portland cement particles. As such, a better understanding of the freeze-thaw damage potential of high performance concrete railroad crossties can be established.

3.4 Experimental Methods

3.4.1 Sensor types

Two sensor types were used in order to measure both the relative humidity and the moisture level: hygrochron sensors called iButtons (DS1923-F5) and moisture sensors called Delmhorst GB-1 Gypsum Sensor Blocks.

The hygrochron sensors feature an internally powered data acquisition system whereby two electrodes joined by a capacitive film varies in its reported dielectric constant based on changing water vapor conditions. A linear relationship between dielectric constant and relative humidity is established and modified for instances of *saturation drift* using the following expression

$$RH_{saturation\ drift\ corrected} = RH_N - \sum_{k=1}^{N} \frac{(0.0156)(\overline{RH_k})(2.54^{-0.3502k})}{1+{}^{(\overline{T_k}-25)}/_{100}} \quad \text{Equation 3-4}$$

where RH_N is the relative humidity at the end of the Nth hour when the device is exposed to high (< 70% RH) or low (< 20% RH) relative humidity, $\overline{RH_k}$ is the average relative humidity through the kth hour that that device has been exposed to high or low relative humidity, and $\overline{T_k}$ is the average temperature (in Celsius) through the kth hour the device has been continuously exposed to high or

low relative humidity. The numbers in the equation are empirical and are derived from curve-fitted data sets [Maxim Integrated, 2013].

The hygrochron sensors were fitted into iButton retainers (DS9098P) which introduced soldering points for multi-conductor shielded cabling in order to enable remote communication with each individual sensor. The sensor and retainer were fitted inside of a plastic dip coated eye bolt. A single layer of GORE-TEX fabric (a fabric that allows water vapor to pass through but not liquid water) was wrapped around each sensor in order to protect the wiring connections.

The moisture sensors are made of gypsum cast around two stainless steel electrodes and powered by an external source to induce an alternating current between the two electrodes. The advantage of an alternating current is that it prevents electrochemical effects from preferentially moving alkalis and other ions within the concrete microstructure, thusly affecting the measured results. Gypsum is a mineral ($CaSO_4 \cdot 2H_20$) that chemically interacts with Portland cement to form ettringite and thaumisite, and ground gypsum is incorporated into Portland cement during its final grinding during manufacturing [Kovler, 1998]. The gypsum sensor within hydrating and hardened concrete is susceptible to deterioration much like gypsum-rich aggregates are due to the leeching of sulfate from the sensor into the hydrated Portland cement paste that forms expansive ettringite or monosulfoaluminate (akin to alkali-silica-reaction (ASR) related expansion due to delayed ettringite attack) [Collepardi, 2003]. These ASR-related mechanisms in concrete are problematic at long time scales [Ferraris, 1995; Swamy, 2002], so they are assumed to be negligible within the 1-year time frame of this study.

The extent of liquid moisture soaked within the gypsum changes the observed impedance of the system – a high impedance denotes a dry sensor while a low impedance denotes a wet sensor. The sensors are manufactured under controlled conditions such that there is uniformity between each sensor as read by a KS-D1 Soil Moisture Meter. For this study, the moisture meter was not selected because of its inability to record and store data. Instead, an Arduino Uno R3 board was configured with an SD card microshield. The Arduino code by which the gypsum sensors collected and recorded data is located in Appendix B1.

Briefly, Pins 6 and 7 on the Arduino Uno R3 board connect to diodes (1N4148), which have a negligibly low resistance when current travels in one direction and a very high resistance in the other direction. As a consequence, an alternating current can be established by alternatively powering pins 6 and 7 off and on. After the current passes the diode connected to Pins 6 or 7, the current passes through the moisture sensor and a 1500 Ω resistor before continuing to Ground. The voltage drop is recorded with respect to Ground. A simple illustration of the moisture sensor block connection to the Arduino Uno R3 is shown in Figure 3-5 while a breakout the current travel path for Pins 6 and 7 is shown in Figure 3-6.

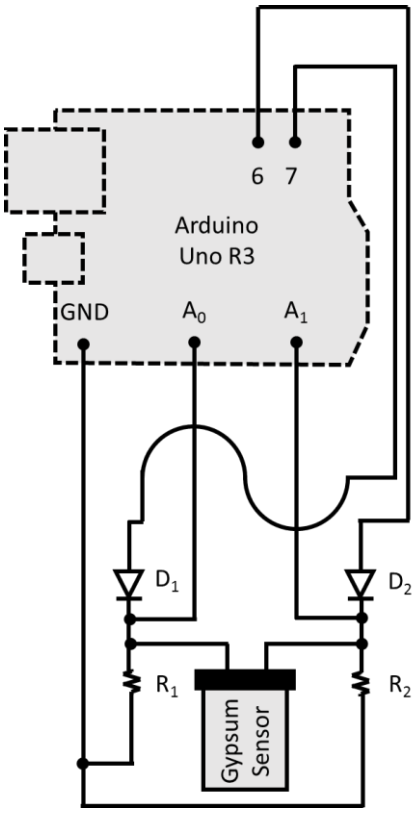

Figure 3-5 Simple illustration of one moisture sensor connected to two 1500 Ω resistors, two diodes (1N4148), and an Arduino Uno R3 microcontroller at Pins 6, 7, A0, A1, and GND.

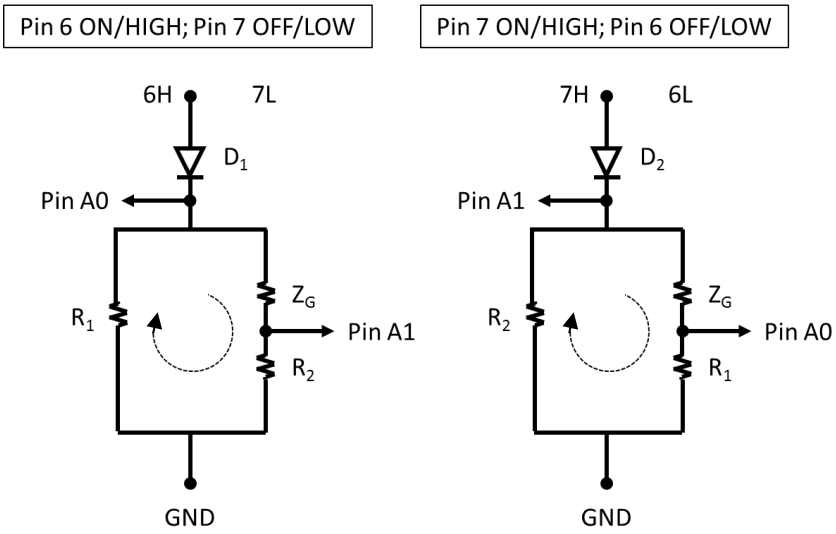

Figure 3-6 Simplified depiction of circuitry when a) Pin 6 voltage is HIGH (left) and b) when Pin 7 voltage is HIGH (right).

In the instance when Pin 6 is set to a HIGH voltage and Pin 7 is set to a LOW voltage (see Figure 3-6a), analog Pin A1 measures the voltage drop with respect to GND across R_2 on the right-hand-side of the circuit branch. The current across the right-hand-side, I_{RHS}, of the circuit can be expressed as

$$I_{RHS} = {\Delta V_{R2}}/{R_2} \qquad \text{Equation 3-5}$$

where ΔV_{R2} is the measured voltage drop with respect to GND across R_2. Analog Pin A0 measures the voltage drop with respect to GND across the two branches of the circuit (left-hand-side and right-hand-side). Seemingly, Pin A0 measures a set of known and unknown resistors in parallel and series. However, Kirchoff's second law states that closed loops within a circuit must have its voltage drops and gains equate to zero. As such

$$\sum \Delta V_{\circlearrowleft} = \Delta V_{ZG} + \Delta V_{R2} - \Delta V_{R1} = 0 \qquad \text{Equation 3-6}$$

where ΔV_{R1} is the measured voltage drop with respect to GND across R_1 and where ΔV_{ZG} is the measured voltage drop with respect to GND across Z_G. As such

$$\Delta V_{ZG} + \Delta V_{R2} = I_{RHS}(Z_g + R_2) = \Delta V_{R1} = I_{LHS}R_1. \qquad \text{Equation 3-7}$$

Although the current along the left-hand-side and right-hand-side of the branches do not equal, by Kirchoff's first law, the current along the right-hand-side across both resistors must equal. As such, Equation 3-5 and 3-7 can be equated

$$I_{RHS} = {\Delta V_{R2}}/{R_2} = {(\Delta V_{ZG} + \Delta V_{R2})}/{(Z_g + R_2)}. \quad \text{Equation 3-8}$$

Following several simplifying mathematical steps, the unknown impedance of the moisture sensor, Z_G, can be solved as

$$Z_g = {R_2}/{\Delta V_{R2}}\,[(\Delta V_{ZG} + \Delta V_{R2}) - \Delta V_{R2}], \text{ or}$$

$$Z_g = {R_2}/{A1}\,[A0 - A1] \quad \text{Equation 3-9}$$

where *A0* and *A1* are the voltage values measured by analog Pins A0 and A1, respectively. An analogous derivation can be made in the instance when Pin 7 is set to HIGH and Pin 6 is set to LOW (see Figure 3-6b). A single Arduino Uno R3 microcontroller board has six analog input pins, meaning that three moisture sensor blocks can be configured if dual readings are made (that is to say, setting Pins 6 and 7 HIGH on a single sensor). In order to increase the number of moisture sensors that can be monitored at a single installation site, a single reading can be taken (e.g. when Pin 7 is set to HIGH) while still exciting both pins in order to achieve an alternating current. In doing so, electrochemical processes can be prevented while a gain in the number of moisture sensors is achieved. Figure 3-7 shows the complete circuitry deployed where Pin 7 is set to HIGH during data recording.

The hardware is powered by a 10000 mAh external battery power pack and is housed inside a metal junction box in order to protect the circuitry from the natural elements (see Figure 3-8).

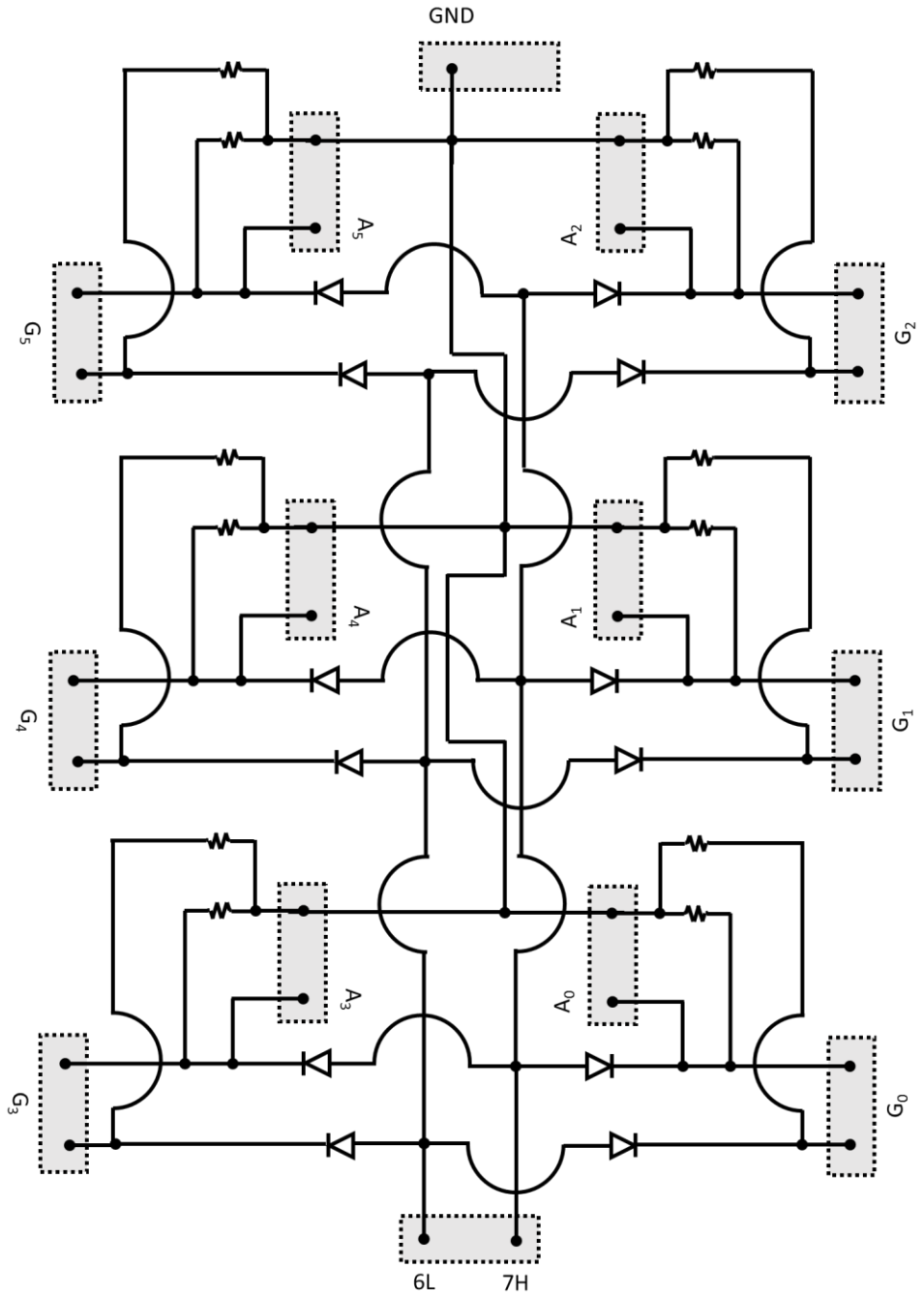

Figure 3-7 Complete circuitry scheme where six moisture sensor blocks (G0-G5) are measured for their change in impedance when Pin 7 on an Arduino Uno R3 microcontroller board is set to HIGH. In order to prevent electrochemical deterioration processes, Pin 6 is also set to HIGH in an alternative manner in order to mimic an alternating current.

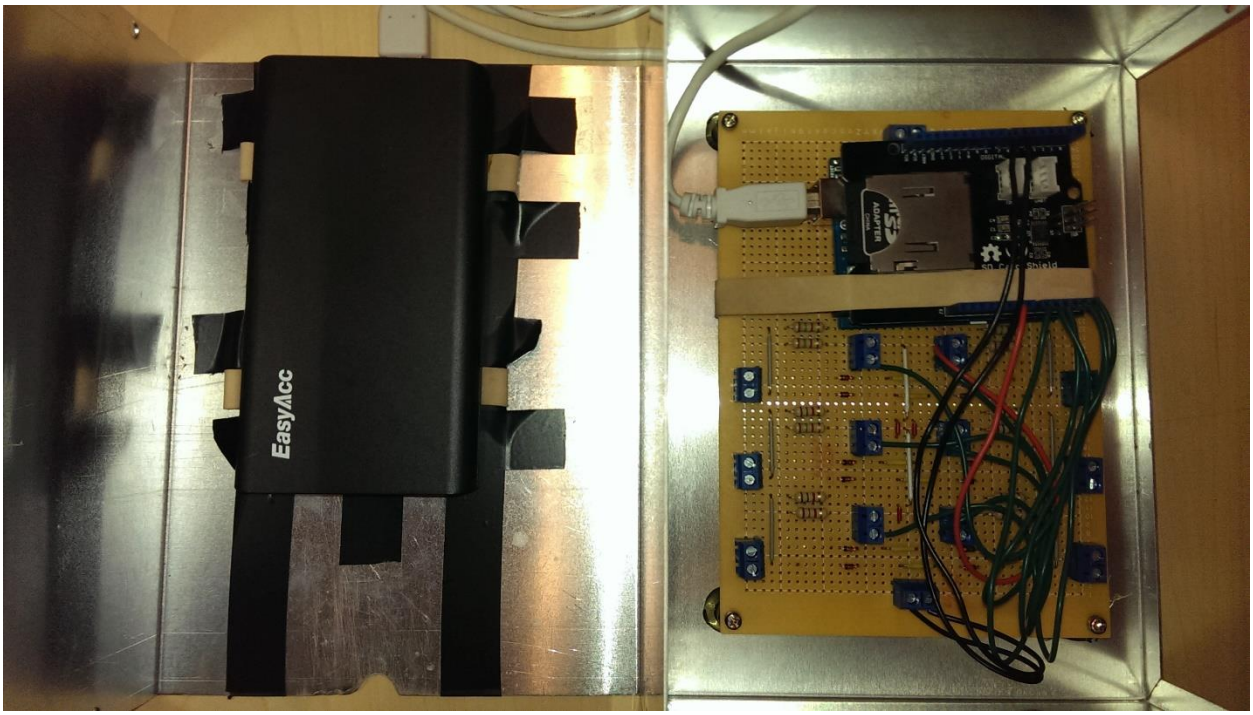

Figure 3-8 Image of hardware where an SD shield is connected above an Arduino Uno R3 microcontroller board. The Arduino and shield are securely fastened with a rubber band onto a circuit board that is wired in accordance in Figure 3-7. A 10000 mAh external battery back provides an approximate seven day charge for the hardware to operate independently. The entire setup is encased in a metal junction box.

3.4.2 Calibration of moisture sensor

The moisture sensor block directly reports the impedance of the sensor. In order to calibrate the sensor reading to a degree of saturation, the mass of the sensor was measured with respect to the impedance. This calibration was accomplished by suspending the sensor at one end of an instrumented cantilever beam of known stiffness. The change in the bending moment before and after immersing the sensor in water is collected across several days. Repeated instances of wetting and drying of the moisture sensor block was performed in order to enhance confidence in the calibration.

3.4.3 Preparation of installation method

Both the hygrochron sensors and the moisture sensors were installed onto a steel angle bracket with unthreaded holes spaced one inch apart (see Figure 3-9). The hygrochron sensors were installed at depths of 0.5, 2.5, 5.5, and 8.5 inches from the top surface of the model concrete

crosstie. The moisture sensors were installed at depths of 0.5, 2.5, and 8.5 inches from the same top surface (see Figure 3-10).

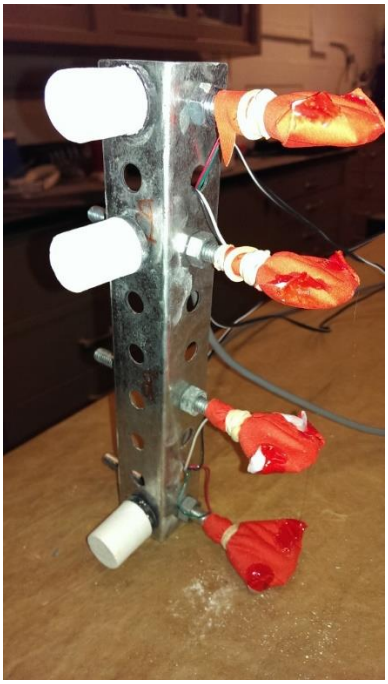

Figure 3-9 Construction of hygrochron sensors seated inside an iButton retainer installed in a plastic dip coated eye bolt and sealed with a single layer of GORE-TEX fabric. A rubber band securely holds the fabric in place. Moisture sensor blocks are additionally installed along the orthogonal face of the angled steel bracket.

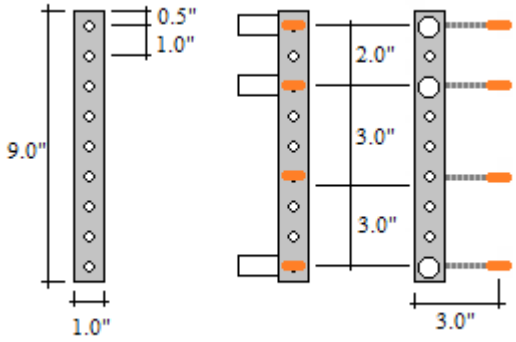

Figure 3-10 Depiction of nine inch tall bracket (left) with half-inch clearance at top and bottom. Hygrochron sensors (orange) and moisture sensors (white) are affixed at depths as depicted (right).

3.4.4 Instrumentation of model concrete crossties and installation in model ballast

The steel angle brackets were installed into two molds measuring 9-inch by 9-inch by 16-inches. These dimensions are comparable to the cross-section dimensions of a typical concrete

crosstie. One of the molds was fashioned with steel fastening anchors such that a polyurethane pad and rail section could be affixed at a later time (see Figure 3-11a). The instrumented bracket was positioned such that the hygrochron sensor and moisture sensor were geometrically centered about the rail seat area and additionally symmetric to each other across the horizontal centerline of the mold (see Figure 3-11b). The concrete mixture design is shown in Table 3-2, and is intended to be comparable to typical high performance concrete crossties with a water-to-cement mass ratio of 0.30.

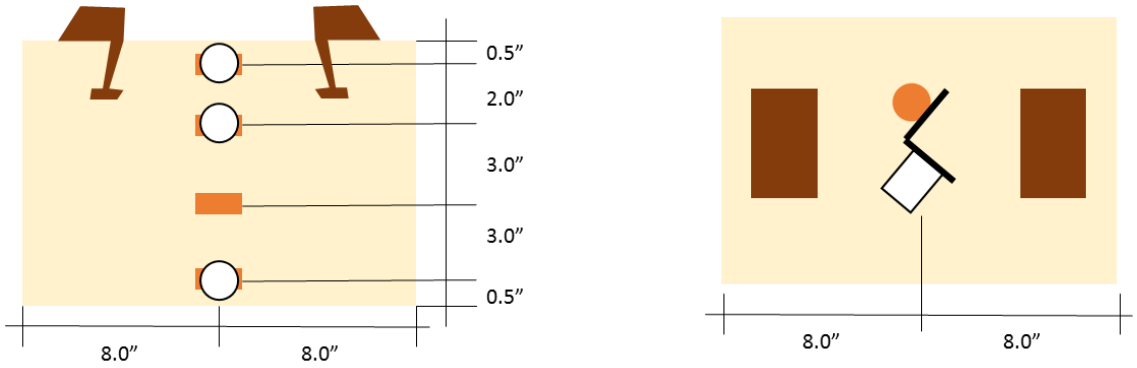

Figure 3-11 Diagram of instrumented model crosstie with both hygrothermal sensors and moisture sensors installed at various depths (left). The plan view (right) of the model crosstie depicts the approximate positioning of the sensors such that they are geometrically centered within the rail seat area and symmetric to each other across the horizontal centerline.

Table 3-2 Nominal concrete mix design of model crossties.

Material Type	**Pounds Per Cubic Yard**	**Kilograms Per Cubic Meter**
Type I Portland Cement	718	426
#7 Aggregate	2085	1236
Sand	1257	746
Water	216	128
High Range Water Reducer	12 fl. oz / 100 lb. cementitious (782 mL per 100 kg cementitious)	

The model crossties were demolded (see Figure 3-12) and cured in an environmentally controlled room at 23°C and 50% RH. Thereafter, the model crossties were installed in model ballast in Rantoul, IL. The model ballast is a 1-1.5 inch top-size yard ballast that conforms to Union Pacific Railroad (UPRR) Class-2 Ballast Specifications. The model ballast sits atop an angled asphalt lot, which facilitates rainfall runoff and prevents stagnant water from building within the ballast. The model crossties were installed at one end of the ballast where the distance separating the underside of the model crossties and the surface of the asphalt lot is 5 to 6 inches. The model

crosstie was positioned such that its surface was flush with the model ballast. Additionally, a polyurethane pad and steel rail section was added to the model crosstie with embedded anchors (see Figure 3-13a).

Figure 3-12 De-molded model concrete crossties with PVC access plug where multi-conductor shielded cables are encase.

Figure 3-13 Model crossties installed in model ballast in Rantoul, IL. A polyurethane pad and steel rail section is added to the model crosstie with embedded anchors.

3.5 Results, Discussion, and Empirical Modeling

3.5.1 Relative humidity results over observation period

Although relative humidity of ambient conditions fluctuates daily, the internal relative humidity of concrete members fluctuates in a more seasonal manner. Figure 3-14 shows a model concrete crosstie installed from an environmentally controlled environment to an aggregate ballast

located in Rantoul, IL. Relative humidity sensors near the surface of the model concrete crosstie show a gradual increase in relative humidity while relative humidity sensors inside the bulk material (at 2.5 an and 5.5 inches from the top surface) are fairly unaffected by the installation into an aggregate ballast.

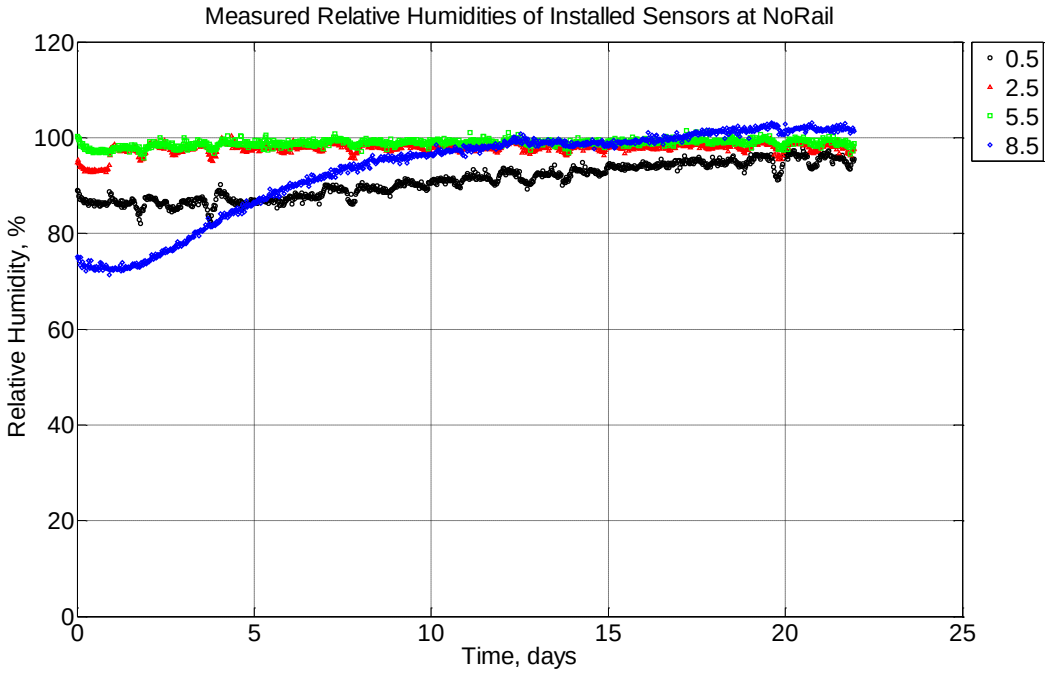

Figure 3-14 Measured relative humidity at depths of 0.5 inches (12.7 mm), 2.5 inches (63.5 mm), 5.5 inches (139.7 mm), and 8.5 inches (215.9 mm) from the surface of a model concrete crosstie (labeled NoRail) without a polyurethane pad nor rail installed in ballast in Rantoul, IL, between November 29, 2014, through December 21, 2014.

3.5.2 Predicting degree of saturation based on measured impedance

The moisture sensor blocks and Arduino algorithm (see Equation 3-9 and Appendix B1) directly report the impedance, Z_G, of each sensor. However, the impedance measurement can be calibrated against varying degrees of moisture. Figure 3-16 shows the graphical result of two uniformly manufactured moisture sensors undergoing 5 instances of drying and soaking cycles. The curves across the 5 instances overlay each other, so a power-law function is fitted to a representative section of the data to with a high fit of R^2 of 0.98. As such, the independently measured impedance value, Z_G, and estimated degree of saturation, S, can be related by the following power-law expression

$$Z_g = 817.14S^{-1.284}. \qquad \text{Equation 3-10}$$

This expression can be solved for in terms of S to yield

$$S = \left({}^{Z_g}/_{817.14}\right)^{({}^{1}/_{-1.284})}. \qquad \text{Equation 3-11}$$

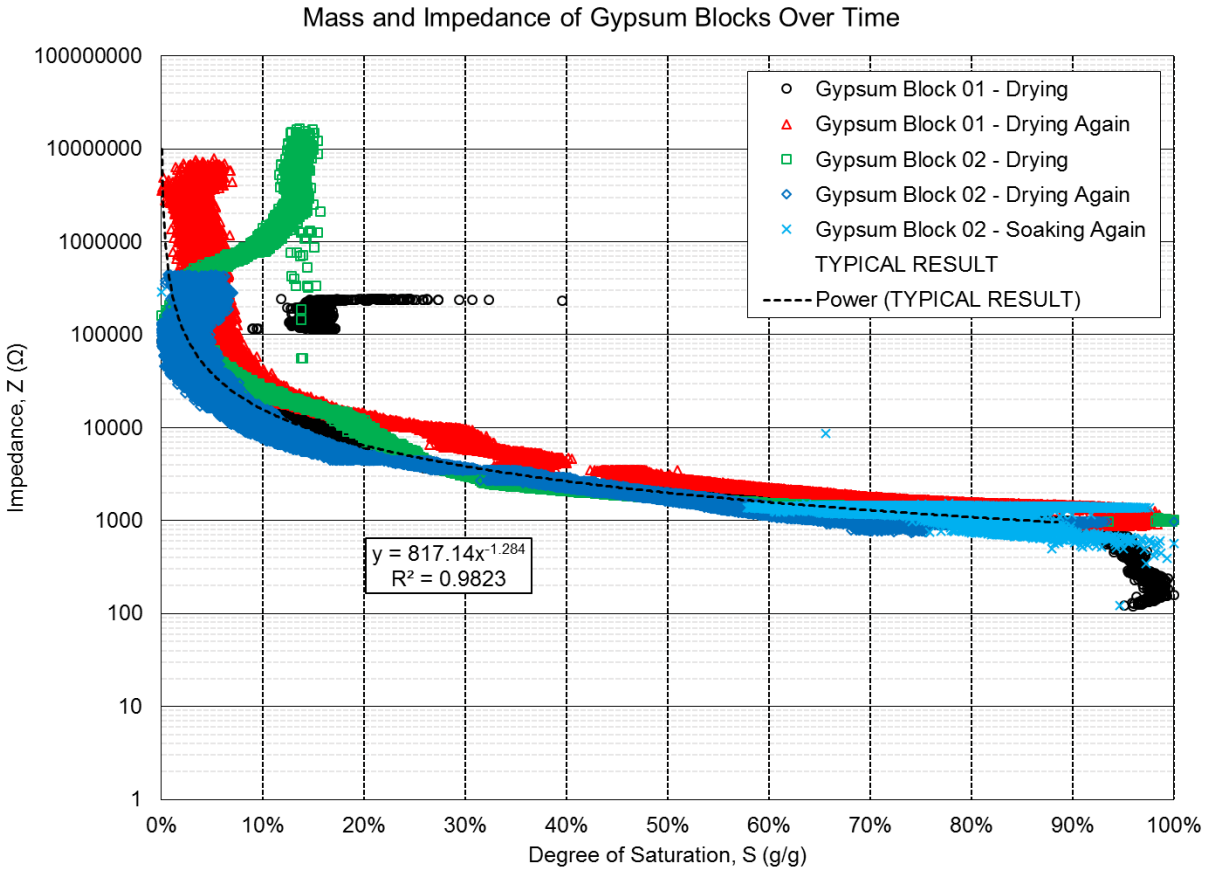

Figure 3-15 Change of mass and impedance of two moisture sensors undergoing drying and soaking. The change in mass is normalized to the soaked mass in order to create a degree of saturation.

3.5.3 Degree of saturation results over observation period

The degree of saturation inside the model concrete crossties is estimated based on Equation 3-11 and the measured impedance value of the moisture sensor block. The result of three moisture sensors soon after installation in aggregate ballast in shown in Figure 3-16. It is evident that the two sensors near the surface (0.5 and 8.5 inches) are nearly at 0 % degree of saturation while the

interior sensor (2.5 inches) maintains a high degree of saturation at 100%. However, soon after installation into the aggregate ballast, the moisture sensors indicate an increase in liquid moisture. In particular, the sensor at the top surface (0.5) gradually increases to a high degree of saturation by day 12. The sensor at 8.5 inches from the top surface shows an upward trend before stabilizing at a relatively low degree of saturation. The sensor at 2.5 inches shows very little change until several weeks later (February 10, 2015) (see Figure B2-13 in Appendix B)when its values are comparable to the other sensors embedded at 0.5 and 8.5 inches suggesting that the internal moisture conditions in this young-age concrete (mixed 40 days prior to the data presented in Figure 3-16) is high.

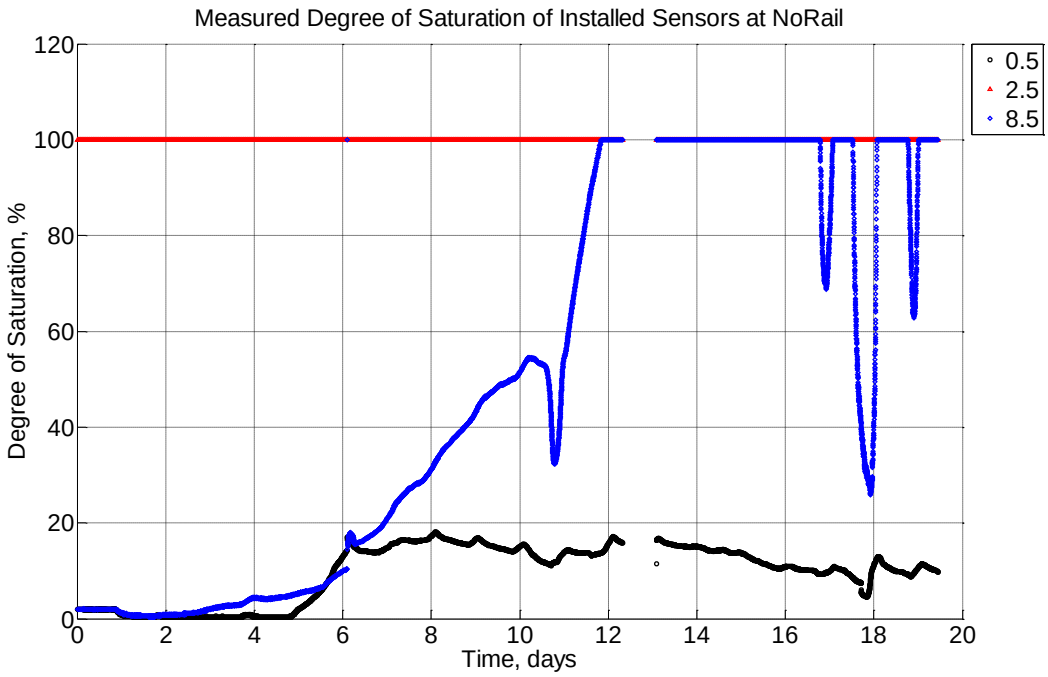

Figure 3-16 Measured degree of saturation at depths of 0.5 inches (12.7 mm), 2.5 inches (63.5 mm), and 8.5 inches (215.9 mm) from the surface of a model concrete crosstie (labeled NoRail) without a polyurethane pad nor rail installed in model ballast in Rantoul, IL, between December 1, 2014, through December 21, 2014.

Two sensors (at 0.5 and 8.5 inches from the top surface) exhibit unusual troughs that are sudden and coincidental on days 10, 17, 18, and 19. On these days, it is evident that ambient temperatures fell to below 0^{o}C (see Figure A10-5). It is likely that portions of the water inside the concrete crosstie and within the moisture sensor block transformed from liquid water to solid ice. As such, the impedance between the two electrodes would be altered because of the change in

conductivity of liquid water and ice. These instances of depressed degree of saturation are artificial and the analysis can be improved by calibrating the moisture sensor at multiple temperature ranges. Moreover, the stagnation of the gypsum sensor block at S = 100% at 2.5 inches draws the question whether the gypsum sensor is preferentially retaining water due to a finer pore size distribution. The approximate range of moisture diffusivity for gypsum is 5.4×10^{-6} to 4.8×10^{-3} m^2/hr from dry to saturated [Tesárek *et al.*, 2004] as compared to the diffusivity of concrete from 6.8×10^{-7} m^2/hr [Qin and Hiller, 2014] to 2.02×10^{-6} m^2/hr [Kang *et al.*, 2012], meaning that moisture diffusion through concrete should be occurring more slowly in relation to the gypsum sensor block. As a consequence, the measured values in the gypsum should not represent a state in which the moisture level is preferentially higher in the gypsum sensor than the concrete bulk material.

3.5.4 Comparing degree of saturation with relative humidity measurements

Measured relative humidity (such as in Figure 3-14) can be compared against measured degree of saturation (such as in Figure 3-16) to produce a correlation of data (see Figure 3-17). This depiction of the data is in keeping with how sorption isotherms are displayed. However, several key differences are noted:

- The temperature represented within Figure 3-17 is not constant, therefore there is no isothermal constraint on the result.
- Equilibrium of relative humidity and equilibrium of degree of saturation are not reliably attained due to extreme fluctuations due to ambient conditions.
- The distribution of pore sizes is assumed to be constant. This assumption is irrespective of the nature of high performance concrete which has unreacted Portland cement particles leading to densification of pore structure when exposed to additional liquid water.

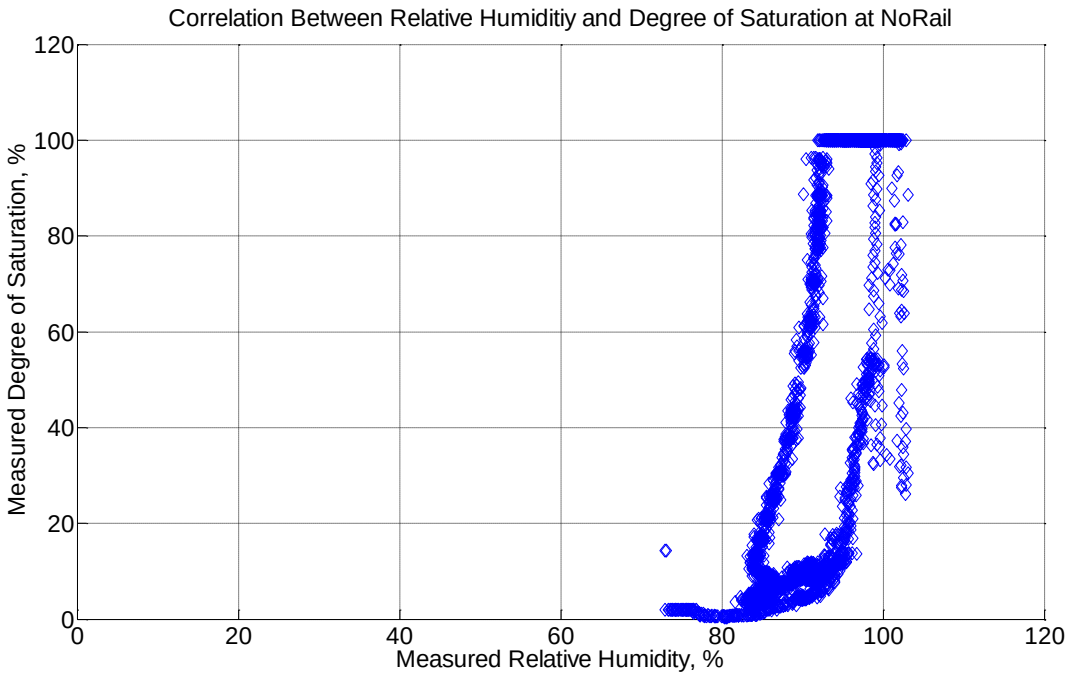

Figure 3-17 Correlation between measured relative humidity and degree of saturation at depth of 8.5 inches (215.9 mm) from the top surface of a model concrete crosstie (labeled NoRail) without a polyurethane pad nor rail installed in model ballast in Rantoul, IL. The data represents two periods from December 1, 2014, though December 21, 2014, and June 20, 2015, through September 11, 2015.

3.5.5 Comparing degree of saturation with predictive adsorption isotherm

Any number of adsorption isotherms can be compared against the result in Figure 3-17. Figure 3-18 shows one such adsorption isotherm by Pruckner [Pruckner, 2013]. It is readily apparent that the predictive adsorption isotherm does not represent the observed data set nor would many other isotherms. This is principally due to the experimentally measured degree of saturation reducing to 0% at instances when the relative humidity is greater than 80%. Such a behavior is mostly likely attributable to a low water-to-cement ratio leading to ongoing hydration of unreacted cement particles.

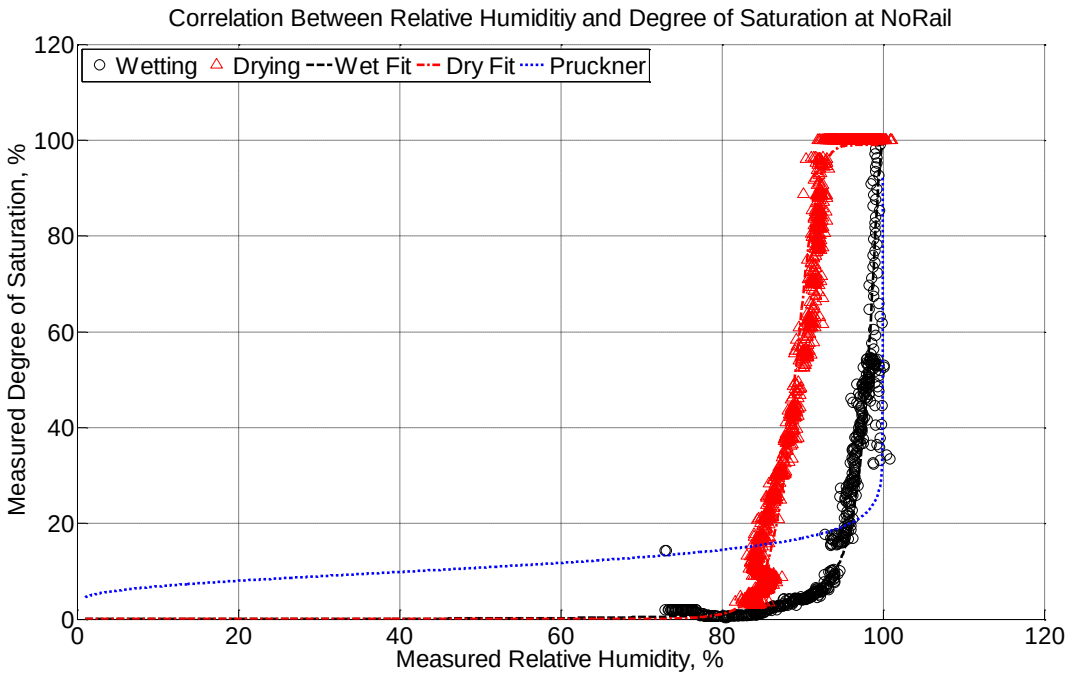

Figure 3-18 Correlation between measured relative humidity and degree of saturation at depth of 8.5 inches (215.9 mm) from the top surface of a model concrete crosstie (labeled NoRail) without a polyurethane pad nor rail installed in model ballast in Rantoul, IL. The black circles represent a wetting cycle that occurs from December 6, 2014, though December 13, 2014, while the red triangles represent a drying cycle that occurs from June 20, 2015, through September 11, 2015.

The correlation between degree of saturation and relative humidity in Figure 3-18 is also separated into two distinct phases: wetting and drying. When done so, it is apparent that there is hysteresis between the two curves. As such, the notion of a complex pore structure (cylindrical, ink-bottle, e.g.) is evident. Moreover, it is important to note that the wetting curve is accomplished in less than one week whereas the drying curve is accomplished in approximately three months. The drying curve was achieved by placing a breathable water-resistant canvas tarp over the model concrete crosstie. This is indicative of typically faster absorption rates of concrete versus slower desorption rates.

An implication of freeze-thaw damage is that there can persist a long period of highly saturated concrete while a precipitation event would have occurred months earlier. Additionally, the hysteretic nature of the correlation between degree of saturation and relative humidity indicates that a single measurement of relative humidity (93% RH, e.g.) can be interpreted in two vastly different manners: a degree of saturation as low as 15% and as high as 100%. As such, a single

measurement of relative humidity must be understood in a contextual manner as it cannot be understood as a singular event.

In the case where incomplete hydration of the Portland cement particles is evident (leading to a result where degree of saturation values fall to 0% while relative humidity remains high at values of 80% RH), it is possible to empirically fit an expression to predictively estimate the degree of saturation based on a measured relative humidity value. It is observed that a 3-parameter S-shaped curve can adequately represent the wetting and drying curves. As such, the degree of saturation, *S*, can be estimated as

$$S = S_o\left(\beta_o \frac{1-\beta_o}{1+\left(1-RH/1-RH_b\right)^m}\right) \qquad \text{Equation 3-12}$$

where S_o is 100% RH, β_o is a fit parameter affecting the y-axis range, RH_b is a fit parameter affecting the x-axis range, and m is a fit parameter affecting the curvature of the graph. The values used for both the wetting and drying curves are shown in Table 3-3 and the fit between the model and experimental data are shown in linear scale in Figure 3-18 and log scale in Figure 3-19. These wetting and fitting curves represent envelopes of degree of saturation based on measured relative humidity values. In the event that relative humidity does not follow this envelope, then an intermediary expression predictively governs the relationship between degree of saturation and relative humidity.

Table 3-3 Fit parameters used for 3-parameter S-shaped curves for wetting and drying curves.

Parameter	**Wetting Curve**	**Drying Curve**
β_o	0.01	0.01
RH_b	98% RH	89% RH
m	2	7.5

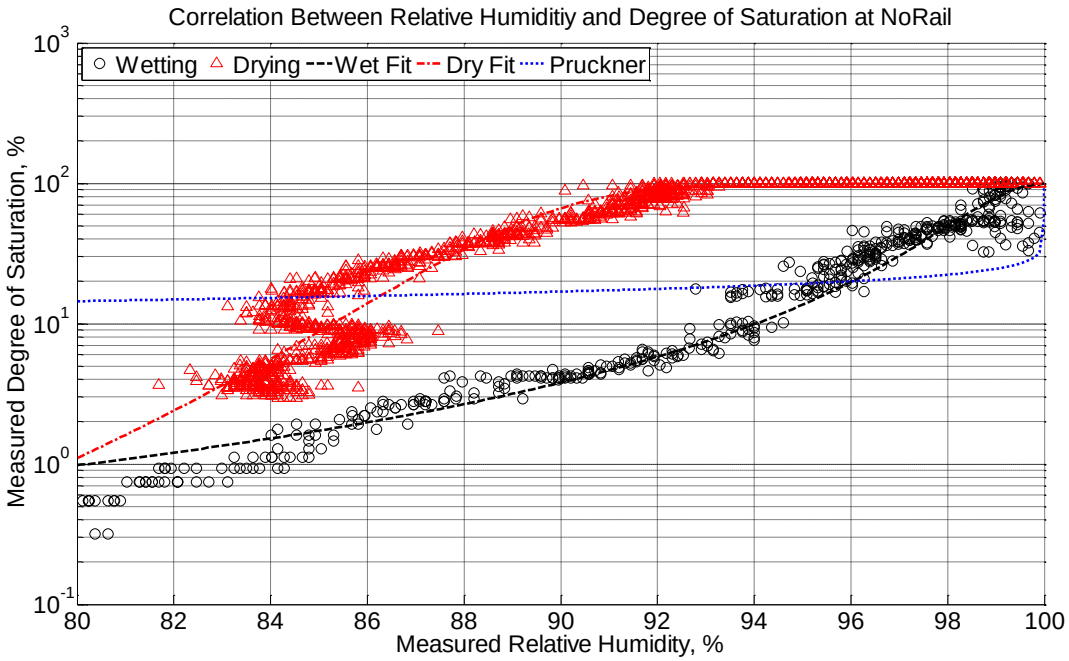

Figure 3-19 Correlation between measured relative humidity and log-scale degree of saturation at depth of 8.5 inches (215.9 mm) from the top surface of a model concrete crosstie (labeled NoRail) without a polyurethane pad nor rail installed in model ballast in Rantoul, IL. The black circles represent a wetting cycle that occurs from December 6, 2014, though December 13, 2014, while the red triangles represent a drying cycle that occurs from June 20, 2015, through September 11, 2015.

3.6 Summary of Chapter

Concrete crossties are subjected to freeze-thaw climates across North America which can leave them susceptible to freeze-thaw cyclic damage. Model concrete crossties were instrumented with hygrothermal sensors and moisture sensors in order to monitor their internal relative humidity and degree of saturation in model aggregate ballast in Rantoul, IL. A simple adsorption isotherm is applied in order to predict the correlation between degree of saturation and relative humidity. It is found that:

- Relative humidity and degree of saturation steadily increase inside a model concrete crosstie whose cross-sectional dimensions are typical of a conventional concrete crosstie when installed in un-fouled model ballast. Conversely, the two values steadily decrease when dry conditions are maintained.
- Although the persistence of a high relative humidity value, alone, is not sufficient to suggest that the concrete crosstie is saturated, a persistently high degree of saturation

measurement from a moisture sensor is sufficient to make such a claim. The results in this study indicate that model concrete crossties installed in aggregate ballast are often saturated above 86%, meaning that they are susceptible to freeze-thaw damage.

- An adsorption isotherm is not sufficient to characterize the correlation between relative humidity and degree of saturation inside high performance concrete installed in the field. This is likely due to a number of factors, including lack of constant temperature, inability of achieve equilibrium due to fast-changing external environments, and non-constant pore size distribution.
- An empirically fitted set of 3-parameter S-shaped curves can appropriate predict the correlation between relative humidity and degree of saturation of high performance concrete when installed in the field. However, these calibrated curves are subject to modification based on concrete mixture design (affecting the pore size distribution), history of hydration (where a fully hydrated Portland cement paste would have minimal changes in pore structure due to precipitation of solid-phased products), and are path-dependent functions (where intermediary wetting or drying traverse paths that are bounded by the empirically fitted curves). As such, these correlation curves are most useful when appropriately calibrated for a family comparable concrete members.

3.7 References

Adolphs, J., and Setzer, M. J. "Energetic classification of adsorption isotherms." *Journal of Colloid and Interface Science* 184 (1996): 443 – 448.

Beaudoin, J. J., and Cameron, M. "Dimensional changes of hydrated Portland cement paste during slow cooling and warming." *Cement and Concrete Research* 2 (1972): 225 – 240.

Bentz, D. P. "Influence of internal curing using lightweight aggregates on interfacial transition zone percolation and chloride ingress in mortars." *Cement and Concrete Composites* 31 (2009): 285 – 289.

Bentz, D. P., Ehlen, M. A., Ferraris, C. F., and Garboczi, E. J. "Sorptivity-based service life predictions for concrete pavements." *7th International Conference on Concrete Pavements* NIST, Orland, FL (2001): 181 – 193.

Bonnaud, P. A., Ji, Q., Coasne, B., Pellenq, R.J.-M., and van VLiet, K. J. "Thermodynamics of water confined in porous calcium-silicate-hydrates." *Langmuir* 28 (2012): 11422 – 11432.

Carlos, C. "Microscopic observations of internal frost damage and salt scaling." *University of California, Berkeley* (2005): PhD Dissertation.

Collepardi, M. "A state-of-the-art review on delayed ettringite attack on concrete." *Cement and Concrete Composites* 25 (2003): 401 – 407.

Dobruskin, V. K. “Effect of meniscus geometry on equilibrium pressures of the Lennard-Jones liquids.” *Langmuir* 24 (2008): 9375 – 9380.

Espinosa, R. M., and Franke, L. “Influence of the age and drying process on pore structure and sorption isotherms of hardened cement paste.” *Cement and Concrete Research* 36 (2006): 1969 – 1984.

Fagerlund, G. “The critical degree of saturation method of assessing the freeze/thaw resistance of concrete.” *RILEM Committee 4* (1977).

Ferraris, C. F. “Alkali-Silica Reaction and High Performance Concrete.” NISTIR 5742, Building and Fire Research Laboratory (1995). Report.

Hansen, K. K. “Sorption Isotherms – A Catalogue.” *Technical Report* 162 (1986). The Technical University of Denmark. Department of Civil Engineering. Building Materials Laboratory.

Henkensiefken, R., Castro, J., Bentz, D., Nantung, T., and Weiss, J. “Water absorption in internally cured mortar made with water-filled lightweight aggregate.” *Cement and Concrete Research* 39 (2009): 883 – 892.

Kovler, K. “Setting and hardening of gypsum-Portland cement-silica fume blends, Part I: Temperature and setting expansion.” *Cement and Concrete Research* 28 (1998): 423 – 437.

Li, W., Pour-Ghaz, M., Castro, J., and Weiss, J. “Water absorption and critical degree of satuation relating to freeze-thaw damage in concrete pavement joints.” *Journal of Materials in Civil Engineering* 24 (2012): 299 – 307.

Litvan, G. G. (1988). “The mechanism of frost action in concrete-theory and practical implications.” *Proceedings of Workshop on Low Temperature Effects on Concrete*, National Research Council of Canada, Montreal, Canada, 115 – 134.

Litvan, G. G., and Sereda, P. J. (1980). “Freeze-thaw durability of porous building materials.” *Durability of Building Materials and Components*, ASTM STP 691, P. J. Sereda and G. G. Litvan, Eds. ASTM International, West Conshohocken, PA, 455 – 463.

Maxim Integrated. (March 2013). *DS1923 Revision 5*. Retrieved from http://datasheets.maximintegrated.com/en/ds/DS1923.pdf.

Mindess, S., Young, J. F., and Darwin, D. *Concrete 2nd Edition*. 2003, Upper Saddle River, NJ: Prentice Hall.

Poyet, S., and Charles, S. “Temperature dependence of the sorption isotherms of cement-based materials: Heat of sorption and Clausius-Clapeyron formula.” *Cement and Concrete Research* 39 (2009): 1060 – 1067.

Pruckner, F. “Relative humidity measurements for assessing moisture conditions in concrete structures.” *Beton-und Stahlbetonbau* 108 (2013): 865 – 874. Language: German.

Rotronic Instrument Corp. (December 2005). *The Rotronic Humidity Handbook*. Retrieved from http://www.southeastern-automation.com/PDF/Rotronic/Humidity_Handbook.pdf.

Shimada, H., Sakai, K., and Litvan, G. G. (1991). “Acoustic emissions of mortar subjected to freezing and thawing.” *Durability of Concrete: Second International Conference* V. M. Malotra, Ed. American Concrete Institute, Detroit, MI, 263 – 278.

Swamy, R. N. (Ed). *The Alkali-Silica Reaction in Concrete*. 2002, New York: CRC Press.

Tesárek, P., Černý, R., Drchalová, J., and Rovnaníková, P. “Mechanical, hygric and thermal properties of flue gas desulfurization gypsum.” *Acta Polytechnica* 44 (2004): 83 – 88.

Xi, Y., Bažant, Z. P., and Jennings, H. M. “Moisture diffusion in cementitious materials.” *Advanced Cement Based Materials* 1 (1994): 248 – 257.

Yang, Q. “Inner relative humidity and degree of saturation in high-performance concrete stored in water or salt solution for 2 years.” *Cement and Concrete Research* 29 (1999): 45 – 43.

Zeman, J. C., Edwards, J. R., Lange, D. A., and Barkan, C. P. L. "Evaluating the potential for damaging hydraulic pressure in the concrete tie rail seat." *Proceedings of the 2010 Joint Rail Conference* (2010): Urbana, IL.

CHAPTER 4 – FREEZE-THAW DAMAGE POTENTIAL OF HIGH PERFORMANCE CONCRETE BASED ON CLIMATIC DATA AND CONCRETE QUALITY

4.1 Abstract

Historical climatic data from weather stations is available throughout North America and is routinely used for estimating the number of freeze-thaw cycles within a geographic region. However, climatic data is limited to ambient readings. With regards to freeze-thaw damage susceptibility in concrete, the combination of both internal moisture and internal temperatures must be considered. In this modeling study, the framework for predicting internal relative humidity and temperature profiles in high performance concrete is utilized to predict the number of mutual instances where internal critical degrees of moisture saturation and freezing temperatures are achieved. Two case studies across two winter seasons are considered. Hourly weather data from Rantoul, Illinois, United States, and Lytton, British Columbia, Canada, is collected from mid-2013 through mid-2015 and utilized to predict the number of freeze-thaw cycles. The number of cycles can be considered as a susceptibility index that can be generated for concrete with varying exposure conditions and varying quality (based on water-to-cement ratio). It is demonstrated that these susceptibility indices are reduced when additional constraints (degree of saturation, freezing temperature rate, and concrete quality) are considered.

4.2 Introduction and Background

4.2.1 Current characterization of freeze-thaw damage potential in concrete

Conventional concrete and high performance concrete installed in outdoor environments are susceptible to the natural elements including instances of freezing and thawing ambient temperatures and the absorption of water due to moisture precipitation. When liquid water undergoes freezing, it expands 9% of its original volume. When liquid water inside concrete microstructure freezes, it similarly expands in volume and exerts stresses onto the brittle microstructure which leads to cracking. This repeated cycling of freezing and thawing temperatures inside moisture saturated concrete leads to freeze-thaw damage as manifested in D-cracking, aggregate pop-outs, and surface scaling [Mehta and Monteiro, 2006]. Moreover, recent research suggests that a minimal degree of saturation must be present (approximately 86-88%) in

order for significant freeze-thaw damage to manifest itself [Li *et al.*, 2012]. This critical degree of saturation is found by Li *et al.* to produce freeze-thaw cyclic damage irrespectively of the amount of protecting air-entrained voids.

In most instances of concrete infrastructure installed in outdoor environments, the state of internal moisture is assumed to be significantly high (e.g. concrete pavements sitting atop (sub-) base that is highly saturated due to its proximity to the water table). As such, the cycling of ambient air temperatures from freezing to thawing is primarily used to characterize the extent of freeze-thaw cycles that the concrete material undergoes. Hershfield in 1974 constructed a map across the United States of the number of freeze-thaw instances that occurred given weather station data alone. Fraser in 1959 similarly measured the frequency of freeze-thaw cycles occurring in Canada. Hershfield reports instances of approximately 200 freeze-thaw cycles in the central American Rocky Mountain range while Fraser reports approximately 80 freeze-thaw cycles in the southern Canadian Rocky Mountain range. This discrepancy between the two locations exemplifies the importance of intermediary temperatures in order to produce a single freeze-thaw event (a region that is consistently frozen or consistently thawed does not, for example, lead to a large number of freeze-thaw cycles). Therefore, freeze-thaw cyclic damage is expected to be of greater risk in intermediary climates with persistently high precipitation and a large number of freeze-thaw cycles.

The advent of high performance concrete with the use of pozzolanic admixtures and chemical admixtures has led to concrete that is purported to be more durable because it has higher strength, is more impermeable, and can consume excess moisture by chemically reacting with unhydrated cement particles (due to a purposely low water-to-cementitious ratio by mass). As such, the number of freeze-thaw cycles as measured by ambient air temperatures is not expected to affect high performance concrete in the same manner as conventional concrete. It is, thus, of importance to note the instances in which freezing temperatures occur when high performance concrete has moisture levels above a critical degree of saturation.

4.2.2 Modeling internal temperature and degree of saturation

The internal temperature and moisture gradients inside concrete can be modeled in a number of different ways including 1-dimensional solutions. It has been previously shown that a separation of variables method to predict internal temperature values, $T_i\,(z,t)$, using estimated solar radiation, ambient air temperatures, and thermal properties in cold weather is sufficient (see Chapter 2). This expression, in a multi-layered system of materials, is expressed as

$$T_{ij}(z,t) = \Delta_{11} e^{-\upsilon_1 z} \sin(\omega t - \upsilon_i z + \delta_{11} + \phi) + \Delta_{12} e^{\upsilon_1 z} \sin(\omega t + \upsilon_i z + \delta_{12} + \phi) \quad \text{Equation 4-1}$$

for $0 \le z \le H_1$;

$$T_{ij}(z,t) = \Delta_{i1} e^{H_{i-1}\upsilon_{i-1} + \upsilon_i (H_{i-1} - z)} \sin(\omega t - \upsilon_i z + \delta_{i1} + \phi) + \Delta_{i2} e^{H_{i-1}\upsilon_{i-1} - \upsilon_i (H_{i-1} - z)} \sin(\omega t + \upsilon_i z + \delta_{12} + \phi) \quad \text{Equation 4-2}$$

for $H_{i-1} \le z \le H_i$, and $i = 2, 3, \ldots, n-1$; and

$$T_{nj}(z,t) = \Delta_n e^{H_{n-1}\upsilon_{n-1} + \upsilon_n (H_{n-1} - z)} \sin(\omega t - \upsilon_n z + \delta_{n1} + \phi) \quad \text{Equation 4-3}$$

for $z \ge H_{n-1}$. The variables Δ_{i1}, δ_{i1}, υ_i for $i = 1, 2, \ldots, n$ and Δ_{i2}, δ_{12} for $i = 1, 2, \ldots, n-1$, ω, z, H_i, and ϕ in Equations 4-1 through 4-3 are found elsewhere (see Chapter 2) [Wang and Roesler, 2014].

The moisture levels inside concrete can be predicted using a moisture transport model and a correlation between relative humidity and degree of saturation. A 1-dimensional transport model to predict internal relative humidity using diffusivity and ambient relative humidity is sufficient (see Chapter 2) and expressed as

$$\frac{\partial RH(t,z)}{\partial t} = div(D \cdot grad(RH(t,z))) - \frac{\partial RH_s(t,z)}{\partial t} \quad \text{Equation 4-4}$$

where RH is a function of time (sec), t, and depth (m), z; $\frac{\partial RH_s(t,z)}{\partial t}$ is the change in relative humidity due to hydration for early-age concrete (assumed as $\frac{\partial RH_s(t,z)}{\partial t} = 0$ for hardened concrete; and D is the moisture diffusivity, which is a function of both internal relative humidity and concrete

porosity. The moisture diffusivity factor is non-linear and can be expressed by an effective diffusivity [Bažant and Najjar, 1972]

$$D = D_o\left(\alpha_o \frac{1-\alpha_o}{1+\left(1-RH/1-RH_c\right)^n}\right) \quad \text{Equation 4-5}$$

where D_o (m^2/s) is the moisture diffusivity at complete saturation; n is a regression coefficient ranging from 6 to 16 for concrete [Leech *et al.*, 2003]; $\alpha_o = D_1/D_o$, where D_1 is the diffusivity at 0% RH; and RH_c is the bifurcate point above which capillary suction governs (typically 75 to 80%) [Qin and Hiller, 2014]. The moisture diffusivity at complete saturation can be related to the water-to-cementitious ratio as shown in Table 4-1.

Table 4-1 Moisture diffusivity at saturation estimated from w/c ratio (from [1]Kang *et al.*, 2012, and [2]Qin and Hiller, 2014).

w/c	D_o (10^{-6} m^2/hour)[1]	D_o (10^{-6} m^2/hour)[2]
0.28	2.02	0.68
0.40	2.10	1.59
0.50	2.26	-
0.68	2.87	2.57

The boundary condition at the top of the concrete is modified in order to better represent wetting events due to precipitation (rain or melting snow). The boundary condition at the bottom of the concrete is assumed to sit atop well-drained ballast; however, it has been found that persistent high humidity exists in such an environment (see Chapter 2). As such, the boundary condition at the underside of this concrete is assumed to be 10-times the value at the topside. Table 4-2 shows weather conditions which increase the measured relative humidity value to 100% RH over a given time frame.

Table 4-2 Modified boundary condition at the top of concrete as subject to reported weather conditions (adapted from Qin and Hiller, 2014).

Reported Weather Condition	Modified Wetting Duration
Drizzle	RH_{upper} = 100 % for 1 hour
Fog	
Mist	
Light Rain	RH_{upper} = 100 % for 4 hours
Light Thunderstorms and Rain	
Thunderstorms and Rain	RH_{upper} = 100 % for 8 hours
Rain	
Heavy Thunderstorms and Rain	RH_{upper} = 100 % for 10 hours
Heavy Rain	
Light Snow	
Snow	RH_{upper} = 100 % for 15 hours
Heavy Snow	RH_{upper} = 100 % for 20 hours

Equation 4-4 predicts the internal relative humidity distribution inside of concrete, and a further correlation from relative humidity to degree of saturation must be made in order to understand freeze-thaw cyclic damage. A number of adsorption isotherms (Freundlich, Langmui, BET, e.g.) can make these correlations, yet empirical fits are often selected because of the number of material challenges often posed by concrete. In the case of high performance concrete where unhydrated cement particles chemically react with the presence of water, it is found that a 3-parameter S-shaped curve adequately predicts the correlation between relative humidity and degree of saturation (see Chapter 3). The correlation is found to be

$$S = S_o\left(\beta_o \frac{1-\beta_o}{1+\left({}^{1-RH}/_{1-RH_b}\right)^m}\right) \qquad \text{Equation 4-6}$$

where S_o is 100% RH, β_o is a fit parameter affecting the y-axis range, RH_b is a fit parameter affecting the x-axis range, and m is a fit parameter affecting the curvature of the graph. The fitted-values used for both the wetting and drying curves are shown in Table 4-3. These wetting and fitting curves represent envelopes of degree of saturation based on measured relative humidity values. In the event that relative humidity does not follow this envelope, then an intermediary expression must govern the relationship between degree of saturation and relative humidity.

Table 4-3 Fit parameters used for 3-parameter S-shaped curves in Equation 4-6 for wetting and drying curves.

Parameter	Wetting Curve	Drying Curve
β_o	0.01	0.01
RH_b	98% RH	89% RH
m	2	7.5

4.2.3 Rate and duration of temperature freezing

Freeze-thaw damage susceptibility of concrete is often assessed with representative concrete prisms pursuant to ASTM C666 *Standard Test Method for Resistance of Concrete to Rapid Freezing and Thawing*. In this testing technique, fully saturated concrete samples are subjected to temperature variations from thawed (4±2°C) to freezing (-18±2°C) and back to thawed within a 2 to 5 hour period. These temperature fluctuations represent a ±8.8°C/hr to ±22°C/hr freezing or thawing rate assuming the total time period is simply halved and no considerations are taken for asymmetric thawing times (where ASTM C666 allows for no less than 25% of total time for Procedure A to be committed to thawing and no less than 20% of total time for Procedure B to be committed to thawing). These high freezing and thawing rates accelerate the instances of freeze-thaw cycles from several long years to several short weeks. As a consequence of this accelerated testing, the duration of freezing and thawing is also shortened than what would normally be observed in in-situ concrete where the duration of freezing and thawing temperatures may remain persistent across several hours. Across persistently frozen temperatures, ice crystal growth is permitted which creates an increasing amount of stress on the concrete microstructure. In accelerated testing pursuant to ASTM C666, the period of transition between freezing and thawing cycle is not permitted to exceed 10 minutes, meaning that ice crystal growth and associated stresses are not greatly appreciable.

The prescribed freeze-thaw damage criteria from ASTM C666 (for loss of dynamic modulus of elasticity to 60% of its original value and/or length change exceeding 0.10% expansion) occurring before 300 accelerated freeze-thaw cycles is empirically correlated to observed damaged of in-situ conventional concrete within its designed service-life. The accelerated number of 300 freezing and thawing cycles does not (nor must it) coincide with 300 freeze-thaw cycles as observed in ambient weather. Instead, it is assumed that the prescribed 300 freeze-thaw cycles coincides with concrete whose freeze-thaw cycles are occurring within a fully

saturated microstructure. The thrust of this modeling study is to understand the effect of freeze-thaw cycles that occur in concrete when it is not fully saturated. As such, it is possible to predict the number of instances in which:

- A freeze-thaw cycle occurs due to ambient air temperature fluctuations (assuming that the microstructure is completely saturated),
- A freeze-thaw cycle occurs due to internally predicted temperature fluctuations (assuming that the microstructure is completely saturated),
- A freeze-thaw cycle occurs due to ambient air temperature fluctuations (assuming a variable internal degree of saturation), and
- A freeze-thaw cycle occurs due to internally predicted temperature fluctuations (assuming a variable internal degree of saturation).

It is also possible to investigate the instances of freeze-thaw cycles that occur due to temperature freezing rates between ±8.8^{o}C/hr to ±22^{o}C/hr; however, this accelerated freezing rate has little bearing on the performance of in-situ concrete as this freezing rate is artificially induced in accelerated testing and is not necessarily required in actual environmental conditions. The time duration of freezing temperatures is also not considered in this study, nor is the mutual instance of partially saturated concrete with varying freezing rates. These effects are of interest for future study, but deviate from the primary scope presented in this study.

4.3 Significance of Research

High performance concrete is subject to freeze-thaw conditions which adversely affects the durability of conventional concrete but does not similarly affect the durability of high performance concrete. This difference is mostly attributable to high performance concrete's large impermeability to external water and internal curing of unhydrated cement particles. In order to better understand the resiliency of high performance concrete against cyclic freeze-thaw damage, it is necessary to understand the mutual instances of freezing temperatures and high degree of saturation. This refined consideration for the number of freeze-thaw cycles of high performance concrete can lead to enhanced design specifications for high performance concrete installed in wet, wintry environments.

4.4 Modeling Framework

4.4.1 Weather data as an input

Publicly available temperature and relative humidity data from a weather station (KTIP) in Rantoul, IL, United States, from September 3, 2013, through September 8th, 2015. Similar data is also retrieved from a weather station (CWLY) near Lytton, BC, Canada, is retrieved from October 8th, 2013, through March 17th, 2015. In conjunction with latitudinal and longitudinal information known at both locations (and daily solar noon times across the observed time period), the internal temperature profile distribution within a 230 mm thick modeled concrete section overlaid atop a well-drained aggregate ballast layer is solved using Equation 4-2. The reported relative humidity values are additionally utilized (along with reported weather conditions) to solve the internal relative humidity profile distribution within a 230 mm thick modeled concrete section using Equation 4-4.

4.4.2. Adaptive correlation between relative humidity and degree of saturation

The predicted internal relative humidity values must be correlated to degree of saturation. However, the microstructure of cement-based materials leads to hysteric adsorption isotherms where capillary condensation governs the shape of drying and wetting curves at high relative humidity values. Figure 4-1 shows experimental data of an instrumented concrete prism (measuring 9-inch by 9-inch by 16-inch) installed in well-drained aggregate ballast during two events: a short, 7-day wetting event and a long, 83-day drying event. The hysteric nature of the sorption is evident despite effects arising from non-constant temperatures, changing alkalinity of the pore fluid due to change in total moisture content in the microstructure, and changing pore size distribution due to ongoing hydration (attributable to low water-to-cementitious ratio which results in un-hydrated cement particles at late age) and due to precipitation of solid crystals as a result of supersaturation. Two 3-parameter S-shaped curves are utilized to mimic the shape of the experimental data and take the form described by Equation 4-6 with fit parameters described by Table 4-3.

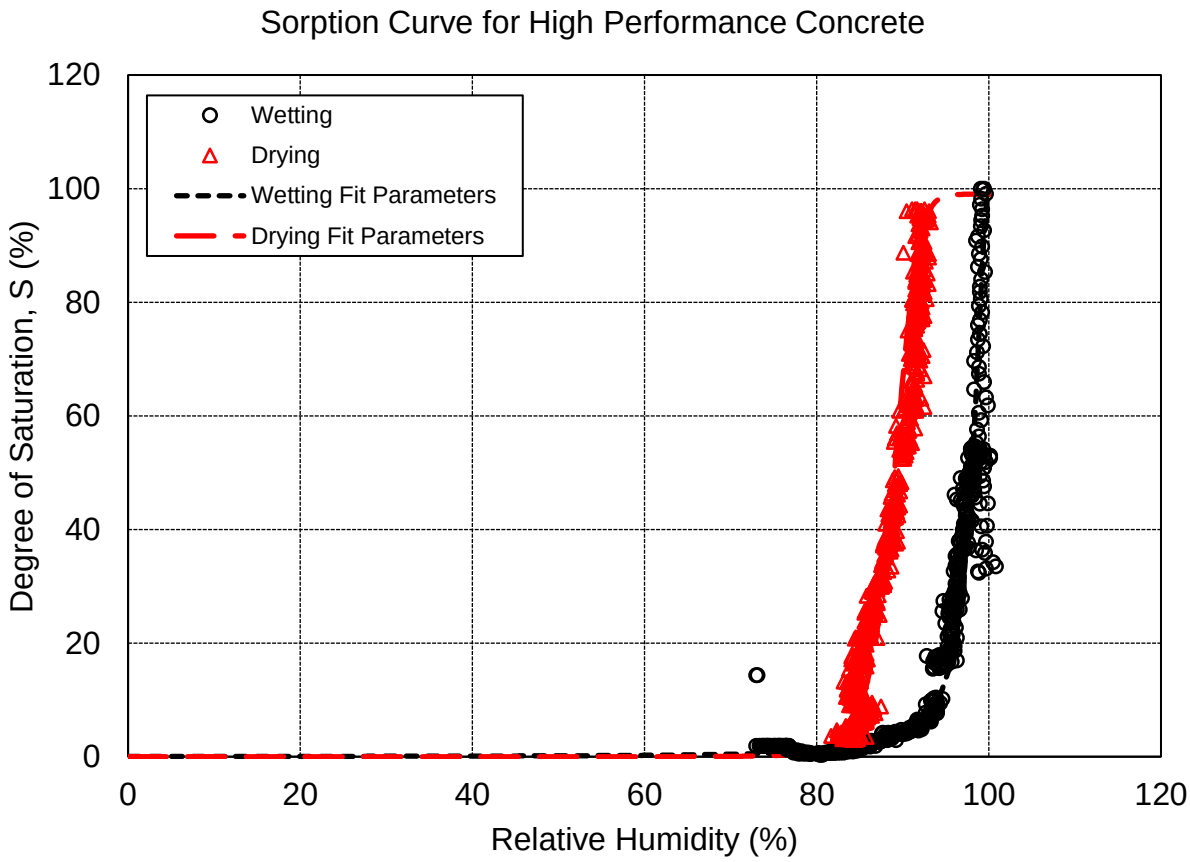

Figure 4-1 Correlation between measured relative humidity and measured degree of saturation of instrumented high performance concrete prism. The black circles represent a wetting cycle that occurs from December 6, 2014, through December 13, 2014, while the red triangles represent a drying cycle that occurs from June 20, 2015, through September 11, 2015. Each data set is fitted with separate 3-parameter S-shaped curves.

In the event that a cement-based material is partially wetted and then fully dried, the resulting drying curve must take a new, revised form not fully described by Equation 4-6 where the drying path is an intermediary travel path between the two limiting (upper and lower) envelopes. In such a case, the drying path, S_{drying}, must begin at the last wetted point, S_{wetted}, as described in the following expression

$$S_{drying} = S_{wetted}\left(\beta_o \frac{1-\beta_o}{1+\left(1-RH/1-RH_b\right)^{m}}\right) \qquad \text{Equation 4-7}$$

where the fitting parameters are those values described in Table 4-3 for a drying curve. Equation 4-7 can be plotted for instances when the initial degree of saturation is brought to 100, 95, 95, 90,

85, 80, 60, 40, or 20% before it is fully dried (see Figure 4-2). It is evident that each drying curve maintains a characteristic plateau where the degree of saturation is maintained momentarily while relative humidity decreases in value. After an initial drying plateau, the drying curves collapse onto the drying envelope as described by Equation 4-7.

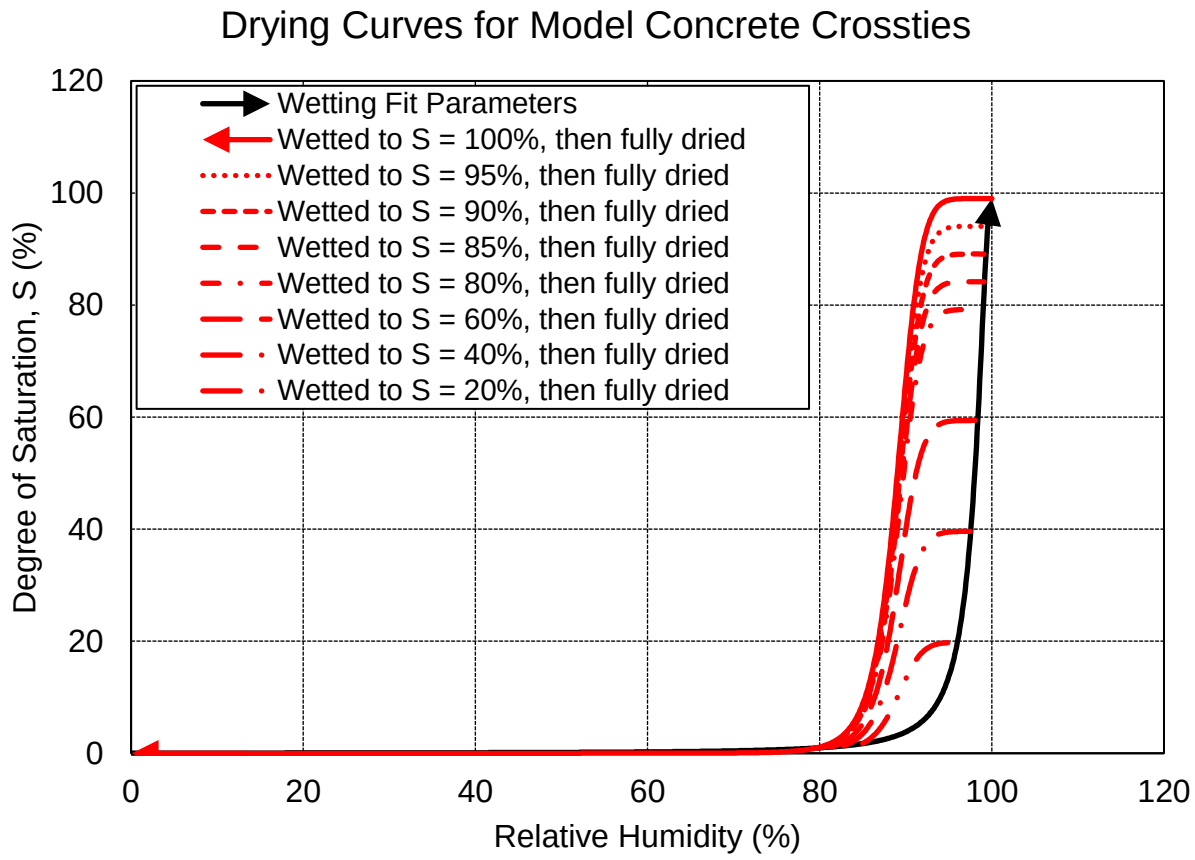

Figure 4-2 Modeled instances of drying when the concrete is initially wetted to S = 100, 95, 90, 85, 80, 60, 40, or 20% of its degree of saturation.

Similarly, a wetting event when a cement-based material is partially dried results in a revised set of curves. The wetting path, $S_{wetting}$, begins at the last dried point, S_{dried}, as described in the following expression

$$S_{wetting} = (S_o - S_{dried})\left(\beta_o \frac{1-\beta_o}{1+\left(1-RH/1-RH_b\right)^m}\right) + S_{dried} \qquad \text{Equation 4-8}$$

where the fitting parameters are those values described in Table 4-3 for a wetting curve. Similarly, Equation 4-8 can be plotted for instances of where the degree of saturation is initially brought to

100% before it is dried to values of 0, 20, 40, 60, 80, 85, 90, or 95% and subsequently re-wetted to 100% (see Figure 4-3). Again, the characteristic shape of the wetting curve is maintained across these multiple instances.

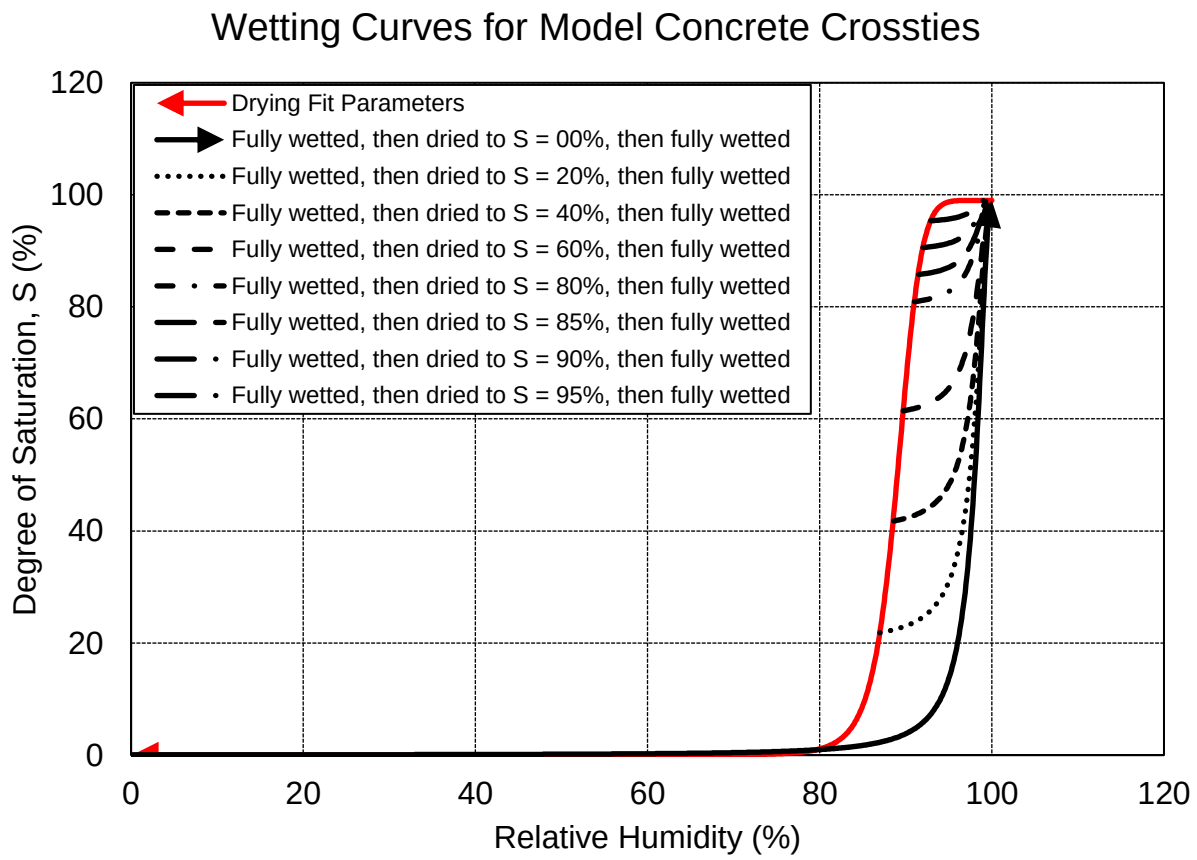

Figure 4-3 Modeled instances of wetting when the concrete is initially wetted to S = 100%, then dried to S = 0, 20, 40, 60, 80, 85, 90, and 95% of its degree of saturation before being re-wetted to S = 100%.

Equations 4-7 and 4-8 thusly empirically correlate a predicted relative humidity value (from Equation 4-4) to a degree of saturation if it is known whether the high performance concrete is undergoing drying or wetting. It is possible to ascertain whether concrete is undergoing drying or wetting by observing the difference in experimentally measured relative humidity values. In the case when the difference between two successively measured relative humidity values is negative, then it is assumed that the high performance is undergoing drying. Alternatively, if the difference between successively measured relative humidity values is positive, then the high performance concrete is assumed to be undergoing wetting.

A simplified scenario is also assumed when applying Equation 4-7 and 4-8 in this study. In the case when the modeled concrete switches from drying to wetting (or vice-versa), then a switch occurs from Equation 4-7 and 4-8 (or vice-versa). However, the last predicted saturation value may be an intermediary point that does not lie on either governing (upper or lower) envelope. In such a case, it is necessary to interpolate S_{dried} and S_{wetted} as the switch between Equation 4-7 to 4-8 is made. If not, a non-continuous solution of S is found which can vary by approximately 2-5%. However, the number of instances between rapid drying and wetting cycles inside concrete is observed to be minimal, so this consideration is not of great consequence. As such, the decision between either Equation 4-7 or 4-8 is binary and an interpolated S value is not determined.

4.4.3 Criteria for freeze-thaw event

Four scenarios are evaluated to depict the effect of differing assumptions to produce a singular freeze-thaw cycle event. The first scenario is the observation of ambient air temperatures at a thawed temperature dropping to below 0^{o}C before reverting to a thawed temperature. This sequence of temperatures constitutes a single reported freeze-thaw event. The second scenario is the observation of modeled temperatures values inside the concrete (at depths of 5, 15, 25, 50, 100, 150, and 200 mm from the top surface) at a thawed temperature dropping to below 0^{o}C before finally reverting to a thawed temperature. This sequence of temperatures constitutes a single reported freeze-thaw event.

A third scenario additionally constrains a freeze-thaw event (as described in the first two scenarios) by a fluctuation of temperatures occurring when the degree of saturation is greater than a critical degree of saturation (ranging from 5, 10, 25, 50, and 85%). Lastly, a fourth scenario applies the previously mentioned constraints with regards to temperature fluctuation while adding a freeze-thaw rate dependency (of a minimum freezing rate of -8, -10, -12, -15, -18, and -22 ^{o}C/hr).

4.5 Modeling Results

4.5.1 Predicted temperature and saturation of model concrete in Rantoul, IL, United States

The recorded air temperature for a two year period in Rantoul, IL, from weather station KTIP is shown in Figure 4-4. Additionally, the predicted internal temperature of concrete at several depths is also shown. Shorter time durations of temperature data are presented in Appendix A. It is evident that there are daily fluctuations, but there is a general seasonal trend of high temperatures in the summer months and low temperatures in the winter months. Moreover, the vertical range of the data (daily fluctuation) is constrained to a more narrow range as the observation is into the model concrete at deeper depths. This is indicative of thermally insulating behavior and is wholly expected.

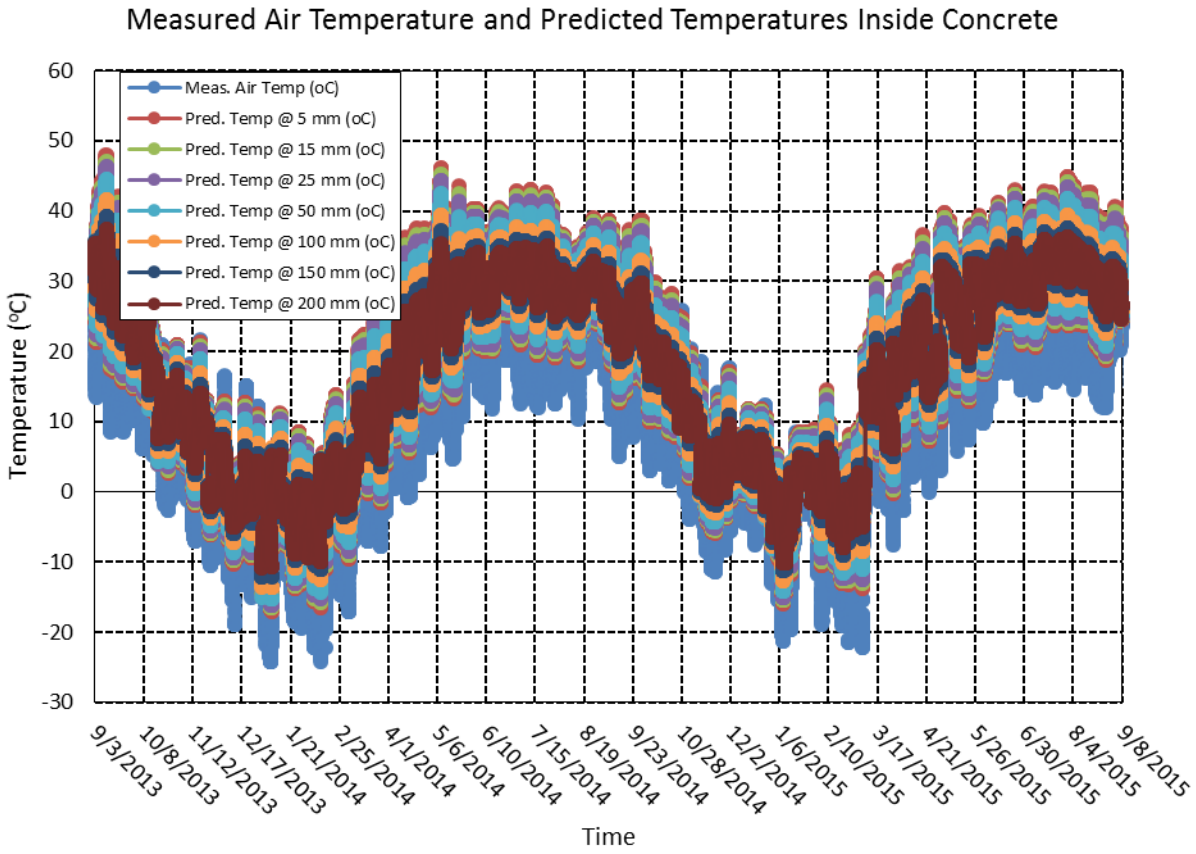

Figure 4-4 Measured air temperature and predicted temperature inside model concrete in Rantoul, IL, from September 3, 2013, through September 8, 2015. Predicted internal temperature values are computed using a 2-layered system whose upper concrete layer is defined by a thermal conductivity, λ, value of 1.85 kcal/hmC^o and a thermal diffusivity, α, value of 0.0025 m^2/h. The underlying aggregate ballast layer is defined by a thermal conductivity, λ, value of 2.58 kcal/hmC^o and a thermal diffusivity, α, value of 0.0030 m^2/h.

The predicted degree of saturation of model concrete located in Rantoul, IL, is shown in Figure 4-5. The prediction is initialized with an even distribution of 85% RH. One observation of this data set is the effect of the boundary condition at the topside (5 mm) and underside (200 mm) of the model concrete. The boundary condition at the underside exacerbates wetting conditions as described by Table 4-2 by a factor of 10. As a result, the extent of high moisture saturation increases over a longer period of time at the underside than at the topside which experiences large increases in saturation followed by significant drying. Similar to temperature, seasonal fluctuations are observed. In the precipitously wet winter months, there is a general spike in the amount of predicted saturation. In the summer months, there is generally a lower amount of precipitation so there is also a lower amount of saturation. At the interior of the concrete (150 mm), it is observed

that saturation steadily increases with respect to time. This is most likely due to the increase of relative humidity with slow drying occurring.

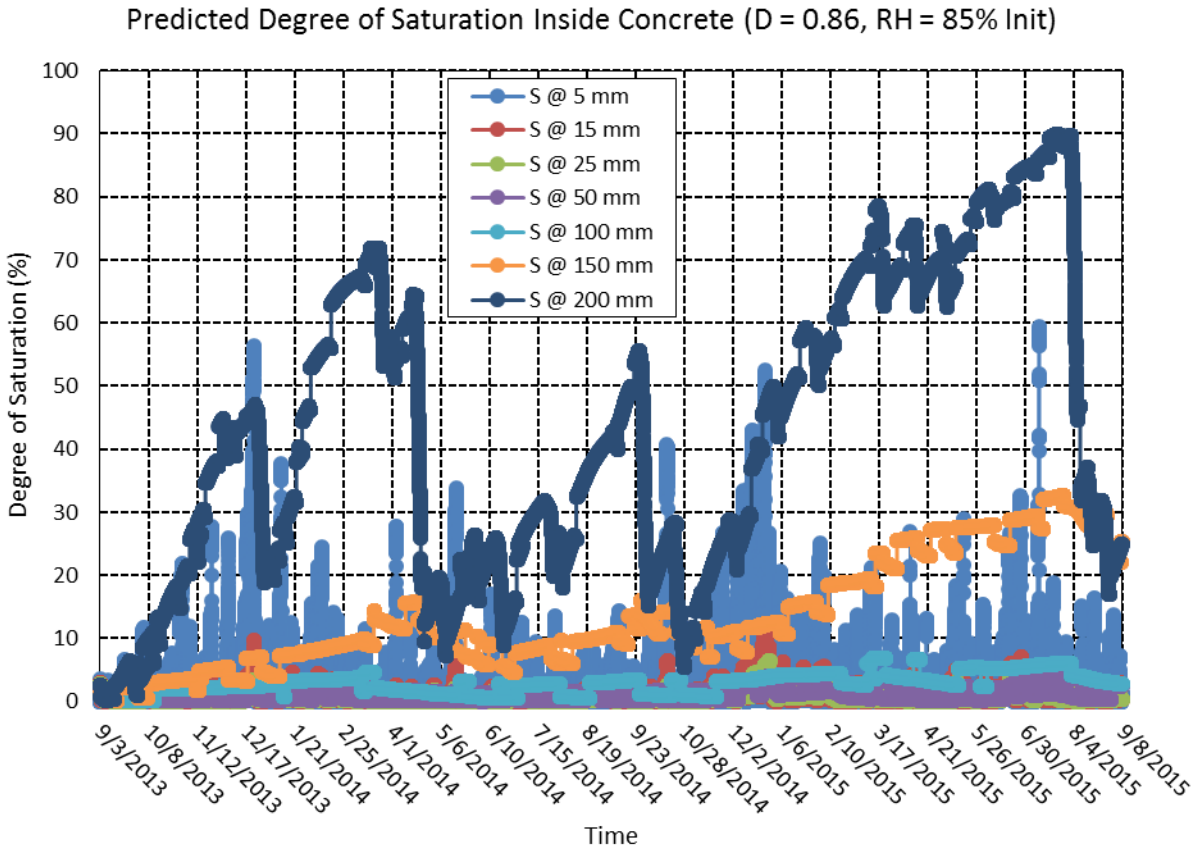

Figure 4-5 Predicted degree of saturation inside a 1-layered concrete system in Rantoul, IL, from September 3, 2013, through September 8, 2015. The concrete is defined by a diffusivity (at S = 100%) value of 0.86×10^{-6} m^2/hr, a regression coefficient, *n*, of 15, α value of 0.05, and an empirical correlation between relative humidity and degree of saturation. The simulation is initialized with an even distribution of 85 %RH throughout the depth of the concrete.

4.5.2 Predicted temperature and saturation of model concrete in Lytton, BC, Canada

The recorded air temperature of Lytton, BC, from weather station CWLY is shown in Figure 4-6. Much like the temperature values shown in Figure 4-4, there is also seasonal fluctuations that are observed. Figure 4-7 shows the predicted degree of saturation of model concrete in Lytton, BC, initialized with an even distribution of 85% RH. Again, there is an observation of seasonal variation of degree of saturation between wet, wintry months and dry, summer months. At the underside of the model concrete (200 mm), it is evident that there is a

slight offset rightward suggesting that the well-drained ballast is able to retain moisture past significant moisture events that occur earlier in the simulation. Also, contrasted against Figure 4-5, it is observed that for the same material conditions (diffusion coefficient and initialization of moisture conditions), there is a starkly higher number of instances of degree of saturation. This is indicative of the differences in weather conditions leading to this result.

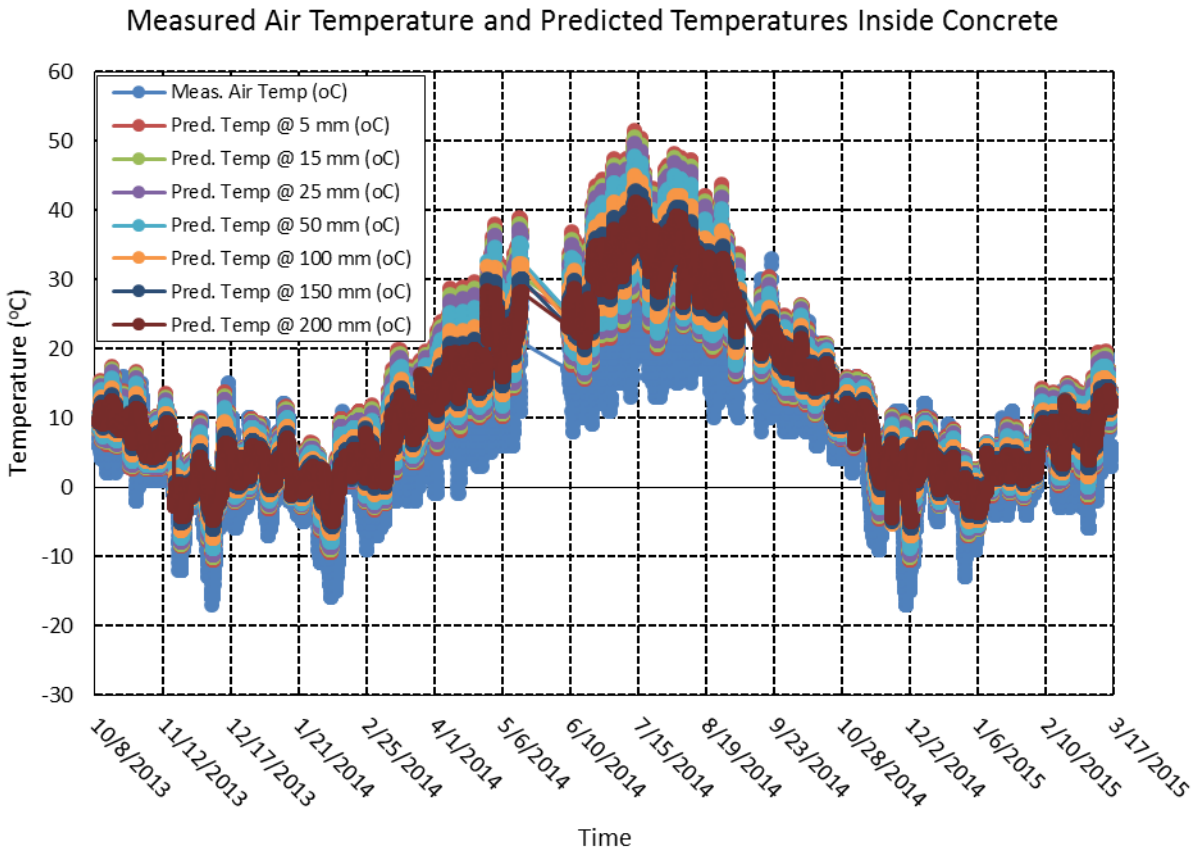

Figure 4-6 Measured air temperatures and predicted temperature inside model concrete in Lytton, BC, from October 8, 2013, through March 17, 2015. Predicted internal temperature values are computed using a 2-layered system whose upper concrete layer is defined by a thermal conductivity, λ, value of 1.85 kcal/hmC^o and a thermal diffusivity, α, value of 0.0025 m^2/h. The underlying aggregate ballast layer is defined by a thermal conductivity, λ, value of 2.58 kcal/hmC^o and a thermal diffusivity, α, value of 0.0030 m^2/h.

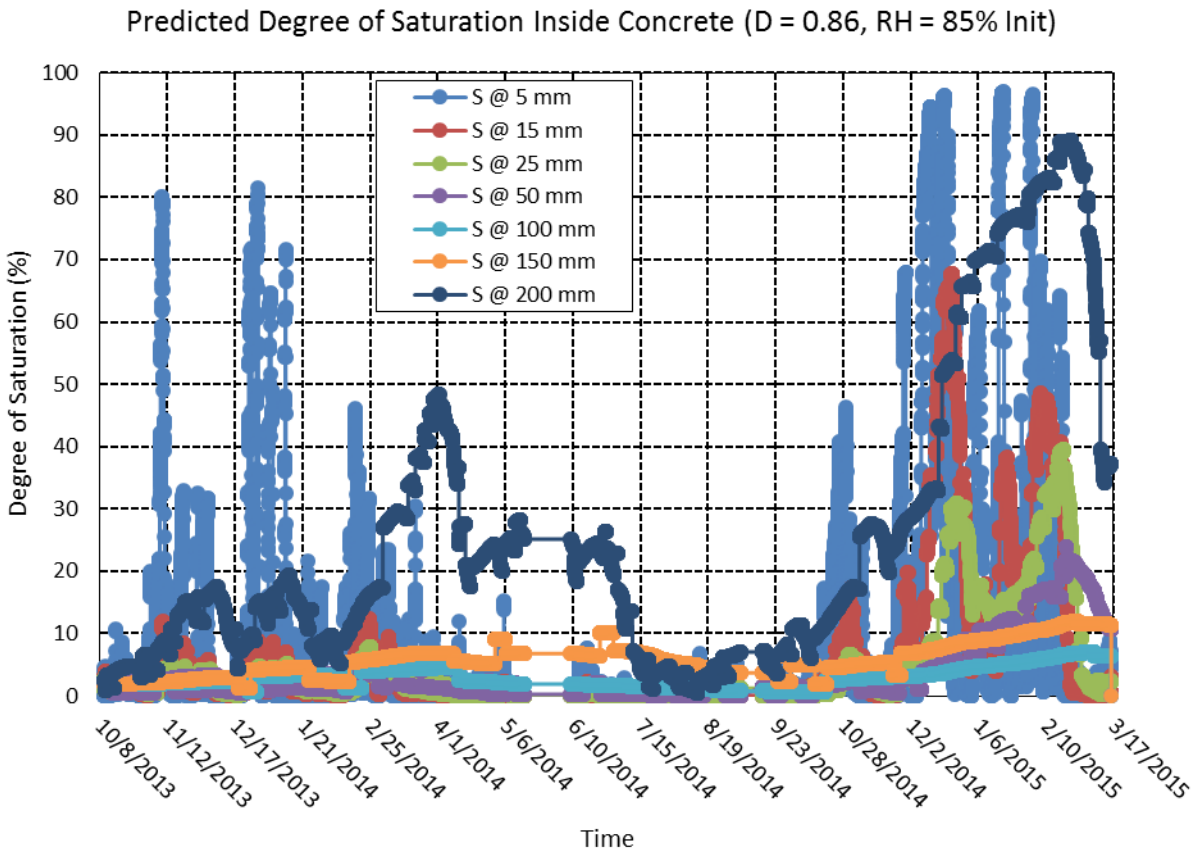

Figure 4-7 Predicted degree of saturation inside a 1-layered concrete system in Lytton, BC, from October 8, 2013, through March 17, 2015. The concrete is defined by a diffusivity (at S = 100%) value of 0.86×10^{-6} m^2/hr, a regression coefficient, *n*, of 15, α value of 0.05, and an empirical correlation between relative humidity and degree of saturation. The simulation is initialized with an even distribution of 85 %RH throughout the depth of the concrete.

4.6 Discussion of Modeling Results and Framework

A brief overview of modeling results and discussion is presented in the following section. For a complete overview of all considered test cases, refer to Appendix C.

4.6.1 Difference between observed air temperatures and internal concrete temperatures

The cycling of temperatures from above freezing to below and back constitutes a freeze-thaw cycle. As previously discussed, the number of freeze-thaw cycles in conventional concrete is estimated based on a fully saturated microstructure. Figure 4-8 shows the cumulative number of freeze-thaw cycles that occur in Rantoul, IL, over the observed time period when a temperature threshold of 0°C is considered. At the end of the first winter season, the number of freeze-thaw

cycles by recorded air temperatures is approximately 90. After a second winter season, the cumulative number of freeze-thaw cycles increases to approximately 180. This observed number is in agreement with Hershfield's estimated number of freeze-thaw cycles in this region of 90-100 freezing thawing cycles per year. Although only two winter seasons are considered in the scope of this study, it is important to note that there are inherent discrepancies between seasons (due to long time-scale weather phenomenon). As such, an apt result for concrete resiliency would be to average over a longer time span.

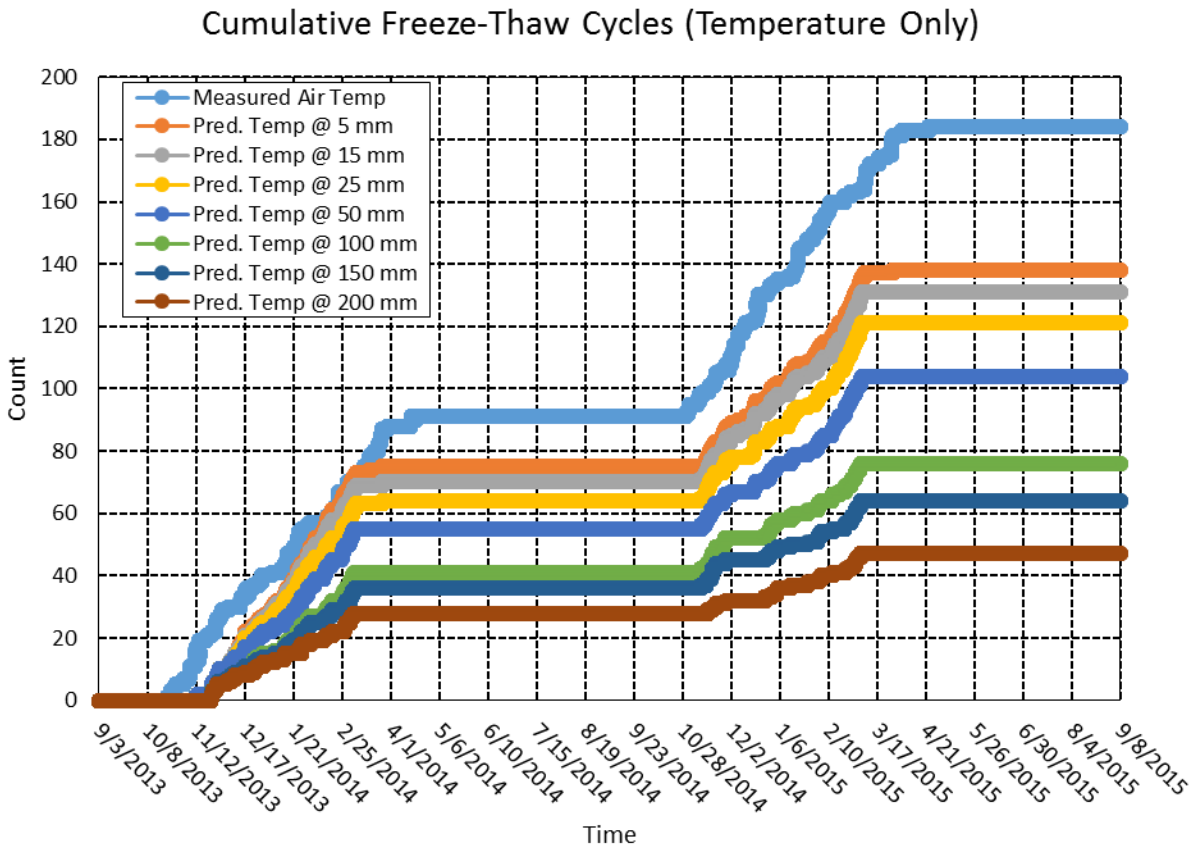

Figure 4-8 Cumulative number of freeze-thaw cycles in Rantoul, IL, from September 3, 2013, through September 8, 2015. Predicted internal temperature values are computed using a 2-layered system whose upper concrete layer is defined by a thermal conductivity, λ, value of 1.85 kcal/hmC^{o} and a thermal diffusivity, α, value of 0.0025 m^2/h. The underlying aggregate ballast layer is defined by a thermal conductivity, λ, value of 2.58 kcal/hmC^{o} and a thermal diffusivity, α, value of 0.0030 m^2/h.

In the case when the concrete (conventional or otherwise) is fully saturated, then the cumulative number of freeze-thaw cycles becomes depth-dependent as observed in the model

concrete in Figure 4-8. Near the surface (5 mm), the number of freeze-thaw cycles is significantly diminished when compared to the number of freeze-thaw cycles observed due to air temperature alone. This result is impactful as it suggests that a singular characteristic freeze-thaw number of concrete infrastructure in a given region assuming a fully saturated microstructure is insufficient to fully describe the extent of freeze-thaw cycles. At shallow depths, the number of cycles is higher than at deeper depths. Moreover, the number of freeze-thaw cycles as measured by air does not equal the number of freeze-thaw cycles at shallow depths. This is due to the heat-capacity of concrete where it can retain heat from solar radiation. As nighttime air temperatures fall in early or late winter to near or below freezing, the concrete can sufficiently retain heat such that it does not fall below freezing.

The pore size distribution of concrete microstructure can suppress the freezing point of liquid moisture contained within the fine-sized pores [Fagerlund, 1973]. As such, it is of interest to observe the impact of a reduced freezing threshold value, such as -5^{o}C (see Figure 4-9). In this graph, the criterion for a freeze-thaw event is generally diminished in both the ambient air temperature cycling and internally predicted temperature cycling. At the suppressed temperature criterion of -5^{o}C, water within larger sized capillary pores are more likely to freeze and expand while finer-sized pores may continue to remain in liquid form due to dissolved ions within the pore solution that has the effect of suppressing the freezing-point of liquid water. Calorimetric studies of pore water in cement paste have been used to observe freezing at temperatures of -8^{o}C to -40^{o}C depending upon the pore size [Bager and Sellevold, 1986; Beddoe and Setzer, 1988].

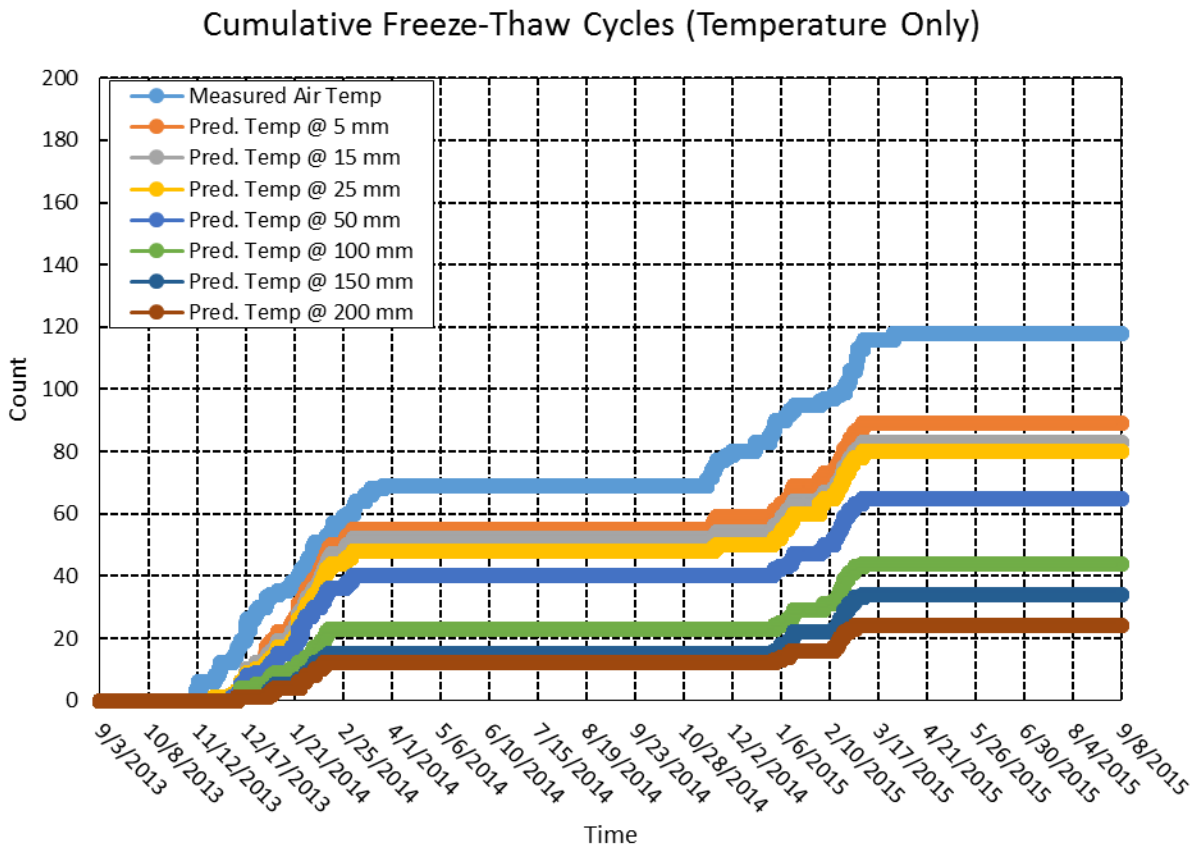

Figure 4-9 Cumulative number of freeze-thaw cycles in Rantoul, IL, from September 3, 2013, through September 8, 2015, modified with a freezing criterion threshold of -5°C. Predicted internal temperature values are computed using a 2-layered system whose upper concrete layer is defined by a thermal conductivity, λ, value of 1.85 kcal/hmC° and a thermal diffusivity, α, value of 0.0025 m^2/h. The underlying aggregate ballast layer is defined by a thermal conductivity, λ, value of 2.58 kcal/hmC° and a thermal diffusivity, α, value of 0.0030 m^2/h.

4.6.2 Validation of predictive model against experimentally measured values

The observation of the reduction of cumulative freeze-thaw cycles from predicted internal temperatures in concrete (Figure 4-8) is similarly seen in another location: Lytton, BC. Figure 4-10 shows the number of cumulative freeze-thaw cycles as predicted with the 1-dimensional model using another set of weather conditions. Moreover, a finite-width instrumented concrete crosstie installed in ballast is also shown to undergo an unequal number of freeze-thaw cycles based on the depth of the sensor. Near the surface (0.5 in), the number of cumulative freeze-thaw cycles is significantly reduced from what occurs in the ambient air temperatures. Additionally, at successively deeper depths, the number of cycles is diminished. At comparable deep depths of 200

mm or 8.5 in, the number of freeze-thaw cycles in the predictive model reaches 20 which compares favorably to the measured value of 20.

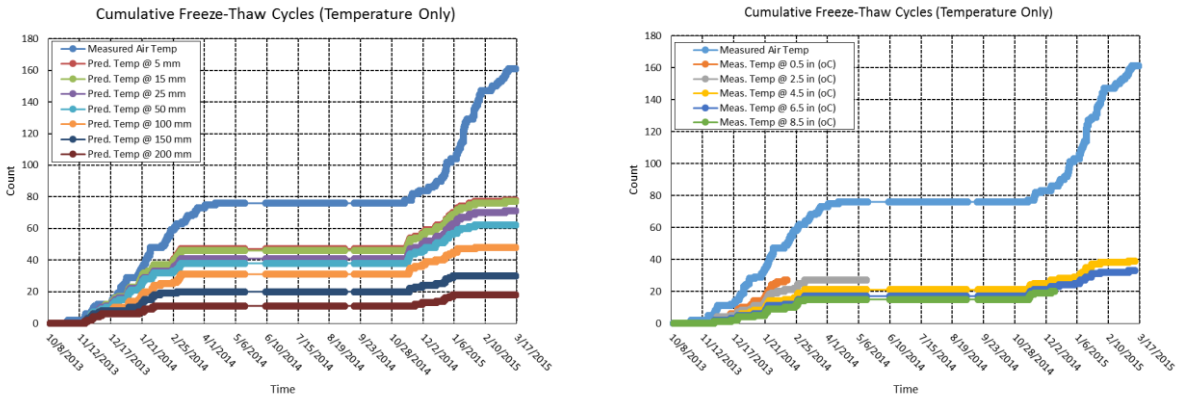

Figure 4-10 Predicted (left) and measured (right) cumulative number of freeze-thaw cycles in Lytton, BC, from October 8, 2013, through March 17, 2015. Predicted internal temperature values are computed using a 2-layered system whose upper concrete layer is defined by a thermal conductivity, λ, value of 1.85 kcal/hmC^o and a thermal diffusivity, α, value of 0.0025 m^2/h. The underlying aggregate ballast layer is defined by a thermal conductivity, λ, value of 2.58 kcal/hmC^o and a thermal diffusivity, α, value of 0.0030 m^2/h. The measured internal temperature values are from a concrete crosstie labeled CXT447USA.

4.6.3 Effect of predicted degree of saturation on number of freeze-thaw cycles

A freeze-thaw cycle can also occur when the concrete microstructure is not fully saturated. In such a case, it is possible to add a constraint which discounts a freeze-thaw occurrence if a minimum degree of saturation is not present in the microstructure. Figure 4-11 shows the cumulative number of freeze-thaw cycles in Lytton, BC, as a minimum degree of saturation constraint is added to freezing air temperatures. When any degree of saturation is valid (S > 0%), then the number of freeze-thaw cycles reverts to the same number of cycles that occur due to freezing air temperatures. In Lytton, BC, it is observed that in the first winter season, approximately 80 freeze-thaw cycles occur. At the end of the second winter, approximately 160 cumulative freezing thawing cycles have occurred. This number compares well with Fraser's reported estimate of 80 freeze-thaw cycles per year in this region of Canada.

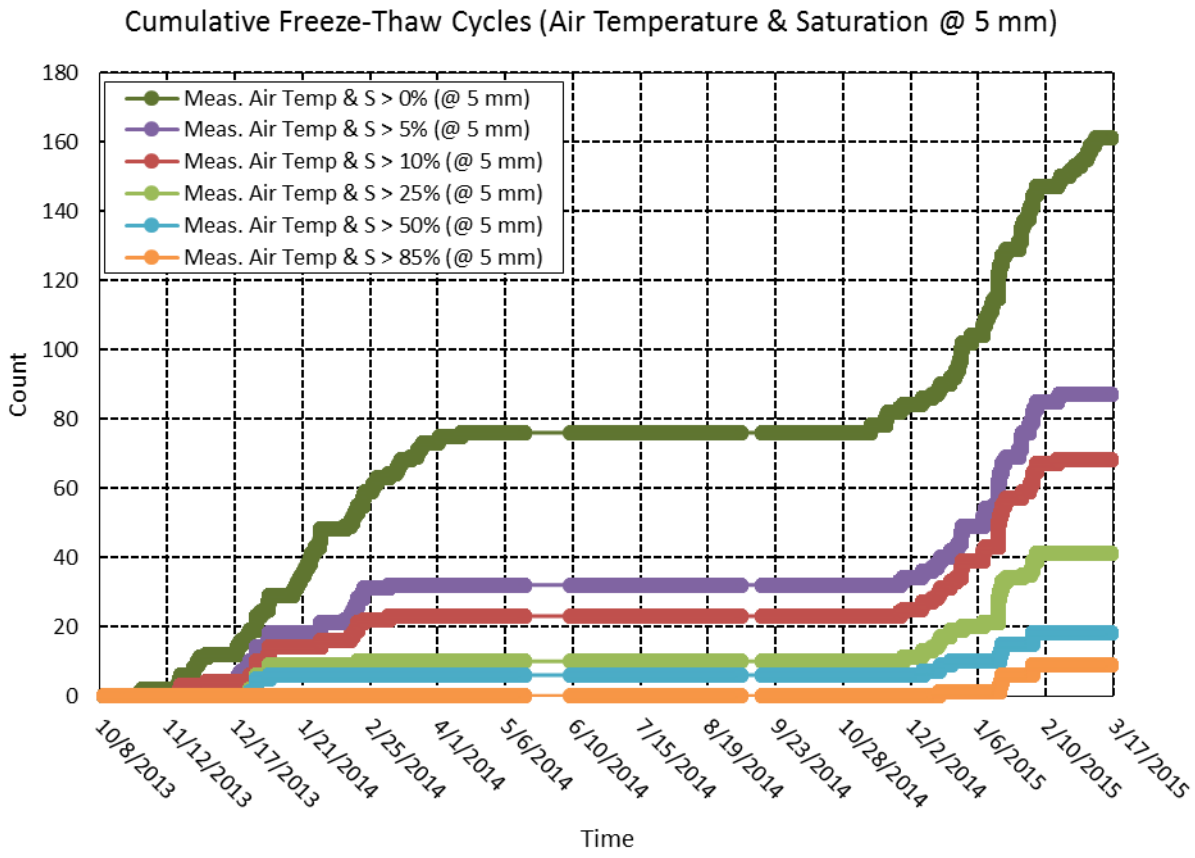

Figure 4-11 Cumulative number of freeze-thaw cycles in Lytton, BC, from October 8, 2013, through March 17, 2015, at a depth of 5 mm when both freezing air temperatures and minimum degree of saturation is achieved at time of freezing. Predicted degree of saturation is defined by a diffusivity (at S = 100%) value of 0.86×10^{-6} m^2/hr, a regression coefficient, *n*, of 15, α value of 0.05, and an empirical correlation between relative humidity and degree of saturation. The simulation is initialized with an even distribution of 85 %RH throughout the depth of the concrete.

When a minimum degree of saturation of 5% is added as a constraint, then the number of freeze-thaw cycles is appreciably diminished. As the minimum degree of saturation is increased upward to 85% (a value comparable to Li *et al.*'s reported critical degree of saturation), then the number of freeze-thaw cycles is greatly diminished. This observation is also seen in Figure 4-12 which shows the same minimum degree of saturation criteria applied to predicted internal temperatures at a shallow depth of 5 mm. If degree of saturation is considered in freeze-thaw analysis, it is observed that overall freeze-thaw cycles significantly drop in value. However, this observation does not definitively claim that the concrete is less likely to undergo freeze-thaw damage. Instead, the observation is that the correlation between 300 freeze-thaw cycles in

accelerated ASTM C666 testing of fully saturated concrete samples is not readily lendable to partially saturated high performance concrete.

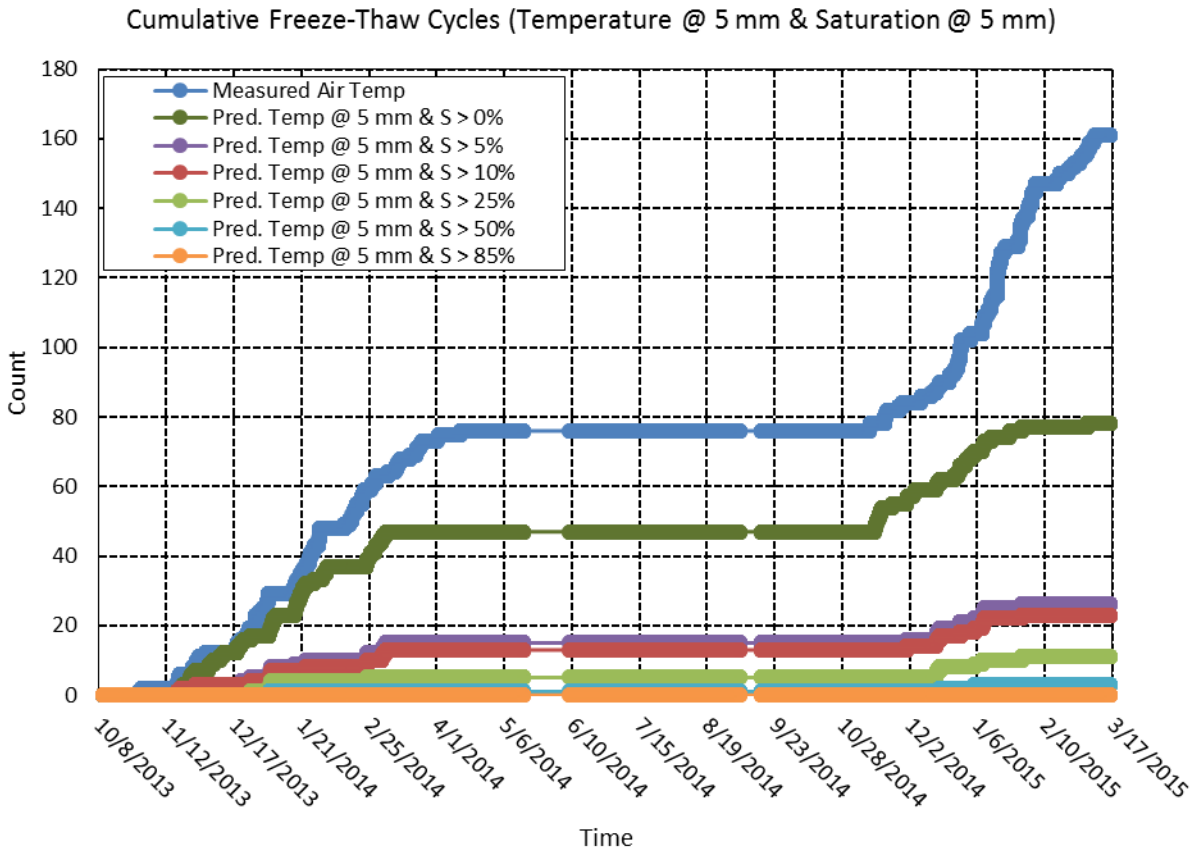

Figure 4-12 Cumulative number of freeze-thaw cycles in Lytton, BC, from October 8, 2013, through March 17, 2015, at a depth of 5 mm when both freezing temperatures and minimum degree of saturation is achieved at time of freezing. Predicted internal temperature values are computed using a 2-layered system whose upper concrete layer is defined by a thermal conductivity, λ, value of 1.85 kcal/hmC^{o} and a thermal diffusivity, α, value of 0.0025 m^2/h. The underlying aggregate ballast layer is defined by a thermal conductivity, λ, value of 2.58 kcal/hmC^{o} and a thermal diffusivity, α, value of 0.0030 m^2/h. Predicted degree of saturation is defined by a diffusivity (at S = 100%) value of 0.86×10^{-6} m^2/hr, a regression coefficient, n, of 15, α value of 0.05, and an empirical correlation between relative humidity and degree of saturation. The simulation is initialized with an even distribution of 85 %RH throughout the depth of the concrete.

Moreover, it is known that high performance concrete exhibits freeze-thaw like damage; however, it is possible that the underlying mechanism causing the damage is changed. In fully saturated conventional concrete, for example, the repetitive cycling between freezing and thawing temperatures induces large hydraulic pressures. In high performance concrete, the dis-connected pore structure and lack of capillary pores leads to very little overall moisture carrying capacity.

With a higher water-to-cement ratio, any appreciable increase in hydraulic stress due to a minimal amount of freezing water can be sustained against the high strength ceramic. It is possible, instead, that sustained freezing temperatures (as opposed to cyclic freezing and thawing) can be a significant driving force for freeze-thaw damage. In any case, the modeling result of Figures 4-11 and 4-12 suggests that there is a significant decrease in the number of freeze-thaw cycles when degree of saturation is additionally added as a constraint.

4.6.4 Reduction of freeze-thaw cycles due to rate of freezing criteria

Another point of consideration is that ASTM C666 is an accelerated testing regiment with high freezing rates of fully saturated concrete prisms. Figures 4-13 and 4-14 shows the cumulative number of freeze-thaw cycles of model concrete when air temperature and predicted internal temperature at a shallow depth of 5 mm are additionally constrained with increasing temperature freezing rates. This constraint demonstrates that fast freezing rates do not often occur in typical weather environments and do reduce the number of freeze-thaw cycles. However, it is not likely that an artificially fast freezing rate in an accelerated testing regiment should necessarily be representative of actual environmental freezing conditions nor does it demonstrably suggest that a large number of freeze-thaw cycles should be discounted.

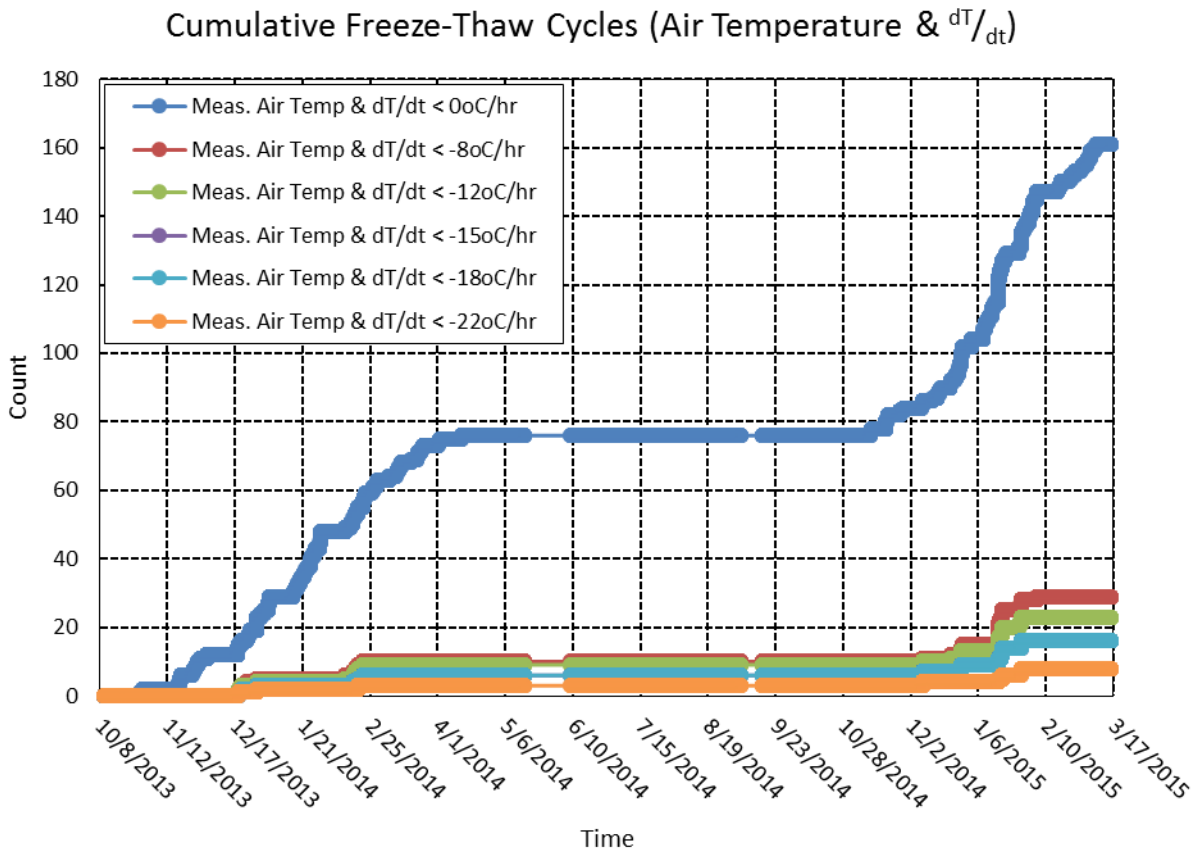

Figure 4-13 Cumulative number of freeze-thaw cycles in Lytton, BC, from October 8, 2013, through March 17, 2015, when both freezing air temperatures and minimum rate of freezing is achieved at time of freezing.

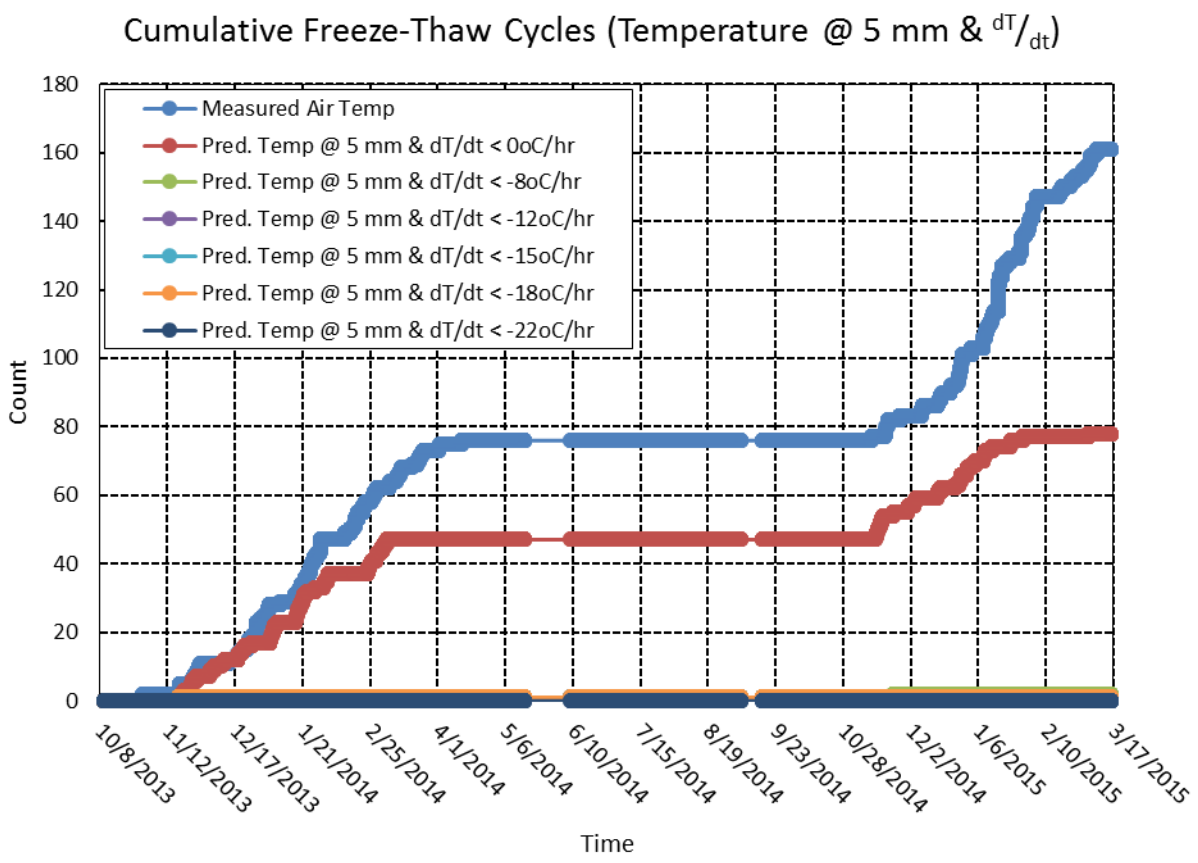

Figure 4-14 Cumulative number of freeze-thaw cycles in Rantoul, IL, from September 3, 2013, through September 8, 2015, when both freezing temperatures at a depth of 5 mm and minimum rate of freezing is achieved at time of freezing. Predicted internal temperature values are computed using a 2-layered system whose upper concrete layer is defined by a thermal conductivity, λ, value of 1.85 kcal/hmC^o and a thermal diffusivity, α, value of 0.0025 m^2/h. The underlying aggregate ballast layer is defined by a thermal conductivity, λ, value of 2.58 kcal/hmC^o and a thermal diffusivity, α, value of 0.0030 m^2/h.

Additionally, the occurrence of freeze-thaw cycles can be summarized with the mean, median, and mode. Table 4-4 shows statistically relevant values of the freezing rate when time intervals between successively measured temperature values is greater than 15 minutes. Table 4-5 similarly shows the relevant values of the freezing rate when time intervals between successively measured temperature values is greater than 60 minutes. When a successive time interval is 1 minute or less, then a change of temperature of 1^{o}C can result in a maximum freezing rate of 60^{o}C/hr. Alternatively, limiting the observed freezing rates to time intervals of 60 minutes (see Table 4-5) results in a maximum freezing rate of 3^{o}C/hr. While the maximum freezing rate can yield unfavorable freeze-thaw damage in hardened concrete, the mean freeze rate is 1.36^{o}C/hr as

shown in Table 4-4 and 0.94°C/hr as shown in Table 4-5. The mean freeze rate can increase upwards to 5.07°C/hr when a 1-minute time interval between measured temperature values is considered. In any of these cases, the average freezing rate is significantly less than the freezing rate of 8.8°C/hr to 22°C/hr as stipulated in ASTM C666. Moreover, the realistic maximum freezing rate of 2-3°C/hr observed in a 60-minute time interval is comparable to that seen in concrete pavement studies.

Table 4-4 Mean, median, and mode of freezing rates in Lytton, BC, from October 8, 2013, through March 17, 2015. Instances of freeze rate are as large as 8°C/hr because of observed 2°C change in the span of a 15-minute time interval.

Mean Freeze (-) Rate (°C/hr)	Std. Dev. Freeze (-) Rate (°C/hr)	Mode Freeze (-) Rate (°C/hr)	Median Freeze (-) Rate (°C/hr)	Min Freeze (-) Rate (°C/hr)	Max Freeze (-) Rate (°C/hr)
1.36	0.76	1.00	1.00	0.01	8.00

Table 4-5 Mean, median, and mode of freezing rates in Lytton, BC, from October 8, 2013, through March 17, 2015. Instances of freeze rate are as large as 3°C/hr because of observed 3°C change in the span of a 60-minute time interval.

Mean Freeze (-) Rate (°C/hr)	Std. Dev. Freeze (-) Rate (°C/hr)	Mode Freeze (-) Rate (°C/hr)	Median Freeze (-) Rate (°C/hr)	Min Freeze (-) Rate (°C/hr)	Max Freeze (-) Rate (°C/hr)
0.94	0.56	0.50	1.00	0.01	3.00

4.6.5 Effect of water-to-cement ratio on number of freeze-thaw cycles in concrete

A diffusion coefficient of $D_o = 0.86 \times 10^{-6}$ m^2/hr is representative of a low water-to-cement ratio of approximately 0.30 by mass. When concrete is subjected to micro- and macro-scale cracking, then external water can more easily permeate into the interior of the structure. As such, the diffusivity can increase steadily over time. Alternatively, the initial concrete mixture design can be made with a conventional water-to-cement ratio of approximately 0.35 to 0.45 by mass. In order to observe the effect of changing water-to-cement ratio and extent of cracking, the diffusion coefficient can be changed in the model. Figure 4-15 shows the saturation history of model concrete in Lytton, BC, when the diffusion coefficient is increased by 50% its original value to 1.29×10^{-6} m^2/hr. When compared against Figure 4-7, it is observed that saturation peaks are slightly increased in magnitude. This results in a minimal change in the number of cumulative

freeze-thaw cycles as shown in Figure 4-16. It is expected that as the diffusion coefficient increases in value, the number of freeze-thaw cycles increases until it reaches the maximum boundary limit that is equal to the number of freeze-thaw cycles due to air temperature fluctuations alone.

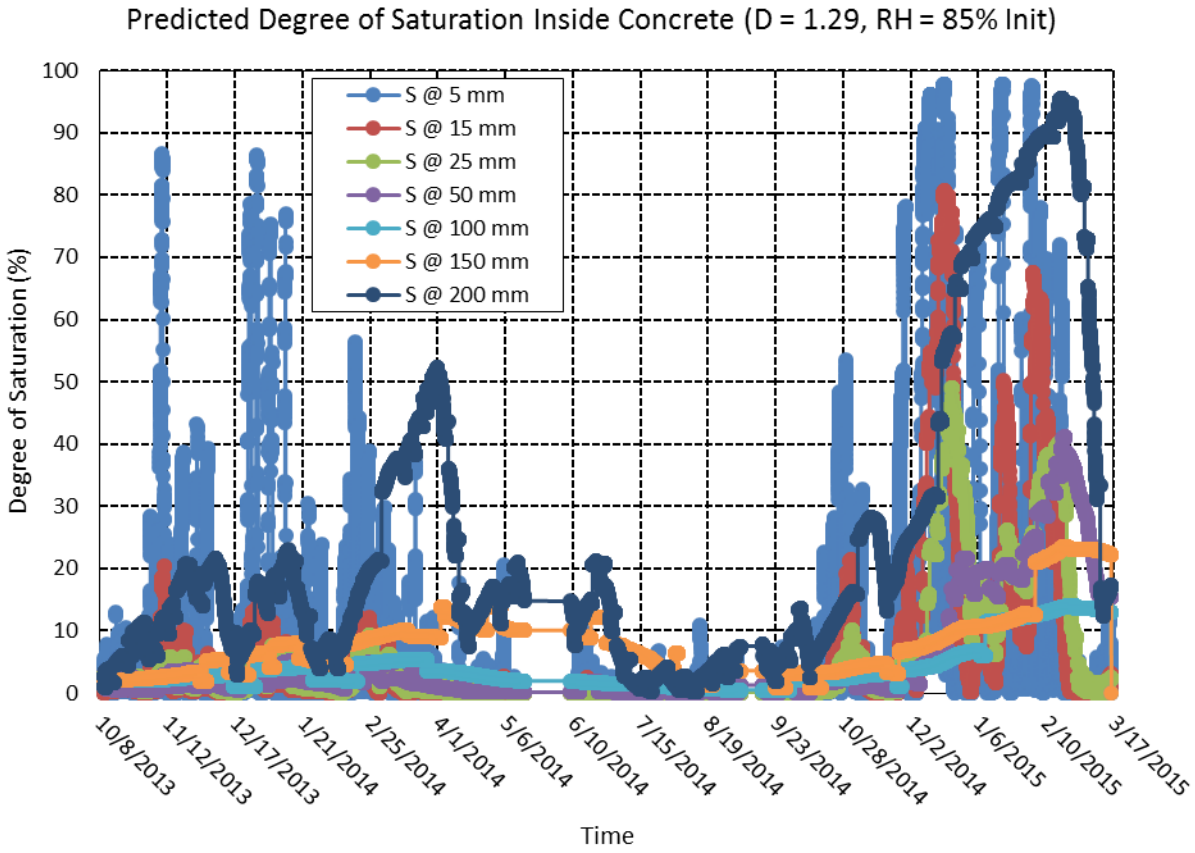

Figure 4-15 Predicted degree of saturation inside a 1-layered concrete system in Lytton, BC, from October 8, 2013, through March 17, 2015. The concrete is defined by a diffusivity (at S = 100%) value of 1.29×10^{-6} m^2/hr, a regression coefficient, *n*, of 15, α value of 0.05, and an empirical correlation between relative humidity and degree of saturation. The simulation is initialized with an even distribution of 85 %RH throughout the depth of the concrete.

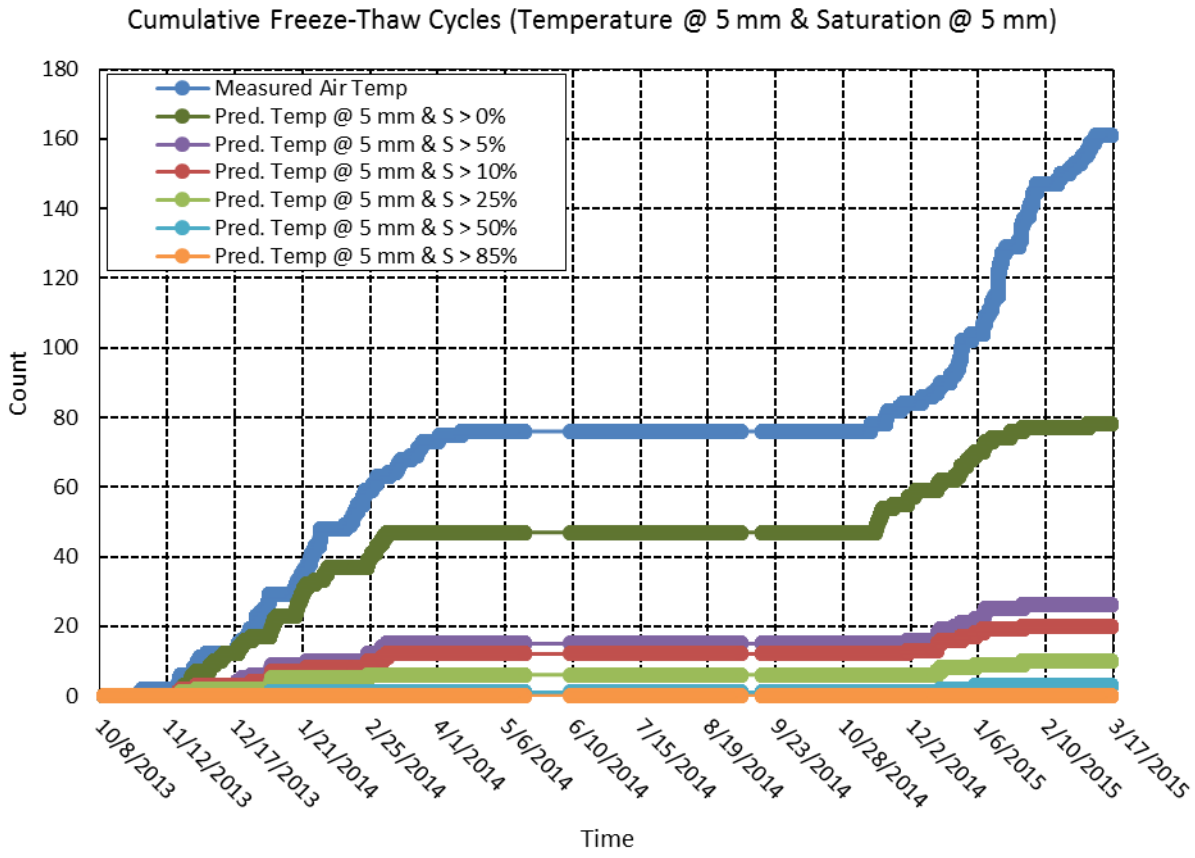

Figure 4-16 Cumulative number of freeze-thaw cycles in Lytton, BC, from October 8, 2013, through March 17, 2015, at a depth of 5 mm when both freezing temperatures and minimum degree of saturation is achieved at time of freezing. Predicted internal temperature values are computed using a 2-layered system whose upper concrete layer is defined by a thermal conductivity, λ, value of 1.85 kcal/hmC^{o} and a thermal diffusivity, α, value of 0.0025 m^2/h. The underlying aggregate ballast layer is defined by a thermal conductivity, λ, value of 2.58 kcal/hmC^{o} and a thermal diffusivity, α, value of 0.0030 m^2/h. Predicted degree of saturation is defined by a diffusivity (at S = 100%) value of 1.29×10^{-6} m^2/hr, a regression coefficient, *n*, of 15, α value of 0.05, and an empirical correlation between relative humidity and degree of saturation. The simulation is initialized with an even distribution of 85 %RH throughout the depth of the concrete.

4.6.6 Recommendations for practitioner design

The simple 1-dimensional model for temperature can be simplified by instead comparing the cumulative number of freeze-thaw cycles that occur in ambient air conditions and estimating an empirical relationship to the number of freeze-thaw cycles that occur within the concrete crosstie. Figures 4-17 and 4-18 show the cumulative number of freeze-thaw cycles of ambient air temperatures if the freezing point criterion is suppressed from 0^{o}C to -1, -2, -3, -4, and -5^{o}C. At each suppressed value, the cumulative curve is diminished. When compared to the predicted

cumulative freeze-thaw cycles in concrete at the near surface (i.e. 5 mm), it is observed that the curve is comparable to ambient freeze-thaw cycles that are suppressed to the freezing point threshold of -2 to -3°C. As a recommendation, it is possible to refer to Hershfield's and Fraser's historical data sets and revise the number of freeze-thaw cycles to a freezing point criterion of -2°C in order to approximately predict the number of freeze-thaw cycles occurring at the surface of the concrete crosstie at a freezing point threshold of 0°C.

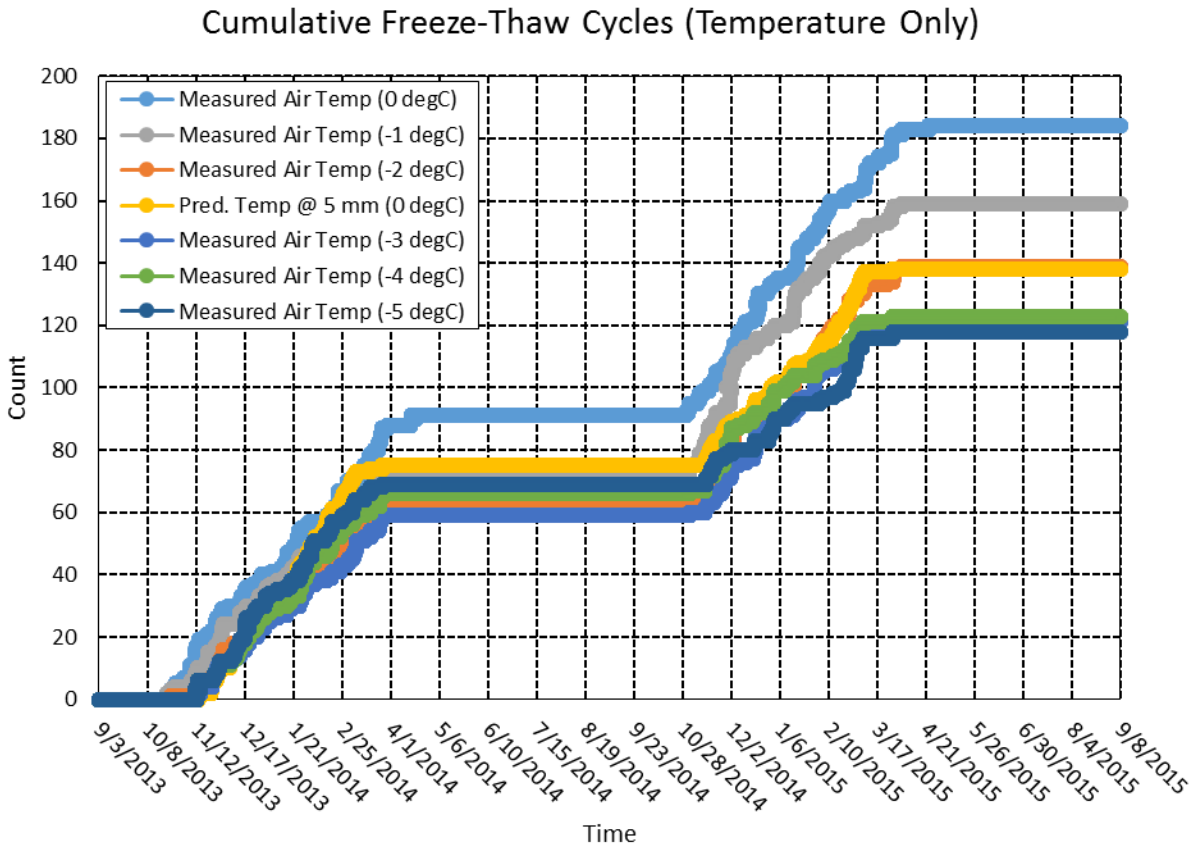

Figure 4-17 Cumulative number of freeze-thaw cycles in Rantoul, IL, from September 3, 2013, through September 8, 2015, using variable temperatures (0°C to -5°C) as the freezing point threshold of ambient air. The cumulative number of freeze-thaw cycles predicted at a shallow depth of 5 mm using 0°C as a freezing point threshold is also shown. Predicted internal temperature values are computed using a 2-layered system whose upper concrete layer is defined by a thermal conductivity, λ, value of 1.85 kcal/hmC° and a thermal diffusivity, α, value of 0.0025 m^2/h. The underlying aggregate ballast layer is defined by a thermal conductivity, λ, value of 2.58 kcal/hmC° and a thermal diffusivity, α, value of 0.0030 m^2/h.

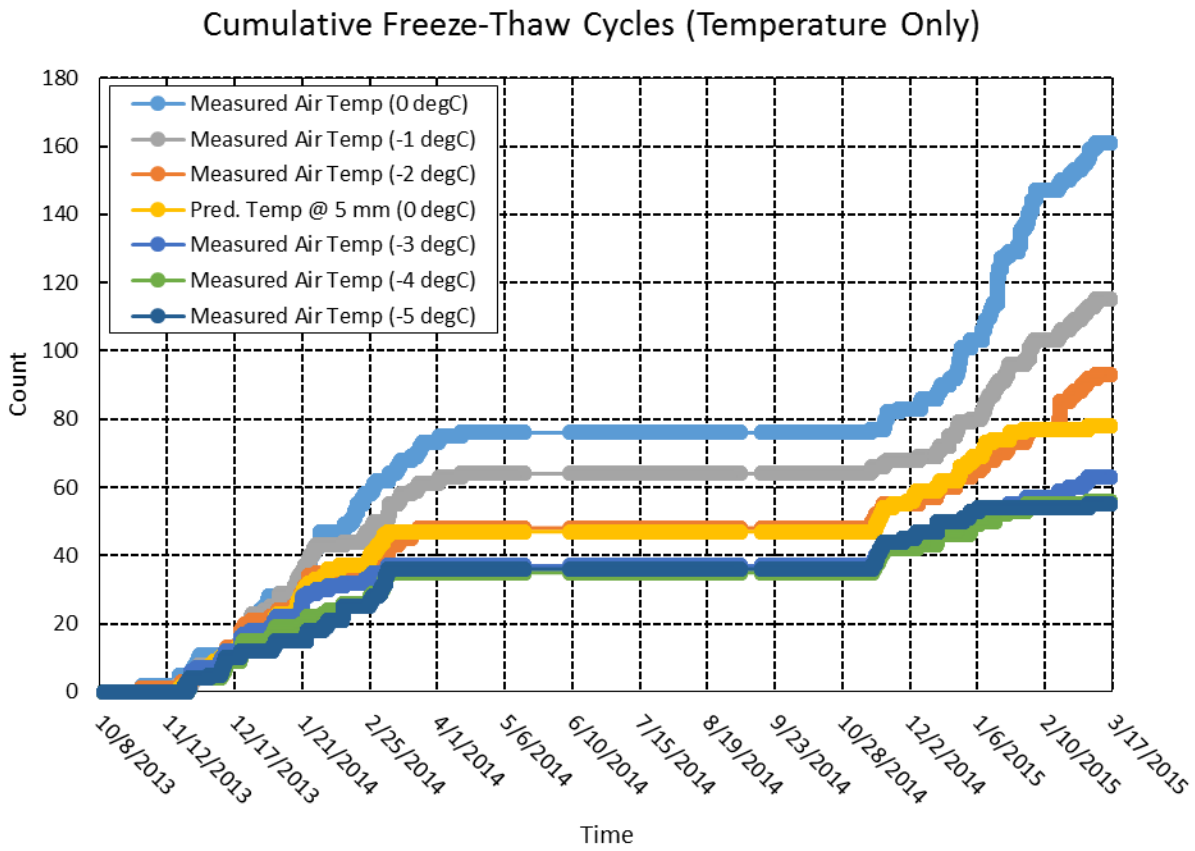

Figure 4-18 Cumulative number of freeze-thaw cycles in Lytton, BC, from October 8, 2013, through March 17, 2015, using variable temperatures (0°C to -5°C) as the freezing point threshold of ambient air. The cumulative number of freeze-thaw cycles predicted at a shallow depth of 5 mm using 0°C as a freezing point threshold is also shown. Predicted internal temperature values are computed using a 2-layered system whose upper concrete layer is defined by a thermal conductivity, λ, value of 1.85 kcal/hmC° and a thermal diffusivity, α, value of 0.0025 m^2/h. The underlying aggregate ballast layer is defined by a thermal conductivity, λ, value of 2.58 kcal/hmC° and a thermal diffusivity, α, value of 0.0030 m^2/h.

An estimation of the number of freeze-thaw cycles at the surface, $FT_{surface}$, based on ambient air conditions can then be compared against the changing number of freeze-thaw cycles that occurs within the bulk of the material as a function of depth, d (mm), to yield

$$FT(d) = FT_{surface}e^{-\varphi d} \qquad \text{Equation 4-9}$$

where φ is a form-fitting factor ranging from 0.005 to 0.007 as suggested by the data in Figure 4-19. There is a good fit with R^2 values of 0.99 and 0.97 suggesting that this simple empirical

correlation between ambient air temperatures can be used to approximately predict the number of freeze-thaw cycles at any given depth within the concrete material.

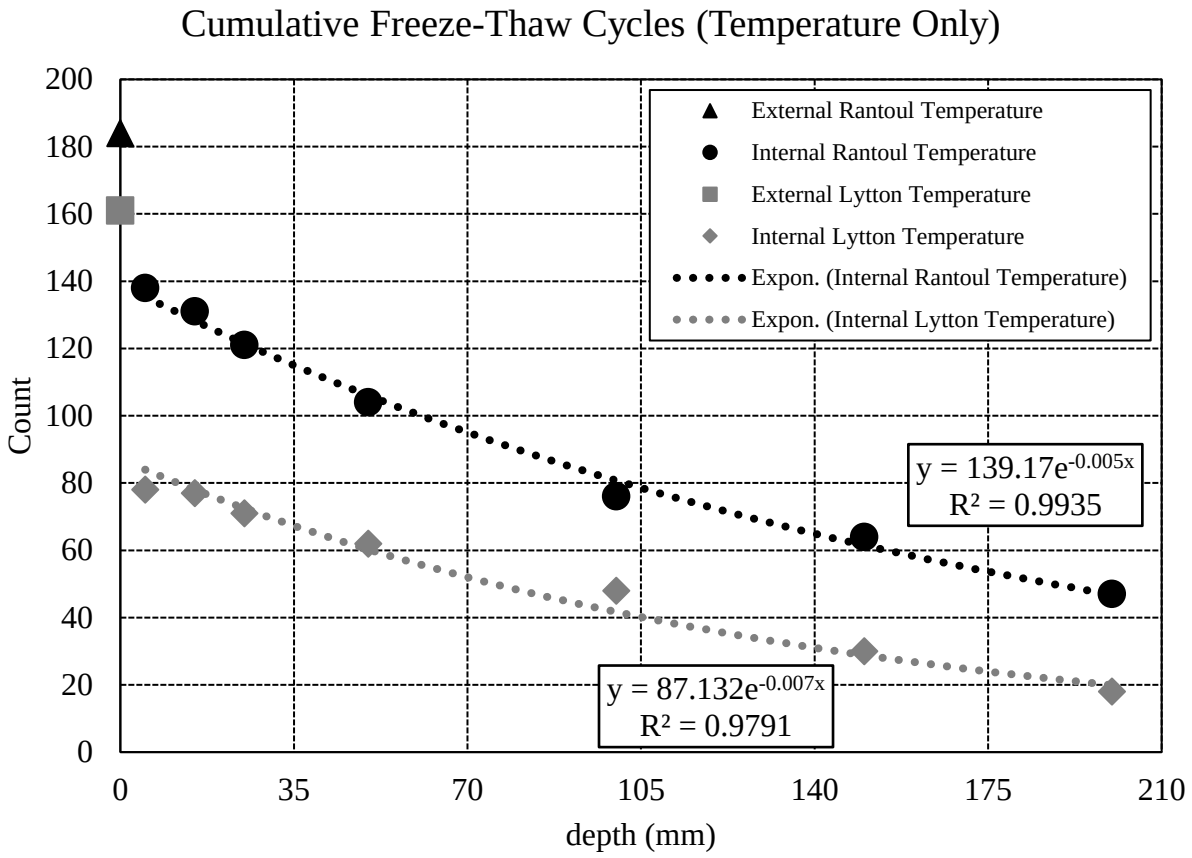

Figure 4-19 Decay of modeled number of cumulative number of freeze-thaw cycles as a function of depth for both Rantoul, IL, and Lytton, BC.

4.7 Summary of Chapter

High performance concrete crossties may be subjected to freeze-thaw climates where recorded air temperatures fluctuate from above freezing to below freezing particularly during winter months. Freezing temperatures represent potential for damage only when there is high degree of saturation in the concrete material. By observing the change in constraints to monitor the cumulative number of freeze thaw cycles in Rantoul, IL, and Lytton, BC, it is found that:

- Freeze-thaw cycling of air temperature alone does not well characterize the extent of internal freeze-thaw cycling of internally predicted temperatures of a 1-dimensional model concrete system.

- The number of freeze-thaw cycles in model high performance concrete can be discounted when an insufficient amount of moisture is present in the microstructure. It is also seen that the number of instances in which the degree of saturation inside concrete exceeding 85% is predicted to be less than previously thought, but significant corroboration of this model is needed with experimental data.
- A simple correlation between the number of freeze-thaw cycles in ambient air and concrete surface can be established if the freezing point criterion for ambient air is suppressed to -2 to -3^{o}C. Additionally, an exponentially decaying fit can predict the number of freeze-thaw cycles within the bulk of the material if the number of freeze-thaw cycles at the surface is known or estimated.

In general, this modeling study demonstrates that the correlation between the potential extent of damage due to freeze-thaw cycling and the results of ASTM C666 is not well understood for high performance concrete where the microstructure is not fully saturated. It would be beneficial to better understand the mechanism that drives freeze-thaw damage in high performance concrete as it may be belied by another factor such as extent of freezing time duration.

4.8 References

ASTM Standard C666, 2003 (2008), Standard Test Method for Resistance of Concrete to Rapid Freezing and Thawing," ASTM International, West Conshohocken, PA.

Bager, D. H., and Sellevold, E. J. "Ice formation in hardened cement paste, Part I – room temperature cured pastes with variable moisture contents." *Cement and Concrete Research* 16 (1986): 709 – 720.

Bažant, Z., and Najjar, L. "Nonlinear water diffusion in nonsaturated concrete." *Materials and Structures* 5 (1972): 3 – 20.

Beddoe, R. E., and Setzer, M. J. "A low-temperature DSC investigation of hardened cement paste subjected to chloride action." *Cement and Concrete Research* 18 (1988): 249 – 256.

Fagerlund, G. "Determination of pore-size distribution from freezing-point depression." *Matériux et Constructions* 33 (1973): 215 – 225.

Fraser, J. K. "Freeze-thaw frequencies and mechanical weathering in Canada." *ARCTIC North America* 12 (1959).

Hershfield, D. M. "The frequency of freeze-thaw cycles." *Journal of Applied Meteorology* 13 (1974): 348 – 354.

Kang, S-T, Kim, J-S, Lee, Y., Park, Y-D, and Kim, J-K. "Moisture diffusivity of early age concrete considering temperature and porosity." *KSCE Journal of Civil Engineering* 16 (2012): 179 – 188.

Leech, C., Lockington, D., and Dux, P. "Unsaturated diffusivity functions for concrete derived for concrete derived from NMR images." *Materials and Structures* 36 (2003): 413 – 418.

Li, W., Pour-Ghaz, M., Castro, J., and Weiss, J. "Water absorption and critical degree of saturation relating to freeze-thaw damage in concrete pavement joints." *Journal of Materials in Civil Engineering* 24 (2012): 299 – 307.

Mehta, P. K, and Monteiro, P. J. M. *Concrete: Microstructure, Properties, and Materials 3rd Edition*. 2006, New York: McGraw-Hill Companies, Inc.

Qin, Y., and Hiller, J. E. "Simulating moisture distribution within concrete pavement slabs: model development and sensitivity study." *Materials and Structures* 47 (2014): 351 – 365.

Wang, D., and Roesler, J. R. "One-dimensional temperature profile prediction in multi-layered rigid pavement systems using a separation of variables method." *International Journal of Pavement Engineering* 15 (2014): 373 – 382.

CHAPTER 5 – EFFECT OF AGGREGATE VOLUME FRACTION AND CONSOLIDATING VIBRATION ON RHEOLOGY OF PORTLAND CEMENT-BASED MATERIALS AND SURROGATE MATERIALS

5.1 Acknowledgment

The development of this chapter is accomplished with extensive rheological testing of fresh Portland cement-based concrete, mortar, and paste materials in addition to surrogate fluids in both the Newmark Civil Engineering Laboratory and the Mechanical Engineering Laboratory. This work produced approximately 10 tons of fresh concrete for testing. For this laborious work that cannot have been accomplished by the author alone, I am immensely grateful to undergraduate students Clare Curtin, Mark Keller, and Kevin Marks; concrete lab manager Jamar Brown; and Professor Randy Ewoldt and graduate student Jeremy Koch.

5.2 Abstract

Fresh Portland cement- based concrete is vibrated in order to achieve good consolidation and compaction around the internal steel reinforcement and to achieve a high-quality surface finish. Fresh concrete, however, behaves as a flowable fluid and external vibration inherently leads to the downward movement of dense aggregates (segregation) and upward movement of entrapped and entrained air bubbles (air-loss). It is desirable to retain a homogenous distribution of aggregates and entrained air voids in hardened concrete in order to enhance the long-term durability of the structural member, in particular against repetitive freeze-thaw cycling damage in wet, wintry environments. As such, it is necessary to expand the concrete community's understanding of the consolidation of concrete (as codified in ACI 309) as it directly relates to the retention of chemically entrained air bubbles. In this study, air content of fresh concrete is studied as the rheology, aggregate volume fraction, and extent of consolidating vibration are changed. It is confirmed that the granularity of concrete and dosage of superplasticizing chemical admixtures strongly affect the rheology of the fresh mixture. It is newly found, however, that the granular nature of fresh concrete under vibration strongly contributes to the loss of entrained air bubbles for mixture types of comparable rheology. This result suggests that a singularly measured set of

rheological parameters of any concrete at rest is not the appropriate set of rheological parameters suitable to describe the flow of fresh concrete under external vibration.

5.3 Introduction and Background

Fresh concrete is vibrated in order to drive out entrapped air and to minimize void-defects (honeycombing, bug-holds, pockets, e.g.) around the reinforcement and form walls. ACI Committee 309 (reports 309.1 and 309.8) provide guidance to practitioners about consolidation methods for concrete. The technical report discusses vibration with regards to optimal final strength and density, but it contains relatively little information about the effects of time of vibration, mold geometry, material proportioning, and retention of chemically entrained air bubbles. As such, quality control of entrained air can be challenging for concrete mixtures that undergo extensive vibration during mixing, transportation, handling, placement, and final consolidation. In this study, Portland cement-based materials and surrogate fluids are used to investigate the change in rheology as affected by aggregate volume content and extent of external vibration on the movement and loss of air content.

5.3.1 Rheology of fluids and Portland cement concrete

Concrete in its fresh state flows and is deformable like a fluid. Fluids can be characterized in a number of different ways. A Newtonian fluid, for example, readily flows at a rate that is directly proportional to the rate at which an external shearing force acts upon it. This proportionality is termed *viscosity*, η, and it is a constant value that is independent of the magnitude of the shearing force. Some fluids do not readily flow at very low shearing rates, however. These fluids require an external shearing force of some appreciable magnitude before they flow. This minimum shearing is called the *yield stress*, σ_y, and is a defining characteristic of the Bingham fluid (plastic) model. After a stress larger than the yield stress is applied the material flows at a rate that is a ratio of the applied shearing stress with respect to the shearing strain rate, $\dot{\gamma}$. At low shearing strain rates, this flow or *apparent viscosity*, η_{app}, is very large while at large shearing strain rates, this apparent viscosity asymptotes to the *plastic viscosity*, μ_p. The plastic viscosity is the apparent viscosity observed at appreciably large shearing strain rates. The description of stress in a Bingham fluid, with a yield stress and plastic viscosity, is typified by

$$\sigma = \sigma_y + \mu_p \dot{\gamma}. \qquad \text{Equation 5-1}$$

The flow-response of a fluid may also be non-linear. In the case when a greater shearing force is required at larger strain rates, the fluid is said to be *shear thickening*. Alternatively, when lesser shearing force is required at larger strain rates, the fluid is said to be *shear thinning*. There exist other models that can characterize these altered behaviors (Herschel-Bulkley, Power Law, e.g.), but the Bingham characterization with a yield stress intercept and plastic viscosity is commonly used for concrete.

The rheology of any fluid can be experimentally measured in a number of different ways. In the case of concrete, the utilization of conventional rheometers like coaxial cylinders or spindles would necessitate sample volumes of 2.5 m^3 in order to adequately characterize the behavior of the fresh flowing fluid [Tattersall and Banfill, 1983]. However, heterogeneous materials like concrete are susceptible to experimental challenges such as slip-flow problems at the interface of the fluid and the rotating device; therefore, vane rheometers have an important advantage in measuring concrete rheology [Liddell and Boger, 1996]. Moreover, the utilization of a vane rheometer induces localized yielding along a "cylindrical surface circumscribed by the vane" that can be theoretically predicted [Laskar and Bhattacharjee, 2011]. The ICAR rheometer was developed by the International Center for Aggregate Research (ICAR) at the University of Texas at Austin in order to better characterize the rheological properties of concrete with a slump larger than 4 inches and self-consolidating concrete [Koehler *et al.*, 2006]. The rheometer is based on the vane geometry which has been observed to greatly reduce the wall-slip effect [Barnes and Nguyen, 2001].

5.3.2 Fluid mechanics of moving spheres within a suspending fluid

The flow of a spherical object immersed entirely within a fluid of constant viscosity can be predicted by elementary fluid mechanics. The upward (or downward) force, F_b, acting on a spherical particle can be described by

$$F_b = \frac{4}{3}\pi r^3 \left(\rho_{sphere} - \rho_{fluid}\right) g \qquad \text{Equation 5-2}$$

where r is the radius of the spherical particle; ρ_{sphere} is the density of the spherical particle; ρ_{fluid} is the density of the suspending fluid; and g is the downward acceleration of gravity. An illustration of an upward moving spherical particle is shown in Figure 5-1. In the case when the difference between the densities of the spherical particle and fluid is negative, then expression yields a positive result, meaning that the buoyant force, F_b, is acting to move the spherical particle upward. Alternatively, in the case when the difference between densities is negative, then F_b acts downwards and the spherical particle moves downward.

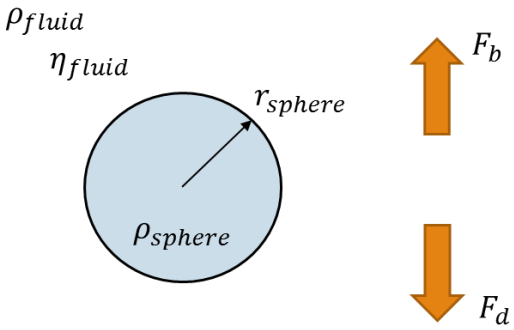

Figure 5-1 Illustration of spherical particle moving upward when wholly suspended in a fluid.

As a spherical particle moves upward or downward in a suspending fluid, it is subject to an arresting drag force which is described by

$$F_d = 6\pi\eta_{fluid} r_{sphere} v \qquad \text{Equation 5-3}$$

where η_{fluid} is the constant viscosity of the suspending fluid and v is the velocity of the spherical particle. Equations 5-2 and 5-3 can be combined to solve for the steady-state, terminal velocity, v, of a spherical particle resulting in Stokes' Law

$$v = \frac{2}{9\eta_{fluid}} r_{sphere}{}^2 g\left(\rho_{sphere} - \rho_{fluid}\right). \qquad \text{Equation 5-4}$$

Equation 5-4 is only valid under laminar flow where the calculated Reynold's number, *Re*, must abide by the constraint

$$Re = \frac{2\rho_{fluid} v r_{sphere}}{\eta_{fluid}} \ll 1. \qquad \text{Equation 5-5}$$

If the *Re* fails the criterion given in Equation 5-5, then the flow of the moving particle is subject to non-symmetric, turbulent conditions, and another equation describing turbulent flow and drag must be employed.

5.3.3 Rheology of Portland cement concrete as affected by aggregate volume fraction

The flow of concrete is altered by its granular nature as it is a Bingham fluid (cement paste) with sand and gravel particles. The interaction between the particles increases the shearing force required to sustain steady flow. As such, the yield stress and plastic viscosity of concrete are modified as the volume of aggregates (and their shape and size distribution) are modified. The Modified Krieger-Dougherty equation predicts the viscosity of the fluid based on the volume fraction, Φ, of the suspension fluid, the maximum concentration of particles, Φ_M, and the underlying viscosity of the suspension fluid, $\eta_{suspension}$ [Struble and Sun, 1993]. The Modified Krieger-Dougherty relationship is expressed as

$$\frac{\eta}{\eta_{suspension}} = \left(1 - \frac{\Phi}{\Phi_M}\right)^{-k\Phi_M} \qquad \text{Equation 5-6}$$

where *k* is a factor that depends on particle shape and applied shear stress. For spherical aggregates, the value is assumed to be 2.5. The maximum concentration of particles is dependent on both particle size distribution and applied shear stress. For spherical aggregates, the value is assumed between 0.6 and 0.7. Other models have been similarly developed to predict the apparent viscosity as affected by an increasing volume content of inclusionary particles [Mooney, 1951; Roscoe, 1952; Krieger and Dougherty, 1959; Dabak and Yucel, 1986; Chong *et al.*, 1994; and Liu, 2000].

The yield stress is similarly affected by the interaction of particles. The Chateau-Ovarlez-Trung model empirically predicts the yield stress as

$$\frac{\sigma_y(\Phi)}{\sigma_y(\Phi=0)} = \sqrt{(1-\Phi)\left(1 - \frac{\Phi}{\Phi_M}\right)^{-2.5\Phi_M}} \qquad \text{Equation 5-7}$$

where $\Phi_M$is 0.56 for monodisperse spherical particles [Mahaut *et al.*, 2008].

5.3.4 Rheology of Portland cement concrete as affected by chemical admixtures

In addition to aggregates, the use of chemical admixtures (superplasticizers, viscosity modifying agents, e.g.) affects the rheology of concrete [Mikanovic and Jolicouer, 2008; Papo and Piani, 2004]. It is often observed that the inclusion of viscosity modifying admixtures in SCC mixes can alter the linear Bingham behavior of the concrete to that of a non-linear Herschel-Bulkely behavior as described by

$$\tau = \tau_o + A\dot{\gamma}^B \qquad \text{Equation 5-8}$$

where *A* and *B* fitted parameters. There also exist other models to describe non-linear rheological behavior including the Roberson-Stiff, Modified Bingham, Casson, De Kee, Yahia and Khayat [Banfill, 2003], Power-law, Sisko, Eyring, and VomBerg [Vikan *et al.*, 2007]. With regard to the type and dosage of chemical admixtures like superplasticizers, the rheology of SCC [Mikanovic and Jolicoeur, 2008] and OPC [Papo and Piani, 2004] can be strongly affected.

5.3.5 Rheology of Portland cement concrete as affected by external vibration

Vibration of concrete is achieved by the use of internal vibrators (immersions, submersible, spud, or poker) and external vibrators (form, table, surface) [Popovics, 1973]. When vibrated strongly, the shearing contact between aggregates is temporarily alleviated allowing for consolidation under gravitational forces [L'Hermite, 1955]. This loss of aggregate-to-aggregate contact leads to a reduction in the yield stress and a reduction in the plastic viscosity. Past research has divided this process into two stages where the first stage of continuous vibration leads to vertical segregation of the aggregates and can be treated similarly to the packing of granular materials [Farouki and Winterkon, 1964]. The second stage results in a dense fluid where vibration waves propagate more efficiently and principally targets the air [Saul, 1958]. When vibration is underway, the traveling compression waves travel more efficiently through water as opposed to cement or aggregate particles which leads to an increase in the hydrostatic pressure [Popovics, 1973]. This loss of hydrostatic pressure results in aggregate-to-aggregate frictional forces being overcome which minimizes distances between aggregate particles, particularly if they are highly angular. At the conclusion of vibration, friction between aggregate particles is re-established.

The first stage of vibration strongly reduces the measured yield stress due to the reduction of aggregate contact. The reduction of the yield stress can be so much that the Bingham fluid can transform to a Power-law fluid [Tattersall and Baker, 1988], that is to say the magnitude of the yield stress is entirely removed and the fresh concrete readily flows. It is this vibration effect that allows for aggregates and entrained air that are at rest to settle downward and float upward, respectively. Ongoing hydration during the transport of highly flowable concrete can stiffen the mix (slump loss) sufficiently resulting in the retention of entrained air [Ghafoori and Barfield, 2010]. However, this retention of entrained air is not always seen in manufacturing processes, particularly if extensive vibration follows final placement.

5.4 Significance of Research

Fresh concrete is vibrated in order optimize strength and density; however, little attention is given to the retention of entrained air bubbles, particularly in highly flowable concrete. When any fresh concrete is vibrated, its rheology changes due to the loss of aggregate-to-aggregate contact. Any movement of air bubbles must occur within the paste phase, meaning that it is necessary to understand the interplay between consolidating vibration, rheology, and movement of entrained air bubbles in order to enhance long-term durability of hardened concrete against freeze-thaw damage.

5.5 Experimental Methods

Two material systems (Portland cementitious paste, mortar, and concrete; and Carbopol 980 Polymer with silica sand and glass marbles) were considered in this study. A significant drawback of measuring the rheology of Portland cementitious materials is that they are undergoing hydration which results in gelling and increasing yield stress and plastic viscosity with respect to time. Carbopol 980 Polymer is an unreactive Bingham fluid that can serve as a surrogate fluid of Portland cement paste. As such, effects of hydration and thixotropy can be discounted.

5.5.1 Materials and equipment

The first material system considered is Portland cement-based paste, mortars, and concrete. The paste is a water-to-cement ratio of 0.30 (by mass) that is dosed with a set-retarding (MasterSet

DELVO), superplasticizing (Sika Viscocrete 2100), and air-entraining (Sika AEA-14) chemical admixtures (see Table 5-1). In order to make mortar, a nominal 62% by volume of river sand is added. The size distribution of sand particles is given in Table 5-2. Specifically, the sand used in the Portland cement-based mortars and concrete conforms to Illinois Department of Transportation (IDOT) FA02 blend. In order to make concrete, gravel is added to the mortar. A comparable concrete mixture using a water-to-cement ratio of 0.40 (by mass) is also considered for its rheological properties. The gravel used in the Portland cement-based concrete is crushed limestone, and its size distribution conforms to IDOT CA07 blend (see Table 5-3). A nominal 45% of coarse aggregate is added by volume.

Table 5-1 Nominal paste mix design.

Material Type	**w/c = 0.30**	
	Pounds Per Cubic Yard	**Kilograms Per Cubic Meter**
Type I Portland Cement	2696	1599
Water	809	480
Set-Retarding Agent	6 fl. oz per 100 lb. cementitious (391 mL per 100 kg cementitious)	
Superplasticizing Agent	10 – 16 fl. oz per 100 lb. cementitious (652 – 1,043 mL per 100 kg cementitious)	
Air-Entraining Agent	0, 3, or 6 fl. oz per 100 lb. cementitious (0, 196, or 391 mL per 100 kg cementitious)	

Table 5-2 Gradation (percent passing) of various sand types.

			Specific Gravity	3/8" (9.5mm)	No. 4 (4.75 mm)	No. 8 (2.36 mm)	No. 10 (2.00 mm)	No. 16 (1.18 mm)	No. 30 (600 µm)	No. 40 (425 µm)	No. 50 (300 µm)	No. 80 (180 µm)	No. 100 (150 µm)	No. 200 (75 µm)
FA	IDOT FA 2	*Lab River Sand*	2.63	100	97 ± 3			65 ± 20			20 ± 10		5 ± 5	
	ASTM C778	*Ottawa Graded Sand*	2.65					100	98 ± 2	70 ± 5	25 ± 5		2 ± 2	
	ASTM C33	*Fine Aggregate*		100	97.5 ± 2.5	90 ± 10		67.5 ± 17.5	42.5 ± 17.5		17.5 ± 12.5		5 ± 5	1.5 ± 1.5

Table 5-3 Gradation (percent passing) of various gravel types.

			Specific Gravity	3" (75 mm)	2.5" (63 mm)	2" (50 mm)	1.5" (37.5 mm)	1" (25 mm)	3/4" (19 mm)	1/2" (12.5 mm)	3/8" (9.5 mm)	No. 4 (4.75 mm)	No. 16 (1.18 mm)	No. 50 (300 µm)	No. 200 (75 µm)
CA	IDOT CA 7	*Limestone*	2.75				100	95 ± 5		45 ± 15		5 ± 5			
	IDOT CA 12	*Limestone*							100	95 ± 5	85 ± 10	60 ± 10	35 ± 10		
	IDOT CA 16	*Chip*	2.67							100	97 ± 3	30 ± 15	2 ± 2		

Carbopol 980 Polymer is a crosslinked polyacrylate polymer that is mixed with water to form a clear gel that is stable at neutral pH. The gel features design-controllable yield stress and viscosities that can suspend particles and air while maintaining a high amount of clarity through the material. The gel has been utilized in other rheological studies as a surrogate material for fiber reinforced concrete [Boulekbache *et al.*, 2010]. In order to make Carbopol-based mortar, ASTM C778 graded sand is used and the particle size distribution is shown in Table 5-2. The silica sand

is observed to be unreactive and does not significantly alter the pH of the Carbopol 980 polymer gel ensuring rheological stability throughout testing. The volume fraction of the graded sand is varied in order to draw insight into the effect of aggregates on rheology.

All materials are mixed in a 2 cubic-foot capacity flatbed pan shearing mixer or in a 5-gallon bucket with a handheld paddle mixer. The rheological properties of the fresh materials were measured using an ICAR Rheometer or an AR-G2 Rheometer both of which measure the rheology using a rotating vane propeller (see Figure 5-2). The ICAR rheometer was developed by the International Center for Aggregate Research (ICAR) at the University of Texas at Austin in order to better characterize the rheological properties of concrete [Koehler *et al.*, 2006]. Both the cementitious and model materials were treated as Bingham plastics, which are characterized by a dynamic yield stress (tangent intercept) and plastic viscosity (slope at large shear strain rate). The static yield stress was also measured, but is not considered in the determination of the Bingham fit parameters.

Figure 5-2 An ICAR concrete rheometer (left) with Carbopol-mortar and an AR-G2 high-precision rheometer (right).

5.5.2 Measuring density, fresh air content, and strength of variably vibrated concrete, mortar, and paste

The unit weight of paste, mortar, and concrete was measured in accordance to ASTM C138 *Standard Test Method for Density (Unit Weight), Yield, and Air Content (Gravimetric) of Concrete* while the fresh air content was measuring using a Type B air meter conforming to ASTM C231 *Standard Test Method for Air Content of Freshly Mixed Concrete by the Pressure Method*. When not subjected to vibration, the container was appropriately filled and compacted in two lifts. The

fresh material is struck even and finished such that the unit weight and the fresh air content can be measured. The fresh material is discarded.

In the case when the fresh material is subjected to vibration, the container is similarly filled with fresh material, struck even, and finished. The container is then placed atop a 60 Hz vibration table (see Figure 5-3). The vibration table is powered on and vibrated to the designated time duration. At the end of vibration, new (un-vibrated) fresh material is added into the container, the material is struck even and finished again. Density and fresh air content values are recorded and the fresh material is discarded.

Figure 5-3 A Type B air meter (ASTM C231) atop a 60 Hz vibration table.

Eight-inch tall concrete cylinders were prepared in accordance to ASTM C39 *Standard Test Method for Compressive Strength of Cylindrical Concrete Specimens* and tested at 7, 14, 28, and 56 days. A minimum of two cylinders were tested for each variable where specimens were variably air-entrained and variably vibrated. Specimens that were not vibrated were simply filled into oiled cylindrical molds in two even lifts and rodded 25 times in each lift. Specimens that were vibrated for 1 or 2 minutes were similarly filled in two lifts, rodded 25 times in each lift, and vibrated atop the 60 Hz vibration table. After vibration, the specimens were struck even and floated to a finished surface and hardened for 24 hours in ambient lab conditions. The specimens were de-molded at 24 hours and moved to a 100% relative humidity environment through 7 days before being stored in a 50% relative humidity environment until testing.

5.5.3 Rheological measurements using vane geometry

A rheometer developed by the International Center for Aggregates Research (ICAR) was utilized to investigate the static and dynamic yield stresses of high flow concrete, mortar, and cement paste. The fresh material is filled in the rheometer container in two lifts and struck with a mallet hammer 25 times around its sides, if necessary, to fully fill the container. The vane is attached to a torque-meter, and the vane is inserted into the fresh material. Once secured in place, two tests are executed: the stress growth test and the flow curve test. In the stress growth test, variable torque is applied in order to attain a constant vane rotation speed. The torque generally increases to a maximum value where after the material yields from a semi-solid state to a semi-liquid state. This transition represents the static yield stress; and the conversion between the maximum torque, T_{max}, to the static yield stress, τ_o, is found by the expression

$$\tau_o = \frac{2T_{max}}{\pi D^3\left(\frac{H}{D}+\frac{1}{3}\right)} \qquad \text{Equation 5-9}$$

where H is the vane height and D is the vane diameter. The stress growth test is terminated by the user once a maximum torque is clearly identified.

In the flow curve test, the vane is rotated to a high speed of 0.5 revolutions-per-second (rps) for 20 seconds to induce breakdown of the material. At the end of 20 seconds, the value of torque required to maintain the 0.5 rps is recorded. Immediately, the rotational speed drops an increment of 0.075 rps to 0.425 where an additional 5 seconds of torque speed is recorded. This process is repeated until the rotational speed drops to 0.05 rps. The test is automatically concluded. In the analysis, the latter 4 seconds of a rotational speed step are averaged to find the average torque and the actual rotational speed (which is close to the target speed). The first second is discarded in order to avoid transient effects of the changing vane rotational speed. Once the average torque, T, and rotational speed, Ω, are known for each of the increment steps, then the Reiner-Riwlin equation is used to solve for the dynamic yield stress, τ_o, and the plastic viscosity, μ [Koehler *et al.*, 2006]

$$\Omega = \frac{T}{4\pi H\mu}\left(\frac{1}{{R_1}^2}-\frac{1}{{R_2}^2}\right)-\frac{\tau_o}{\mu}\ln\left(\frac{R_2}{R_1}\right) \qquad \text{Equation 5-10}$$

where R_1 is the radius of the vane diameter and R_2 is the radius of the container. In instances where not all the material flows, an effective outer radius, $R_{2,eff}$, is considered

$$R_{2,eff} = \sqrt{\frac{T}{2\pi H \tau_o}}. \qquad \text{Equation 5-11}$$

The physical units of torque and rotation speed are transformed to Bingham rheological properties of dynamic yield stress and plastic viscosity. A modified relationship between the physical properties of torque, *T*, and rotational frequency, *N*, accounts for the shearing material atop and below the vane propeller, but this modified relationship is not considered in this study [Laskar and Bhattacharjee, 2011].

Another rheometer called AR-G2 by TA Instruments is used in this study for measurements at low torque value [Costello, 2016]. The propeller is a vane with diameter 28 mm and a height of 42 mm. The diameter of the container is 68 mm. The data output is reported directly in rheological properties (η, σ_y, e.g.). The AR-G2 rheometer was used to study the effect of increasing volume content of fine silica sand to a surrogate fluid of Carbopol gel.

5.5.4 Distribution of peak acceleration inside vibrated mold geometry

A three-axis (triaxial) water-proof accelerometer (W356A12) from PCB Piezotronics is used to measure the peak acceleration inside of an ICAR rheometer container as it is being vibrated with variably intense settings. The accelerometer is firmly affixed onto an aluminum rod and additionally covered in nitrile layer in order to maintain the cleanliness of the sensor. The accelerometer and rod are immersed into the fresh material at varying depths. The depth of the accelerometer varies from 3, 6, or 9 inches from the top surface. The rod and accelerometer column is positioned at either the center of the container (C) or at the outer edge (O). The sensors mounted on the outside are affixed using wax provided by the manufacturer of the accelerometer. Figure 5-4 depicts the profile and plan views of this arrangement.

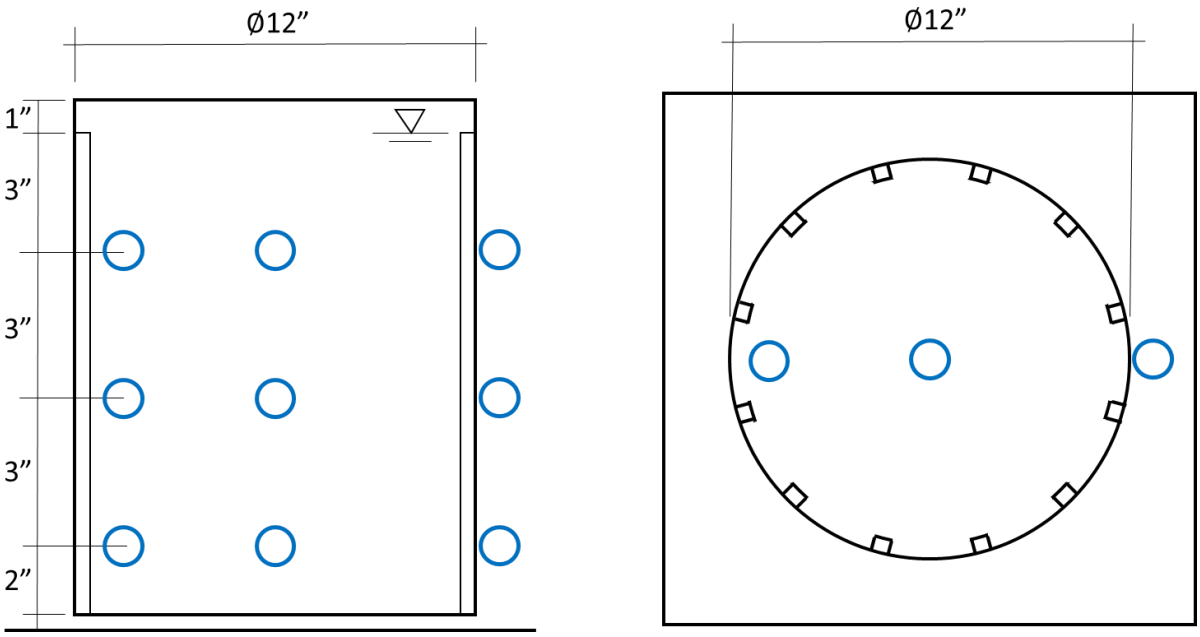

Figure 5-4 Profile (left) and plan (right) view of an ICAR rheometer container sitting atop a 60 Hz vibration table with locations of triaxial accelerometer noted in blue circles.

5.6 Results

5.6.1 Density, fresh air content, and strength of variably vibrated concrete, mortar, and paste

The average density of fresh concrete, mortar, and paste is shown across Figures 5-5 through 5-7. In the instance when no air entraining admixture is used, the density of concrete is approximately 155 pcf, the density of mortar is 145 pcf, and the density of paste is 132 pcf. When air entraining admixtures are incorporated into the fresh mixture, the measured density values appreciably lower. Moreover, when external consolidating vibration times increase, then the average density values increase. In particular, the average density of mortar subjected to external vibration increases. The average density of air-entrained concrete (C30-0608 and C30-1012) increases slightly. The average density of paste is minimally affected by external vibration.

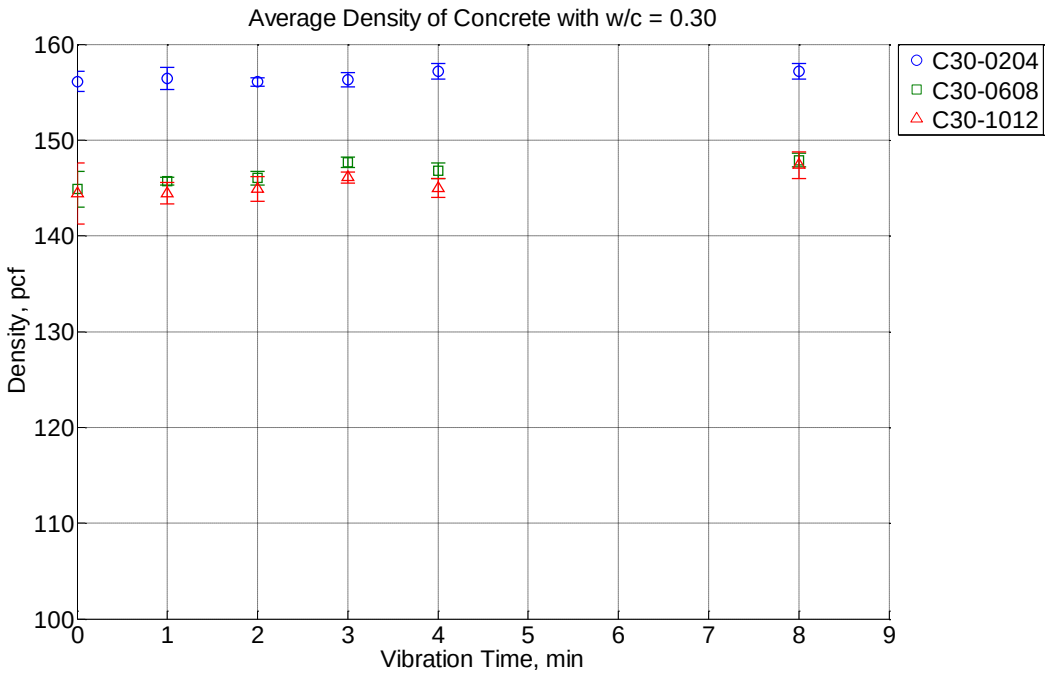

Figure 5-5 Average density of fresh concrete that is dosed with no air entraining admixture (C30-0204), moderate air entraining admixture (C30-0608), or high air entraining admixture (C30-1012). The fresh material is vibrated inside of an ASTM C231 Type B air meter container that is positioned atop a 60 Hz vibration table.

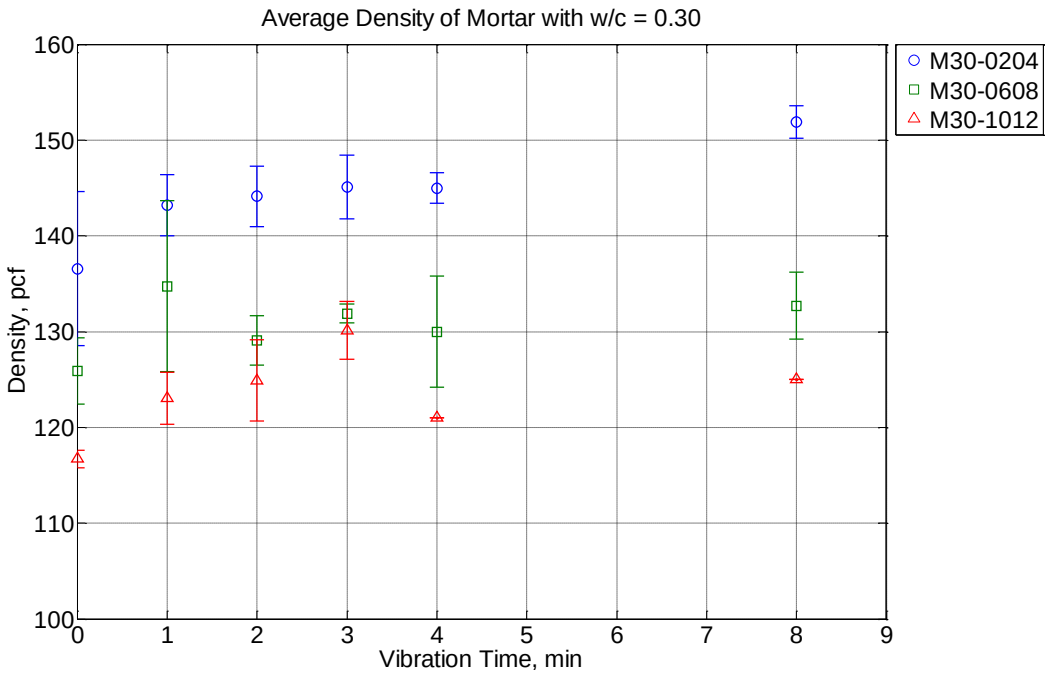

Figure 5-6 Average density of fresh mortar that is dosed with no air entraining admixture (M30-0204), moderate air entraining admixture (M30-0608), or high air entraining admixture (M30-1012). The fresh material is vibrated inside of an ASTM C231 Type B air meter container that is positioned atop a 60 Hz vibration table.

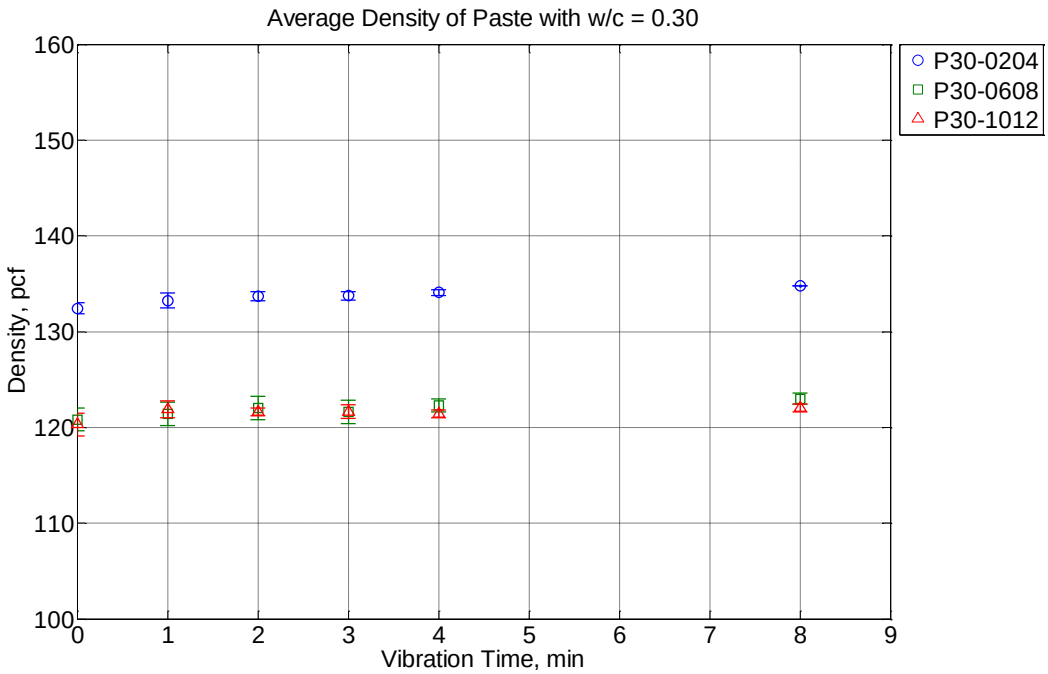

Figure 5-7 Average density of fresh paste that is dosed with no air entraining admixture (P30-0204), moderate air entraining admixture (P30-0608), or high air entraining admixture (P30-1012). The fresh material is vibrated inside of an ASTM C231 Type B air meter container that is positioned atop a 60 Hz vibration table.

Density is increased, in large part, because entrapped air is actively being removed from the fresh material systems. Figures 5-8 through 5-10 show the average uncorrected fresh air content of concrete, mortar, and paste when vibrated inside an ASTM C231 air meter container. In air-entrained concrete (C30-0608 and C30-1012) (see Figure 5-8), there is an appreciable amount of air loss observed in the span of the first 3-4 minutes of vibration time. In all mortar samples, there is appreciable loss of fresh air content in the first 3-4 minutes of vibration time. There is minimal change in the fresh air content in cement paste that is vibrated within the 8 minute time duration.

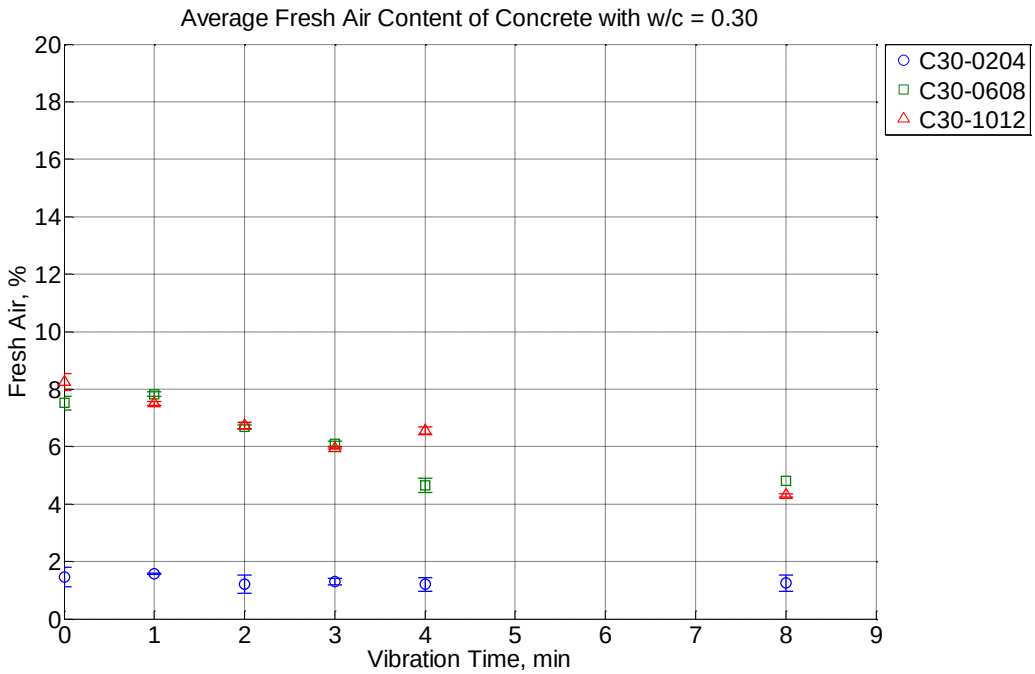

Figure 5-8 Average uncorrected fresh air content of fresh concrete that is dosed with no air entraining admixture (C30-0204), moderate air entraining admixture (C30-0608), or high air entraining admixture (C30-1012). The fresh material is vibrated inside of an ASTM C231 Type B air meter container that is positioned atop a 60 Hz vibration table.

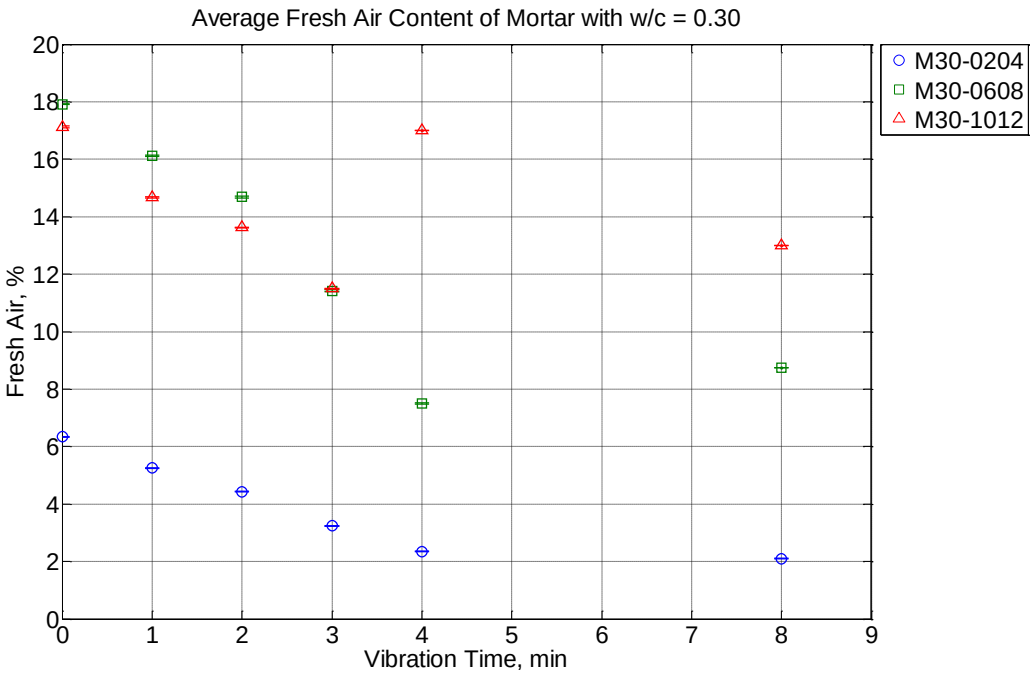

Figure 5-9 Average uncorrected fresh air content of fresh mortar that is dosed with no air entraining admixture (M30-0204), moderate air entraining admixture (M30-0608), or high air entraining admixture (M30-1012). The fresh material is vibrated inside of an ASTM C231 Type B air meter container that is positioned atop a 60 Hz vibration table.

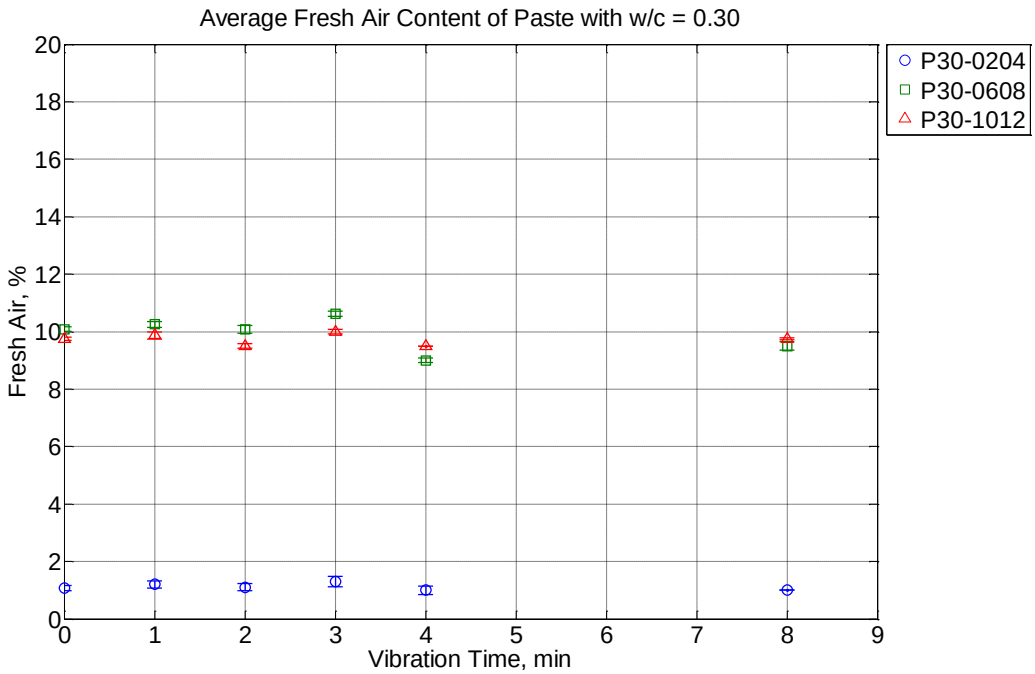

Figure 5-10 Average fresh air content of fresh paste that is dosed with no air entraining admixture (P30-0204), moderate air entraining admixture (P30-0608), or high air entraining admixture (P30-1012). The fresh material is vibrated inside of an ASTM C231 Type B air meter container that is positioned atop a 60 Hz vibration table.

The strength evolution of concrete samples that are variably air-entrained and variably vibrated for 0, 1, or 2 minutes atop a 60 Hz vibration table are shown in Figures 5-11 through 5-13. In Figure 5-11, non-air-entrained concrete is variably vibrated for 0, 1, or 2 minutes. At 56 days, the compressive strength values are comparable at 10-12 ksi. When moderately air-entrained (see Figure 5-12), the compressive strength value falls to 7-8 ksi. Moreover, the compressive strength value at 56 days is moderately reduced due to a 2 minute vibration duration. In Figure 5-13, the 56 day compressive strength of high air entrained concrete varies 4.5-8 ksi. Increased vibration times of high air entrained concrete appreciably lowered 56 day compressive strength values.

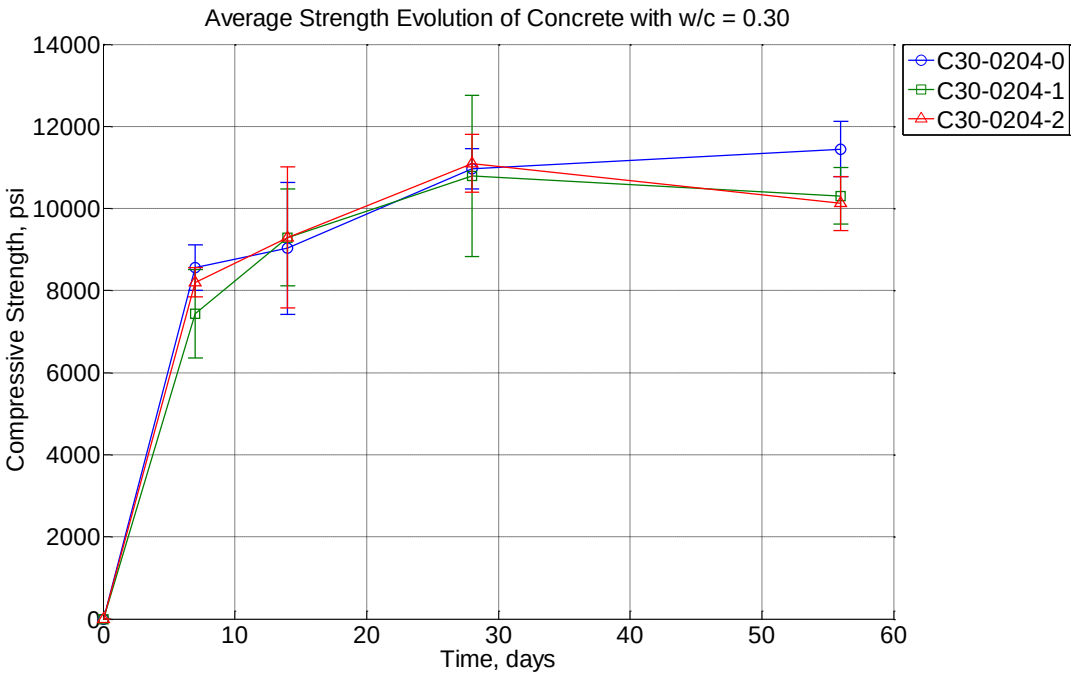

Figure 5-11 Average strength of hardened concrete that is dosed with no air entraining admixture (C30-0204). The fresh material was vibrated inside ASTM C39 4-inch diameter cylinder containers that were positioned atop a 60 Hz vibration table for 0, 1, or 2 minutes.

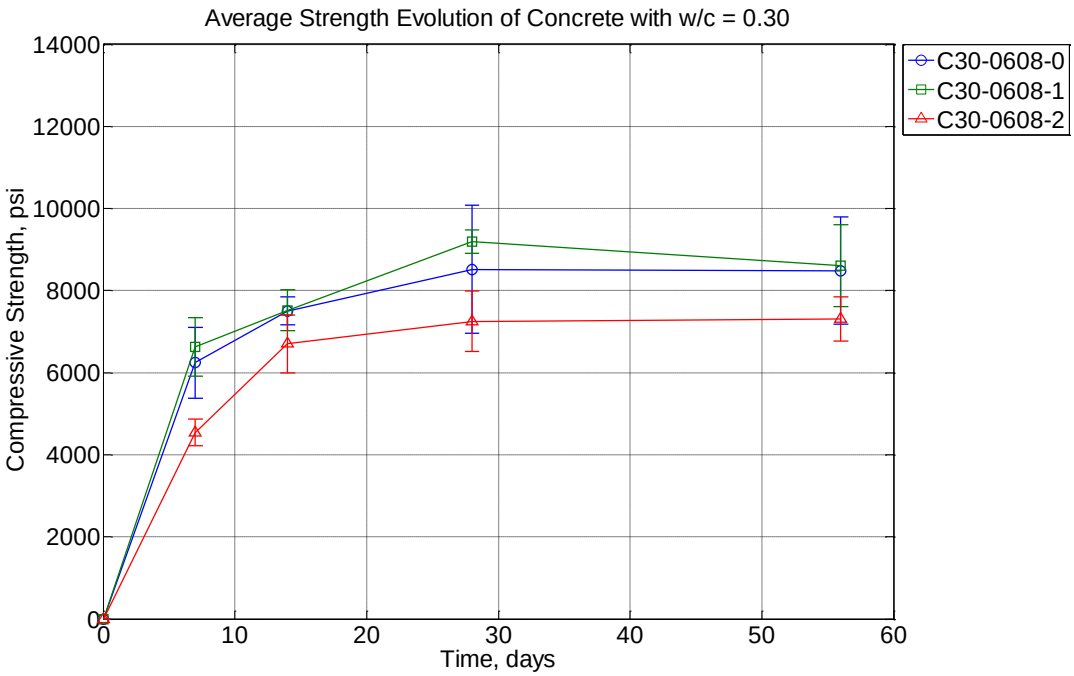

Figure 5-12 Average strength of hardened concrete that is dosed with moderate air entraining admixture (C30-0608). The fresh material was vibrated inside ASTM C39 4-inch diameter cylinder containers that were positioned atop a 60 Hz vibration table for 0, 1, or 2 minutes.

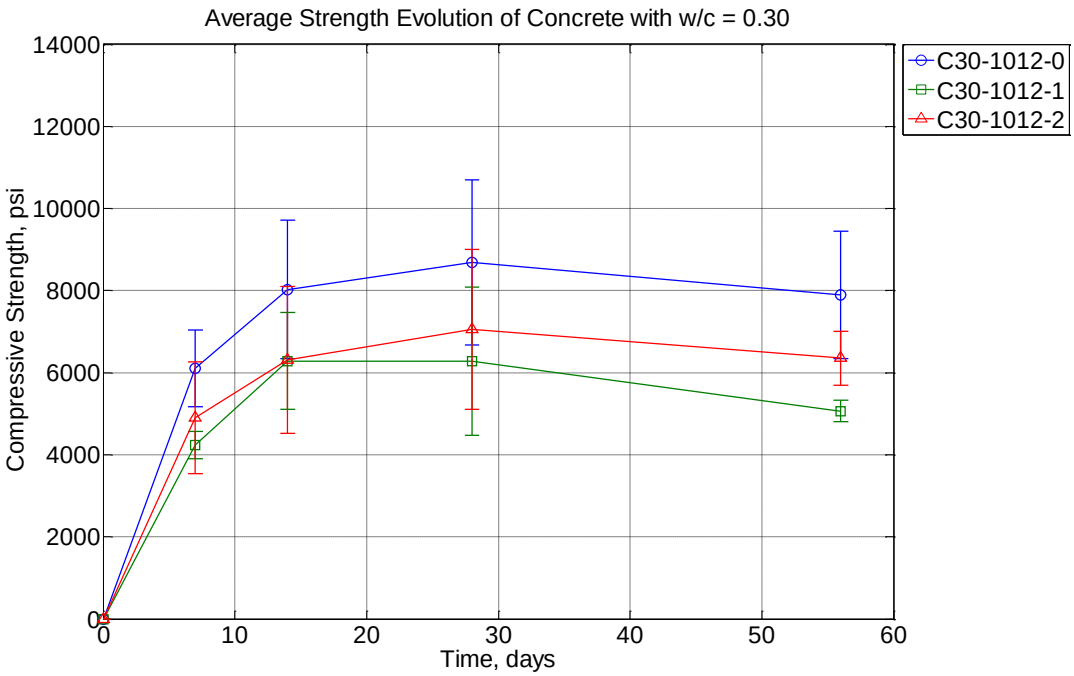

Figure 5-13 Average strength of hardened concrete that is dosed with high air entraining admixture (C30-1012). The fresh material was vibrated inside ASTM C39 4-inch diameter cylinder containers that were positioned atop a 60 Hz vibration table for 0, 1, or 2 minutes.

5.6.2 Rheological measurements of Portland cement-based concrete, mortar, and paste

An ICAR rheometer was used to characterize the Bingham plastic properties of fresh concrete, mortar, and paste. Figures 5-14 through 5-17 depict several data sets of interest for one concrete mixture with no air entrainment and repeatedly measured for its rheological properties at three instances in time. Similar graphs for all other mixtures considered in this study are contained within Appendices D1-D4.

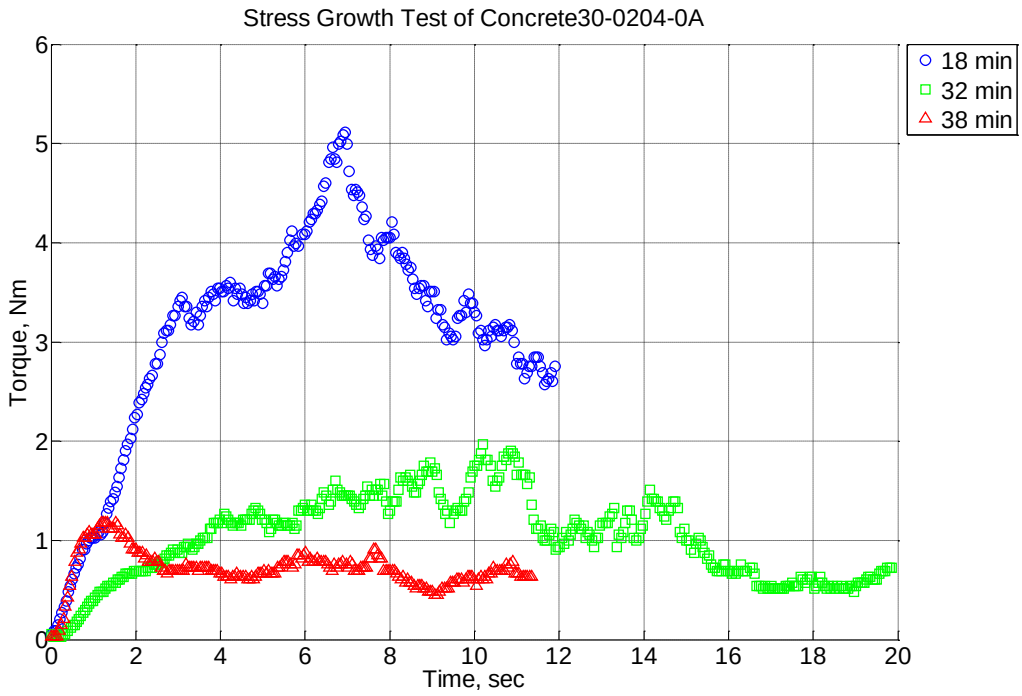

Figure 5-14 Stress growth test of concrete (replicate A) with water-to-cement ratio 0.30, dosed with no air entraining agent, and whose companion compression strength cylinders were vibrated atop a 60 Hz vibration table for 0 minute(s). The test is run on the same concrete material repeatedly at 18, 32, and 38 minutes since water and Portland cement first contacted in the pan mixer.

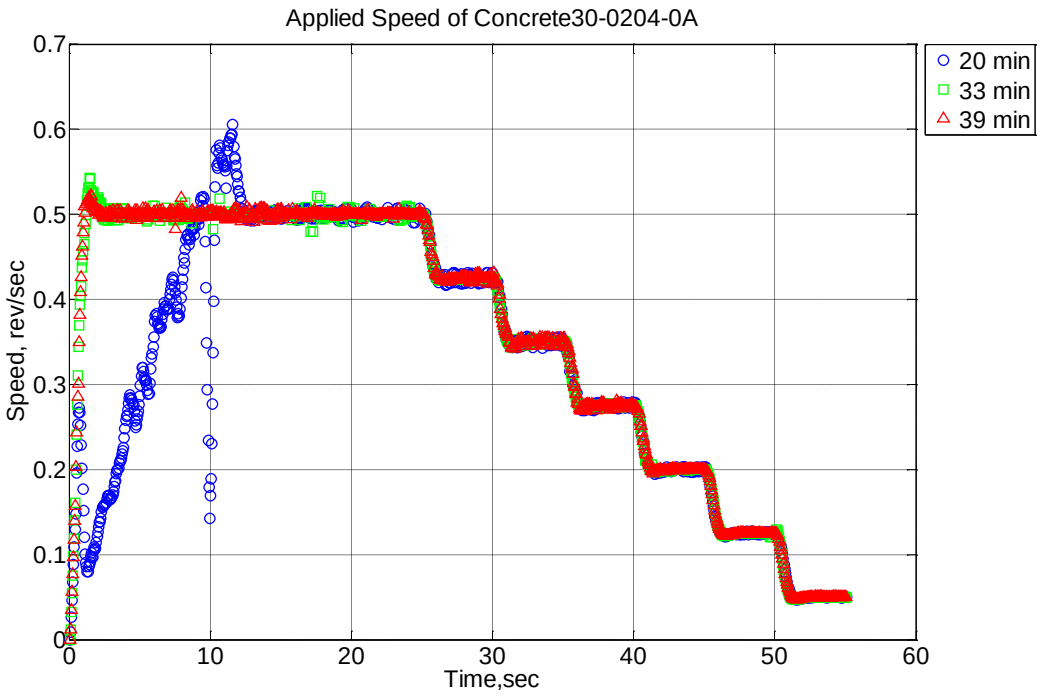

Figure 5-15 Applied vane speed on concrete (replicate A) with water-to-cement ratio 0.30, dosed with no air entraining agent, and whose companion compression strength cylinders were vibrated atop a 60 Hz vibration table for 0 minute(s). The test is run on the same concrete material repeatedly at 20, 33, and 39 minutes since water and Portland cement first contacted in the pan mixer.

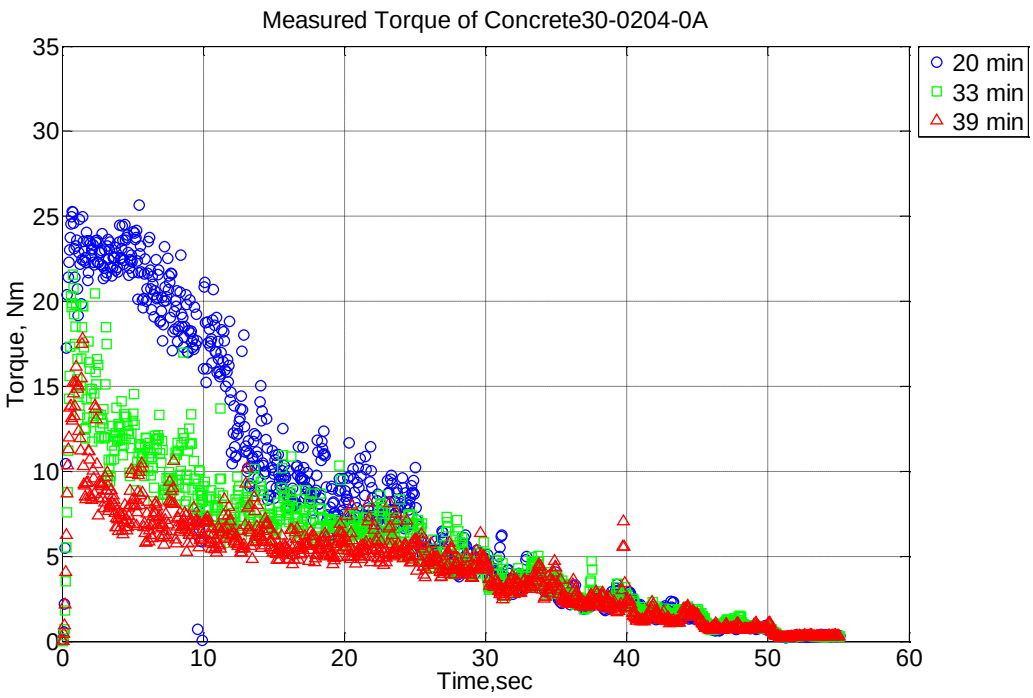

Figure 5-16 Measured torque values at varying speeds on concrete (replicate A) with water-to-cement ratio 0.30, dosed with no air entraining agent, and whose companion compression strength cylinders were vibrated atop a 60 Hz vibration table for 0 minute(s). The test is run on the same concrete material repeatedly at 20, 33, and 39 minutes since water and Portland cement first contacted in the pan mixer.

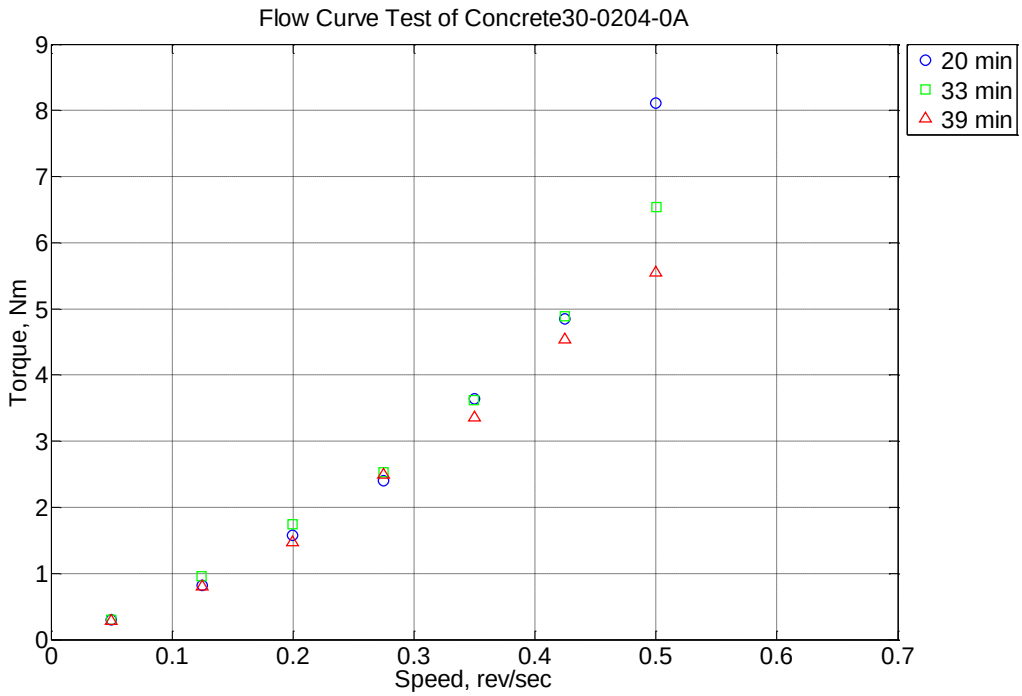

Figure 5-17 Flow curve test of concrete (replicate A) with water-to-cement ratio 0.30, dosed with no air entraining agent, and whose companion compression strength cylinders were vibrated atop a 60 Hz vibration table for 0 minute(s). The test is run on the same concrete material repeatedly at 20, 33, and 39 minutes since water and Portland cement first contacted in the pan mixer.

Repeated static growth tests (see Figure 5-14) were conducted on the same fresh material. In most testing instances, the initial value is tested at the earliest time reported the highest shearing stress value in order to produce bulk flow of material. It is very likely that any repeated test on the same material more easily shears a circumferential zone of paste material. Therefore, any secondary or tertiary static yield stress is less meaningful than an initial value. The static yield stress for this mixture is found by utilizing Equation 5-9, and it is observed to progressively fall from 1192 Pa at 18 minutes to 458 Pa at 32 minutes and finally 275 Pa at 38 minutes. These values are summarized in Table 5-4.

Table 5-4 Repeated static yield stress, dynamic yield stress, and plastic viscosity of concrete (replicate A) with water-to-cement ratio 0.30 and dosed with no air entraining agent.

Hydration Time (min)	Static Yield Stress (Pa)	Dynamic Yield Stress (Pa)	Plastic Viscosity (Pa.s)	R^2 (%)
18	1192	-	-	-
20	-	0	261	91
32	458	-	-	-
33	-	0	230	97
38	275	-	-	-
39	-	0	205	99

Dynamic yield stress (i.e. shear-stress intercept) can be found by correlating the applied vane speed (see Figure 5-15) with the measured torque (see Figure 5-16) with Equations 5-10 and 5-11 to produce a flow curve (i.e. rheograph) plot (see Figure 5-17). In doing so, it is important to realize artifacts of testing where the target vane speed is not fully achieved. In Figure 5-15, the target vane speed initiated at 20 minutes of hydration time requires approximately 10 seconds whereas other test initializations require less than 1 second. In the estimation of measured vane speed, values beyond 20 seconds are considered in the calculation as these are past the user-inputted breakdown time where material is desired to reach steady-state flow. If material has not yet reached steady-state flow, then the averaged vane speed values are not suitable for analysis. Similarly, the measured torque may not reach steady-state within a the latter 4 seconds of a 5 second measurement period at a given vane speed due to thixotropic effects. In such a case, it may be possible to observe artificial shear-thickening behaviors in a rheograph as is partially observed in Figure 5-17 at testing times of 20 and 33 minutes.

The slope and y-intercept of the Ω-T plot are used in Equations 5-10 and 5-11 to estimate the dynamic shear stress and plastic viscosity. Table 5-4 summarizes these values for Figure 5-17 and also shows an R^2 value for linear regression analysis. The plastic viscosity values of 261, 230, and 205 Pa.s across 20, 33, and 39 minutes of testing is appreciably consistent indicating that this calculated value is a meaningful value for the material system. Moreover, the dynamic shear stress is fairly consistent across multiple material systems as observed in rheographs in Appendices D1-D4.

5.6.3 Rheological measurement with increasing fine aggregate content

The rheological properties in Appendices D1-D4 are affected by the volume fraction of particles interacting with each other as suggested by Equations 5-6 and 5-7. A surrogate fluid named Carbopol is a yield-stress fluid that was tested for its rheology using an AR-G2 rheometer and the result is shown in Figure 5-18 as CarboMortar24-00. Increasing volume fractions of ASTM C778 graded silica sand up to 40 % by volume is added to the Carbopol gel and the rheology is measured. There is a general upward movement of the envelope of the rheograph for increasing volume fractions of silica sand. The nature of the test is a flow sweep from a high strain rate to a low strain rate. As a result, an extrapolation of the slope at high strain rates intercepts the y-axis at a non-zero value. However, at very low strain rates, the required shear stress is quickly diminished. This behavior is often experimentally observed in high-resolution measurements and is often overlooked in the measurement of concrete rheology. When these very low strain rates are discarded, then a Bingham curve can readily be applied.

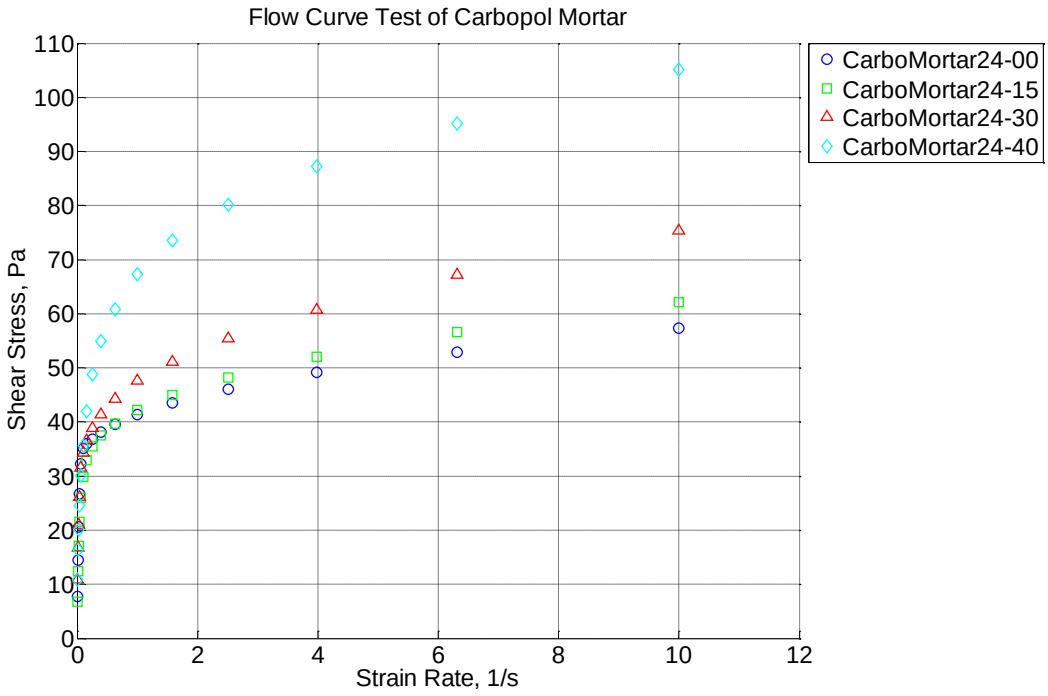

Figure 5-18 Flow curve test of Carbopol gel with 0.24 % solids and mixed with 0, 15, 30, or 40 % by volume of ASTM C778 graded silica sand.

Larger amounts of silica sand are considered in Figure 5-19 where additional volume fractions of 45, 50, 53, and 56 % (by volume) are measured for their rheology. Similar to Figure

5-18, the envelope of the rheograph increases for increasing volume fraction of sand. Interestingly, the behavior at low shear strain rates is affected at 53 and 56 % volume fraction where the data set does not follow a smooth path directly to the origin. Instead, seemingly increasing shear stresses are required at low shear strain rates (i.e. shear-thinning) which exceeds the y-axis intercept estimated by the slope at large strain rates. This behavior is attributable to the interaction of particles leading to an increase in shear stress required to maintain flow. In concrete rheology, this can often be seen at low shear strain rates such as in Figure D2-14 where the rheograph seemingly transitions for a shear-thickening to a shear-thinning material with increasing hydration time.

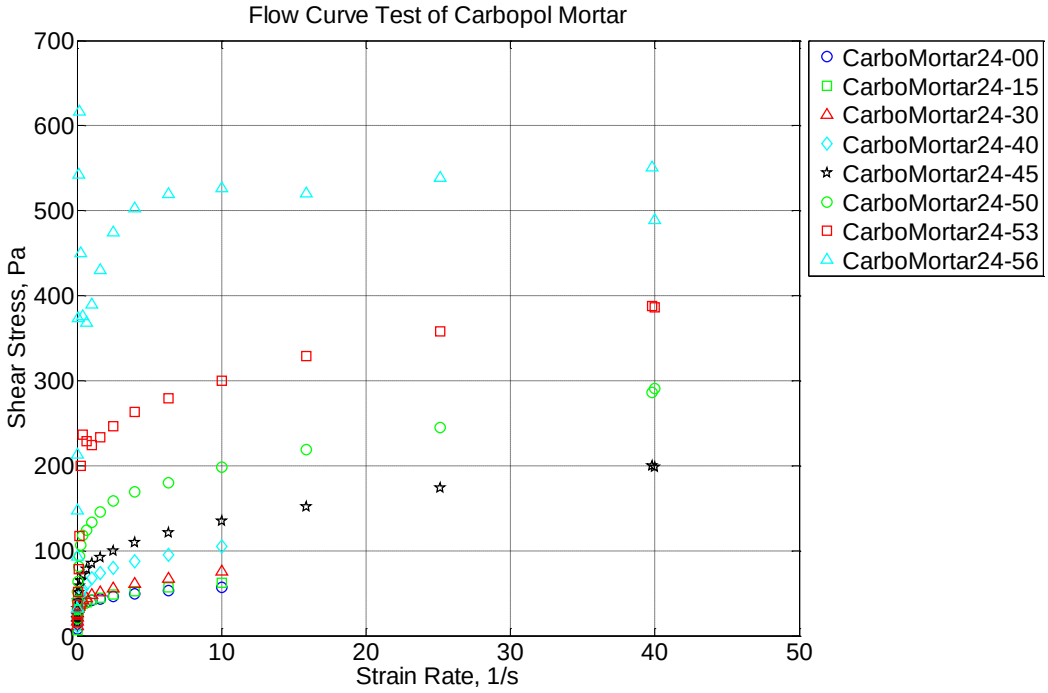

Figure 5-19 Flow curve test of Carbopol gel with 0.24 % solids and mixed with 0, 15, 30, 40, 45, 50, 53, and 56 % by volume of ASTM C778 graded silica sand.

When under flow, aggregate-to-aggregate interaction is minimized and particles are shearing past each other. However, at low strain rates, the aggregates in a jammed system are interacting with each other leading to an increase in the required amount of torque to continue flow of the fresh material. As a consequence, the shear stress at low strain rates is appreciably larger than the y-intercept (dynamic) shear stress value estimated from the slope at high strain rates. This phenomenon aptly explains the often large static shear stress measured for any granular system when compared to the dynamic shear stress.

5.6.4 Rheological measurement under vibration

The rheology of a granular fluid is known to change when external vibration is applied. A triaxial accelerometer is immersed in fresh material or affixed to the outside of the ICAR rheometer container (see Figure 5-4). The accelerometer is immersed to a depth of 3, 6, or 9 inches from the top surface of the fresh material and positioned at the center (C), inner surface of the container (S), or outer surface of the container (O). The presence of fresh concrete, mortar, or paste modifies the inertial mass of material being vibrated, so acceleration values of each material system are measured and reported in Appendices D5-D7.

A typical acceleratory response (measured at 1 kHz) is shown in Figure 5-20 where acceleration is measured before external vibration is applied, during a 2-3 second time duration of vibration atop a 60 Hz vibration table, and a period of time after external vibration is turned off. The ICAR container was vibrated such that the maximum level of vibrational energy was applied. The three signals (x, y, z) are individually analyzed. All maximum and minimum local peaks are identified and filtered in order to remove the lower- and highest-most quartile of data. This filtering was done in order to remove sudden peaks in the acceleratory response as was commonly observed throughout testing. The difference between the average maximum and minimum peaks is found and corrected for any offset in order to determine the amplitude of the mean peak acceleration. These average peak acceleration values are reported for concrete, mortar, and paste in Tables 5-5 through 5-7. The resultant mean peak acceleration, R, is found by calculating the magnitude of the vector at any given time for an x, y, and z local maximum or minimum peak. This processes produces an array of resultant values which are then averaged and similarly reported in Tables 5-5 through 5-7.

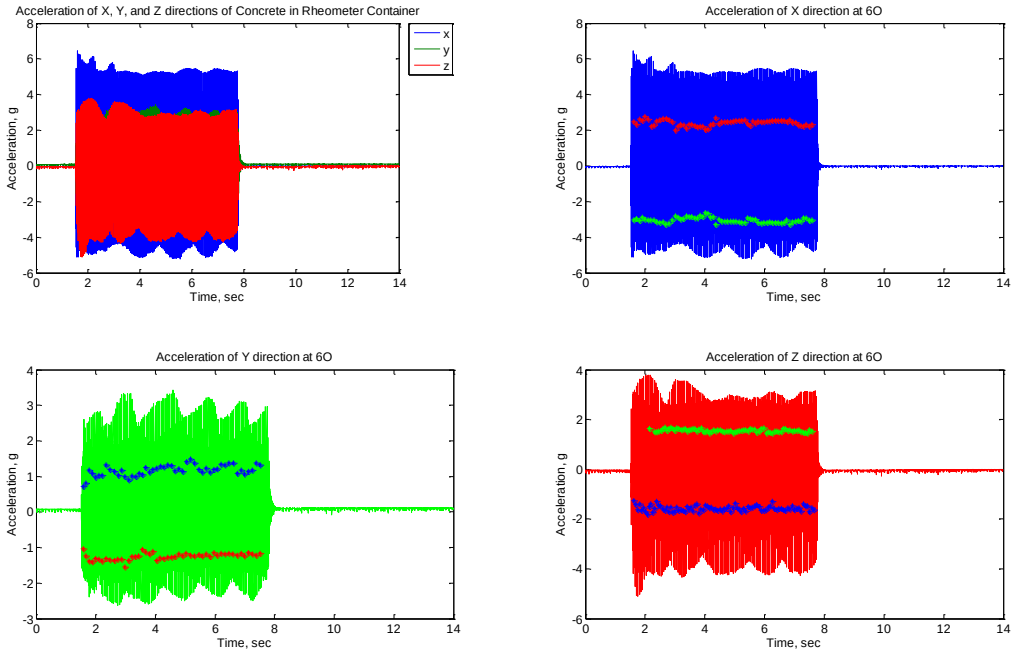

Figure 5-20 Measured acceleration values (x, y, and z) inside fresh concrete with water-to-cement ratio 0.40. The accelerometer sensor is positioned at a depth of 6 inches from the top surface of the fresh material and is at the outer surface of the container.

Table 5-5 Mean peak acceleration values (g) of triaxial accelerometer (x, y, and z) immersed in fresh concrete material with water-to-cement ratio 0.40 measured at depths of 3, 6, or 9 inches from the top surface at the center (C), inner surface of the ICAR container (S), or outer surface of the ICAR container (O).

C40	**'3C'**	**'3O'**	**'3S'**	**'6C'**	**'6O'**	**'6S'**	**'9C'**	**'9O'**	**'9S'**
x	1.91	2.05	1.34	2.08	3.04	2.52	2.29	0.54	1.49
y	1.51	0.86	2.52	1.34	1.24	2.79	0.94	0.62	0.86
z	0.96	2.93	1.49	1.33	1.56	1.29	0.72	3.19	0.97
R	3.17	3.48	3.34	2.87	3.11	3.95	3.04	3.21	1.64

Table 5-6 Mean peak acceleration values (g) of triaxial accelerometer (x, y, and z) immersed in fresh mortar material with water-to-cement ratio 0.30 measured at depths of 3, 6, or 9 inches from the top surface at the center (C), inner surface of the ICAR container (S), or outer surface of the ICAR container (O).

M30	**'3C'**	**'3O'**	**'3S'**	**'6C'**	**'6O'**	**'6S'**	**'9C'**	**'9O'**	**'9S'**
x	0.35	2.63	1.50	0.90	2.60	1.27	1.03	0.43	0.64
y	0.71	1.34	3.21	1.47	1.50	0.99	1.19	1.27	0.60
z	1.14	1.22	1.44	1.63	1.10	2.07	2.81	2.75	1.31
R	1.19	2.97	3.17	1.84	2.98	2.75	3.19	2.72	1.96

Table 5-7 Mean peak acceleration values (g) of triaxial accelerometer (x, y, and z) immersed in fresh paste material with water-to-cement ratio 0.30 measured at depths of 3, 6, or 9 inches from the top surface at the center (C), inner surface of the ICAR container (S), or outer surface of the ICAR container (O).

P30	**'3C'**	**'3O'**	**'3S'**	**'6C'**	**'6O'**	**'6S'**	**'9C'**	**'9O'**	**'9S'**
x	1.38	1.24	2.83	3.10	2.41	3.99	1.02	0.64	2.05
y	3.27	0.83	3.00	2.70	1.81	3.37	0.74	0.77	1.42
z	1.54	1.13	0.69	2.14	1.20	1.71	2.51	3.50	1.48
R	3.16	2.37	4.63	3.78	3.07	4.02	2.25	3.79	2.93

The distribution of mean peak acceleration is found to vary throughout the geometry of the ICAR rheometer container. In concrete (see Table 5-5), the largest acceleration is 3.95 g near the inner surface of the container 6 inches from the top surface while the smallest acceleration is 1.64 g near the inner surface of the container 9 inches from the top surface. This result suggests that materials vibrated in a well-controlled manner are likely not uniformly consolidated.

After the material is characterized for mean peak acceleration values, then the triaxial accelerometer is removed and rheological measurements are taken of non-vibrated and maximum vibrated fresh materials (see Figures 5-21 through 5-23). In the three material systems (concrete, mortar, and paste) for the non-vibrated case, there is a typical y-intercept (shear stress) and linear slope (plastic viscosity). When vibrated at the highest vibration energy level, the distribution of the mean peak accelerations vary inside the container and vary across the height of the vane rheometer, meaning that an average torque response is measured. When the average torque required to measure the target vane speed, it is observed in the rheographs of Figures 5-21 through 5-23 that there is a reduction. If a higher-resolution rheometer had been used, shear-thickening behavior is likely to have been observed in the non-vibrated case (see Figure 5-18), but shear-thickening behavior is prominently seen in the vibrated case. This has been observed in other works [Tattersall and Baker, 1988], and is largely attributed to the loss of aggregate-to-aggregate interactions due to increased hydrostatic pressures.

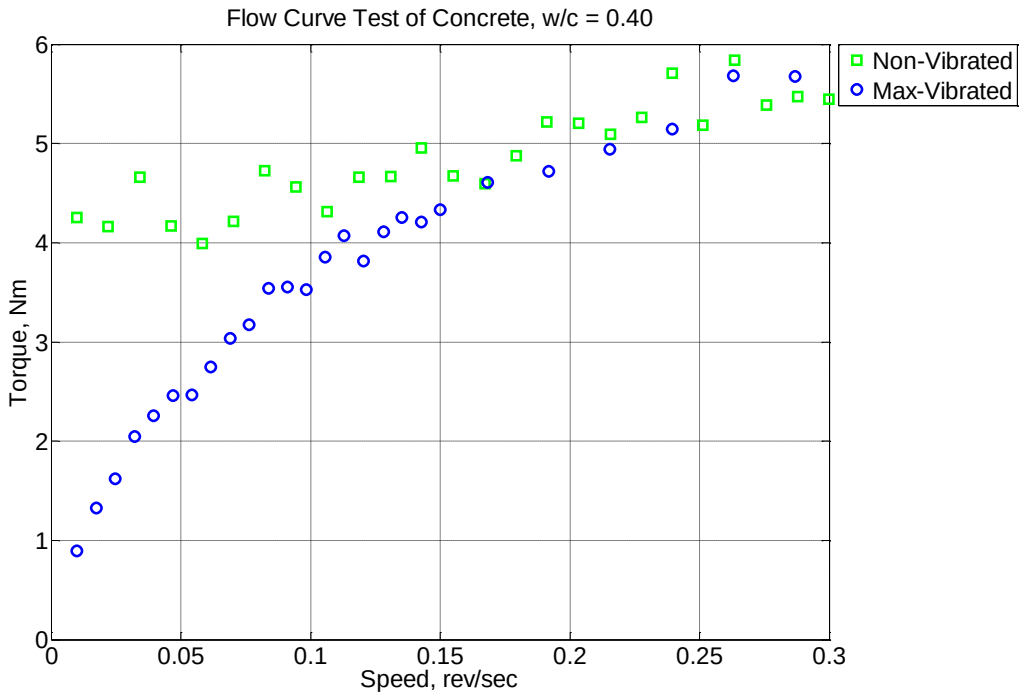

Figure 5-21 Flow curve test of concrete with water-to-cement ratio 0.40 without external vibration and with external vibration from a 60 Hz vibration table.

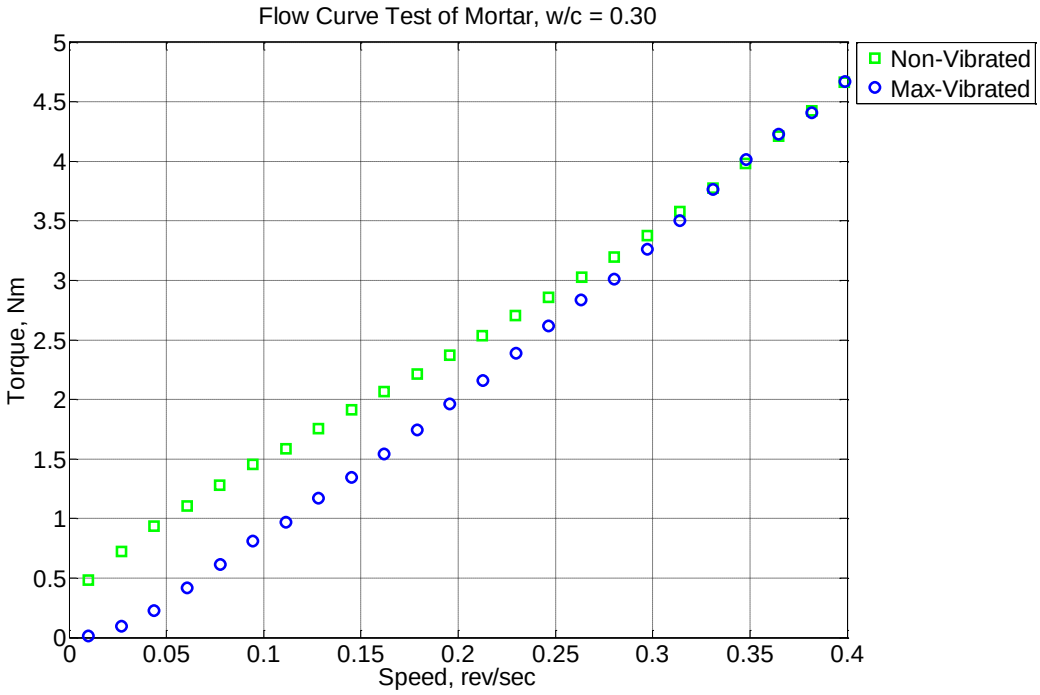

Figure 5-22 Flow curve test of mortar with water-to-cement ratio 0.30 without external vibration and with external vibration from a 60 Hz vibration table.

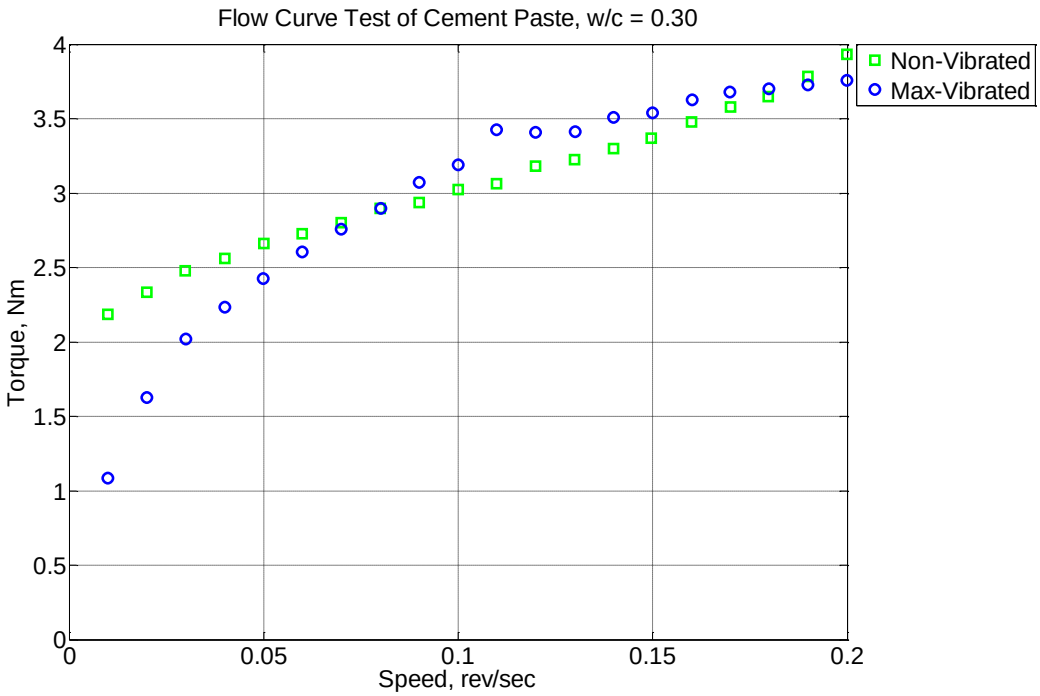

Figure 5-23 Flow curve test of paste with water-to-cement ratio 0.30 without external vibration and with external vibration from a 60 Hz vibration table.

5.7 Discussion of Results

5.7.1 Compression strength and air content

The compressive strength of concrete lowers in value due to higher air content. The loss of strength is primarily attributed to the loss of cross-sectional area. Additionally, the inclusion of spherical voids leads to stress intensification at the void boundary which lowers the strength. Figure 5-24 shows the trend of strength loss for increasing fresh air content in the concrete samples.

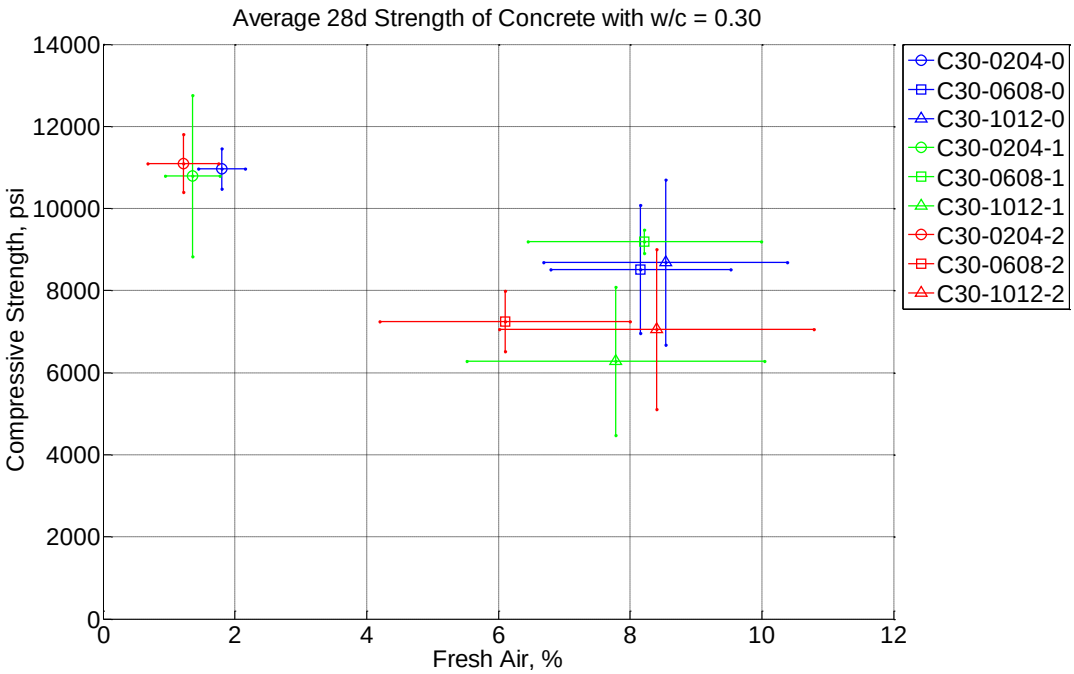

Figure 5-24 Average (and standard deviation) compression strength of concrete with water-to-cement ratio of 0.30 with increasing measured average (and standard deviation) fresh air content values.

5.7.2 Rheological properties with increasing hydration time

The rheological properties of concrete, mortar, and paste are strongly dependent upon the time of hydration because hydration products increase the stiffness of the material system until it is set and hardened. Set-retardants were used in this study in order to slow the hydration time and gain useful information from rheological measurements. Figures 5-25 through 5-28 show the first measured static yield stress from each of the materials considered in this study (concrete with a water-to-cement ratio 0.40, concrete with a water-to-cement ratio 0.30, mortar with a water-to-cement ratio 0.30, and paste with a water-to-cement ratio 0.30). These data points are the first values measured and represent a breakdown of both the granular aggregate system and the breakdown of hydration products. In the four figures, there is a general rapid increase in the first measured static yield stress value with respect to hydration time. The large variability suggests that characterizing concrete with respected to its static yield stress is not of interest for this study.

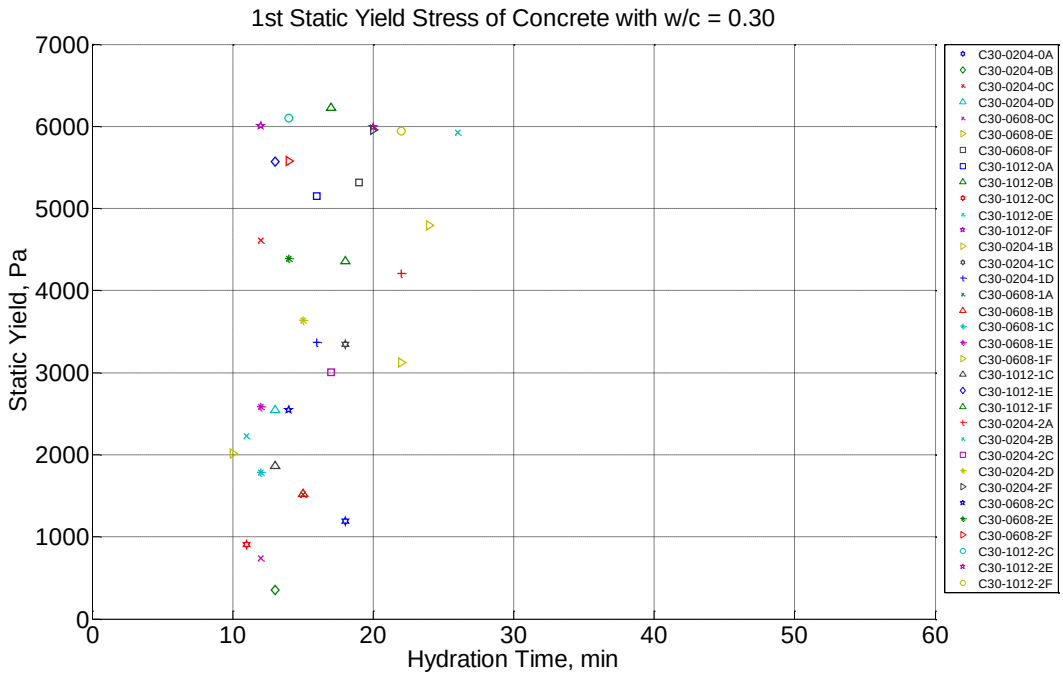

Figure 5-25 First measured static yield stress value of fresh concrete with water-to-cement ratio 0.40. The hydration time is the duration between water and cement first coming into contact in the mixer and the stress growth test being initiated.

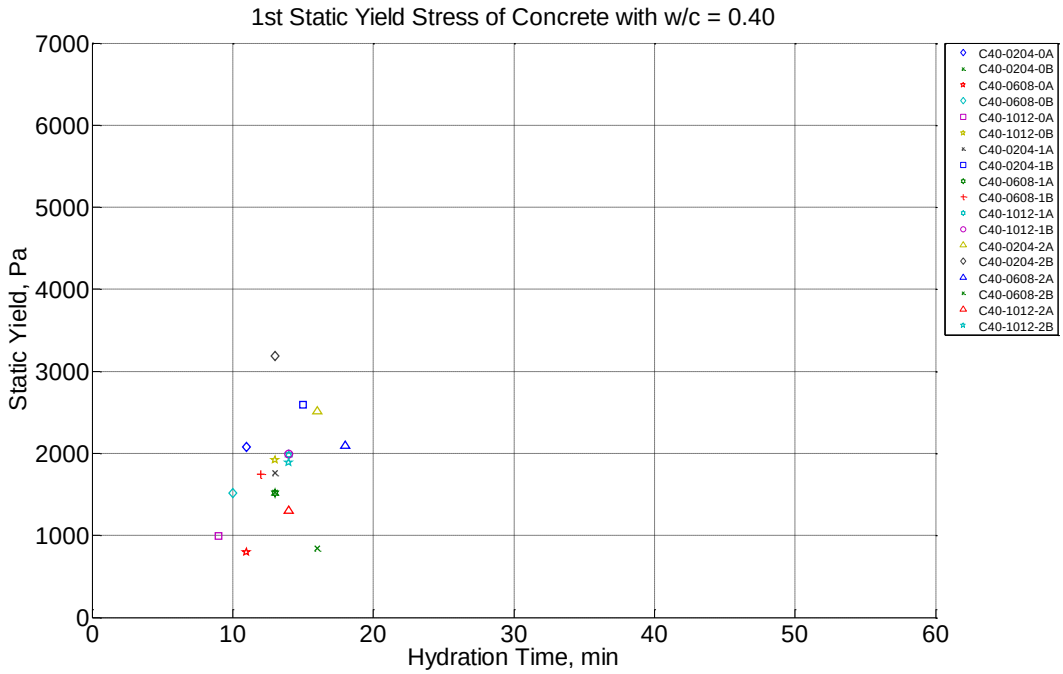

Figure 5-26 First measured static yield stress value of fresh concrete with water-to-cement ratio 0.30. The hydration time is the duration between water and cement first coming into contact in the mixer and the stress growth test being initiated.

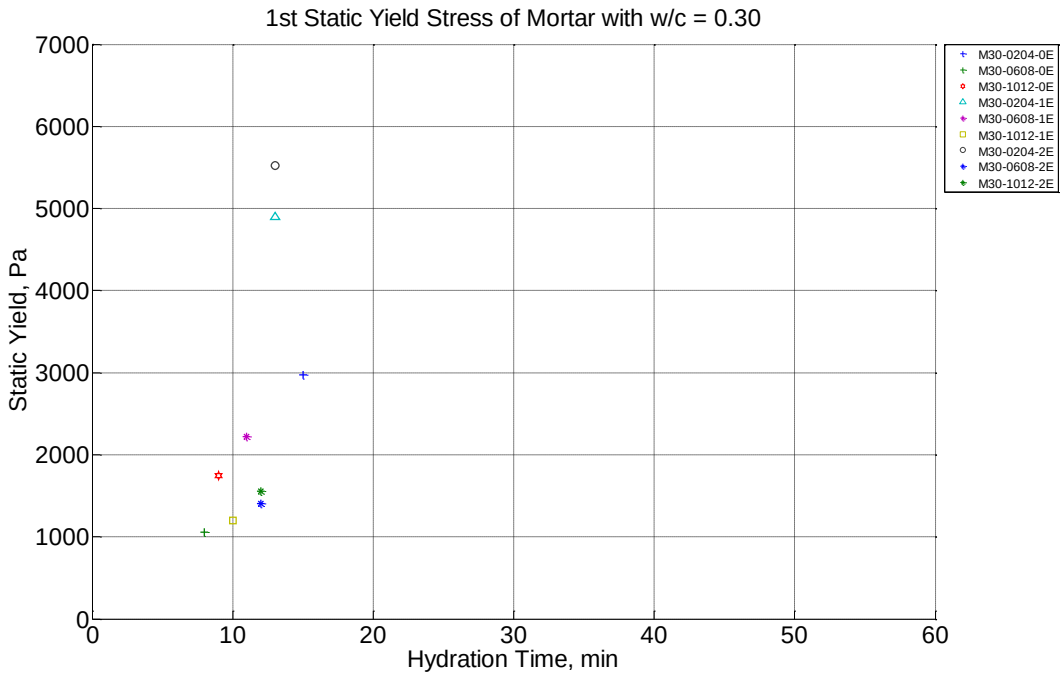

Figure 5-27 First measured static yield stress value of fresh mortar with water-to-cement ratio 0.30. The hydration time is the duration between water and cement first coming into contact in the mixer and the stress growth test being initiated.

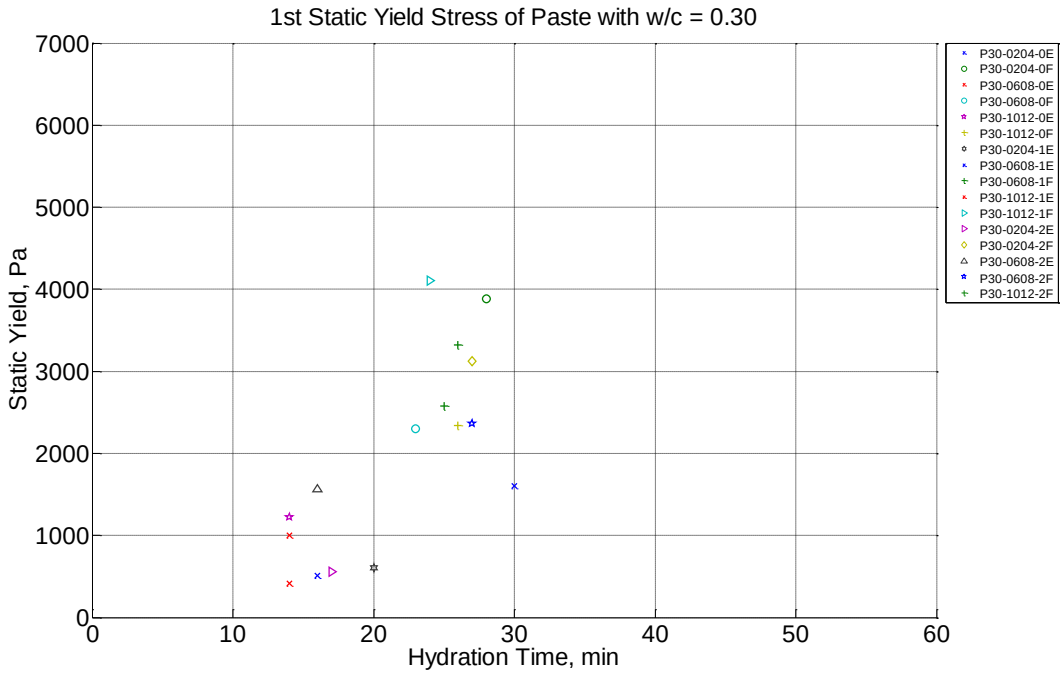

Figure 5-28 First measured static yield stress value of fresh paste with water-to-cement ratio 0.30. The hydration time is the duration between water and cement first coming into contact in the mixer and the stress growth test being initiated.

The dynamic yield stress is measured and the measurement can be repeated with the same material without significantly altering the value. Figures 5-29 through 5-32 show the repeated dynamic yield stress calculated from four material systems (concrete with water-to-cement ratio 0.40, concrete with water-to-cement ratio 0.30, mortar with water-to-cement ratio 0.30, and paste with water-to-cement ratio 0.30). With the exception of superplasticized concrete with water-to-cement ratio 0.30, the material systems generally have stable dynamic yield stress values that are repeatable with increasing hydration time. There is a slight increase in calculated shear stress due to ongoing hydration, but the ability of the ICAR rheometer to breakdown the fluid and generate flow is consistent for each material type when setting has not occurred. In this study, it is of importance that the dynamic shear stress is equitable across different hydration times, so any vibration of the material would generally allow for individual constituents (air bubbles or aggregates) to undergo movement governed by a singular, characteristic value.

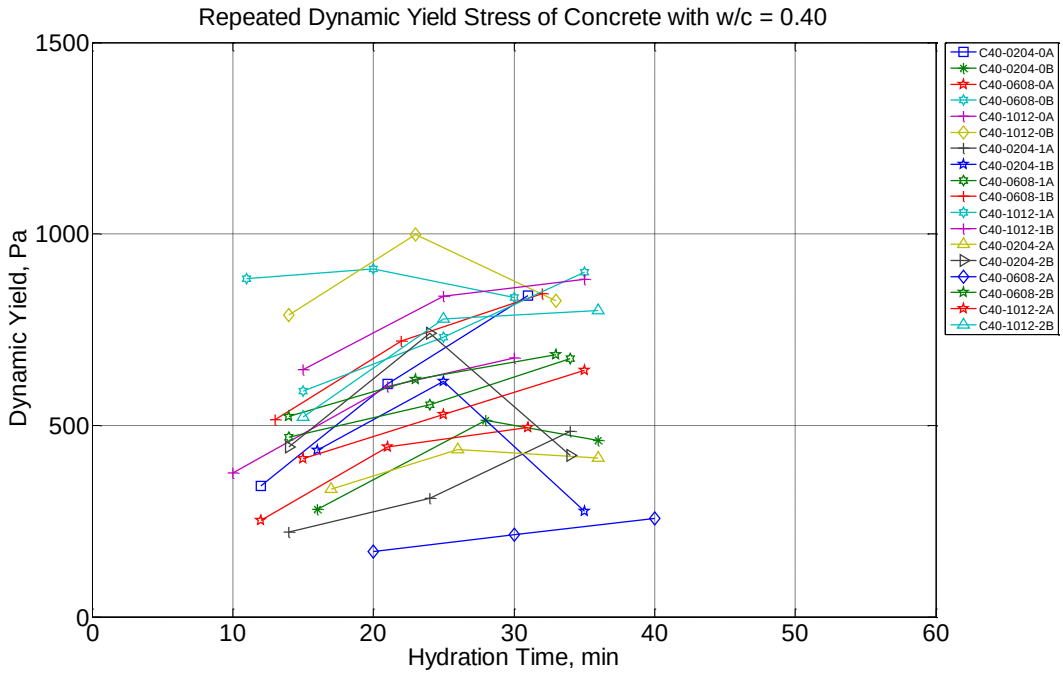

Figure 5-29 Repeated dynamic yield stress value of fresh concrete with water-to-cement ratio 0.40. The hydration time is the duration between water and cement first coming into contact in the mixer and the stress growth test being initiated.

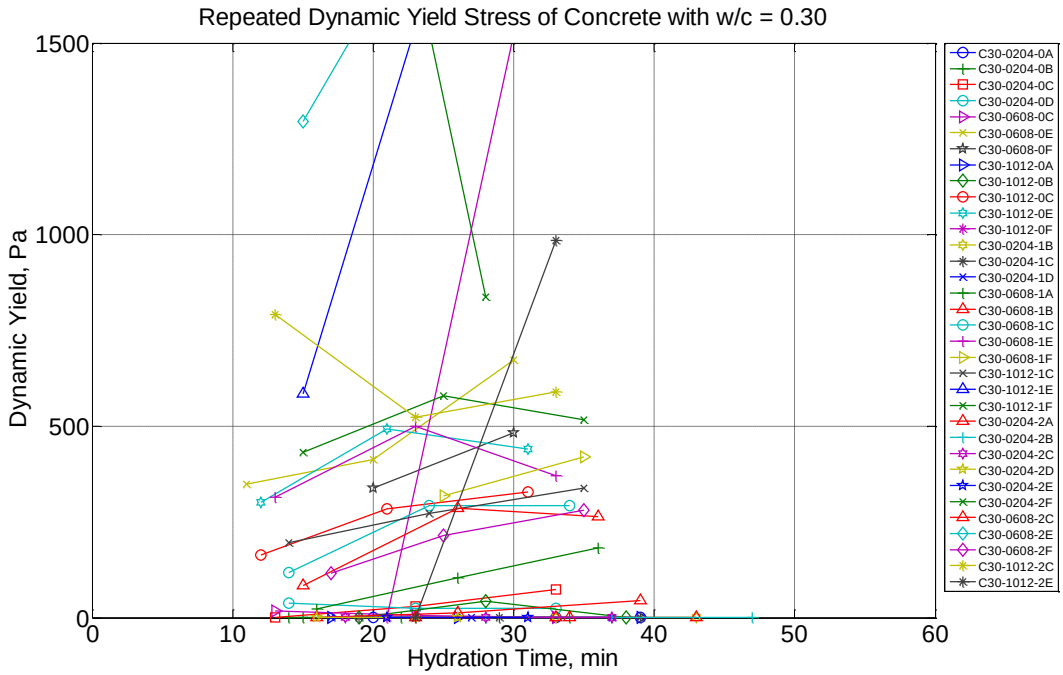

Figure 5-30 Repeated dynamic yield stress value of fresh concrete with water-to-cement ratio 0.30. The hydration time is the duration between water and cement first coming into contact in the mixer and the stress growth test being initiated.

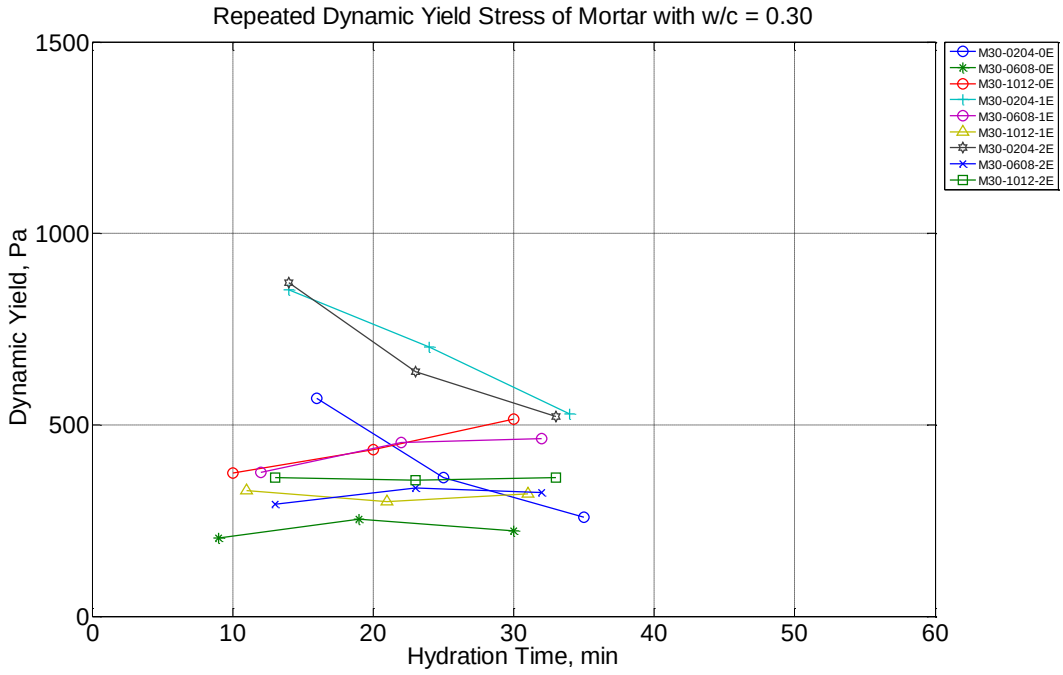

Figure 5-31 Repeated dynamic yield stress value of fresh mortar with water-to-cement ratio 0.30. The hydration time is the duration between water and cement first coming into contact in the mixer and the stress growth test being initiated.

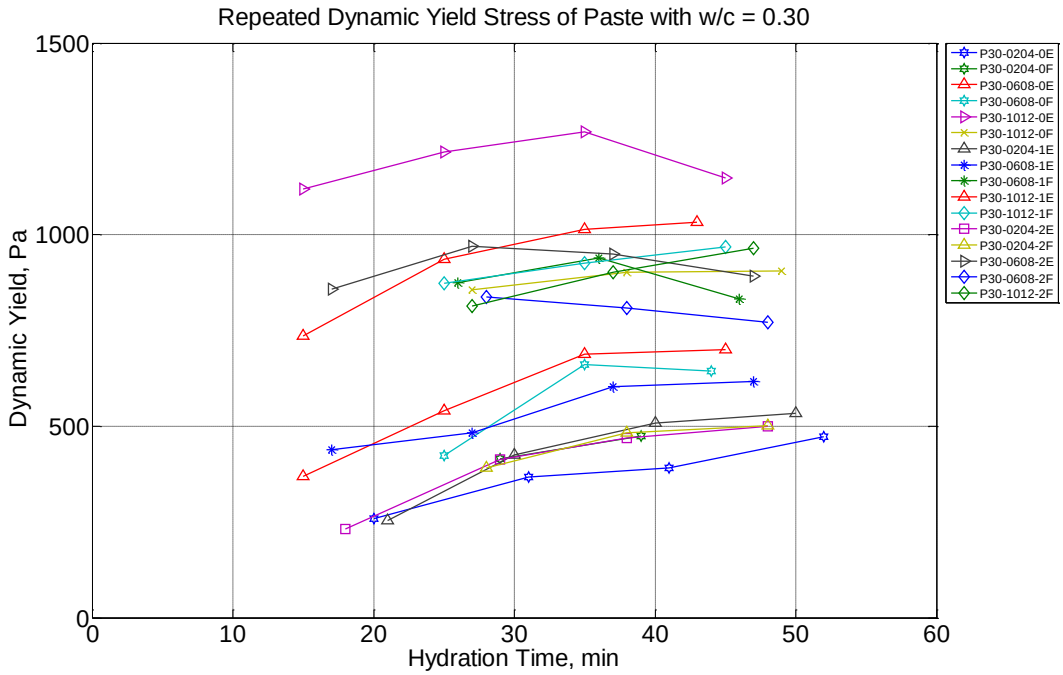

Figure 5-32 Repeated dynamic yield stress value of fresh paste with water-to-cement ratio 0.30. The hydration time is the duration between water and cement first coming into contact in the mixer and the stress growth test being initiated.

Similarly, the plastic viscosity value can be repeated on the same material and a characteristic value can be found for all the material systems in this study except for superplasticized concrete with water-to-cement ratio 0.30. In general, the repeatability of concrete with low water-to-cement ratio and superplasticizer yields varying results and is indicative of the sensitivity of high-flow concrete design against bleeding of the paste away from the aggregates. Moreover, the superplasticizing agent particularly reduces the dynamic yield stress of the system (see Figure 5-30) often leading to a mix where aggregates can more freely segregate and air bubbles more freely escape the system (see Figure 5-8). However, the superplasticizer can also work to increase the viscosity of the material system which drastically slows the movement of particles (see Figures 5-33 and 5-34) once movement is underway.

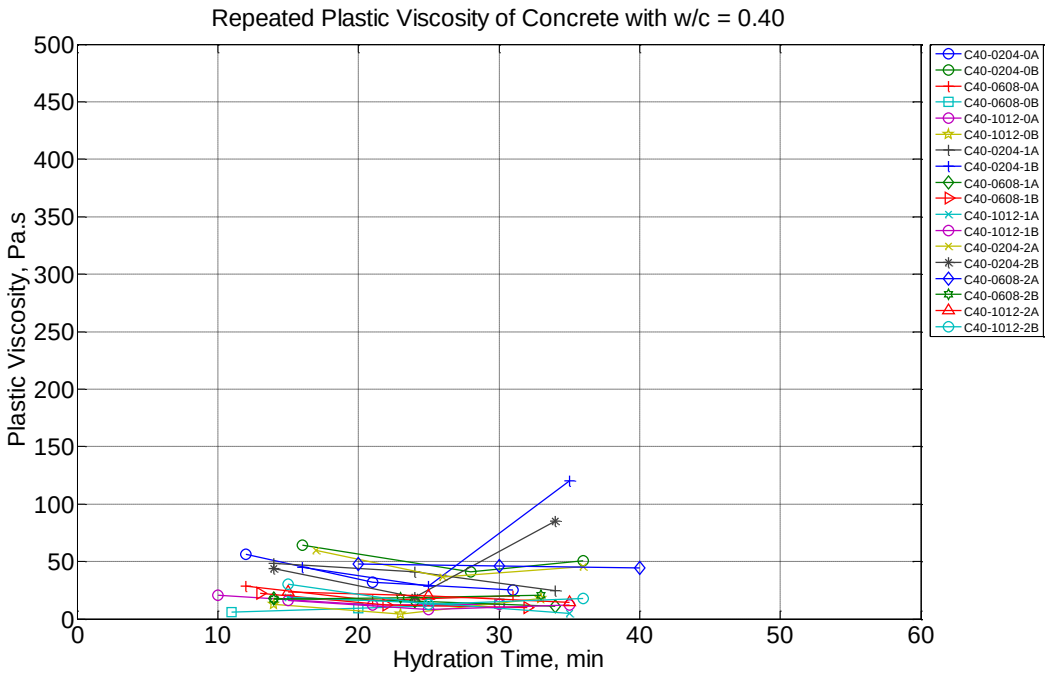

Figure 5-33 Repeated plastic viscosity value of fresh concrete with water-to-cement ratio 0.40. The hydration time is the duration between water and cement first coming into contact in the mixer and the stress growth test being initiated.

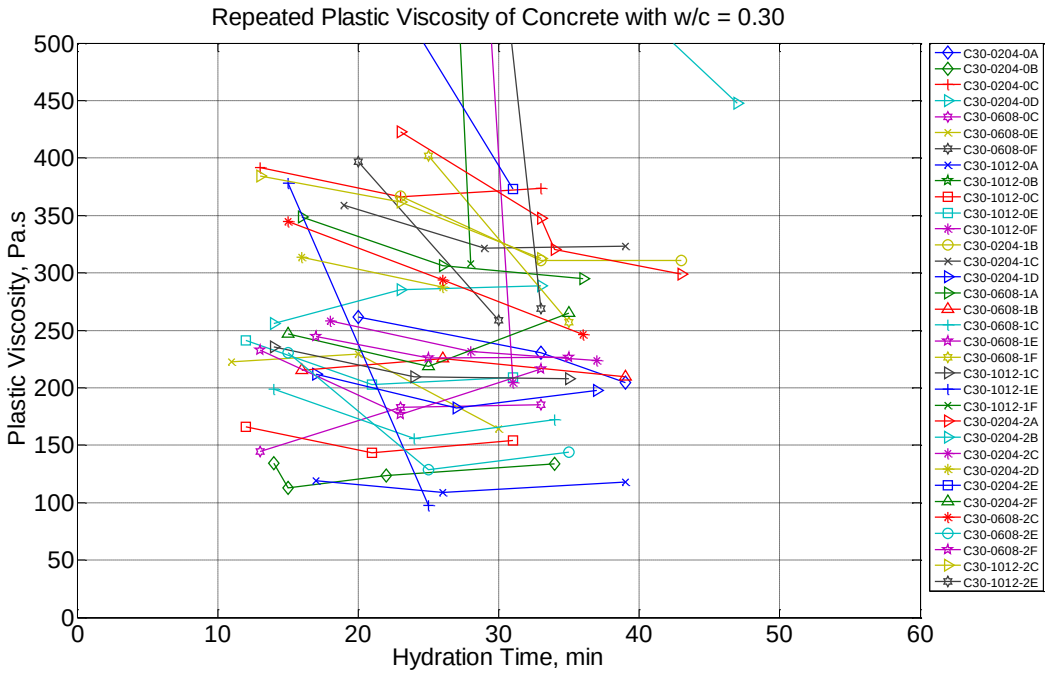

Figure 5-34 Repeated plastic viscosity value of fresh concrete with water-to-cement ratio 0.30. The hydration time is the duration between water and cement first coming into contact in the mixer and the stress growth test being initiated.

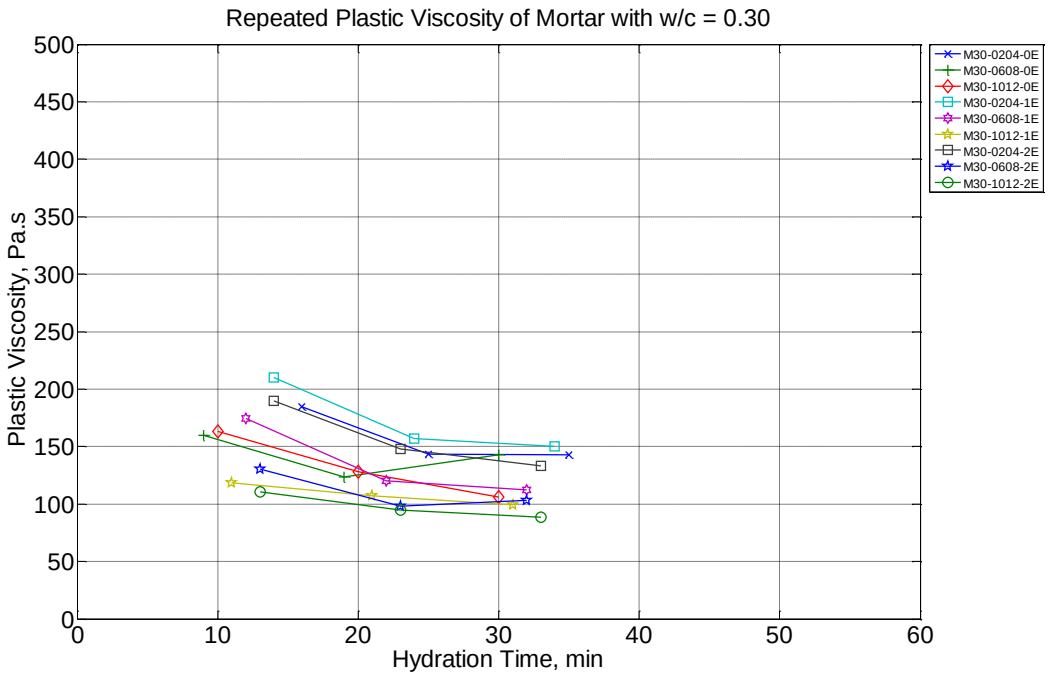

Figure 5-35 Repeated plastic viscosity value of fresh mortar with water-to-cement ratio 0.30. The hydration time is the duration between water and cement first coming into contact in the mixer and the stress growth test being initiated.

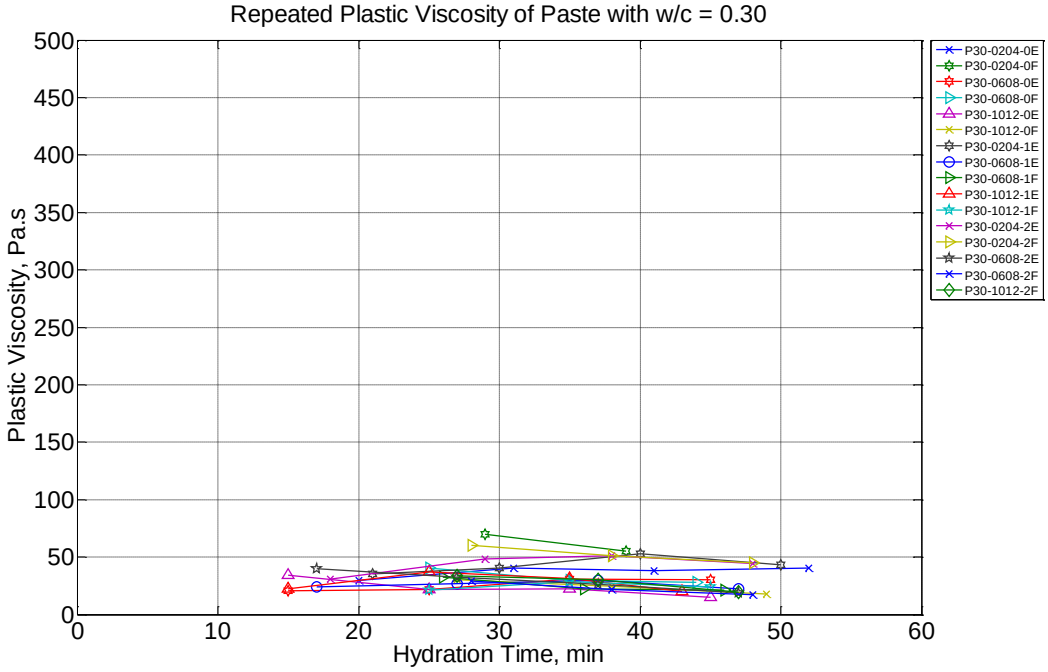

Figure 5-36 Repeated plastic viscosity value of fresh paste with water-to-cement ratio 0.30. The hydration time is the duration between water and cement first coming into contact in the mixer and the stress growth test being initiated.

5.7.3 Rheological properties with increasing aggregate content

The Modified Krieger-Dougherty relationship and the Chateau-Ovarlez-Trung model (see Equations 5-6 and 5-7) can be used to compare the increase in volume fraction of silica sand in a surrogate fluid (see Figures 5-18 and 5-19). Figure 5-37 shows the experimentally determined values of plastic viscosity against Equation 5-6 assuming K = -1.0 and ϕ_M = 0.56. There is general agreement of the data set from 0 to 45 % (by volume) to the model. At large volume fraction values, the agreement is not good. It is possible that at high volume fractions, the shearing action between the aggregate particles is causing an irreversible breakdown of the polyacrylate polymer chains. Figure 5-38 shows the experimentally determined values of shear stress compared against Equation 5-7 assuming K = -2.0 and ϕ_M = 0.56. There is good agreement from 0 to 63% volume fraction of ASTM C778 graded silica sand.

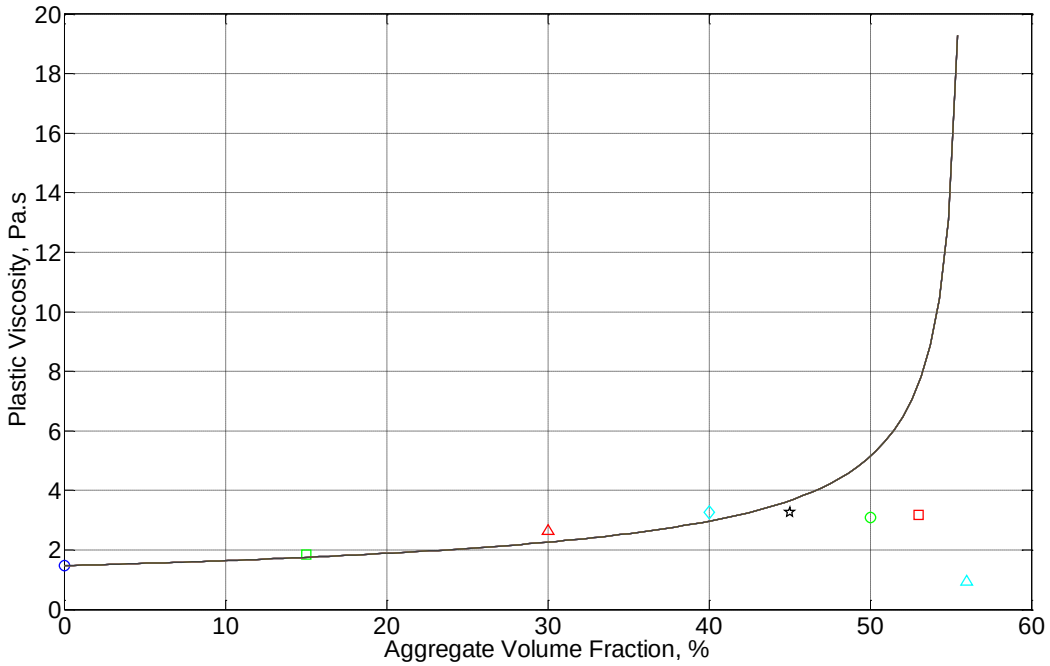

Figure 5-37 Experimentally measured plastic viscosity values in a surrogate fluid with increasing volume fractions of ASTM C778 graded silica sand. The Modified Krieger-Dougherty relationship is shown as a model line.

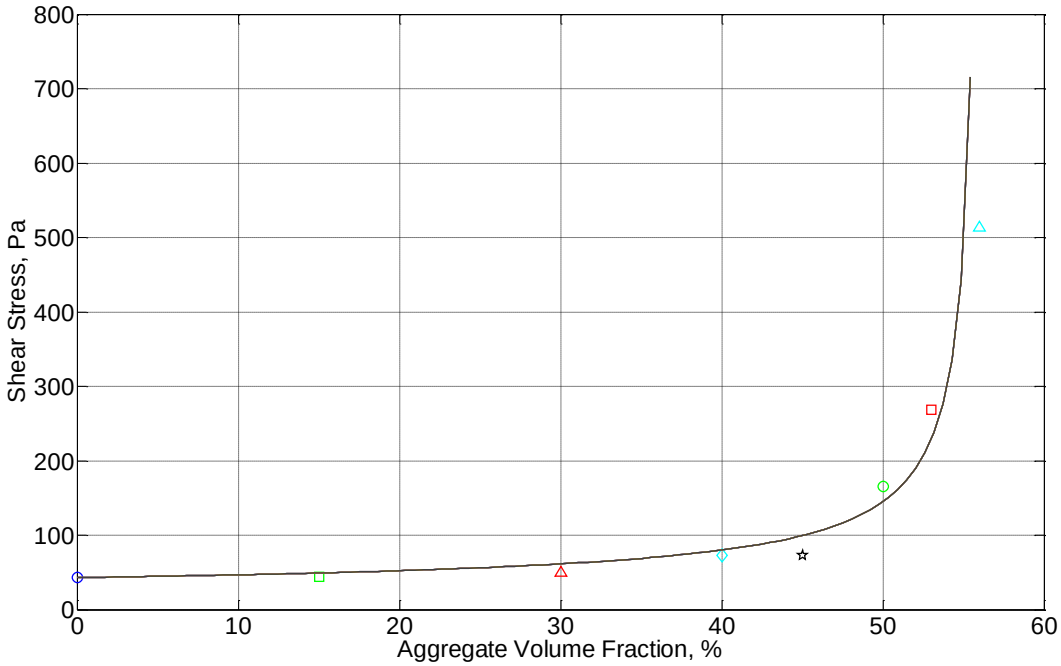

Figure 5-38 Experimentally measured shear stress values in a surrogate fluid with increasing volume fractions of ASTM C778 graded silica sand. The Chateau-Ovarlez-Trung model is shown as a model line.

5.7.4 Rheological properties with increasing vibration intensity

More recent work explains this change in rheology due to the breakup of granular force-chains as seen in Figures 5-21 through 5-23 [Hanotin and de Richter, 2015]. Under steady-state conditions (where there is no stress or strain gradient due to ramping up or ramping down of external vibration), then a constitutive model can be formulated

$$\left[\frac{\dot{\gamma}(t)}{\gamma_c} + f_b\right]\sigma(t) = [G + \eta_H f_b]\dot{\gamma}(t) + \eta_H \frac{\dot{\gamma}(t)^2}{\gamma_c} \qquad \text{Equation 5-12}$$

where $\sigma(t)$ and $\dot{\gamma}(t)$ are the time-dependent shear stress and shear strain rates, respectively; γ_c is the critical strain at which inter-granular forces are initially broken (i.e. the corresponding strain at the static shear stress magnitude); η_H is a model-fitted parameter that is equivalent to the plastic viscosity when the model fitted parameter for external vibration, f_b, is set to zero; and G is a model-fitted parameter. When no vibration is subjected to the material system, then Equation 5-12 transforms to

$$\sigma(t) = G\gamma_c + \eta_H\dot{\gamma}(t) \qquad \text{Equation 5-13}$$

where G can now be found when the dynamic shear stress (under no vibration) is separately measured. Under vibration, Equation 5-12 transforms to

$$\sigma(t) = \left[\frac{G}{f_b} + \eta_H\right]\left(\frac{\gamma_c f_b}{\dot{\gamma}(t)+\gamma_c f_b}\right)\dot{\gamma}(t) + \left[\eta_h + \frac{\dot{\gamma}(t)^2}{\gamma_c f_b}\right]\left(\frac{\gamma_c f_b}{\dot{\gamma}(t)+\gamma_c f_b}\right). \qquad \text{Equation 5-14}$$

For a simple consideration of a material with a shear stress of 100 Pa, a plastic viscosity of 10 Pa.s, and a critical strain rate of 0.1 (m/m), then the rheograph can be predicted across varying degrees of external vibration of the fit-parameter f_b (see Figure 5-39).

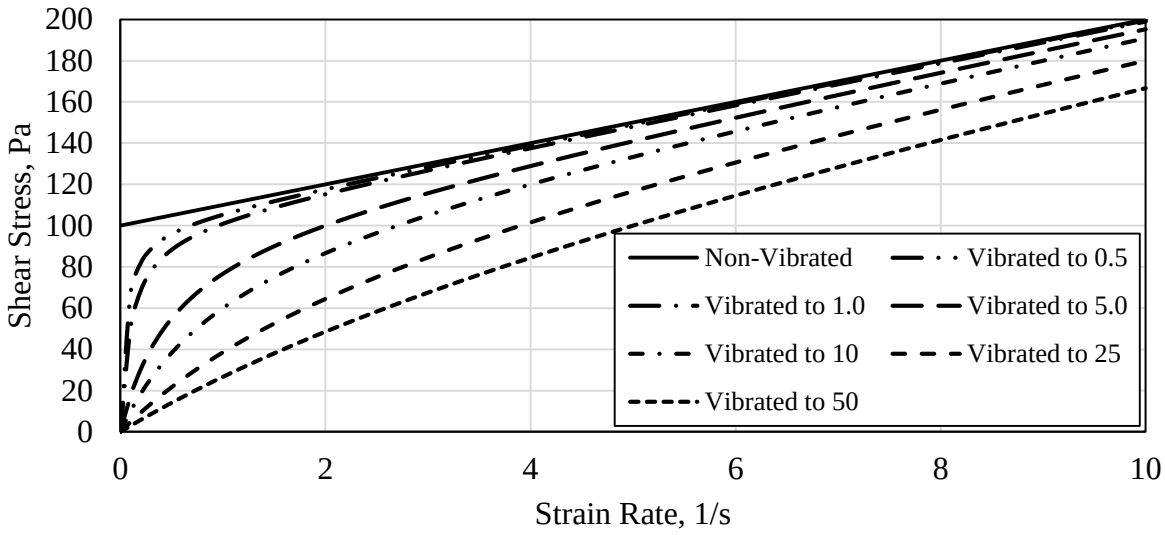

Figure 5-39 Predicted rheographs of a fluid undergoing varying degrees of vibration.

5.7.5 Extent of air loss (speed) due to aggregate content and external vibration

The presence of an air bubble and the movement of the air bubble is complicated by the presence of aggregates. The rheology of concrete as it is measured cannot aptly predict the flowability of a buoyantly rising air bubble. Instead, it is of interest to better understand the flow of an air bubble rising through a mortar suspension or paste suspension. Table 5-8 shows the range of plastic viscosity values observed from Figures 5-33 through 5-36. These plastic viscosity values can be modified by Equation 5-6 to predict the underlying viscosity of the suspension fluid. In doing so, the plastic viscosity of the paste (i.e. suspension) can be computed for each concrete and

mortar mixture. In doing so, Equation 5-4 can be applied in order to predict the rise speed of individual air bubbles in neat fluids of equivalent plastic viscosity. Small sized, 10 μm diameter air bubbles rise at rates of 0.1 to 1 nm/s. Given ample vibration time, these small bubbles do not rise sufficiently to escape the system. A 1000 μm diameter air bubble, alternatively, can rise at speeds of 10-1000 μm/s. The buoyancy of these larger sized air bubbles causes them to rise faster and for a comparable amount of vibration time are quicker to leave the fresh material system.

Table 5-8 Measured plastic viscosity values and computed viscosity values predicted by the Modified Krieger-Dougherty relationship.

	w/c	**μ_p (Pa.s)**	**Φ_{CA}**	**Φ_{FA}**	**μ_{mortar} (Pa.s)**	**μ_{paste} (Pa.s)**	**$V_{10\ \mu m}$ (nm/s)**	**$V_{100\ \mu m}$ (μm/s)**	**$V_{1000\ \mu m}$ (μm/s)**
Concrete	0.40	0 - 50	0.45	0.50	0 - 5.5	0 - 0.605	0.92 - ∞	9.18 - ∞	918 - ∞
	0.30	100 - 500	0.45	0.50	11 - 55	1.21 - 6.05	0.092 - 0.459	0.918 - 4.59	91.8 - 459
Mortar	0.30	100 - 200	-	0.62	-	11 - 22	0.0252 - 0.050	0.252 - 0.505	25.2 - 50.5
Paste	0.30	25 - 50	-	-	-	-	0.011 - 0.022	0.111 - 0.222	11.1 - 22.2

5.8 Summary of Chapter

Concrete is air-entrained using chemical admixtures in order to enhance the freeze-thaw durability. Concrete may also be superplasticized in order to increase the fluidity of the mixture. However, this enhance fluidity and subsequent consolidation techniques are not optimized for the retention of entrained air bubbles which can rise up under buoyant forces and exit the fresh material system during handling and vibration thus reducing the resiliency of the concrete material to withstand cyclic freeze-thaw damage. Fresh cement-based materials and surrogate fluids were studied for their rheology as physical constituents (i.e. aggregates) and external vibration were applied. It is found that:

- Consolidating vibration increase density and decreases fresh air content in mixture types that contain aggregates (i.e. concrete and mortar). Consolidating vibration does not affect Portland cement paste samples as strongly.
- The compression strength of concrete is affected by the amount of fresh air content and partially affected by the extent of external vibration where entrained air may cluster at the

underside of an aggregate leading to a locally weak zone, thus reducing compression strength.

- The experimentally measured rheology of Portland cement-based and surrogate fluids are strongly affected by aggregate volume content. Already existing models (Modified Krieger-Dougherty and Chateau-Ovarlez-Trung) can adequately predict the response due to changing volume aggregate contents.
- The experimentally measured rheology of a Portland cement-based system is strongly affected by superplasticizing admixtures which leads to large variability in the measured yield stress and plastic viscosity, which ultimately affects workability.
- The experimentally measured rheology of any granular system is strongly affected by external consolidation which significantly suppresses the dynamic yield stress, meaning that entrained air bubbles and aggregates are subject to faster rise speeds than would normally be predicted for a material whose rheology is measured at rest. A granular, force-chain model may be suitable if the vibration parameter can be better understood and correlated against mean peak acceleratory values.
- The extent and attenuation of peak vibration inside a fluid may not be uniform in even simply geometries suggesting that consolidation of concrete by table-top or immersion probe vibrators may not be well understood for granular systems.

5.9 References

ACI 309.1R-08. Report on Behavior of Fresh Concrete During Vibration. Reported by ACI Committee 309. 2008.

Banfill, P. F. G. "The rheology of fresh cement and concrete – a review." *11th Cement Chemistry Congress* (2003): Durban.

Banfill, P. F. G., Teixeria, M. A. O. M., and Craik, R. J. M. "Rheology and vibration of fresh concrete: predicting the radius of action of poker vibrators from wave propagation." *Cement and Concrete Research* 41 (2011): 932 – 941.

Banfill P. F. G., Yongmo, X., and Domone, P. L. J. "Relationship between the rheology of unvibrated fresh concrete and its flow under vibration in a vertical pipe apparatus." *Magazine of Concrete Research* 51 (1999): 181 – 190.

Barnes, H. A. and Nguyen, Q. D. "Rotating vane geometry – a review." *Journal of Non-Newtonian Fluids Mechanics* 98 (2001): 1 – 14.

Boulekbache, B., Hamrat, M., Chemrouk, M., and Amziane, S. "Flowability of fibre-reinforced concrete and its effect on the mechanical properties of the material." Construction and Building Materials 24 (2010): 1664 – 1671.

Chong, J. S., Christiansen, E. B., and Baer, A. D. “Rheology of concentrated suspensions.” *Journal of Applied Polymer Science* 15 (1971): 2007 – 2021.

Costello, B. “The AR-G2 Magnetic Bearing Rheometer.” *TA Instruments Product Information* (accessed February 9, 2016): http://www.tainstruments.com/pdf/literature/RH085_AR_G2_performance.pdf

Dabak, T., and Yucel, O. “Shear viscosity behavior of highly concentrated suspensions at low and high shear rates.” *Rheologica Acta* 25 (1986): 527 – 533.

Farouki, O. T., and Winterkorn, H. E. “Mechanical properties of granular systems.” *Highway Research Record* 52 (1964): 10 – 42.

Ghafoori, N. and Barfield, M. “Effects of hauling time on air-entrained self-consolidating concrete.” *ACI Materials Journal* 107 (2010): 275 – 281.

Hanotin, C., and de Richter, S. K. “Viscoelasticity of vibrated granular suspension.” *Journal of Rheology* 59 (2015): 253 – 273.

Koehler, E. P., Fowler, D. W., Ferraris, C. F., and Amziane, S. “A new, portable rheometer for fresh self-consolidating concrete.” *ACI Special Publication 233-7* (2006): 97 – 116.

Krieger, I. M., and Dougherty, T. J. “A mechanism for non-Newtonian flow in suspension of rigid spheres.” *Transactions of the Society of Rheology* 3 (1959): 137 – 148.

L’Hermite, R. “Up to date ieas in concrete technology.” *La Documentation Technique du Batiment et des Travaux Publics* (1955): Paris.

Laskar, A. I. and Bhattacharjee, R. “Toque-speed relationship in a concrete rheometer with vane geometry.” *Construction and Building Materials* 25 (2011): 3443 – 3449.

Liddell, P. V. and Boger, D. V. “Yield stress measurements with the vane.” *Journal of Non-Newtonian Fluid Mechanics* 63 (1996): 235 – 261.

Liu, D. M. “Particle packing and rheological property of highly-concentrated ceramic suspensions: φ_m determination and viscosity prediction.” *Journal of Materials Science* 35 (2000): 5503 – 5507.

Mahaut, F., Mokéddem, S., Chateau, X., Roussel, N., and Ovarlez, G. “Effect of coarse particle volume fraction on the yield stress and thixotropy of cementitious materials.” *Cement and Concrete Research* 38 (2008): 1276 – 1285.

Mikanovic, N., and Jolicoeur, C. “Influence of superplasticizers on the rheology and stability of limestone and cement pastes.” *Cement and Concrete Research* 38 (2008): 907 – 919.

Mooney, M. J. “The viscosity of a concentration suspension of spherical particles.” *Journal of Colloid Science* 6 (1951): 162 – 170.

Papo, A., and Piani, L. “Effect of various superplasticizers on the rheological properties of Portland cement pastes.” *Cement and Concrete Research* 34 (2004): 2097 – 2101.

Popovics, S. “A review of the concrete consolidation by vibration.” *Materiaux et Constructions* 6 (1973): 453 – 463.

Roscoe, R. “The viscosity of suspensions of rigid spheres.” *British Journal of Applied Physics* 3 (1952): 267 – 269.

Saul, A. G. A. “Suggested mechanical principles underlying the vibration of concrete.” *Technical Report* TRA 303 *Cement and Concrete Association* (1958): London.

Struble, L. J., and Sun, G.-K. “Cement viscosity as a function of concentration.” *Proceedings of the Materials Research Society Symposium* 289 (1993): 173 – 176.

Tattersall, G. H., and Baker, P. H. “The effect of vibration on the rheological properties of fresh concrete.” *Magazine of Concrete Research* 40 (1988): 79 – 89.

Tattersall, G. H. and Banfill, P. F. G. *The rheology of fresh concrete*. 1983, London: Pitman Books.

Vikan, H., Justnes, H., Winnefeld, F., and Figi, R. “Correlating cement characteristics with rheology of paste.” *Cement and Concrete Research* 37 (2007): 1502 – 1511.

CHAPTER 6 – EXTENSION OF VIBRATORY RADIUS OF ACTION IN FRESH PORTLAND CEMENT-BASED MATERIALS AND SURROGATE FLUIDS DUE TO INCREASING AGGREGATE VOLUME FRACTION

6.1 Acknowledgement

The development of this chapter is accomplished with extensive testing of fresh concrete, mortar, paste, and surrogate materials. This work produced approximately 10 tons of fresh material throughout testing which was regularly discarded. For this laborious work that cannot have been accomplished by the author alone, I am thankful to undergraduate students Clare Curtin, Mark Keller, and Kevin Marks.

6.2 Abstract

Consolidation and vibration of fresh concrete is largely driven by the need to achieve adequate compaction, optimize ultimate mechanical strength properties, and reduce honeycombing and other surface defects (e.g. bugholes). However, extensive vibration can also result in aggregate segregation, excessive bleeding, and loss of entrained air. In this study, the effect of an immersion vibratory probe on fresh Portland cement paste, mortar, concrete, and model materials is assessed. The average peak acceleration within the fresh, bulk material is measured as a function of distance away from the vibration source. The rheological properties (plastic viscosity and yield stress slope intercept) are additionally measured for each material mix. It is generally found that the peak acceleration attenuates appreciably more than current design guidelines suggest. The attenuation is closely related to the presence of aggregates which can extend the radius of vibratory action in mixes of comparable rheology but with higher (jamming) volume content. Moreover, finite-width molds in which fresh material is consolidated can be subject to constructive and destructive wave interference that can have impacts on locally over-consolidated volume of fresh material when vibrated at one end.

6.3 Introduction and Background

6.3.1 The practice of concrete vibration

Concrete is vibrated in order to drive out entrapped air and to minimize defects (honeycombing, bug-holes, pockets, e.g.) around the reinforcement and form walls. ACI Committee 309 (reports 309.1. and 309.8) provide guidance about consolidation methods for concrete practitioners [ACI 309]. Figure 6-1 shows the principle of internal vibration and surface vibration where rapidly recurring compression waves emanate from the source of vibration. Often, each pulse is generated by an eccentrically positioned mass rotating about an axis encased in a housing. The eccentricity of the vibrator thus imparts energy onto the fresh material through the housing directly (as is the case in an immersion pencil probe vibrator) or imparts energy onto the formwork directly. Thereafter, the formwork imparts the energy onto the fresh material.

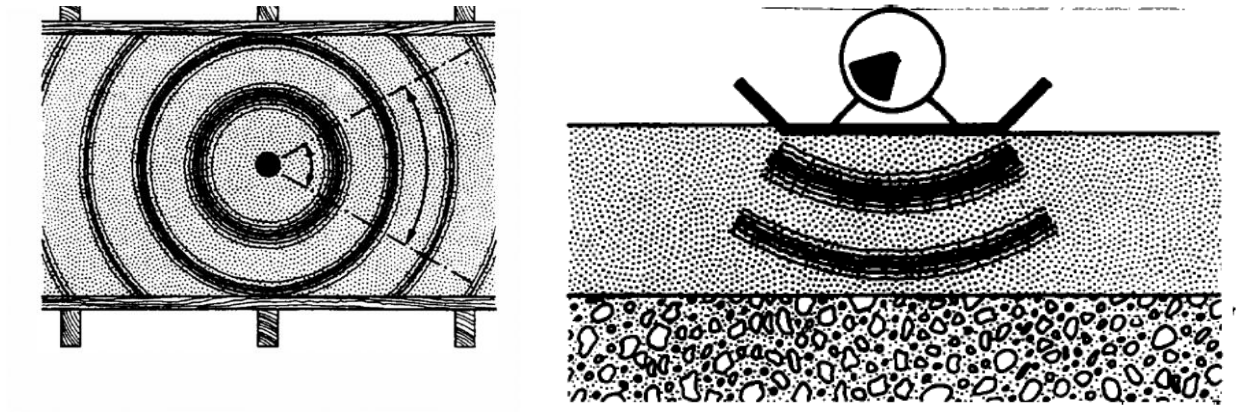

Figure 6-1 Circularly emanating compression waves from internal (left) and external (right) source of vibration (from ACI 309).

The effectiveness of the vibration source to impart energy onto the fresh material is dependent upon several factors, including the frequency of the impulse and the amplitude of the impulse. The efficiency of consolidating vibration is often considered with regards to final material density and ultimate compressive strength. Figure 6-2 shows optimized curves of frequency and amplitude in order to achieve a radius of action in which favorable density is achieved across a large volume of fresh material. Peaks in the curve suggest that a frequency or amplitude that is set too large in value can lead to a reduction in the volume of material being ideally compacted. This set of curves informs the industry to design consolidating vibration equipment to target

approximately 200 – 240 Hz and a large amplitude (as allowable by the frequency) in order to maximize adequate consolidation of the fresh concrete material. However, relatively little information is relayed about the effects of time of vibration, mold geometries, material proportioning, and entrained air bubble size distribution as affected by these two parameters. As such, control of entrained air can be challenging for concrete products that undergo vibration during final placement.

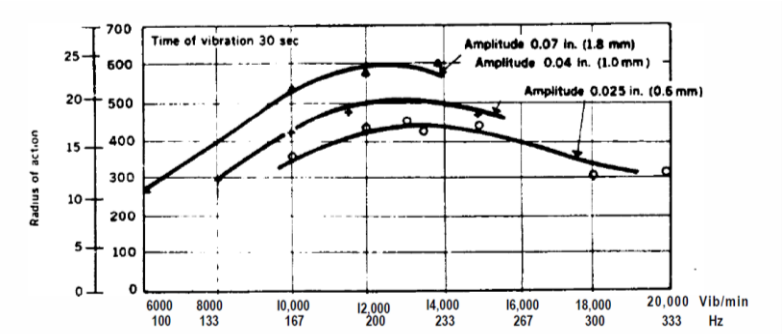

Figure 6-2 Maximization of radius of action of a 2.5 inch diameter immersion probe with varying frequency and amplitude settings (from ACI 309).

The selection of amplitude and frequency imparts energy into the fresh material system that decays due to attenuation. ACI 309 recommends the use of Dessoff's formulation to predict the attenuation of the energy distribution as a function of distance [Dessoff, 1937]. The formulation is corrected by others to show [Banfill *et al.*, 2011; Grampiex, 2013]

$$s_2 = s_1\sqrt{\frac{R_1}{R_2}e^{-(\frac{\Omega}{2})(R_2-R_1)}} \qquad \text{Equation 6-1}$$

where s_2 and s_1 are the amplitudes of the compression waves at distances R_2 and R_1, respectively, from the centerline of the immersion probe; and Ω is a coefficient of damping factor, usually 0.04 to 0.08 for plastic flowing concrete.

6.3.2 Propagation of vibration in fresh Portland cement concrete

The effect of external vibration is observed to vary with respect to the distance from the source of vibration. Near the source of vibration, there is an area of semi-liquid fluid while far from the source of vibration, there is an area of semi-solid fluid. The transformation from the semi-fluid to semi-solid can be described as the vibrational radius action. In the semi-fluid, the

vibrational source more strongly affects the material through shear wave propagation while in the semi-solid, the vibration is transmitted via compressive waves [Banfill *et al.*, 2011]. In the semi-fluid region, it is postulated that the kinetic energy of the vibration source reduces the dynamic yield stress to a near-zero value resulting in a nearly ideal Newtonian fluid with Power-law behavior [Tattersall and Baker, 1988]. In Tattersall and Baker's work, the authors found that the dominant factor affecting the fluidization of the concrete was the peak velocity, *v*, of the vibration. The variation of velocity with respect to time, *t*, is described as [Banfill *et al.*, 1999]

$$v = 2\pi A f \sin 2\pi f t \qquad \text{Equation 6-1}$$

where *f* is the frequency, *A* is the amplitude. The maximum velocity is thus [Tattersall and Baker, 1988]

$$v_{peak} = 2\pi A f. \qquad \text{Equation 6-2}$$

At a point of maximum velocity, the dynamic shearing stress can be driven to near-zero, meaning that the fresh concrete material is fluidized (see Chapter 5 for additional discussion on concrete rheology). Banfill *et al.* describe additional material dependent limits that vibration can have no effect because the amplitude is too low or the frequency is too high (a term the authors describe as the *fluidity*). Moreover, the authors describe the propagation of shear and compression wave forms within fresh concrete. Near the vibration probe, the maximum velocity fluidizes the concrete with a shearing force that exceeds the material's dynamic yield stress. In such an instance, the fresh concrete behaves as a fluid and can preferentially transmit shear waves by aggregate-to-aggregate interactions. When the vibrational shearing force is attenuated to a value below the material's dynamic yield stress, then the fresh concrete behaves as a solid and can preferentially transmit compression waves. In their experimental work, Banfill *et al.* measure peak acceleratory values inside fresh concrete as it is vibrated and compared the values to predicted shear- and compression-waves traveling (and attenuating) through the fresh material (see Figure 6-3). In their work, the authors propose that the predicted inversion of the shear and compression waveforms is indicative of the "radius of action" where material is either fluidized or plastic-solid.

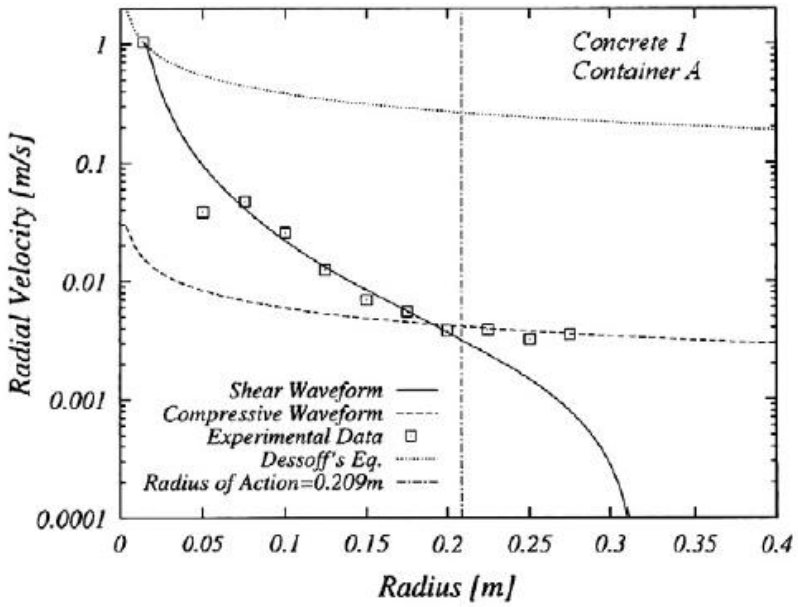

Figure 6-3 Experimentally measured acceleratory values inside fresh concrete vibrated by an immersion probe and compared against predicted shear- and compression-waveform distributions (from Banfill *et al.*, 2011).

6.4 Significance of Research

Concrete is vibrated by a number of different means in order to achieve good consolidation. One mean of vibration in precast operations is probe vibration where the radius of action as evidence from the surface of the concrete is expected to adequately consolidate concrete. In this study, it is observed that the volume content of aggregates plays a strong role in extending the radius of action in fresh concrete. Moreover, high volume fraction of aggregates in Portland cement-based and surrogate fluid granular systems is seen to affect the dominant waveform as evidenced by the longitudinal and transverse mean peak acceleration values, meaning that a better understanding consolidation practices must be understood.

6.5 Experimental Methods

Two material systems (Portland cementitious paste, mortar, and concrete; and Carbopol 980 Polymer with silica sand and glass marbles) were considered in this study. A significant drawback of measuring the rheology of Portland cementitious materials is that they are undergoing hydration which results in gelling and increasing yield stress and plastic viscosity with respect to

time. Carbopol 980 Polymer is an unreactive Bingham fluid that can serve as a surrogate fluid of Portland cement paste. As such, effects of hydration and thixotropy can be discounted.

6.5.1 Materials and equipment

The first material system considered is Portland cement-based paste, mortars, and concrete. The paste is a water-to-cement ratio of 0.30 (by mass) that is dosed with a set-retarding (MasterSet DELVO), superplasticizing (Sika Viscocrete 2100), and air-entraining (Sika AEA-14) chemical admixtures (see Table 6-1). The size distribution of sand particles is given in Table 6-2. Specifically, the sand used in the Portland cement-based mortars and concrete conforms to Illinois Department of Transportation (IDOT) FA02 blend. In order to make concrete, gravel is added to the mortar. A comparable concrete mixture using a water-to-cement ratio of 0.40 (by mass) is also considered for its rheological properties. The gravel used in the Portland cement-based concrete is crushed limestone, and its size distribution conforms to IDOT CA07 blend (see Table 6-3).

Table 6-1 Nominal paste mix design.

Material Type	**w/c = 0.30**	
	Pounds Per Cubic Yard	**Kilograms Per Cubic Meter**
Type I Portland Cement	2696	1599
Water	809	480
Set-Retarding Agent	6 fl. oz per 100 lb. cementitious (391 mL per 100 kg cementitious)	
Superplasticizing Agent	10 – 16 fl. oz per 100 lb. cementitious (652 – 1,043 mL per 100 kg cementitious)	
Air-Entraining Agent	0, 3, or 6 fl. oz per 100 lb. cementitious (0, 196, or 391 mL per 100 kg cementitious	

Table 6-2 Gradation (percent passing) of various sand types.

			Specific Gravity	3/8" (9.5mm)	No. 4 (4.75 mm)	No. 8 (2.36 mm)	No. 10 (2.00 mm)	No. 16 (1.18 mm)	No. 30 (600 µm)	No. 40 (425 µm)	No. 50 (300 µm)	No. 80 (180 µm)	No. 100 (150 µm)	No. 200 (75 µm)
FA	IDOT FA 2	*Lab River Sand*	2.63	100	97 ± 3			65 ± 20			20 ± 10		5 ± 5	
	ASTM C778	*Ottawa Graded Sand*	2.65					100	98 ± 2	70 ± 5	25 ± 5		2 ± 2	
	ASTM C33	*Fine Aggregate*		100	97.5 ± 2.5	90 ± 10		67.5 ± 17.5	42.5 ± 17.5		17.5 ± 12.5		5 ± 5	1.5 ± 1.5

Table 6-3 Gradation (percent passing) of various gravel types.

			Specific Gravity	3" (75 mm)	2.5" (63 mm)	2" (50 mm)	1.5" (37.5 mm)	1" (25 mm)	3/4" (19 mm)	1/2" (12.5 mm)	3/8" (9.5 mm)	No. 4 (4.75 mm)	No. 16 (1.18 mm)	No. 50 (300 µm)	No. 200 (75 µm)
CA	IDOT CA 7	*Limestone*	2.75				100	95 ± 5		45 ± 15		5 ± 5			
	IDOT CA 12	*Limestone*							100	95 ± 5	85 ± 10	60 ± 10	35 ± 10		
	IDOT CA 16	*Chip*	2.67							100	97 ± 3	30 ± 15	2 ± 2		

Carbopol 980 Polymer is a crosslinked polyacrylate polymer that is mixed with water to form a clear gel that is stable at neutral pH. The gel features design-controllable yield stress and viscosities that can suspend particles and air while maintaining a high amount of clarity through the material. In order to make Carbopol-based mortar, ASTM C778 graded sand is used and the particle size distribution is shown in Table 6-2.

The volume fraction of the river sand, silica sand, and limestone aggregate is varied in order to draw insight into the effect of aggregates on the attenuation of peak vibratory acceleration. All materials are mixed in a 2 cubic-foot capacity flatbed pan shearing mixer or in a 5-gallon bucket with a handheld paddle mixer. The rheological properties of the fresh materials were measured using an ICAR Rheometer which measures the rheology using a rotating vane propeller. The ICAR rheometer was developed by the International Center for Aggregate Research (ICAR) at the University of Texas at Austin in order to better characterize the rheological properties of concrete [Koehler *et al.*, 2006]. Both the cementitious and model materials were treated as Bingham plastics, which are characterized by a dynamic yield stress (tangent intercept) and plastic viscosity (slope at large shear strain rate). The static yield stress was also measured, but is not considered in the determination of the Bingham fit parameters.

6.5.2 Average peak acceleration of cement paste, mortar, concrete, and model materials

A 6 inch by 6 inch by 48 inch (15.24 cm by 15.24 cm by 122 cm) Plexiglas mold was constructed to hold fresh Portland cement-based materials and Carbopol 980 polymer-based materials. A 220 Hz 1 inch (2.54 cm) diameter DeWalt pencil vibrator was positioned at one end of the prismatic mold approximately 3 inches (7.6 cm) away from the three form walls to a depth of 5.5 inches (14 cm). A three-axis (triaxial) water-proof accelerometer (W356A12) from PCB Piezotronics is used to measure the peak acceleration and was positioned using an adjustable lever arm at increasing distances from the immersion probe at a constant depth of 3 inches (7.62 cm). The accelerometer is firmly affixed onto an aluminum rod (attached to the lever arm) and additionally covered in nitrile layer in order to maintain the cleanliness of the sensor. The accelerometer and rod are immersed into the fresh material at a constant depth and varying distances. The distance of the accelerometer varies from 5 to 45 inches (12.7 to 114.3 cm) from

the top surface. Figure 6-4 shows the relative location of the immersion rod and the multiple locations where the accelerometer was positioned.

Figure 6-4 Illustration of immersion pencil (probe) vibrator in 48-inch long Plexiglas mold where stars represent the nominal location of an immersed accelerometer spaced 1 or 2 inches apart during vibratory testing.

6.6 Results and Discussion

6.6.1 Rheological measurements of paste, mortar, and concrete

Table 6-4 shows the rheological properties of paste (labeled Mortar30 – 00% CA; 00% FA; 100% CP) and mortar with increasing volume fractions of fine aggregate (20, 40, and 60 % FA). Table 6-5 shows the rheological properties of mortar (labeled Concrete30 – 00% CA; 40% FA; 60% CP) and concrete with water-to-cement ratio 0.30 and increasing volume fractions of coarse aggregates (22, 33, and 45% CA). Table 6-6 similarly shows the rheological properties of mortar (labeled Concrete40 – 00% CA; 40% FA; 60% CP) and concrete with water-to-cement ratio 0.40 and increasing volume fractions of coarse aggregates (22, 33, 43, and 54% CA). It is generally observed that the measured plastic viscosity increases per increasing aggregate volume as suggested by Equation 5-6 in Chapter 5. The measured yield stress varies upon increasing aggregate volume fraction, but it is seen that at very high volume fraction of fine or coarse aggregate, the measured yield stress is appreciably larger when compared against the same mixture type with no aggregates as suggested by Equation 5-7 in Chapter 5. At high volume fractions (45% CA in Table 6-5 and 54% CA in Table 6-6), the concrete mixture was overly resistant to flow and exceeded the torque limit of the ICAR rheometer, so no rheological values are reported.

Table 6-4 Bingham parameters of fresh paste and mortar with increasing fine aggregate volume content values.

Sample Name	Yield Stress (Pa)	Plastic Viscosity (Pa.s)
Mortar30 – 00% CA; 00% FA; 100% CP	164.2	31.8
Mortar30 – 00% CA; 20% FA; 80% CP	114.2	49.1
Mortar30 – 00% CA; 40% FA; 60% CP	90.1	68.3
Mortar30 – 00% CA; 60% FA; 40% CP	276.6	423.7

Table 6-5 Bingham parameters of fresh mortar and concrete (with water-to-cement ratio 0.30) with increasing coarse aggregate volume content values.

Sample Name	Yield Stress (Pa)	Plastic Viscosity (Pa.s)
Concrete30 – 00% CA; 40% FA; 60 % CP	90.1	68.3
Concrete30 – 22% CA; 40% FA; 38 % CP	87.8	269.3
Concrete30 – 33% CA; 34% FA; 33 % CP	130.0	448.4
Concrete30 – 45% CA; 28% FA; 27 % CP	n/a	n/a

Table 6-6 Bingham parameters of fresh mortar and concrete (with water-to-cement ratio 0.40) with increasing coarse aggregate volume content values.

Sample Name	Yield Stress (Pa)	Plastic Viscosity (Pa.s)
Concrete40 – 00% CA; 48% FA; 52 % CP	207.3	10.5
Concrete40 – 22% CA; 37% FA; 40 % CP	130.1	22.8
Concrete40 – 33% CA; 33% FA; 34 % CP	208.5	33.5
Concrete40 – 43% CA; 27% FA; 30 % CP	467.3	101.1
Concrete40 – 54% CA; 22% FA; 25% CP	n/a	n/a

6.6.2 Average peak acceleration of paste, mortar, and concrete

The efficiency of vibration can be observed for Portland cement-based mixtures types by filling a beam with fresh material with known rheological properties and batched aggregate volume fractions, and subjecting the fresh material to vibration at one end. These fresh materials are additionally dosed with a set-retarding admixture (6 fl. oz per 100 lb of cementitious material) in order to slow the rate of hydration during the vibratory testing. Figure 6-5 shows the results of a three-axis (triaxial) water-proof accelerometer (W356A12) from PCB Piezotronics measuring the acceleration values inside fresh concrete at a distance of 2 inches from DeWalt pencil probe vibrator. The vibrator is pulsed repeatedly for approximately 1-second time durations and the acceleration is measured across these pulses. The accelerometer is sampling at a 1 kHz rate for a 220 Hz (typical) input vibration which is less than a ratio of 10 which is ideal for capturing the full

spectrum of the signal. In order to identify useful trends, all data is treated uniformly where the upper and lower quartile of maximum and minimum peaks are discarded and an average response of the signal can be found. Although this average value does not accurately characterize the full signal response, it is useful for comparison purposes.

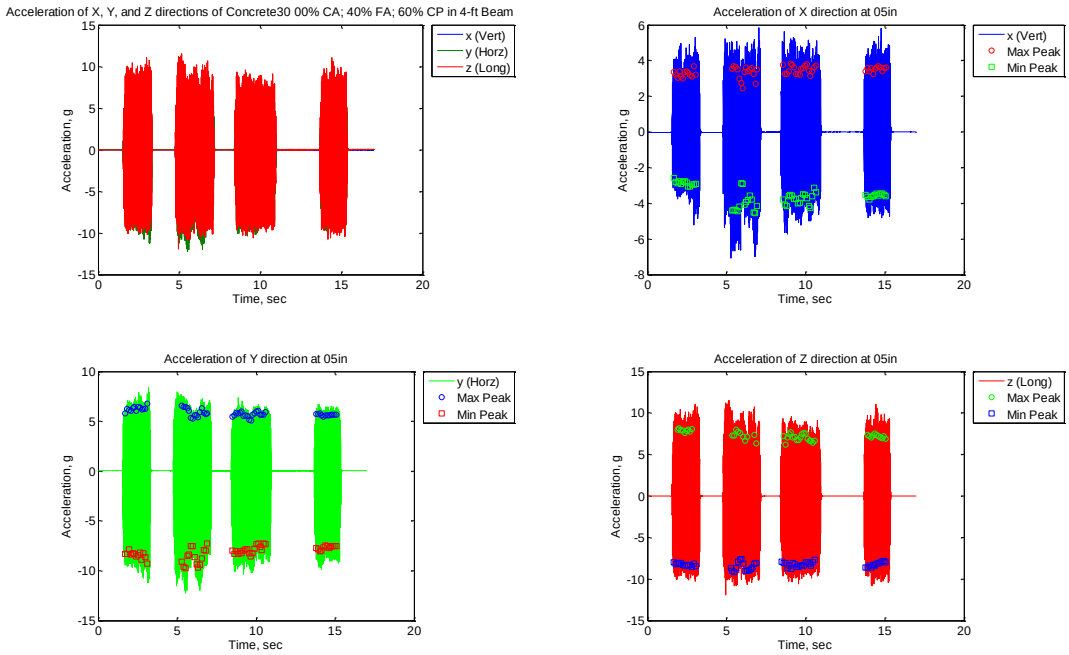

Figure 6-5 Measured acceleration values (x, y, and z) inside fresh Portland cement-based concrete with water-to-cement ratio 0.30 (by mass), 0% CA (by volume), and 40% FA (by volume). The accelerometer sensor is positioned at a depth of 3 inches from the top surface of the fresh material along the centerline of the 6-inch wide prismatic beam at a distance of 5 inches from the edge. The immersion (pencil) probe is positioned 3 inches from the edge.

The strong acceleration signal is typically in the longitudinal direction (length of the beam, see Figure 6-4) which corresponds to the Z channel of the accelerometer. This strong signal was used in order to identify all maximum and minimum peaks within the pulse. The corresponding times from the Z-axis are then found for the weaker signals in the transverse/horizontal direction (width of the beam, see Figure 6-4), and the transverse/vertical direction (height of the beam, see Figure 6-4). The orientation of the accelerometer was fixed, so the acceleration response in the x, y, and z-directions are fixed across all measurements. This process is repeated for all acceleration results in order to produce Figures 6-6 and 6-7 (and Appendices E1 through E5).

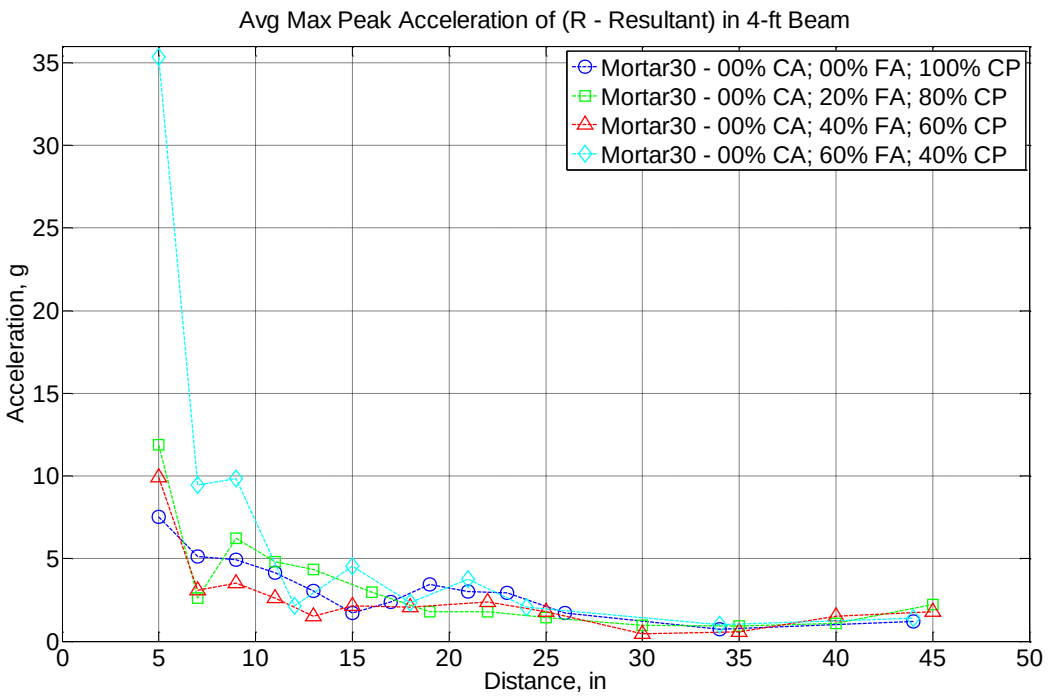

Figure 6-6 The distribution of acceleration values (R – resultant) inside fresh Portland cement-based mortar with water-to-cement ratio 0.30 (by mass), 0% CA (by volume), and increasing volume fraction of FA (by volume) as a function of distance from the edge of the prismatic beam mold. The accelerometer sensor is positioned at a depth of 3 inches from the top surface of the fresh material along the centerline of the 6-inch wide prismatic beam. The immersion (pencil) probe is positioned 3 inches from the edge.

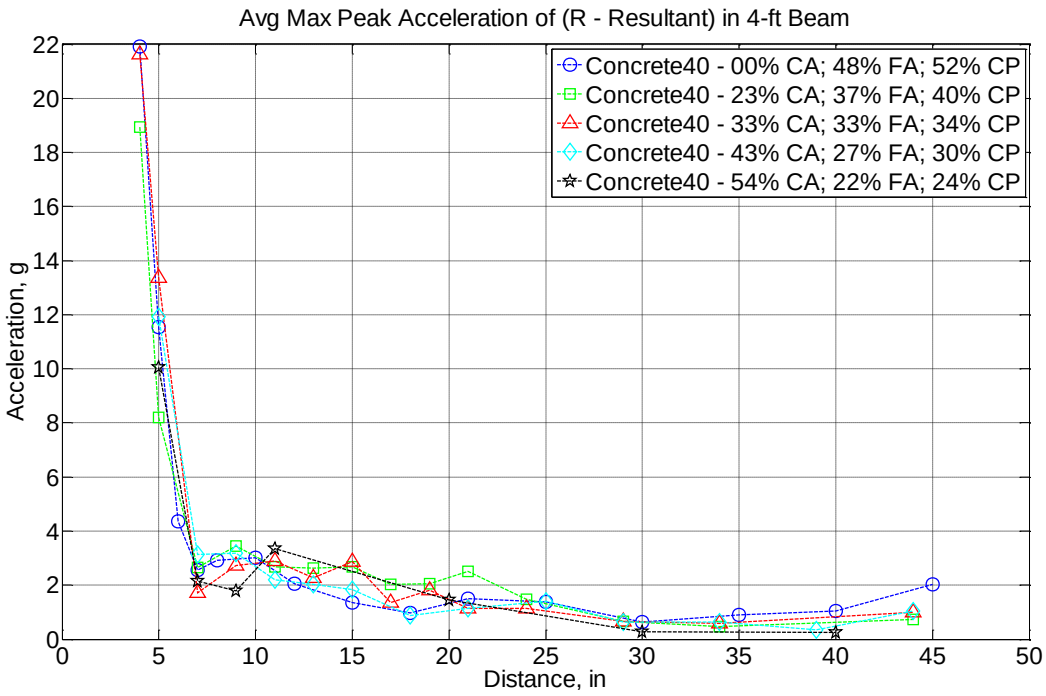

Figure 6-7 The distribution of acceleration values (R – resultant) inside fresh Portland cement-based concrete with water-to-cement ratio 0.40 (by mass) and increasing volume fraction of CA (by volume) as a function of distance from the edge of the prismatic beam mold. The accelerometer sensor is positioned at a depth of 3 inches from the top surface of the fresh material along the centerline of the 6-inch wide prismatic beam. The immersion (pencil) probe is positioned 3 inches from the edge.

Figures 6-6 and 6-7 show the average of multiple impulse vibrations where the resultant of the three (x, y, and z) axes are shown. It is generally seen in both figures that there is an attenuation of the peak acceleration with respect to distance from the immersion probe located at 3 inches. In ACI 309, a decay equation (see Equation 6-1) is used to describe the decay of a concrete system subjected to probe vibration. Appendix 6 shows the application of this equation to the vibration results in the x, y, and z acceleration values in addition to the resultant acceleration. In general, the equation over-predicts the value of acceleratory vibration within the fresh material. Banfill *et al.* also find that the Equation 6-1 over-predicts the distribution of peak acceleration values inside fresh concrete (see Figure 6-3).

In another view, ACI 309 suggests that material undergoing peak acceleration values above 2 to 3 g as sufficiently fluidized. In such a case, fresh mortar material (see Figure 6-6) is fluidized at distances approximately 10 to 20 inches away from the source of vibration. The extent by which the material is fluidized is partly seen to be affected by the aggregate volume fraction, which

strongly affects the measurable plastic viscosity of the fresh mixture. As the sand volume fraction in Figure 6-6 increases, the peak acceleration value increases both in magnitude (vertical) near the probe and in a small shift rightward suggesting that more material is becoming fluidized. The value of peak acceleration nearest to the vibration probe increases from 7 to 12 g to as high as 35 g when the aggregate volume fraction is at 60% (by volume). At this volume fraction, the particles are likely in a jammed state (a value close to 56% volume fraction for mono-sized distribution of spheres) which strong affects the results [Mahaut *et al.*, 2008]. This jamming is not well observed in Figure 6-7 where coarse aggregate content (by volume) reaches only 54% and there is no stark change in the distribution of the peak acceleration.

Concrete with a water-to-cement ratio 0.30 is also considered for its peak acceleration distribution (see Appendix 7, Figure E7-8). Although the resultant peak acceleration of this fresh material similarly undergoes an upward and rightward shift due to increasing aggregate content akin to Figure 6-6, it is subject to considerable error relating to the dosage of superplasticizing chemical admixture. The variability of chemical admixtures results in variability that is eliminated in Figure 6-7 whose mix with water-to-cement ratio of 0.40 is workable without the incorporation of chemical admixtures.

6.6.3 Rheological measurements of model materials

Similar to the rheological results of the Portland cement-based mixture types, the model material consisting of Carbopol gel and increasing volume fractions of graded silica sand and glass marbles leads to an increase of the plastic viscosity as shown in Tables 6-7 and 6-8. There is a comparable trend of the yield stress where the value generally increases for increasing volume fraction of material.

Table 6-7 Bingham parameters of Carbopol gel with varying volume content of graded silica sand (FA).

Sample Name	Yield Stress (Pa)	Plastic Viscosity (Pa.s)
Carbo24 – 0% CA; 00% FA; 100% CP	12.1	0.7
Carbo24 – 00% CA; 20% FA; 80% CP	23.2	1.4
Carbo24 – 00% CA; 40% FA; 60% CP	56.0	2.7
Carbo24 – 00% CA; 49% FA; 51% CP	34.6	8.0
Carbo24 – 00% CA; 60% FA; 40% CP	1370.3	77.2

Table 6-8 Bingham parameters of Carbopol gel with varying volume content of 1-inch (2.5 cm) diameter glass marbles (CA).

Sample Name	Yield Stress (Pa)	Plastic Viscosity (Pa.s)
Carbo24 – 00% CA; 49% FA; 51% CP	34.6	8.0
Carbo24 – 20% CA; 39% FA; 41% CP	66.4	9.5
Carbo24 – 33% CA; 33% FA; 34% CP	181.6	18.5
Carbo24 – 45% CA; 27% FA; 28% CP	241.0	50.6

6.6.4 Average peak acceleration of model materials

The mean resultant acceleration of the Carbopol-based gel and surrogate mortar and concrete are shown in Figures 6-8 and 6-9. In Figure 6-8, a similar trend to Figure 6-6 is observed where increasing sand volume fractions leads to a shift upward and rightward, meaning that increasingly more volume is becoming engaged by vibration. In the case of fine aggregate volume fraction of 60% (by volume), the peak acceleration is appreciably higher at 16 g as opposed to 5 to 11 g at lower volume fractions near the vibration probe. In terms of magnitude, the peak acceleration in Figure 6-8 is approximately 16 g compared to Figure 6-6 with a peak acceleration of approximately 35 g. Although the sand volume content is comparable, the rheological properties between Tables 6-4 and 6-7 are not. In Table 6-7, the plastic viscosity at 60% FA (by volume) is approximately a fifth in magnitude. This observation suggests that the aggregate volume fraction has the capability to extend the volume of material being fluidized, but the aggregate volume fraction does not predict the mean peak resultant acceleration. Other factors such as the stiffness of the particles, the size distribution, and the rheological properties of the underlying fluid likely play a strong role.

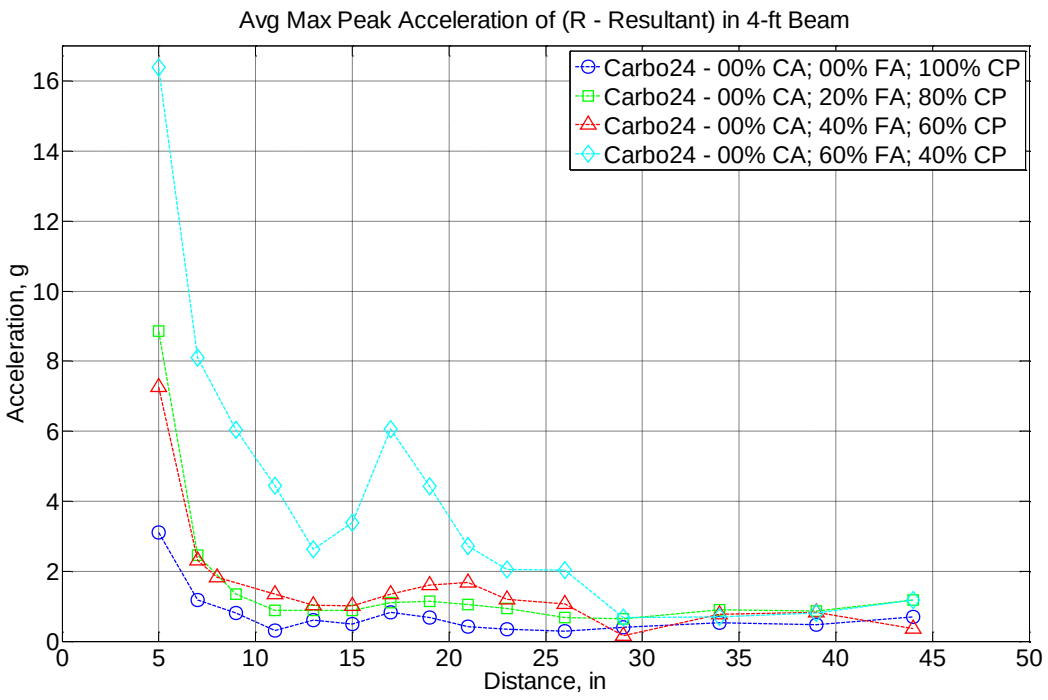

Figure 6-8 The distribution of acceleration values (R – resultant) inside fresh surrogate fluid Carbopol gel with a solids content of 0.24% (by mass), 00% CA (by volume), and increasing volume fraction of FA (by volume) as a function of distance from the edge of the prismatic beam mold. The accelerometer sensor is positioned at a depth of 3 inches from the top surface of the fresh material along the centerline of the 6-inch wide prismatic beam. The immersion (pencil) probe is positioned 3 inches from the edge.

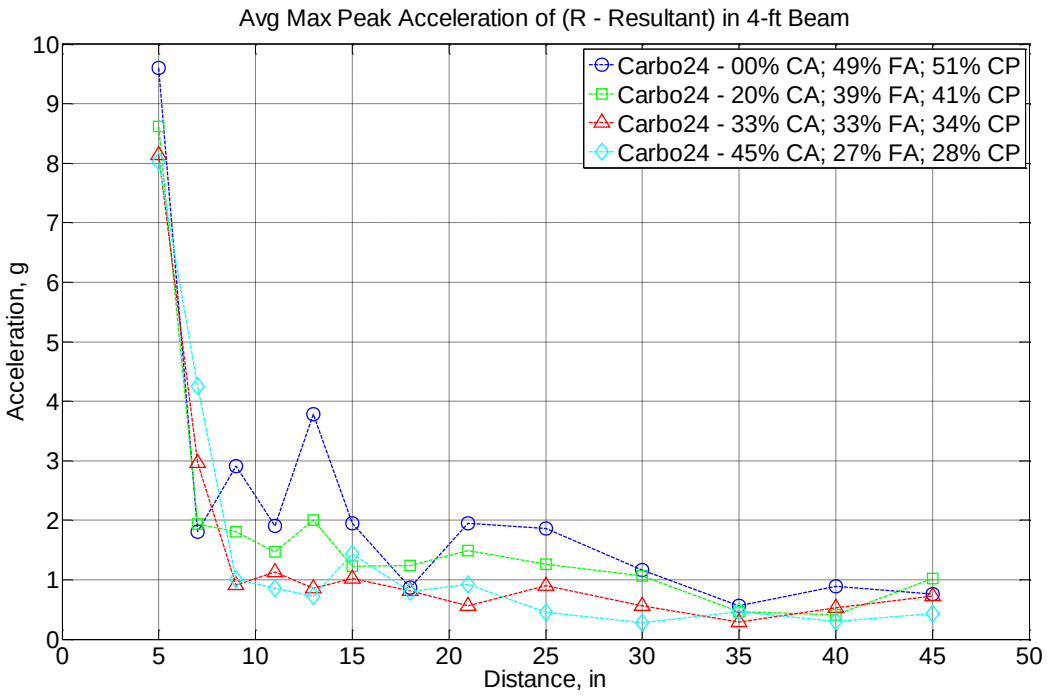

Figure 6-9 The distribution of acceleration values (R – resultant) inside fresh surrogate fluid Carbopol gel with a solids content of 0.24% (by mass) and increasing volume fraction of CA (by volume) as a function of distance from the edge of the prismatic beam mold. The accelerometer sensor is positioned at a depth of 3 inches from the top surface of the fresh material along the centerline of the 6-inch wide prismatic beam. The immersion (pencil) probe is positioned 3 inches from the edge.

In Figure 6-9, there is similarity to Figure 6-7 near the vibration probe at 5 inches where the peak resultant acceleration value is relatively unchanging for increasing volume fractions of CA. At a greater distance from the vibration probe, there is attenuation of the vibratory acceleration. However, in the inert gel fluid in Figure 6-9, there is an unexpected decrease in the mean peak acceleration near 12 inches for increasing volume fraction of CA (by volume). In this idealized material system where ongoing hydration, sensitivity to chemical admixtures, and aggregate gradation differences, it is likely that another factor is contributing. It is very likely that the increased volume fraction of particles is affecting the interaction with the side-walls of the Plexiglas form resulting in a greater transmission of reflected waves. These reflected waves in the finite-width Plexiglas container may be more greatly interacting to destructively diminish the resultant peak acceleration.

6.6.5 Constructive and destructive consolidation

Figures 6-10 and 6-11 show concrete with water-to-cement ratio values of 0.30 and 0.40, respectively. In these two figures, the distribution of peak acceleration in the x, y, and z directions are shown as well as the calculated resultant peak acceleration. Additionally, Dessoff's energy distribution is fitted to each data set assuming a damping factor of 0.08. In Figure 6-10 with a dense coarse aggregate content of 45% (by volume), it is seen that there is a changing distribution of the longitudinal (Z direction) and transverse/horizontal (Y direction) of the mean peak acceleration. Near the vibration probe, the transverse/horizontal acceleration is greater than the longitudinal direction. The consistent positioning of the accelerometer sensor suggests that the transverse/horizontal acceleration measurement is most strongly affected by shearing waves while the longitudinal measurement is most strongly affected by the compression waves. Fresh concrete is a semi-fluid with solid particles (aggregates) that can resist shear movement. When agitated and fluidized, the aggregate particles are separated from each other allowing for flow (see Chapter 5). In this state, the underlying mortar (or paste) fluid is a liquid that should not be able to transmit shearing waves, but can do so because of shearing particle interactions. At greater distances from the vibration probe, the aggregates are no disjoined, meaning that the bulk material behaves more as a solid and compression waves more strong typify the response of the fresh material. Banfill *et al.* utilize this phenomenon in order to predict the transition from the shearing- to compression-dominant waveform to estimate the radius of action.

In this study, instead, the shearing- and compression-dominant waveforms can be experimentally viewed with the use of the triaxial accelerometer. In Figure 6-10, it is seen that near the vibration probe, shearing is in fact occurring as evidenced by a larger transverse/horizontal peak acceleration versus the longitudinal peak acceleration. However, at an intermediary distance of 6 inches, the peak acceleration in the longitudinal direction is larger. This behavior reverts at 9 inches, and reverts once more at 15 inches. This oscillation between transverse/horizontal and longitudinal peak waveforms is similarly seen in Figure 6-11 for a concrete with a volume content of 33% of CA.

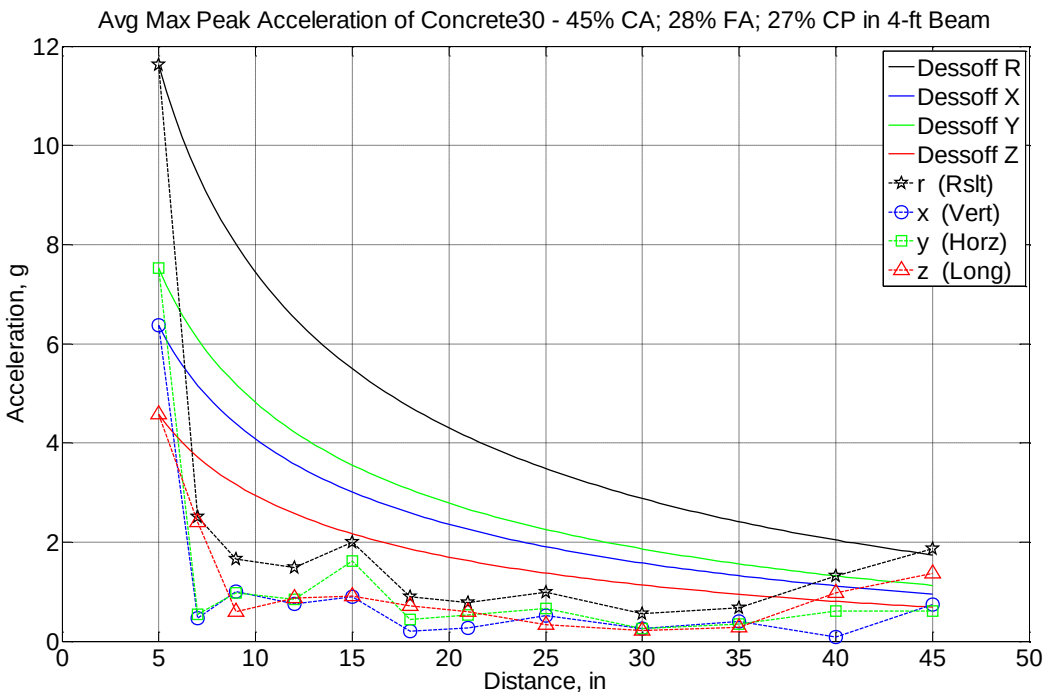

Figure 6-10 The distribution of acceleration values (x, y, and z) inside fresh Portland cement-based concrete with water-to-cement ratio 0.30 (by mass), 45% CA (by volume), and 28% FA (by volume) as a function of distance from the edge of the prismatic beam mold. The accelerometer sensor is positioned at a depth of 3 inches from the top surface of the fresh material along the centerline of the 6-inch wide prismatic beam. The immersion (pencil) probe is positioned 3 inches from the edge. Dessoff's energy distribution is fitted to each data set assuming a damping factor of 0.08.

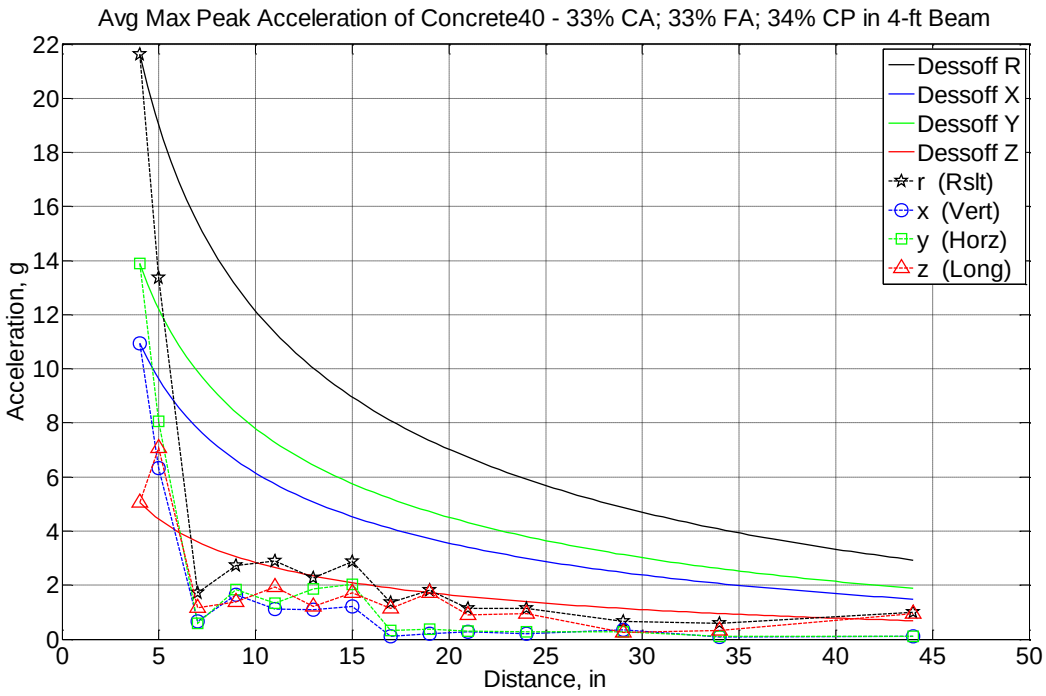

Figure 6-11 The distribution of acceleration values (x, y, and z) inside fresh Portland cement-based concrete with water-to-cement ratio 0.40 (by mass), 33% CA (by volume), and 33% FA (by volume) as a function of distance from the edge of the prismatic beam mold. The accelerometer sensor is positioned at a depth of 3 inches from the top surface of the fresh material along the centerline of the 6-inch wide prismatic beam. The immersion (pencil) probe is positioned 3 inches from the edge. Dessoff's energy distribution is fitted to each data set assuming a damping factor of 0.08.

The observation of oscillating transverse/horizontal and longitudinal peak accelerations is likely driven by the finite-width dimension of the Plexiglas mold. The repeating nature of the peak acceleration is likely attributable to constructive and destructive waveforms that are reflecting off the mold walls. When the aggregate content increases, then the rigidity of contact between the fresh fluid and the elastic-solid form wall is enhanced leading to greater reflection. Ray path analysis would likely suggest areas of constructive interference and this is evidenced in the mean resultant peak accelerations where a secondary peak is observed at a distance farther from the vibration probe (see Figures 6-8, 6-9, and 6-10). Figure 6-12 shows the log-scale distribution of the peak accelerations as measured in linear-scale in Figure 6-10, where it is more apparent that there is an inversion between which waveform (longitudinal or horizontal) is dominant at a given distance. Moreover, the sensitivity to this transverse/horizontal peak acceleration is dominated by fine aggregate volume content as seen in Figures 6-13 and 6-14. In these two figures, the jamming fraction of fine aggregate at 60% (in mortar and surrogate fluid) strongly increases the

transverse/horizontal mean peak acceleration. This suggests greater shearing forces are transmitted through greater aggregate-to-aggregate interaction within fluidized concrete.

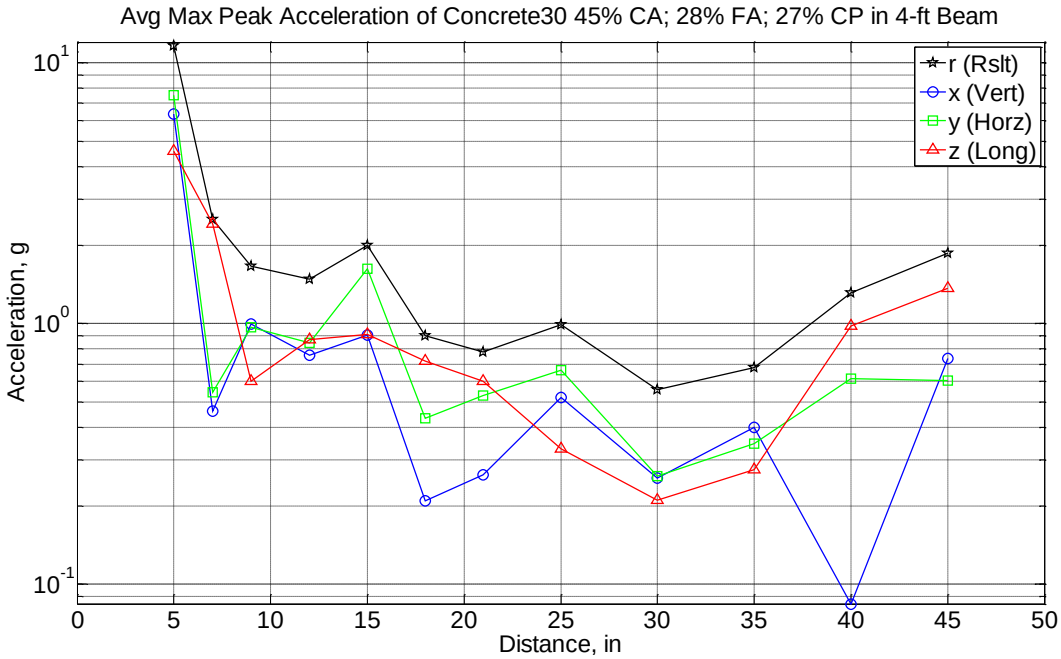

Figure 6-12 The log-scale distribution of acceleration values (x, y, and z) inside fresh Portland cement-based concrete with water-to-cement ratio 0.30 (by mass), 45% CA (by volume), and 28% FA (by volume) as a function of distance from the edge of the prismatic beam mold. The accelerometer sensor is positioned at a depth of 3 inches from the top surface of the fresh material along the centerline of the 6-inch wide prismatic beam. The immersion (pencil) probe is positioned 3 inches from the edge.

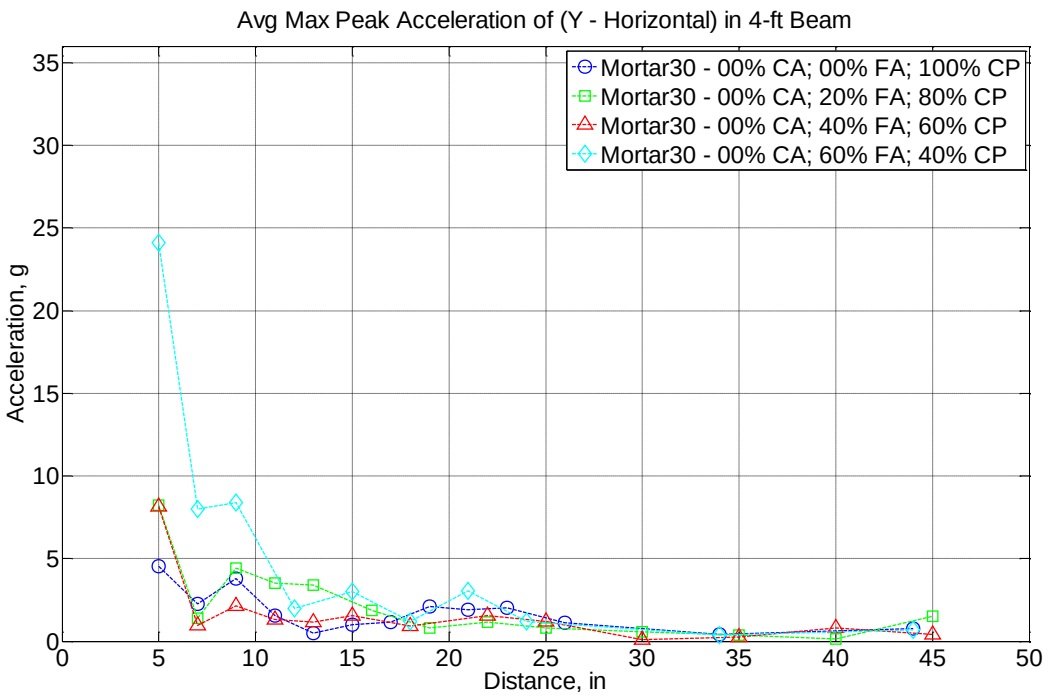

Figure 6-13 The distribution of acceleration values (Y – horizontal) inside fresh Portland cement-based mortar with water-to-cement ratio 0.30 (by mass), 0% CA (by volume), and increasing volume fraction of FA (by volume) as a function of distance from the edge of the prismatic beam mold. The accelerometer sensor is positioned at a depth of 3 inches from the top surface of the fresh material along the centerline of the 6-inch wide prismatic beam. The immersion (pencil) probe is positioned 3 inches from the edge.

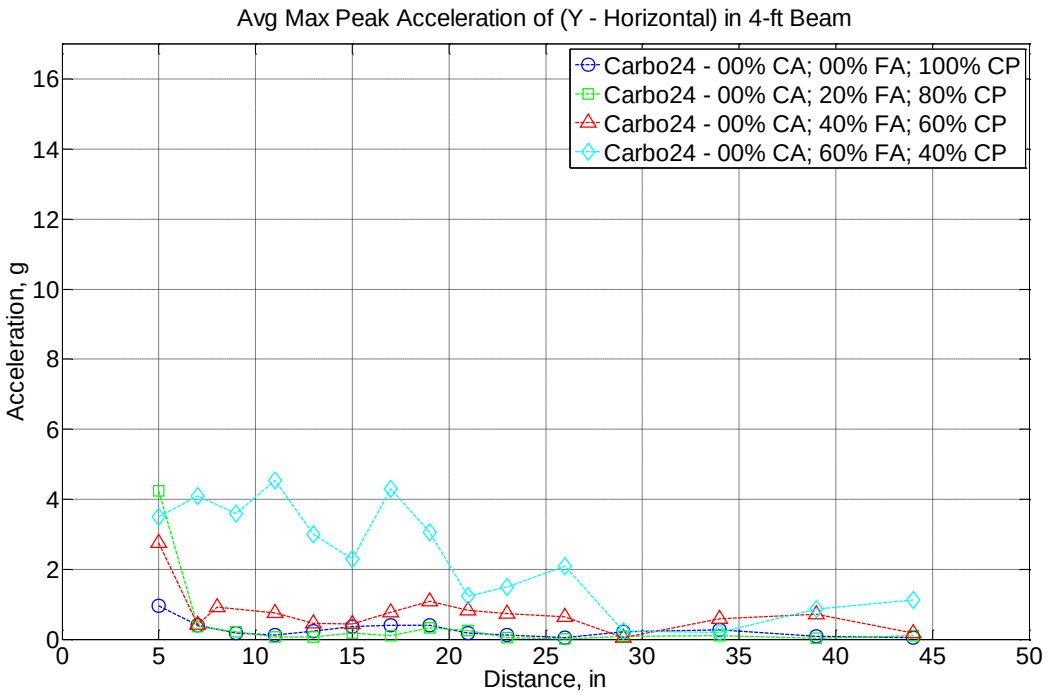

Figure 6-14 The distribution of acceleration values (Y – horizontal) inside fresh surrogate fluid Carbopol gel with a solids content of 0.24% (by mass), 00% CA (by volume), and increasing volume fraction of FA (by volume) as a function of distance from the edge of the prismatic beam mold. The accelerometer sensor is positioned at a depth of 3 inches from the top surface of the fresh material along the centerline of the 6-inch wide prismatic beam. The immersion (pencil) probe is positioned 3 inches from the edge.

6.7 Summary of Chapter

Portland cement-based mortar and concrete is consolidated in precast operations where finite-width molds and immersion probes can be used. In such a case, the extension of the consolidating radius of action can be strongly affected by the mixture design of the fresh material. In this study, it is observed that:

- The extension of the radius of action as evidenced with a triaxial accelerometer immersed in fresh material is dependent upon the volume fraction of aggregates, which is strongly associated with the plastic viscosity of the fresh mixture.
- Aggregate particles of similar size (particularly of fine aggregates, i.e. sand) has a strong impact on the extension of the radius of action despite total aggregate content far surpassing typical jamming fractions of 56%. As such, aggregate gradation plays a strong role in extending the radius of action.

- The increase in plastic viscosity due to higher aggregate content increases the shearing capacity of fluidized concrete because of aggregate-to-aggregate contact, meaning that the extension of the radius of action can extend farther, but also be overcome by areas of localized destructive interference of vibration waves due to the finite-width dimension of the mold.
- Current design guidelines for consolidation of concrete may not fully represent superplasticized concrete mixtures within finite-width molds.

6.8 References

ACI 309.1R-08. Report on Behavior of Fresh Concrete During Vibration. Reported by ACI Committee 309. 2008.

Banfill, P. F. G., Teixeria, M. A. O. M., and Craik, R. J. M. "Rheology and vibration of fresh concrete: predicting the radius of action of poker vibrators from wave propagation." *Cement and Concrete Research* 41 (2011): 932 – 941.

Dessoff, M. "Sur l'Etude de la Pervibration du Beton." *Annales des Ponts et Chaussés (Paris)* 5 (1937): 681 – 688.

Grampiex, G. "Vibration des bétons." *Université Paris-Est* (2013): THESIS.

Koehler, E. P., Fowler, D. W., Ferraris, C. F., and Amziane, S. "A new, portable rheometer for fresh self-consolidating concrete." *ACI Special Publication 233-7* (2006): 97 – 116.

Mahaut, F., Mokéddem, S., Chateau, X., Roussel, N., and Ovarlez, G. "Effect of coarse particle volume fraction on the yield stress and thixotropy of cementitious materials." *Cement and Concrete Research* 38 (2008): 1276 – 1285.

Tattersall, G. H., and Baker, P. H. "The effect of vibration on the rheological properties of fresh concrete." *Magazine of Concrete Research* 40 (1988): 79 – 89.

CHAPTER 7 – EXPERIMENTAL EVIDENCE OF YIELDING OF INTERSTITIAL CEMENT PASTE FLUID DUE TO AGGREGATE MOVEMENT

7.1 Acknowledgment

The development of this chapter is accomplished with extensive mixing, saw-cutting, and scanning of concrete, mortar, and paste materials. For this laborious work that cannot have been accomplished by the author alone, I am thankful to undergraduate students Ivan Chung, Marvin Lim, and Nanaissa Maiga; and graduate student Yu Song.

7.2 Abstract

Buoyant forces must overcome the arresting drag forces in order for air bubbles to rise in viscous, yield stress fluids. Vibration of the Bingham fluid, though, can suppress the large yield stress resulting in increased upward air movement. Portland cement paste, mortar, and concrete can all be characterized as Bingham fluids. However, experimental results show the loss of air within the fresh material due to vibration to be more pronounced in mortar and concrete. In part, the incorporation of fine and coarse aggregates extends the radius of vibratory action. Moreover, it is hypothesized that the extent of yielding of cement paste fluid is exacerbated by the differential movement of aggregates. In this study, a new image analysis method is used to quantify the air size distribution in hardened concrete, mortar, and paste cylinders; and the total air content in variably vibrated concrete, mortar, and paste modulus of rupture beams. The variably vibrated concrete beams have increasing amounts (by volume) of coarse and fine aggregates in order to better understand the effect of aggregates on the loss of fresh air content. It is found that there is only appreciable loss of air in fresh material systems when the yield stress is very low (or highly superplasticized) and when aggregates are present in large volume fractions.

7.3 Introduction and Background

7.3.1 Hardened air analysis: ASTM C457 method

Air content can be measured in fresh concrete using ASTM C231 *Standard Test Method for Air Content of Freshly Mixed Concrete by the Pressure Method*. A new Super Air Meter (SAM)

developed by Oklahoma State University extends the capability of the Type B pressure-meter with differentially pressured states so that it can predict the spacing factor and freeze-thaw performance of the concrete [Ley and Bradden, 2014]. Both of these test methods, however, are assessments of the air system when it is contained within fresh concrete material and potentially does not reflect the actual entrained air system in concrete if the concrete is over-consolidated or over-finished during its final placement. Another test, ASTM C457 *Standard Test Method for Microscopical Determination of Parameters of the Air-Void System in Hardened Concrete*, is a method which determines the air content, specific surface, void frequency, spacing factor, and cement paste-to-air void content in hardened concrete. In this test method, a polished cross-section of hardened concrete is observed under a microscope and a linear traverse is made and the number of air, paste, or aggregates phases are counted. The total air content, spacing factor, and void frequency are calculable and are often thought of as critical factors where low air contents, spacing factors greater than 0.20 mm, and void frequencies less than 300/m can result in freeze-thaw damage susceptible concrete in aggressive wet, wintry environments.

7.3.2 Hardened air analysis: flatbed scanner technique

A new technique is adapted to measure the total air content in polished, 2-dimensional sections [Peterson *et al.*, 2002]. In the original method, the optical microscope is replaced with a high-resolution flatbed scanner (see Figure 7-1). Peterson *et al.* blackened the surface of the polished cross-section of concrete with black ink and impregnated the air voids with a fine, white powder in order to enhance the contrast (see Figure 7-2). In such a manner, total air void content can be measured. However, due to the blackened surface, paste content information is measured through a second, repeated scanned image.

Figure 7-1 Optical microscope conventionally used in ASTM C457 to measured air-void parameters is replaced with a high-resolution flatbed scanner in order to draw the same information from a 2-dimensional scanned image.

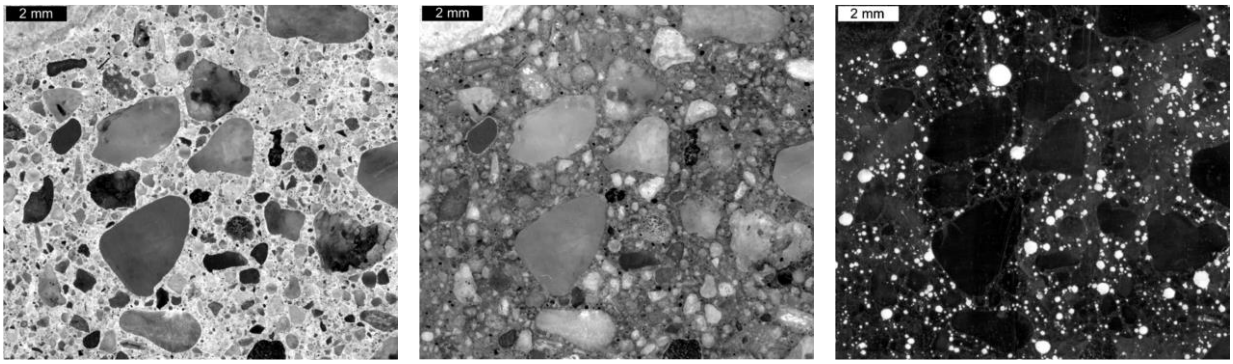

Figure 7-2 A polished 13.0 x 11.7 mm square cross-section of concrete (left) is stained phenolphthalein (center) and with black ink (right) and its air voids are impregnated with fine, white powder in order to enhance the contrast in a scanned image (from Peterson *et al.*, 2002).

In a new method that extends Peterson *et al.*'s concept, a polished cross-section of concrete is stained with 5% phenolphthalein solution to create a pink hued surface of the hydrated cement paste [Song *et al.*, 2015]. A fluorescent orange powder is impregnated into the air voids. After the image is scanned, each of three phases can be identified from a single scanned image: paste, air, and aggregates. Air voids contained within porous aggregate can be filtered through a corrective algorithm in order to reconstruct a 3-phase scanned image (see Figures 7-3 and 7-4) that is quantifiable and statistically significant for its air-void parameters.

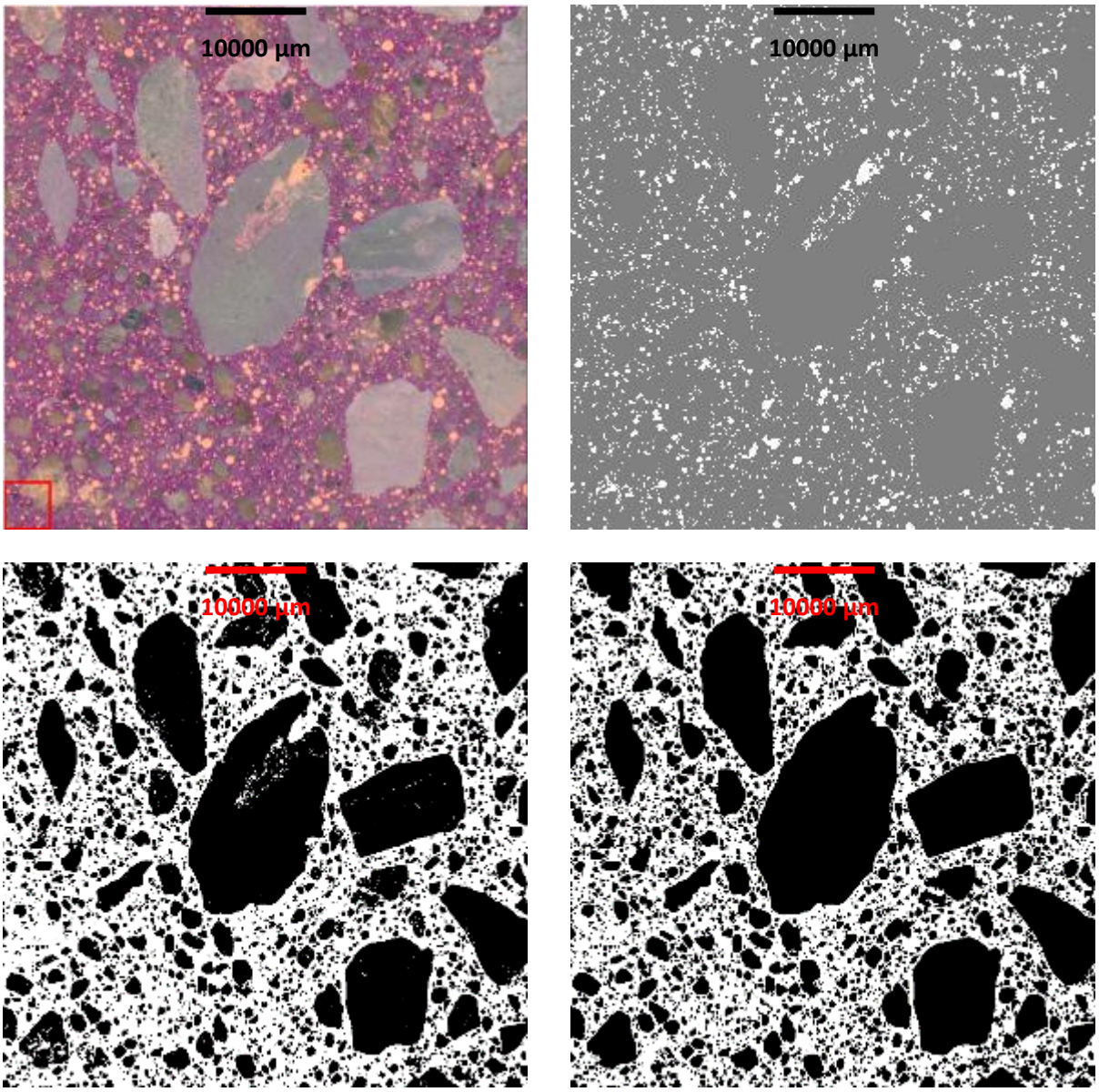

Figure 7-3 A polished cross-section of concrete (50 x 50 mm, e.g.) is stained with phenolphthalein and its air voids are impregnated with fine, orange powder (top left) in order to enhance the contrast of the air voids (top right) and aggregates (bottom left). A hole-fill correction is applied in order to account for voids contained wholly within aggregates (bottom right) (from Song *et al.*, 2015).

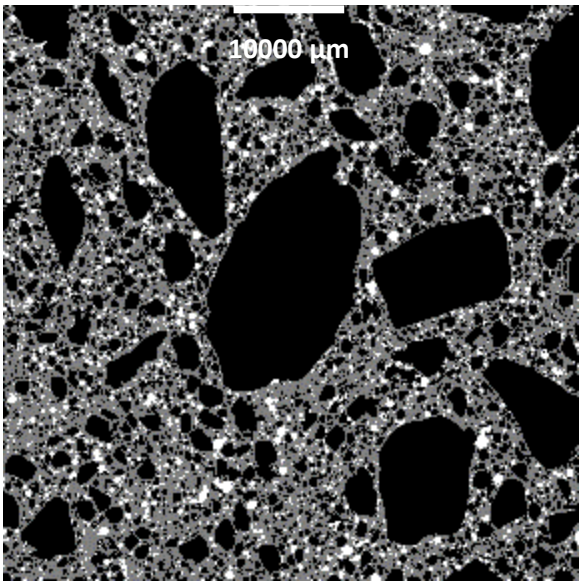

Figure 7-4 A re-constructed, 3-phase image of polished concrete (50 x 50 mm, e.g.) (from Song *et al.*, 2015).

7.4 Significance of Research

The hardened air void system is critically important for concrete that is designed to withstand a large number of freeze-thaw cycles. In this study, the effect of vibratory consolidation on fresh concrete is investigated for its effect on the hardened air void system in concrete cylinders and beams. By gleaning information about the loss of entrained air, it is possible to better understand the connection between suspended air bubbles in fresh concrete, the material's rheology, and the long-term durability of concrete infrastructure in wet, wintry climates.

7.5 Experimental Methods

7.5.1 Materials and equipment

Portland cement-based paste, mortar, and concrete was made with a water-to-cement ratio of 0.30 (by mass) that is dosed with a set-retarding (MasterSet DELVO), a superplasticizing (Sika Viscocrete 2100), and air-entraining (Sika AEA-14) chemical admixtures (see Table 7-1). The size distribution of sand particles is given in Table 7-2. Specifically, the sand used in the Portland cement-based mortars and concrete conforms to Illinois Department of Transportation (IDOT) FA02 blend. In order to make concrete, gravel is added to the mortar. A comparable concrete mixture using a water-to-cement ratio of 0.40 (by mass) is also considered for its rheological

properties. The gravel used in the Portland cement-based concrete is crushed limestone, and its size distribution conforms to IDOT CA07 blend (see Table 7-3).

Table 7-1 Nominal paste mix design.

Material Type	**w/c = 0.30**	
	Pounds Per Cubic Yard	**Kilograms Per Cubic Meter**
Type I Portland Cement	2696	1599
Water	809	480
Set-Retarding Agent	6 fl. oz per 100 lb. cementitious (391 mL per 100 kg cementitious)	
Superplasticizing Agent	10 – 16 fl. oz per 100 lb. cementitious (652 – 1,043 mL per 100 kg cementitious)	
Air-Entraining Agent	0, 3, or 6 fl. oz per 100 lb. cementitious (0, 196, or 391 mL per 100 kg cementitious)	

Table 7-2 Gradation (percent passing) of various sand types.

			Specific Gravity	3/8" (9.5mm)	No. 4 (4.75 mm)	No. 8 (2.36 mm)	No. 10 (2.00 mm)	No. 16 (1.18 mm)	No. 30 (600 µm)	No. 40 (425 µm)	No. 50 (300 µm)	No. 80 (180 µm)	No. 100 (150 µm)	No. 200 (75 µm)
FA	IDOT FA 2	*Lab River Sand*	2.63	100	97 ± 3			65 ± 20			20 ± 10		5 ± 5	
	ASTM C778	*Ottawa Graded Sand*	2.65					100	98 ± 2	70 ± 5	25 ± 5		2 ± 2	
	ASTM C33	*Fine Aggregate*		100	97.5 ± 2.5	90 ± 10		67.5 ± 17.5	42.5 ± 17.5		17.5 ± 12.5		5 ± 5	1.5 ± 1.5

Table 7-3 Gradation (percent passing) of various gravel types.

			Specific Gravity	3" (75 mm)	2.5" (63 mm)	2" (50 mm)	1.5" (37.5 mm)	1" (25 mm)	3/4" (19 mm)	1/2" (12.5 mm)	3/8" (9.5 mm)	No. 4 (4.75 mm)	No. 16 (1.18 mm)	No. 50 (300 µm)	No. 200 (75 µm)
CA	IDOT CA 7	*Limestone*	2.75				100	95 ± 5		45 ± 15		5 ± 5			
	IDOT CA 12	*Limestone*							100	95 ± 5	85 ± 10	60 ± 10	35 ± 10		
	IDOT CA 16	*Chip*	2.67							100	97 ± 3	30 ± 15	2 ± 2		

The volume fraction of the river sand and limestone aggregate is varied in order to draw insight into the effect of aggregates. All materials are mixed in a 2 cubic-foot capacity flatbed pan shearing mixer. The rheological properties of the fresh materials were measured using an ICAR Rheometer which measures the rheology using a rotating vane propeller. The ICAR rheometer was developed by the International Center for Aggregate Research (ICAR) at the University of Texas at Austin in order to better characterize the rheological properties of concrete [Koehler *et al.*, 2006]. The cementitious materials were treated as Bingham plastics, which are characterized by a dynamic yield stress (tangent intercept) and plastic viscosity (slope at large shear strain rate). The static yield stress was also measured, but is not considered in the determination of the Bingham fit parameters.

The fresh materials were either placed in a 4 inch diameter, 8 inch tall cylindrical plastic mold (10.16 cm diameter, 20.32 cm tall) or 6 inch by 6 inch by 21 inch rectangular steel prism

molds (15.24 cm by 15.24 cm by 53.34 cm). The cylindrical plastic molds were vibrated atop a 60 Hz vibration table for varying amounts of time (0, 1, or 2 minutes) while the prismatic steel beams were vibrated with a 220 Hz 1 inch (2.54 cm) diameter DeWalt pencil vibrator at one end approximately 3 inches (7.6 cm) away from the three form walls to a depth of 5.5 inches (14 cm). At the conclusion of consolidating vibration, the cementitious materials hardened and were sectioned for hardened air analysis.

7.5.2 Sectioning and polishing of hardened samples

Once hardened, the samples were extracted and saw-cut in order to perform image analysis. The cylindrical samples were saw cut horizontally 5 cm (2 in) away from the top and bottom surface (see Figure 7-5). The circular cross-section face near the top is labeled TH (top-half) while the circular cross-section face near the bottom is labeled BH (bottom-half). Another set of cylindrical samples were saw cut vertically and horizontally in order to expose 10.16 cm by 10.16 cm (4 in by 4 in) faces. These faces were labeled according to which vertical half they were from (A or B) and additionally labeled T (for top) or B (for bottom) resulting in labeling of AT, BT, AB, and BB (see Figure 7-5). The beams were saw-cut in order to extract several 15.24 x 15.24 cm (6 x 6 in) faces that are orthogonal to the long-axis of the beam. Each face was labeled according its distance from the edge of the beam nearest the source of vibration (where an excised sample at the point of vibration is nominally 7.62 cm (3 in) from the edge) (see Figure 7-5).

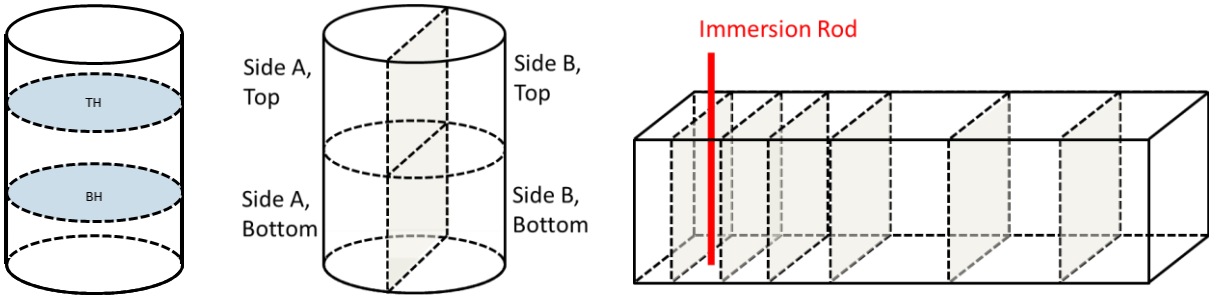

Figure 7-5 Illustration of saw-cut cylinders (left and center) and beams (right); samples extracted for hardened air analysis.

Each excised hardened concrete sample was polished using a 45.72 cm (18 inch) diameter horizontal grinding wheel (see Figure 7-6). Each sample was successively ground using #60, #180, and #600 grit polishing discs in order to create a highly polished surface. The polished surface was then sprayed with an even film of 5% phenolphthalein solution such that the hydrated cement paste

takes on a pink hue due to its high pH. After this polished surface dries, fluorescent orange powder is carefully poured onto the surface and is impregnated into the voids using both a silicone stopper and razor blade. After visual inspection confirming that the air voids were sufficiently impregnated, the polished surface was struck of excess powder with the razor blade, and the polished sample was carefully inverted onto the glass surface of a CanoScan 9000F high resolution scanner.

Figure 7-6 Forty-five cm (18 inch) diameter grinding wheel used to polished hardened concrete sections (from ASW Diamond).

7.5.3 Flatbed scanning and image analysis

Hardened samples originating from a cylindrical specimen were scanned at their interior in a 5 x 5 cm (2 x 2 in) square section at a resolution of 4,800 dpi. Intermediate sized specimens of 10 x 10 cm (4 x 4 in) were scanned at a resolution of 2,400 dpi. Larger hardened samples originating from a beam specimen were scanned in their entirety of 15.24 x 15.24 cm (6 x 6 in) area at a reduced resolution of 1,600 dpi. The selection of image resolution is primarily owed to maintaining scanned filed sizes of approximately 250 MB.

Spectral analysis of the scanned images was undertaken in order to transform the 24-bit RGB scanned image into an 8-bit three (or four) phase image. Multispec software was employed using the ECHO (Extraction and Classification of Homogenous Objects) Classifier in order to segment the scanned image into phases of interest [Landgrebe, 1980]. ECHO is a two-stage conjunctive object-seeking algorithm that utilizes user-populated (defined) spatial features in the scanned image as an identifier to the spectral characteristic. Areas (or cells) are defined by the user as training cells and these cells are subjected to a test of statistical homogeneity against

neighboring cells. Cells that fail to pass this test are determined to contain boundary regions between phases. Cells that past this test are additionally evaluated in order to determine the cell's similarity to neighboring cells. If the cells are determined to be equal, then the two cells are annexed resulting in a larger cell. This process continues until the large cells are extended to their natural boundary. Phases of interest in this study are: air, aggregate, hydrated cement paste, and extra (any area such as a large crack that does not representative of the cementitious sample).

The segmented image from MultiSpec is outputted as a TIFF file and transferred to ImageJ in order to "hole fill" air voids contained within the aggregates as air voids within the hydrated cement paste are of critical concern. Moreover, the air void distribution was found by identifying the area of each identified void and characterizing it by a circumscribed diameter. Any aggregate phase exceeding 500 μm diameter was filtered out in order to establish consistency and repeatability between processed images where very small coarse aggregates and fine aggregates are more difficult to identify during the segmentation analysis. A methodical outlining of this procedure is presented in Song *et al.*, and in this study the distribution is exported to an ASCII file for graphical plotting.

7.6 Results and Discussion

Forty-two cementitious cylinders were cast and sectioned for this study. Initially, the concrete samples with a water-to-cement ratio of 0.30 and 0.40 (by mass) were only planned for their strength evaluation. When this study began, the importance of needing to cast cylinders originating from a singular concrete mixture was not realized. As such, the results in C30 and C40 (representing concrete with water-to-cement ratios of 0.30 and 0.40, respectively) are largely affected by the fact that each fresh mixture had different rheological properties. However, insight into air loss can still be gleaned from the mortar and paste cylinders as well as the concrete, mortar, and paste beams which were cast from singular batches of fresh material.

7.6.1 Rheological measurements of fresh Portland cement-based materials

The rheological properties of concrete with water-to-cement ratios of 0.30 and 0.40 (by mass) are shown in Tables 7-4 and 7-5. The rheological properties of mortar and paste with water-to-cement ratio of 0.30 (by mass) is shown in Table 7-6. The nominal mix design of C30 and C40

is pursuant to Table 6-1 with 27% sand and 43% gravel by volume while the nominal mix design of the mortar is 62% sand by volume. C30 in Table 7-4 is highly superplasticized leading to mixtures with relatively large plastic viscosity values as compared to C40 in Table 7-5. This high plasticity joined with appreciably lower yield stress values leads to C30 behaving more like a self-compacting (or self-leveling) concrete which can easily flow under its own self-weight whereas C40 can retain rigid peaks when undisturbed. The yield stress of the mortar and paste in Table 7-6 is appreciably high while the plastic viscosity is much lower. This is emblematic of the nature of granular systems where frictional forces between aggregates increase the perceived (measureable) yield stress. Highly fluidized mixtures are necessary in order to create flowable concrete mixtures. As a consequence, the interstitial fluid suspending the particles is more highly fluidized than that measureable concrete or mortar material (see discussion on the Modified Krieger-Dougherty and Chateau-Ovarlez-Trung relationships in Chapter 5).

Table 7-4 Bingham parameters of fresh concrete with water-to-cement ratio of 0.30 (by mass), varyingly dosed with air-entraining admixture (0204 is no air entrainer, 0608 is moderate air entrainer, and 1012 is high air entrainer), and variably consolidated atop a 60 Hz vibration table for 0, 1, or 2 minutes.

Sample Name	Yield Stress (Pa)	Plastic Viscosity (Pa.s)
C30-0204-0m	0.03045	391.571
C30-0204-1m	0.03045	359.047
C30-0204-2m	0.03045	258.408
C30-0608-0m	18.2632	144.593
C30-0608-1m	117.616	198.934
C30-0608-2m	432.159	247.118
C30-1012-0m	163.61	165.896
C30-1012-1m	195.657	235.582
C30-1012-2m	115.412	244.565

Table 7-5 Bingham parameters of fresh concrete with water-to-cement ratio of 0.40 (by mass), varyingly dosed with air-entraining admixture (0204 is no air entrainer, 0608 is moderate air entrainer, and 1012 is high air entrainer), and variably consolidated atop a 60 Hz vibration table for 0, 1, or 2 minutes.

Sample Name	Yield Stress (Pa)	Plastic Viscosity (Pa.s)
C40-0204-0m	280.153	64.3644
C40-0204-1m	435.815	44.8335
C40-0204-2m	443.699	43.7441
C40-0608-0m	883.206	5.694
C40-0608-1m	514.958	22.4368
C40-0608-2m	523.495	17.16
C40-1012-0m	788.364	12.4905
C40-1012-1m	645.456	16.268
C40-1012-2m	521.337	30.1637

Table 7-6 Bingham parameters of fresh mortar and paste with water-to-cement ratio of 0.30 (by mass), varyingly dosed with high air-entraining admixture and variably consolidated atop a 60 Hz vibration table for 0, 1, or 2 minutes.

Sample Name	Yield Stress (Pa)	Plastic Viscosity (Pa.s)
M30-1012-0m	983.7	159
M30-1012-1m		
M30-1012-2m		
P30-1012-0m	875.8	33.6
P30-1012-1m		
P30-1012-2m		

The rheology of concrete beams with varying volume fractions of coarse and fine aggregates are shown in Table 7-7 and the rheology of mortar and paste beams are shown in Table 7-8. Initially, two separate concrete mixtures (C30-1 and C30-2) were cast each with 43% coarse aggregate and 27% fine aggregate (by volume) in order to understand the effect of a highly superplasticized mixture (C30-1) versus a lightly dosed superplasticizer (C30-2). The rheology between those two specimens is seen in Table 7-7 where the yield stress of C30-1 is much lower than C30-2 while the plastic viscosity is much larger. Initial results shown in Section 7.5.4 indicates that mixtures with high dosage of superplasticizing admixtures have a strong effect on air loss, so a larger effort with concrete beams with increasing coarse aggregate volume content is

undertaken. For these mixtures, a water-to-cement ratio of 0.40 was selected in order to achieve consistency and repeatability between admixtures but high fluidity was achieved comparable to C30-1.

Table 7-7 Bingham parameters of fresh concrete with water-to-cement ratio of 0.30 or 0.40 (by mass), with varying volume fractions of coarse aggregate (CA) and fine aggregates (FA) by volume, and variably consolidated with a 220 Hz DeWalt pencil (probe) immersion vibrator.

Sample Name	Yield Stress (Pa)	Plastic Viscosity (Pa.s)
C30-1 (CA43-FA27)	205.7	230.4
C30-2 (CA43-FA27)	679	13.3
C40-CA12-FA42	n/a	n/a
C40-CA23-FA37	130.1	22.8
C40-CA33-FA32	208.5	33.5
C40-CA43-FA27	467.3	101.1

Table 7-8 Bingham parameters of fresh mortar and paste with water-to-cement ratio of 0.30 (by mass), with varying volume fractions of coarse aggregate (CA) and fine aggregates (FA) by volume, and variably consolidated with a 220 Hz DeWalt pencil (probe) immersion vibrator.

Sample Name	Yield Stress (Pa)	Plastic Viscosity (Pa.s)
M30-1 (CA00-FA62)	983.7	159
M30-CA00-FA20	1265	13
M30-CA00-FA40	1987	5.5
M30-CA00-FA62	261.6	182.3
P30-1 (CA00-FA00)	875.8	33.6

Similarly, mortar and paste mixtures with increasing volume fraction of sand resulted in increasing yield stress due to particle-to-particle interaction. Increasing the dosage of superplasticizing admixture increases the fluidity resulting in slightly variable results where the plastic viscosity is strongly increased.

7.6.2 Distribution of air sizes in vibrated concrete cylinders

The distribution of air void size of concrete cross-sections with water-to-cement ratio 0.30 and 0.40 are shown in Figures 7-7 and 7-8, respectively. Additional figures from concrete cross-sections are shown in Appendices F1 and F2. The figures all show a general trend of having a

singular peak near 40 μm diameter. The numerical peak in Figures 7-7 and 7-8 are normalized against the mortar content in order to minimize the distortion due to the presence of an unequal amount of coarse aggregates (or extra space) captured within a scanned image. This normalization to the mortar count produces a density of air voids that can be counted within a single image.

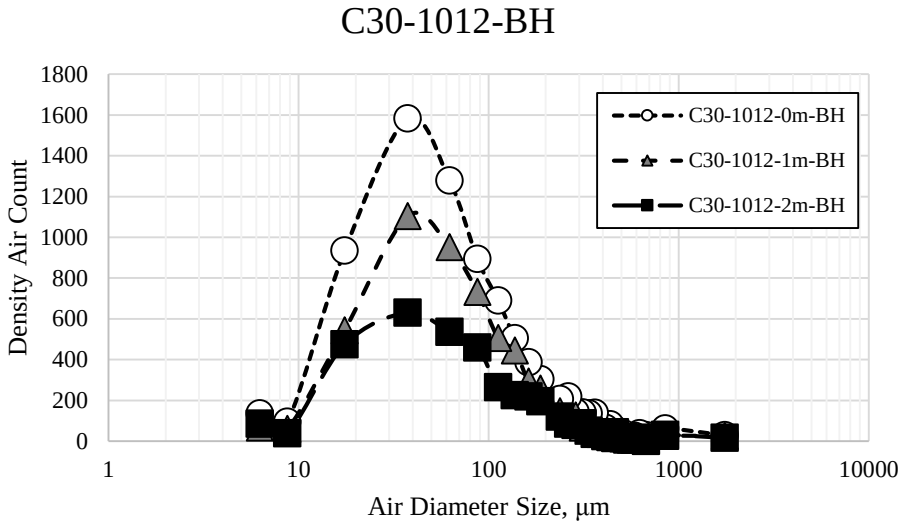

Figure 7-7 Distribution of air void size normalized to the mortar content inside the bottom half of a 4-inch diameter concrete cylinder (with water-to-cement ratio 0.30 by mass) vibrated atop a 60 Hz vibration table for 0, 1, or 2 min. High air-entraining admixture is incorporated into fresh mixture.

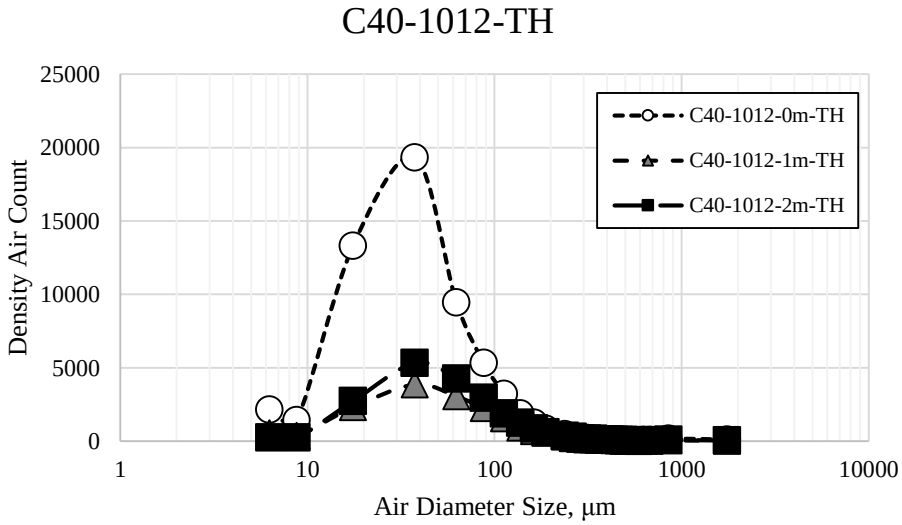

Figure 7-8 Distribution of air void size normalized to the mortar content inside the top half of a 4-inch diameter concrete cylinder (with water-to-cement ratio 0.40 by mass) vibrated atop a 60 Hz vibration table for 0, 1, or 2 min. High air-entraining admixture is incorporated into fresh mixture.

Figure 7-7 shows an idealized result where the distribution of air voids has a large peak when a sample is not vibrated (C30-1012-0m-BH). When subjected to vibration, the yield stress is expected to be overcome resulting in the movement of air bubbles within the fresh material governed by the plastic viscosity. As such, the distribution of air void sizes at 1 min and 2 min of vibration times are appreciably lowered. It is possible to for there to also be a shift in the curve. A leftward shift in the distribution would indicate that finer (smaller-sized) diameter air bubbles are being created whereas a rightward shift would indicate that air bubbles are coalescing. Any shifting of the distribution peak is not readily apparent suggesting that air bubbles are not wholly separating into smaller bubbles nor coalescing into larger bubbles. However, this does not necessarily indicate that clustering of air bubbles is not occurring as it may still be possible to segment distinct air bubbles within an image.

The rheology of C30 and C40 mixtures is not controlled, and C30-0204 is most comparable between mixtures as shown in Table 7-4 where the yield stress is appreciably moot due to the highly superplasticized mixture. In addition, the plastic viscosity is relatively comparable. Appendix F1 and F2 show, however, unpredictable distribution of air void sizes where samples vibrated for more time result in a larger peak. It is not necessarily possible to comment on these results without account for inconsistencies regarding different rheological properties and ongoing hydration processes. Moreover, it is very likely that these samples originating from different mixtures may have had different initial distribution of air content.

Despite the challenges in noting the change in air size distribution in variably vibrated concrete samples with different rheological properties, it is still possible to rigorously examine the quality of the scanned images and the processing technique resulting in the air size distribution. Figures 7-9 and 7-10 show the result of profile sections taken from singular cylindrical samples (see more in Appendices F3 and F4). In Figure 7-9, the distribution of air voids within a singular concrete cylinder sample with a null yield stress is shown to vary significantly depending on the region in which the image was taken. The left half of the cylinder (A) should well complement and mirror the right half (B) of the cylinder while there may be differences noted in the bottom (B) and top (T) of the cylinder. In Figure 7-9, it is seen that the largest peak occurs in the top half of the cylinder (BT) while its mirrored counterpart (AT) is lower in peak magnitude and broader.

Similarly, mirrored faces AB and BB (at the bottom of the cylinder) do not well match in Figure 7-9.

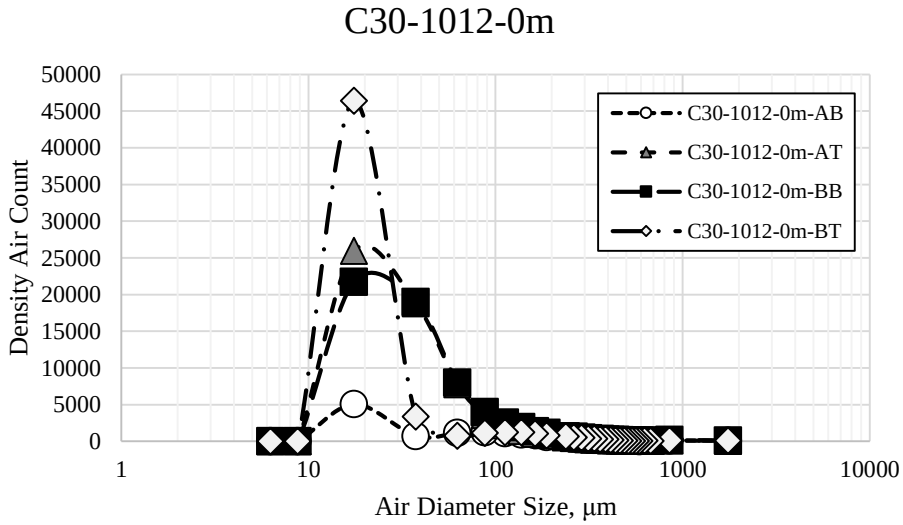

Figure 7-9 Distribution of air void size normalized to the mortar content inside the upper and lower half (left and right) of a 4-inch diameter concrete cylinder (with water-to-cement ratio 0.30 by mass) vibrated atop a 60 Hz vibration table for 0 min. High air-entraining admixture is incorporated into fresh mixture.

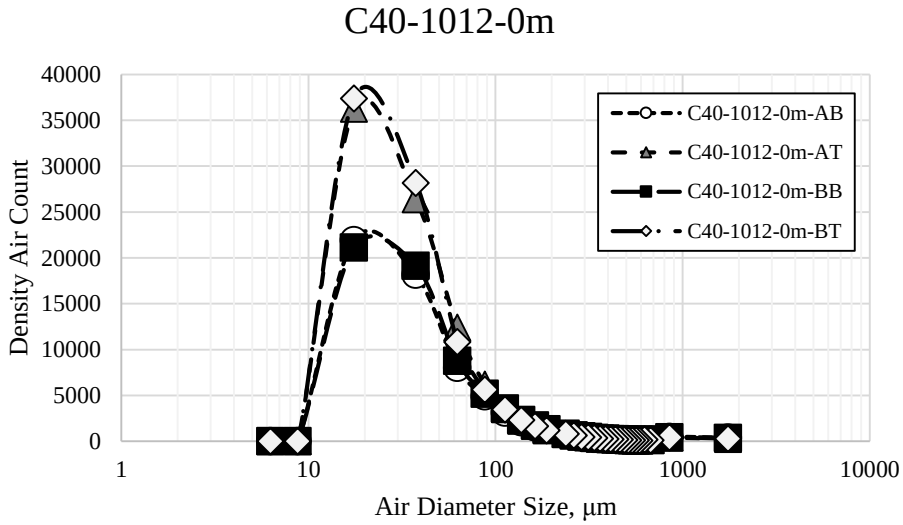

Figure 7-10 Distribution of air void size normalized to the mortar content inside the upper and lower half (left and right) of a 4-inch diameter concrete cylinder (with water-to-cement ratio 0.40 by mass) vibrated atop a 60 Hz vibration table for 0 min. High air-entraining admixture is incorporated into fresh mixture.

The inconsistency across mirrored samples continues into C40 samples with the exception of one as shown in Figure 7-10 where the mirrored halves (AB and BB, and AT and BT) is well matched. The figures in shown in Appendices F3 and F4 suggest that characterizing the air void distribution using a singular sectioned surface (of 16 in^2) is inadequate to capture the nature of the air void system.

7.6.3 Distribution of air sizes in vibrated mortar and paste cylinders

Additional samples of mortar and paste were cast originating from singular mixtures in order to retain even rheological properties during vibration. Appendices F5 and F6 show the air void distribution of these cylinders. Figure 7-11 shows an ideal result where increasing vibration times results in the downward shift of the main peak; however, this is not readily seen in other figures again suggesting that the sample size (scanned area and number of samples) is too small in order to draw meaningful insight. Figure 7-12 shows the bottom half (BH) of a cylindrical paste sample that underwent increasing vibration times but does not show an expected trend.

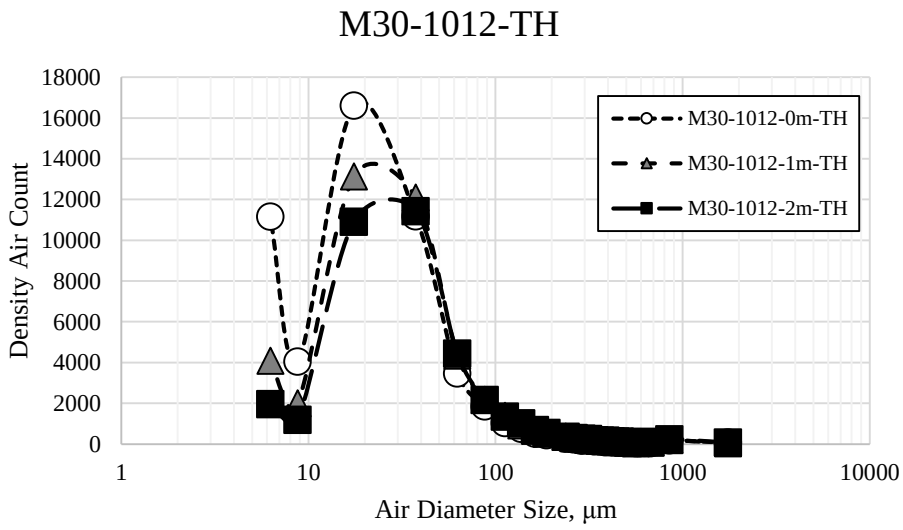

Figure 7-11 Distribution of air void size inside the top half of a 4-inch diameter mortar cylinder (with water-to-cement ratio 0.30 by mass) vibrated atop a 60 Hz vibration table for 0, 1, or 2 min. High air-entraining admixture is incorporated into fresh mixture.

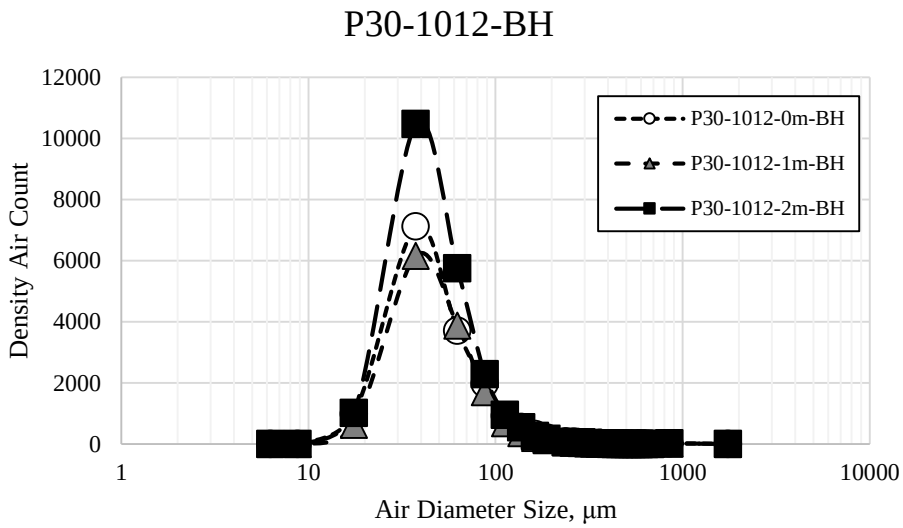

Figure 7-12 Distribution of air void size inside the bottom half of a 4-inch diameter paste cylinder (with water-to-cement ratio 0.30 by mass) vibrated atop a 60 Hz vibration table for 0, 1, or 2 min. High air-entraining admixture is incorporated into fresh mixture.

The profile sections of mortar and paste cylindrical samples are shown in Figures 7-13 and 7-14, respectively. In this case when the rheological properties are comparable, it is possible to see that mirrored samples are equitable in their distribution. More interestingly, it is possible to see that samples originating from the top half (AT and BT) have appreciably lower air voids than samples originating from the bottom half (BT and BB). This is true even in the case of no vibration (see Figure 7-13), meaning that air voids under no vibration can buoyantly rise and escape the material system without significant external vibration. This is the case even when the yield stress is appreciably large (see Table 7-6).

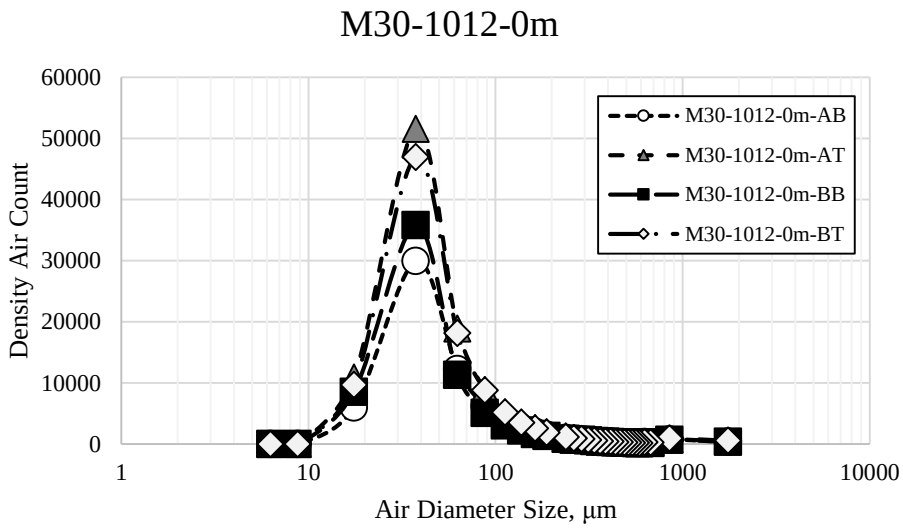

Figure 7-13 Distribution of air void size inside the upper and lower half (left and right) of a 4-inch diameter mortar cylinder (with water-to-cement ratio 0.30 by mass) vibrated atop a 60 Hz vibration table for 0 min. High air-entraining admixture is incorporated into fresh mixture.

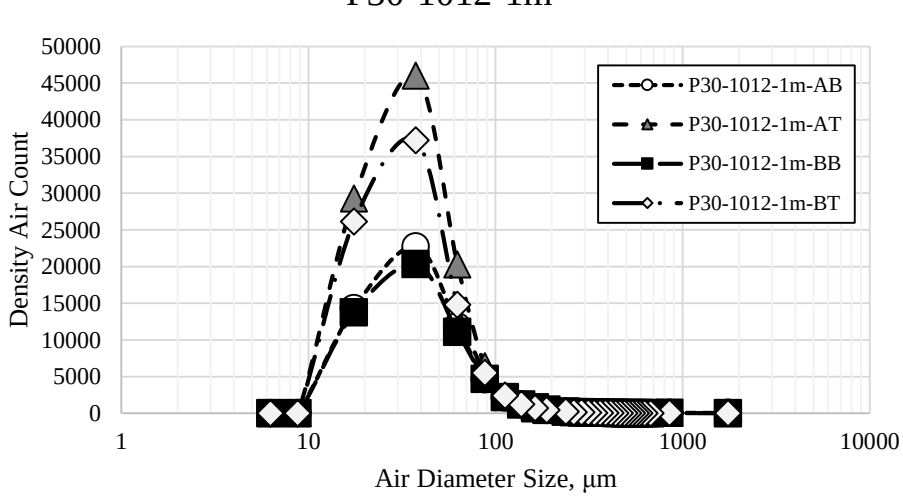

Figure 7-14 Distribution of air void size inside the upper and lower half (left and right) of a 4-inch diameter paste cylinder (with water-to-cement ratio 0.30 by mass) vibrated atop a 60 Hz vibration table for 1 min. High air-entraining admixture is incorporated into fresh mixture.

7.6.4 Total hardened air content in vibrated concrete beams

The nature of vibrating individual concrete cylinders (originating from different mixtures) yields to challenging interpretations. In order to overcome this challenge, multiple modulus of

rupture beams originating from one mixture were cast and vibrated at one end in order to better understand the extent to which air bubbles will move in fresh concrete.

Figures 7-15 and 7-16 show the total air content from samples excised from four separate beams. In Figure 7-15, a highly superplasticized concrete is subjected to either no vibration or vibration for 60 seconds. The mixture rheology is shown in Table 7-7 where the plastic viscosity is rather large. When subjected to 60 seconds of vibration, the extent of total air is greatly diminished particularly near the source of vibration at 3 inches (7.6 cm). As a function of distance, the extent of total air increases until approximately 40 cm where there is a decrease again. This decrease is likely attributable to the confined nature of the beam mold at the extreme end where vibrations carried through the steel mold reverberate strongly at the end. Immersed acceleration data also suggests that there is an increase in peak acceleration near the end of the prismatic member (see Chapter 6) suggesting that this effect is artificially induced by the mold geometry.

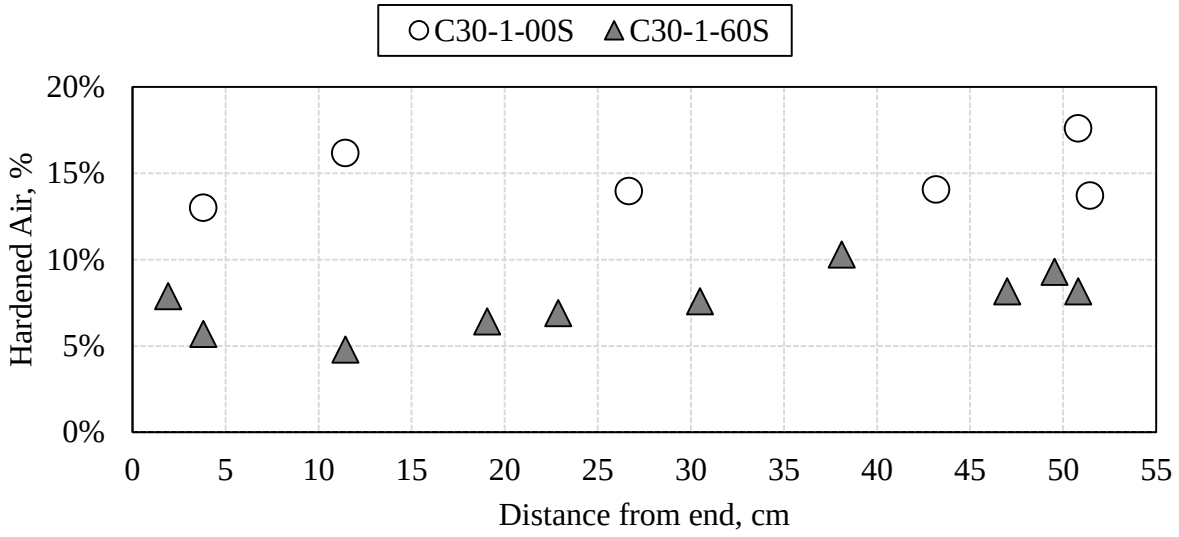

Figure 7-15 Cumulative hardened air content in excised samples of prismatic beams of hardened concrete (water-to-cement ratio of 0.30), coarse aggregate content of 43 % and fine aggregate content of 27 % (by volume) vibrated for 0 sec and 60 seconds at one end using a 220 Hz immersion probe.

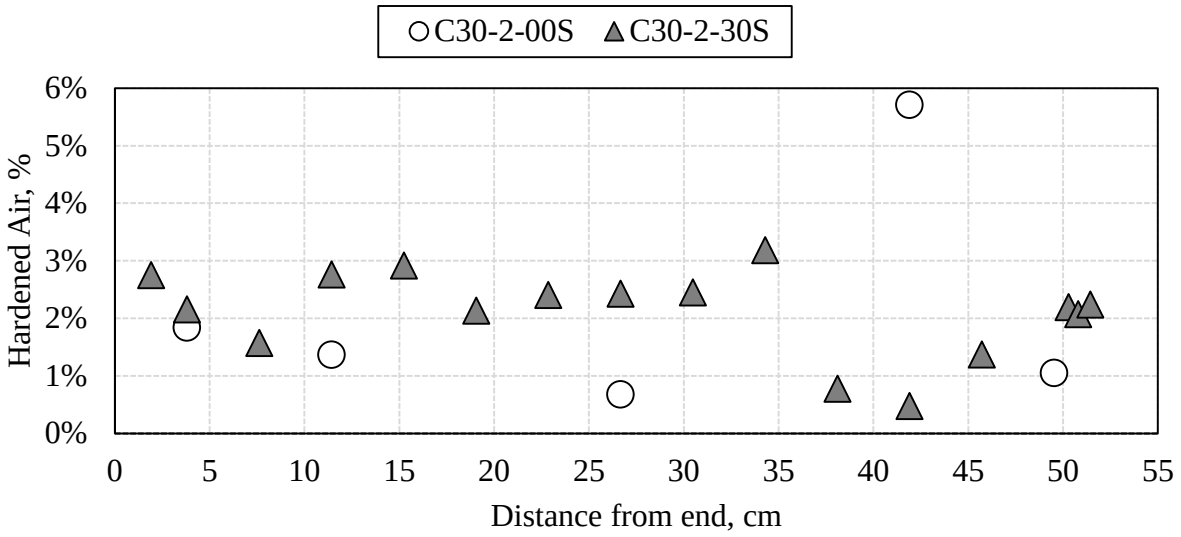

Figure 7-16 Cumulative hardened air content in excised samples of prismatic beams of hardened concrete (second trial with water-to-cement ratio of 0.30), coarse aggregate content of 43 % and fine aggregate content of 27 % (by volume) vibrated for 0 sec and 60 seconds at one end using a 220 Hz immersion probe.

Figure 7-16 shows a second trial of concrete where less superplasticizer is used. In such a case, the yield stress is larger while the plastic viscosity is lower in relation to the first trial of concrete (see Table 7-7). In this case, the two concrete beams are either not vibrated or vibrated for 30 seconds. At 30 seconds, it appears as though the total air content increases with relation to the non-vibrated beam case. This result is unexpected. However, an appreciably dip at 7.62 cm is still evident near the vibration probe. In order to better understand the relationship between air loss and the function of distance, it is necessary to excise from representative samples from concrete beams. Figures 7-17 through 7-20 show twelve beams with varying aggregate contents vibrated in a similar arrangement from 0, 30, to 60 seconds. Each triplet of beams originates from a singular mixture whose rheology is noted in Table 7-7.

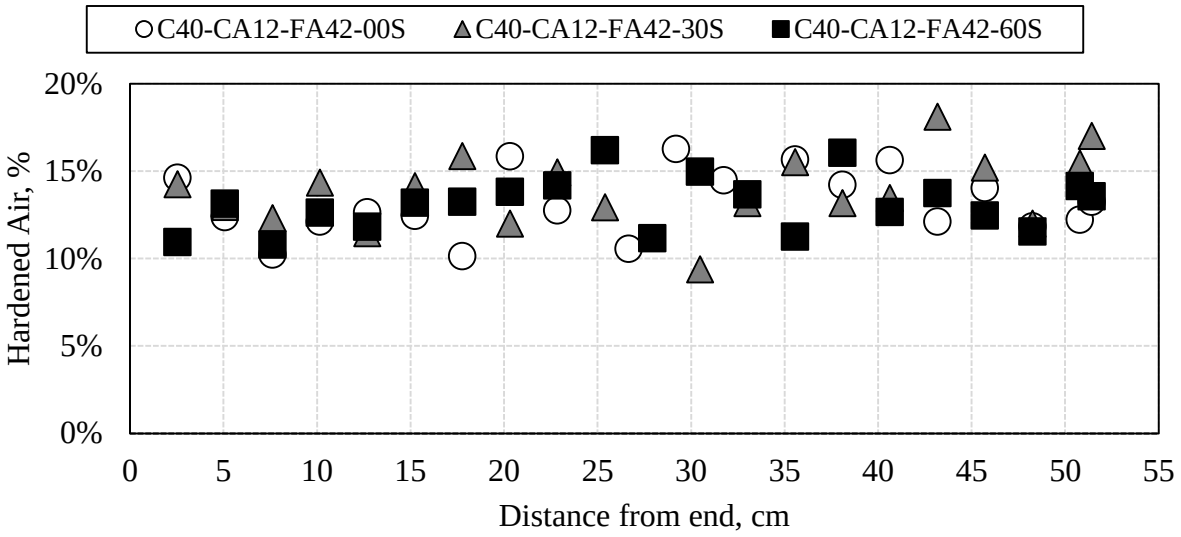

Figure 7-17 Cumulative hardened air content in excised samples of prismatic beams of hardened concrete (water-to-cement ratio of 0.40), coarse aggregate content of 12 % and fine aggregate content of 42 % (by volume) vibrated for 0, 30, and 60 seconds at one end using a 220 Hz immersion probe.

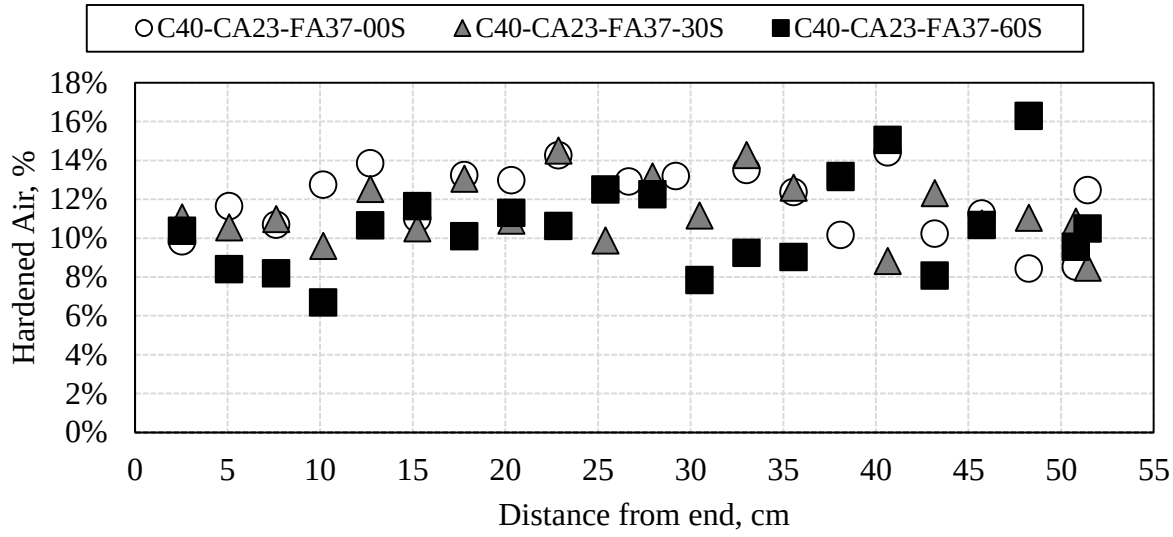

Figure 7-18 Cumulative hardened air content in excised samples of prismatic beams of hardened concrete (water-to-cement ratio of 0.40), coarse aggregate content of 23 % and fine aggregate content of 37 % (by volume) vibrated for 0, 30, and 60 seconds at one end using a 220 Hz immersion probe.

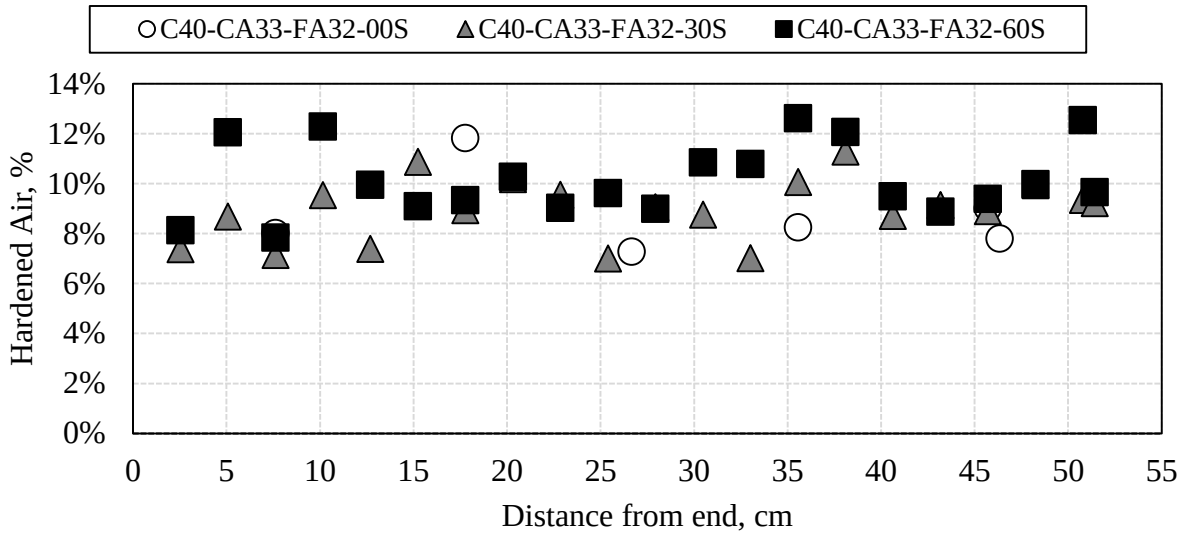

Figure 7-19 Cumulative hardened air content in excised samples of prismatic beams of hardened concrete (water-to-cement ratio of 0.40), coarse aggregate content of 33 % and fine aggregate content of 32 % (by volume) vibrated for 0, 30, and 60 seconds at one end using a 220 Hz immersion probe.

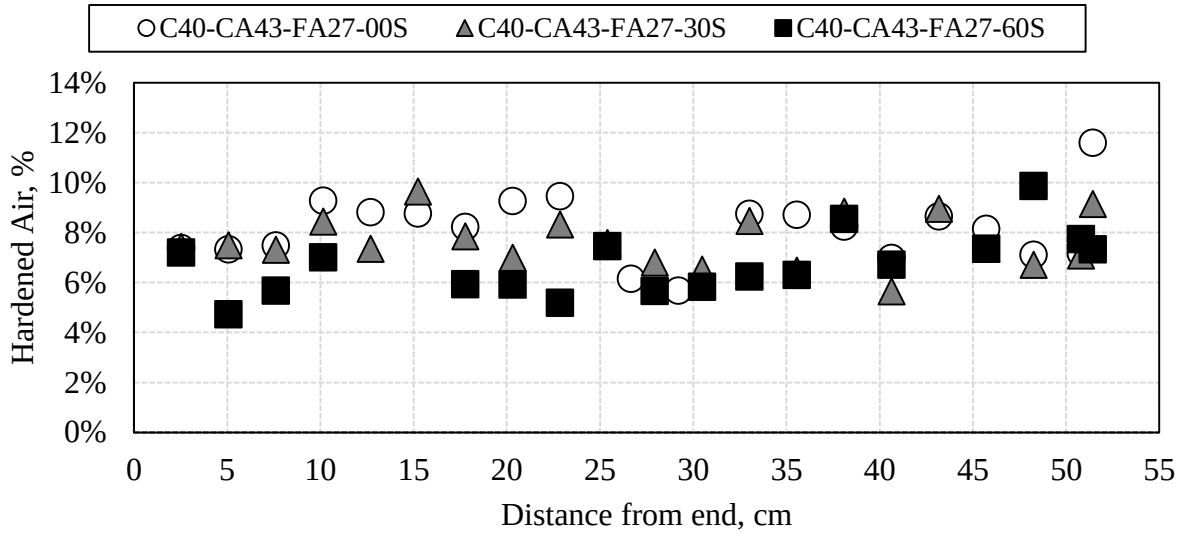

Figure 7-20 Cumulative hardened air content in excised samples of prismatic beams of hardened concrete (water-to-cement ratio of 0.40), coarse aggregate content of 43 % and fine aggregate content of 27 % (by volume) vibrated for 0, 30, and 60 seconds at one end using a 220 Hz immersion probe.

In Chapter 6, there is an observation of dependence between large aggregate content and extent of peak acceleration, so in this chapter, the extent of air loss for increasing aggregate content is also considered. In Figure 7-17, there is 12% coarse aggregate content and 42% fine aggregate content by volume across all three beams vibrated for 0, 30, and 60 seconds. As a function of

distance, the total air content does not seem to appreciably change. In Figures 7-18 and 7-19, any loss of air content seems to be concentrated primarily near the immersion probe at 7.62 cm. In Figure 7-20, the total air content at 60 seconds of vibration seems to be appreciably lowered throughout the length of the beam with respect to the non-vibrated beam. The yield stress for this mixture is larger than it is for previous mixtures, but it is also more plasticized, meaning that the plastic viscosity is larger for the concrete mixture. However, the underlying suspension in this system with large aggregate content is appreciably lower than what is measured (see Chapter 5). As such, the loss of total air in this system is attributable more so to the superplasticized nature of the mix with large coarse aggregate content.

7.6.5 Total hardened air content in vibrated mortar beams

A trail mortar beam (M30-1) was also cast in order to glean differences between concrete and mortar. Figures 7-21 through 7-24 show the results of multiple mortar beam samples excised from variably vibrated molds. Figures 7-21 and 7-22 show relatively little change in total air content whereas Figures 7-23 and 7-24 show a drop in total air content at the site of the immersion probe. Unlike concrete (see Figure 7-20), there does not appear to be a case with mortar where there is an appreciable drop in total air content throughout the entire length of the beam despite there being constructive interference of vibrational energies as suggested by peak acceleration data (see Chapter 6).

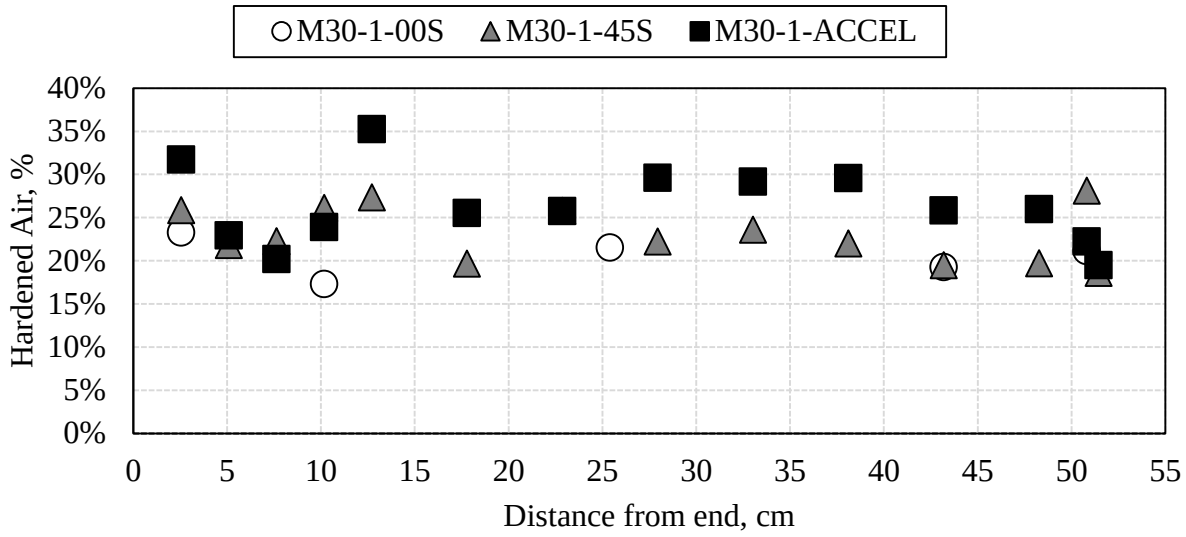

Figure 7-21 Cumulative hardened air content in excised samples of prismatic beams of hardened mortar (water-to-cement ratio of 0.30), fine aggregate content of 62 % (by volume) vibrated for 0, 30, and 60 seconds at one end using a 220 Hz immersion probe.

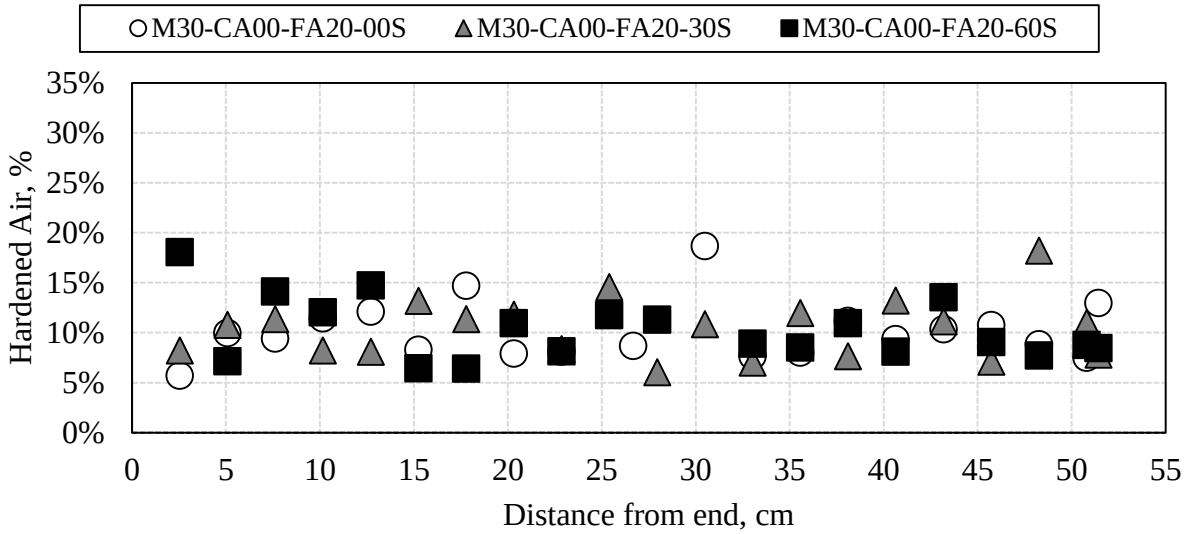

Figure 7-22 Cumulative hardened air content in excised samples of prismatic beams of hardened mortar (water-to-cement ratio of 0.30), fine aggregate content of 20 % (by volume) vibrated for 0, 30, and 60 seconds at one end using a 220 Hz immersion probe.

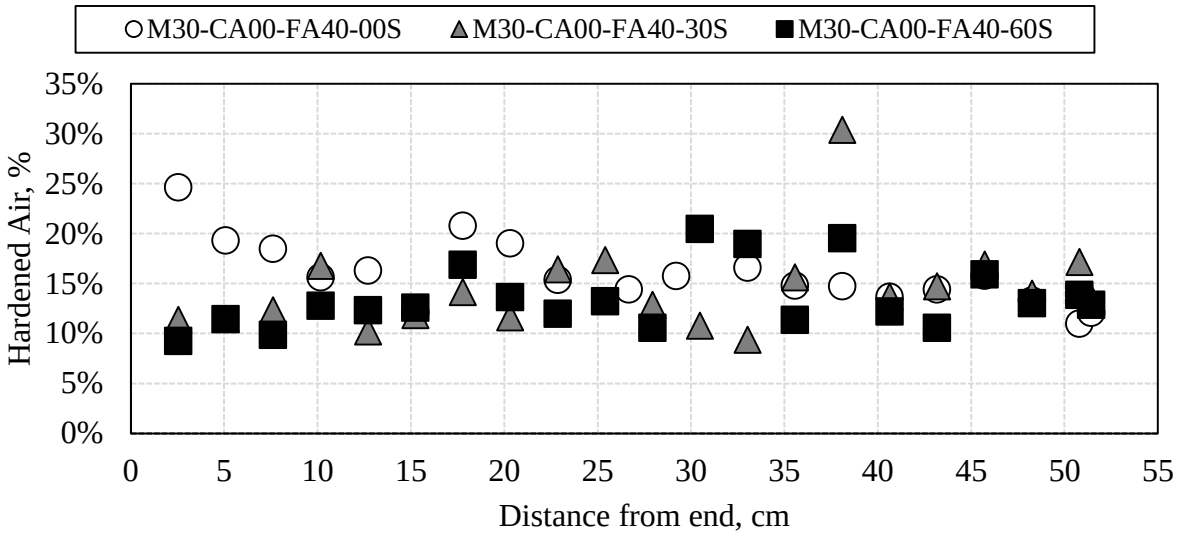

Figure 7-23 Cumulative hardened air content in excised samples of prismatic beams of hardened mortar (water-to-cement ratio of 0.30), fine aggregate content of 40 % (by volume) vibrated for 0, 30, and 60 seconds at one end using a 220 Hz immersion probe.

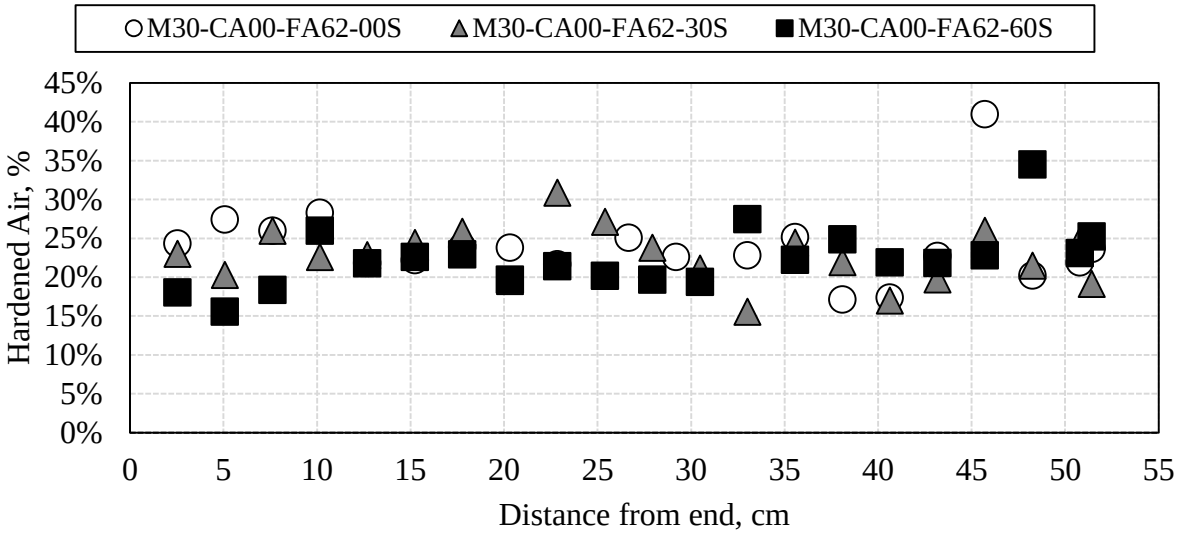

Figure 7-24 Cumulative hardened air content in excised samples of prismatic beams of hardened mortar (water-to-cement ratio of 0.30), fine aggregate content of 62 % (by volume) vibrated for 0, 30, and 60 seconds at one end using a 220 Hz immersion probe.

7.6.6 Total hardened air content in vibrated Portland cement beams

Hardened cement paste beams were also extracted from vibrated molds and three beams are shown in Figure 7-25. Much like mortar beams with low fine aggregate content, there is not a large change between two beams vibrated between 0 and 45 seconds. However, a third beam

subjected to continual vibration (approximately 60 seconds cumulative) called P30-1-ACCEL seems to have suffered extensive loss of total air content particularly at 7.62 cm where the immersion probe was located. This beam was used in order to characterize the extent of peak acceleration in fresh cement paste materials (see Figure 6-6). At extended vibration times, the total air content is appreciably low near the vibration probe at 7.62 cm. However, much like the cylindrical samples, it is necessary for more beam samples to be vibrated in order to better understand the loss of total air content.

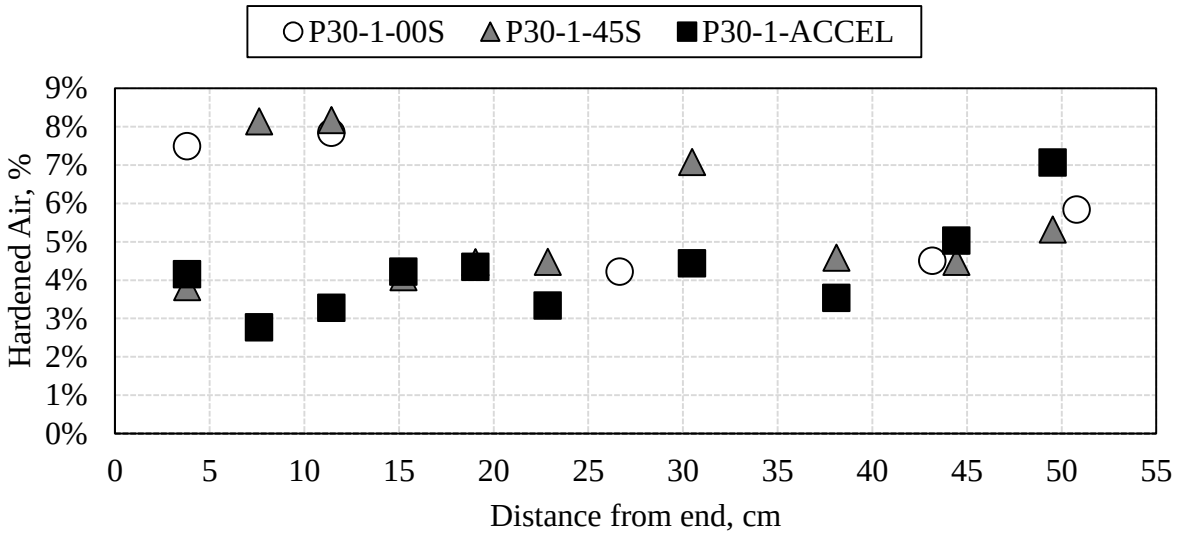

Figure 7-25 Cumulative hardened air content in excised samples of prismatic beams of hardened cement paste (water-to-cement ratio of 0.30) vibrated for 0, 30, and 60 seconds at one end using a 220 Hz immersion probe.

7.7 Summary of Chapter

Air is purposefully entrained into fresh Portland cement-based materials in order to enhance its durability against cyclic freeze-thaw damage. Immersion probe vibrators can suppress the yield stress of the fresh fluid leading to the upward, buoyant loss of entrained air. Concrete, mortar, and paste cylinders and beams were vibrated for varying degrees of time and the hardened air content was measured for excised samples. In this study, it is observed that:

- The distribution of air voids in vibrated concrete cylinders can vary greatly within a single sample when there is a strong expectation for similar results suggesting that a larger sample size of area is needed in order to draw meaningful conclusions.

- Although distribution of air voids are not meaningful across various tested samples, it is observed that their peaks are singularly oriented about a single value and are suppressed downward generally (and not shifted leftward or rightward). This strongly indicates that air bubbles are not being created or destroyed during the vibration process, yet they may still cluster together into single areas (particularly at the underside of aggregates).
- Air loss as a function of distance from a vibration source is greatly affected by two parameters: extent of superplasticizing agent used and extent of coarse aggregate volume fraction. When highly superplasticized, the underlying suspending fluid between particles is greatly suppressed in its yield stress which seemingly allows for air bubbles to more easily move upward. High superplasticity is often required when there is the presence of a large volume fraction of aggregates.

7.8 References

ASTM Standard C231, 2010 (2010), Standard Test Method for Air Content of Freshly Mixed Concrete the by Pressure Method," ASTM International, West Conshohocken, PA.

ASTM Standard C457, 2012 (2012), Standard Test Method for Microscopical Determination of Parameters of the Air-Void System in Hardened Concrete," ASTM International, West Conshohocken, PA.

Koehler, E. P., Fowler, D. W., Ferraris, C. F., and Amziane, S. "A new, portable rheometer for fresh self-consolidating concrete." *ACI Special Publication 233-7* (2006): 97 – 116.

Landgrebe, D. A. "The development of a spectral-spatial classifier for earth observational data." *Pattern Recognition* 12 (1980): 165 – 175.

Ley, T. M., and Bradden, T. "A test method to measure the freeze thaw durability of fresh concrete using overpressure." *Proceedings of the 2nd Transportation and Development Institute Congress*, Stillwater, Oklahoma, 2014, pp 79 – 87.

Peterson, K., Sutter, L., and Van Dam, T. "Air void analysis of hardened concrete with a high-resolution flatbed scanner" *Proceedings of the 24th International Conference on Cement Microscopy*, San Diego, California, 2002, pp 304 – 316.

Song, Y., Zou, R., Castaneda, D. I., Riding, K. A., and Lange, D. A. "Advances in Measuring Air-Void Parameters in Hardened Concrete Using a Flatbed Scanner." (under review). 2015.

CHAPTER 8 – CONCLUSIONS

This dissertation was motivated by a broader effort of the Federal Railroad Administration to better understand structural and material degradation mechanisms of high performance concrete used in railroad crossties specifically in high speed rail applications. This dissertation focused on two major thrusts: understanding the effects of external weather environments on the internal conditions of concrete crossties, and understanding the stability of entrained air bubbles within Bingham plastic (concrete) materials subjected to varying time periods of vibration. An experimental program was devised in order to evaluate and predict the extent of internal temperature and moisture conditions inside concrete crossties in track. Also, experimental work in rheology of fresh concrete, attenuation in peak vibratory acceleration, and extent of hardened air in hardened concrete is undertaken in order to understand the stability of entrained air in fresh concrete subjected to long periods of vibration time. This dissertation lends insight into the durability of high performance concrete used in wet, wintry climates and reinforces the notion that high performance concrete is susceptible to high saturation and thus requires appropriate addition and quality assurance of entrained air.

8.1 Concluding Remarks

In the first thrust of this dissertation, an experimental program was devised and modeling was pursued in order to predict the internal temperature and moisture conditions of concrete crossties in track. In Chapter 2, instrumented crossties were monitored over two winters to measure the internal temperature and relative humidity. These experimental values were compared against two 1-dimensional models that predict temperature (or relative humidity) gradients in a layered system of infinite halfspaces. It was found that the temperature model is adequate to predict the internal temperature distribution particularly during the winter months, but is not appropriate to predict the temperature distribution inside a concrete crosstie during the summer months. Moreover, it was found that additional layered structures of steel (rail) and polyurethane (pads) are not necessary in the estimation of the internal temperature distribution, meaning that the conditions underneath the rail seat area can be simply solved. The relative humidity within the concrete crosstie is similarly predicted using a 1-dimensional mass transport model and it was found that

simply altering the boundary conditions to extend the instance of 100% relative humidity after a significant precipitation even is sufficient to characterize the internal relative humidity.

Internal relative humidity is not wholly indicative of the state of moisture inside a porous solid because it is a direct measurement of the state of gaseous water vapor irrespective of the volume of liquid water. Empirical correlations for concrete have been made that associate the degree of liquid saturation to the internal relative humidity. Any correlation, however, is limited because the pore size distribution within the hydrated Portland cement paste microstructure varies across millions of locations inside concrete crossties. Factors such as water-to-cement ratio, alkalinity of the pore solution, salts, and cracks can strongly influence the distribution of local pore sizes and their interconnectivity to one another. In Chapter 3, a moisture sensor used in agricultural applications is installed into a concrete and its readings are compared against a relative humidity sensor that is also installed. The two measures are correlated to construct a relationship between the state of liquid moisture inside the low water-to-cement ratio (0.30 by mass) concrete and compare favorably with other empirical relationships in that there is a large increase in saturation at very large (< 95%) relative humidity values. Moreover, hysteric behavior is observed indicating that the empirical relationship in high performance concrete can be driven by a number of factors including geometry (e.g, filling and draining of cylindrical pores) and changing pore solution alkaline concentrations.

The established correlation between relative humidity and degree of saturation can be joined with the temperature modeling effort in order to predict the number of mutual instances in which a freezing event occurs whilst the concrete microstructures is critically (S > 86%) saturated. Chapter 4 joins the efforts of Chapters 2 and 3 to predict the number of freeze-thaw cycles of 1-dimensional concrete structures sitting atop well-drained aggregate ballasts in two wet, wintry locations: Lytton, BC, Canada; and Rantoul, IL, USA. The modeling effort in this chapter shows that the number of freeze-thaw cycles experienced at the surface of the concrete (at a depth of 5 mm) is approximately 20% fewer than the number of freeze-thaw cycles that occur in air. Additionally, it is elucidated that there is a gradient of freeze-thaw cycles that occurs within the concrete material due to the thermally insulating nature of the concrete material mass and the aggregate ballast. As such, it is affirmed that freeze-thaw damage is often a scaling problem where damage will initially manifest itself at the surface nearest to the environment. By adopting limiting

criteria (i.e., rate of freezing, extent of freezing, extent of saturation, etc.), it is possible to suppress the number of predicted freeze-thaw cycles in concrete materials; however, it is necessary to better understand limiting factors of in-situ concrete with more laboratory testing of instrumented samples in accelerated freeze-thaw testing (not done in this dissertation).

The first thrust of this dissertation critically establishes that instances of high degree of saturation are possible in high performance concrete members sitting atop well-drained aggregate ballasts, meaning that an air-entrainment system is required in order to withstand freeze-thaw damage. In the second thrust of this dissertation, the stability of entrained air bubbles is studied as the fresh concrete material is subjected to consolidating vibration. The movement of any air bubble within a neat fluid is governed by the viscosity (rheology) of the fluid; however, concrete is a complicated suspension of particles suspended in a chemically changing fluid (i.e. cement paste) that is most simply characterized as a yield-stress fluid (Bingham plastic). As such, it is necessary to better understand the movement of air bubbles in this system as affected by external consolidating vibration and mixture design. In Chapter 5, the change in rheology is observed during increasing intensity of external consolidation and it is found that there is a reduction in the yield-stress value for increasing vibratory energy. This behavior is partly explained by the breakup of aggregate-to-aggregate contact (disruption of force chains) which can be better predicted through more study. Moreover, it is better understood that highly superplasticized concrete mixtures (with low yield-stress and high viscosity) are more susceptible than conventional concrete (high yield-stress and low viscosity) in part because the fluidity of the underlying fluid is more strongly affected in a highly superplasticized mixture (which is often more granular).

The presence of aggregates appears to play a role in the propagation of consolidating vibrational energy which in turn results in the increase of entrained air loss. To better understand this, an experimental program is devised in Chapter 6 where different rheological fluids (Portland cement-based and model materials) are considered. When only neat fluids (cement paste or Carbopol gel) are vibrated, the influence of consolidating vibration is limited to near the vibration source (immersion probe) irrespective of changing rheology. However, in the presence of aggregates, the extension of vibration increases in accordance to increasing aggregate volume content. Current design specifications for the consolidation of concrete in the field emphasize the rheological properties of the mixture in achieving satisfactory compaction; however, the

granularity (volume of aggregates) and rheology are closely interlinked suggesting that a better understanding of the extent of vibratory influence may be better governed by extent of aggregate packing.

Chapter 7 naturally follows the experimental program outlined in Chapters 5 and 6 where the hardened air content is now investigated as a function distance from a vibration source. In this study, polished 2-dimensional sections of concrete, mortar, and paste are investigated for their total air content and distribution of air void diameter size. It is generally found that there is appreciable air loss near the immersion probe vibrator in all instances (concrete, mortar, and paste), but that appreciable air loss significantly away from the source of vibration is possible only in a highly superplasticized mixture where the yield-stress is significantly reduced. The plastic viscosity may vary significantly across mixture types and it is known to govern the speed of buoyant bubble rise; however the suppression of the rheological yield stress seems to more significantly govern the total extent of air loss. In order to overcome the statistical shortcomings of this study, it may be necessary to study larger areas (i.e., greater number of samples) in order to better understand the extent of air loss with a greater degree of statistical significance.

Summarily, this dissertation finds that high performance concrete with low water-to-cement ratio mixture design installed atop well-drained aggregate ballasts is susceptible to instances of high saturation, meaning that it can undergo freeze-thaw damage. In order to make concrete infrastructure more resilient, it is necessary to maintain high quality air entrainment systems in hardened concrete with consideration for highly superplasticized concrete mixtures that undergo vibration (through transportation or consolidation).

8.2 Recommendations for Future Research

The effort in this dissertation focuses on joining disparate knowledge from different fields (e.g., civil engineering, meteorology, and rheology) in order to address a question sought by practitioners: are high-performance concrete crossties sufficiently resilient against freeze-thaw damage without the need for an air-entrainment system? The findings of this dissertation strongly suggest that any concrete infrastructure exposed to wet, wintry climates can be susceptible to freeze-thaw cycles, but a reduction of cumulative cycles may be considered. The work in this

dissertation is limited by available funding and time, however, so it is always possible to delve further into different research topics that can be pursued in the future.

The environmental modeling effort was limited to a 1-dimensional model despite the application being a complicated 3-dimensional system with different civil engineering materials. As a first-principles approach, the 1-dimensional models are adequate to predict the internal distribution of temperature and humidity levels, but are limited to the interior of the finite-width concrete in wintry months considered in this study. A future study can consider a 2- or 3-dimensional set of models that better predict the distribution of temperature and humidity levels. In such a case, a better understanding of scaling damage near boundaries can be accomplished. An initial attempt using finite element modeling is readily possible, but an analytical solution grounded in physical phenomena is often desired.

Internal relative humidity and degree of saturation are complicated to predict in material systems like concrete which have varying pore size distributions (and connectivity) within low- and high-density CSH gel, bulk paste and ITZ paste, porosity in aggregates, fine-width (e.g., drying shrinkage and bursting strain) cracks and large-width (e.g., plastic shrinkage and structural) cracks. A future study can be sought to better relate these two features if in-situ characterization techniques can be established. One such possible technique is to use micro- or milli-wave radiation to back-calculate pore size distribution if in-situ pore solution and degree of saturation can be estimated. This problem in poromechanics is vastly complicated and can merit several decades of additional research.

Lastly, principles of fluid mechanics and rheology can be better adopted into the civil engineering materials discipline in order to better understand the flowability of aggregates past each other in early mixing and placement. Chapters 5, 6, and 7 in this study can be joined neatly with a set of rheological models that predict the interstitial flow and yielding of moving aggregates (translation and rotation). The interstitial yielding of paste between coarse aggregates would allow fine aggregates to sink downward and allow buoyant air bubbles to float upward. This complicated scenario would require expansive computational processing power in order to adequately represent the complexity of fresh concrete as it is used as a civil engineering material.

APPENDIX – SUPPLEMENTAL MATERIAL

Appendices with additional information can be found in the supplemental file in accordance to the following Table of Contents for the Supplemental File.

TABLE OF CONTENTS FOR THE SUPPLEMENTAL FILE